Morphology and timing of submarine mass movements on the northwest British continental margin

Matthew John Owen

Environmental Change Research Centre, Department of Geography, University College London

A thesis submitted for the degree of doctor of philosophy at UCL

June 2013

Declaration:

I, Matthew John Owen confirm that the work presented in this thesis is my own. Where information has been derived from other sources, I confirm that this has been indicated in the thesis.

Acknowledgements

Last, but not least I thank my supervisors. Dave Long, was not an official supervisor, but despite this was always a welcoming presence in Edinburgh, found time to see me and offered helpful advice. Thanks also to Dave for inviting me to participate in research cruise CD 174, and thereby opening the door to my current career. Simon Day, for detailed comment, feedback and criticism; and for orchestrating my participation in BAS research cruise JR 206. Finally, thanks to Mark Maslin, for offering constant encouragement regarding whatever I happened to be doing at the time, even if it was utterly unrelated to this thesis.

Abstract

A variety of factors influence the stability of submarine slopes and this thesis investigates those operating on the northwest British continental margin and Barra Fan. Through analysis of North Atlantic sector submarine mass movements, a conceptual model of continental slope failure is proposed and examined against the Peach slide case study. Situated on the eastern flank of the Rockall Trough, the Barra Fan is subject to cyclonic ocean circulation and has experienced growth since continental uplift during the mid-Pliocene. Surface and shallow-subsurface morphology of the fan is determined using pinger sub-bottom profile (paper records scanned and converted to SEGY format), sidescan sonar and multibeam echosounder data. A number of different acoustic facies are mapped, including: contourites, hemipelagites and debris flows. Analysis of gravity core 56/-10/239 identifies a debris flow containing material of glacial age and AMS ^{14}C dating of planktonic foraminifera constrain emplacement prior to 11.9 ka cal BP. Reference to additional sediment cores located in the Barra Fan region (MD95-2006 and 56/-10/36) allows the development of a chronology for the contourites and hemipelagites interpreted during geophysical investigation. This allows constraint of two periods of slope failure during the late Pleistocene: the first between 21 and 20 ka cal BP, shortly after the British ice sheet's maximum advance; and the second between 12 and 11 ka cal BP at the termination of the Younger Dryas stadial. Processes similar to those on the Norwegian continental margin seem to operate on the northwest British continental margin, the morphology and setting of the Peach slide is similar to Storegga and Trænadjupet, suggesting that similar processes initiated failure. Important roles seem to be played by contouritic and glaciogenic sedimentation, producing excess pore pressure in the fan's sediments with fluid expulsion visible in the acoustic data.

Contents

*Appendices are also included digitally with the accompanying DVD.

List of Figures

List of Tables

List of Equations

1. Introduction

1.1. Introduction to thesis

Continental margin submarine mass movements are an important component of the marine system. They play a major role in transporting sediments from the continental shelf into the deep water of the abyss and the ocean basins. They have the potential to influence climate change through the release of gas hydrates (Kennett, 2003; Maslin et al., 2004), are a hazard to seabed infrastructure (Bea et al., 1983; Gilbert et al., 2007; Hsu et al., 2008) and may be tsunamigenic (Bondevik et al., 2005; Tappin et al., 2008).

This thesis takes two approaches to improve understanding of the processes that cause submarine mass movements to occur.

First, an extensive study of the occurrence and cause of mass movements is undertaken. Through this research a conceptual model of occurrence and cause of submarine mass movement is developed and the relationship between mass movement and climate indicators examined.

Second, the main body of the thesis applies this conceptual model to a study of the Barra Fan and the Peach slide. This submarine mass movement complex, situated on the northwest British continental margin, consists of at least four Pleistocene mass movement deposits (Holmes et al., 1998). This thesis focuses on the most recent Peach 4 debrite: an event that is believed to be of late-glacial age (Holmes et al., 1998; Armishaw, 1999; Armishaw et al., 2000).

This event is regarded as a useful case study for high latitude, passive margin continental slope submarine mass movements and may be analogous to events that may be triggered by contemporary deglaciation in Greenland and Antarctica.

This thesis questions what the key processes operating in the development of the Barra Fan and Peach slide are. To facilitate this a number of specific questions are asked. First, when did the Peach 4 debrite occur? Second, what factors (environmental and geological) are key in the occurrence of mass movement on the northwest British continental margin? Third, how does this greater understanding of sedimentology allow understanding of the processes of causation?

1.2. Rationale

1.2.1. Terminology

In the context of this thesis the term submarine mass movement refers to the downslope transport of sediments on the seabed. The term encompasses a wide range

of processes, including cohesive transport (such as slides and slumps) and disintegrative transport (such as turbidity currents and debris flows) (Coleman and Prior, 1988; Hampton et al., 1996; Mulder and Cochonat, 1996). As such it is important to be cautious when discussing specifics from a general term. For instance some processes may result in high velocity downslope movement (e.g. Grand Banks turbidite (Piper et al., 1999a)) and others in a more gradual creep (Masson et al., 2006). Turbidity currents may deposit sediments over 1000 km from the initial failure (Talling et al., 2007), whereas cohesive transport is associated with shorter distances. A process' attributes (e.g. velocity or cohesion) will influence the severity or magnitude of the hazard posed, such as efficiency of tsunami generation (Ward, 2001; Gisler et al., 2010) or methane release (Buffett and Archer, 2004).

In this thesis the term submarine mass movement is used as an umbrella for all mass movement events. When discussing specific mass movements more precise terms (such as slide, slump, debris flow and turbidity current) are used. Mass movements associated with volcanic flank collapses (e.g. El Golfo debris avalanche (Masson et al., 2002) and Hawaiian landslides (Moore et al., 1989)) are beyond the main scope of this thesis and are only discussed briefly.

When referring to the Peach mass movement complex the term Peach slide (following from Holmes et al., 1998) is used to describe the sequence of four Pleistocene debrite deposits. Within this, the most recent mass movement is referred to as Peach 4. Later chapters of this thesis will use more specific terminology to describe this mass movement's morphology.

1.2.2. Relevance of submarine mass movements

Submarine mass movements pose a significant hazard in terms of tsunami generation (Tappin et al., 2001; Bondevik et al., 2005) and damage to seabed infrastructure such as cables (Piper and Asku, 1987; Piper et al., 1999a; Hsu et al., 2008) and pipelines (Gilbert et al., 2007). Additionally they may play a significant role in the carbon cycle: releasing carbon held in clathrate bonds into the water column and possibly the atmosphere (Norris and Röhl, 1999; Kennett, 2003; Maslin et al., 2004).

Therefore, an improvement in our understanding of the processes and mechanics of submarine mass movement may enable greater understanding of and preparedness for such hazards.

1.3. Methodology

This thesis employs a broad range of techniques to improve understanding of submarine mass movements in general and the Peach slide in particular. A re-examination and analysis of the considerable body of work available on the subject is used to develop a conceptual model of continental margin submarine mass movement occurrence.

The Barra Fan study site was chosen in order to use previously acquired geophysical data and geological samples. This methodology is consistent with the view that there are a vast amount of geological and geophysical data already collected (e.g. OneGeology, 2011) and that before expending financial resources acquiring more data it is wise to fully explore that which is already available.

1.3.1. <u>Previous work on the northwest British continental margin and Barra Fan</u>

A large volume of work, including several PhD theses, has been conducted in the area over the last 20 years. Selby (1989) conducted a seismic and lithostratigraphic analysis of glaciation of the Hebrides Shelf, confirming the presence of shelf-edge ice, though also examining sedimentation on the slope.

Dodd (1995) presents a comparison of the Var Canyon and Barra Fan, primarily based on geotechnical data. Describing her study as a 'first step' towards investigating slope stability on the Barra Fan, Dodd (1995) employed seismic data to produce a refined bathymetric map, however, due to the complexity of the facies no detailed sub-bottom interpretation was performed.

Howe (1996) presents a seismic and sedimentological study into sediment waves at the northern boundary of the Barra Fan, which documents a range of depositional processes including contouritic and what he terms 'hemiturbidite'.

Holmes et al. (1998) present a key study that documents Peach debrites 1 - 4. The study maps the debrites and proposes approximate timing: early Pleistocene for debrite 1 and (on the basis of truncated iceberg scours) post glacial for debrite 4. Work by Maslin et al. (2004) further refine the debrite ages and is discussed in section 2.5.1.3.

Barra Fan sedimentation processes were investigated by Armishaw (1999) who argued in favour of an important role for alongslope and downslope sediment transport in the development of the fan. This thesis, combined with later work, presented evidence of surface sediments consisting of both muddy and sandy contourites reflecting the role of recent bottom current circulation (Armishaw, 1999; Armishaw et al., 2000).

The relationship between Barra Fan sedimentation and the British ice sheet was investigated by Knutz et al. (2001), documenting and dating glacimarine sedimentation. Additional work investigated the Barra Fan drift and provided seismo-stratigraphic age constraint, based on correlation with piston core MD95-2006, of the Peach 3 debrite (Knutz et al., 2002).

1.3.2. <u>New advances in this study</u>

This thesis builds on the previous Barra Fan studies and produces novel results by advancing our knowledge in the following ways. The complexity of the sub-surface and the difficulties of interpreting the seismic data were noted by Dodd (1995), therefore, geophysical work in chapter four takes advantage of software developments to map the shallow-subsurface morphology of the Barra Fan. This new database of scanned seismic data shows the distribution of expelled fluid in the region, as well as preferential accumulation of sediments within the Peach slide scar for the first time. Armishaw (1999) suggests that future work should attempt to date material overlying the most recent debrite. To this end, chapter five of this thesis uses AMS ^{14}C dating of planktonic foraminifera to date the Peach 4 debrite. This is the first time that material, immediately, overlying this slope failure has been dated. Chapter six produces a new synthesis of sedimentation on Barra Fan, which greatly enhances our knowledge of mass movement in the region and the roles played by glaciogenic sedimentation and ocean circulation.

The majority of investigations concerning mass movement on the Barra Fan pre-date the year 2000 (e.g. Wild, 1985; Cook, 1989; Selby, 1989; Holmes, 1994; Dodd, 1995; Howe, 1996; Armishaw et al., 1998; Holmes et al., 1998; Armishaw, 1999; Armishaw et al., 2000), with only limited work conducted more recently (Knutz et al., 2002). As such, it is possible to employ Geographical Information System (GIS) software to provide more detailed and computationally complex analysis than was previously possible. To this end this thesis constructs a model of the Barra Fan using all available data in ArcGIS™.

Employing a combination of geophysics, sedimentology, sediment geochemistry and isotope geochemistry the Barra Fan study is an attempt at an integrated investigation of a mass movement event and the environment in which it occurred. Through geophysical techniques such as multibeam echo sounder bathymetric mapping and sub-bottom profiling the geographical extents and morphological features of a mass movement may be determined, both at the seabed and within the sedimentary column. Sediment core analysis allows much more fine resolution analysis of the interface between failed and unfailed material.

Via the combined investigation of geophysical and geological data it is possible to gain a greater understanding of the timing (via AMS ^{14}C dating of $CaCO_3$ shells in pelagic sediments overlying failed material (e.g. Rothwell et al., 1998)) and processes of sediment failure, transport and deposition (through seabed morphology, distribution of acoustic facies and particle size analysis (Wilson et al., 2004; e.g. Jenner et al., 2007; Tripsanas et al., 2007; Tripsanas et al., 2008)).

1.4. Aim and objectives

The overall aim of this thesis is to answer the questions posed in section 1.1 and in so doing improve understanding of the processes governing the occurrence of continental slope submarine mass movements and the hazards they pose. Within this, the project focuses on the Barra Fan and investigates the timing and morphology of the Peach 4 debrite.

Specific objectives of the Barra Fan site study are:

i. Employ geological and geophysical methods to understand submarine mass movement in the area.

ii. Map the different acoustic facies associated with submarine mass movement and thereby reconstruct the mechanisms of sediment failure and transport.

iii. Make full use of GIS software to improve interpretation and analysis of the Barra Fan environment.

iv. Improve understanding of the more recent submarine mass movements' timing and cause.

v. Make an assessment of the hazard potential of submarine mass movements occurring within the Barra Fan.

A range of techniques, including geophysical interpretation and GIS analysis, will be employed in an attempt to achieve these goals.

1.5. Outline of thesis

In addition to this introductory chapter this thesis is structured in six chapters. Chapter two provides an overview of continental slope submarine mass movements. The third chapter discusses the geological and oceanographic setting of the Barra Fan study site. Chapters four and five present the main body of the project's original geophysical and geological research, with a discussion of results and interpretations in chapter six. Conclusions are presented in chapter seven. Figure 1.1 presents an overview of the thesis' structure and demonstrates how the chapters interrelate.
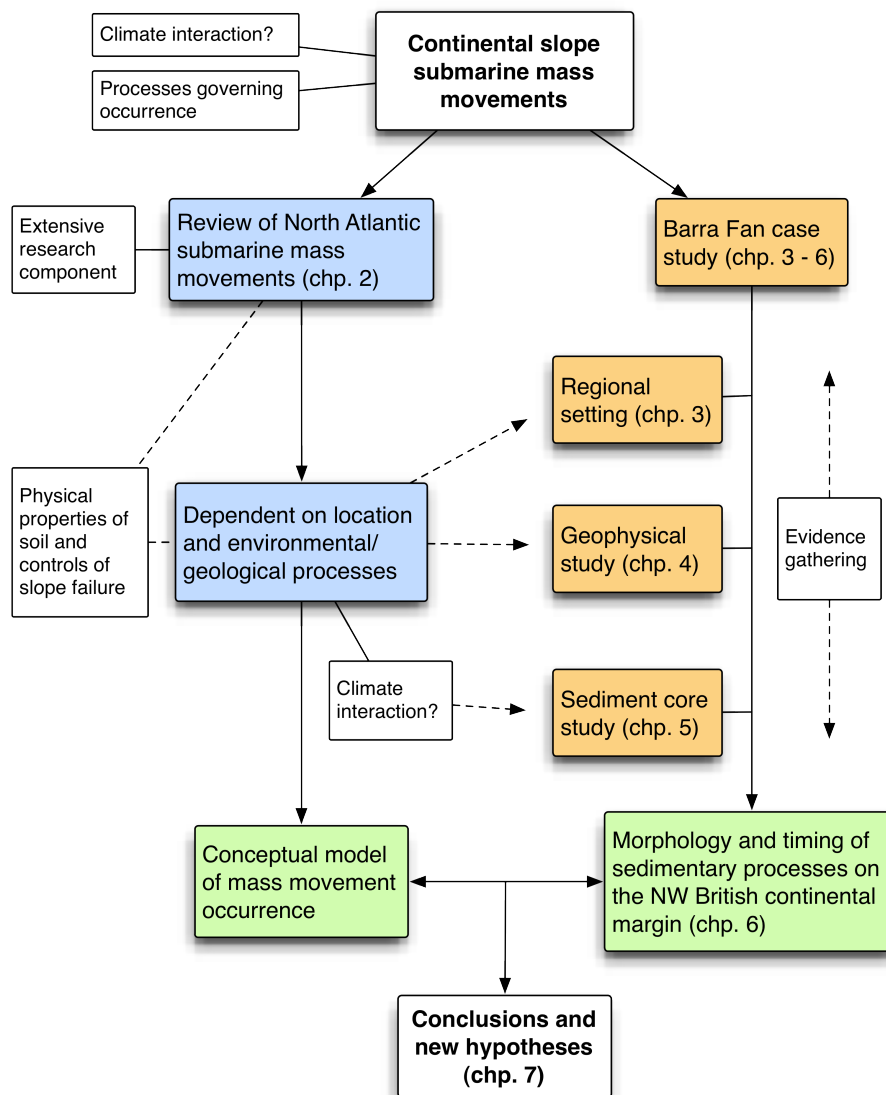
Figure 1.1: Thesis structure and relationships between chapters.

Chapter two presents a review of the occurrence and cause of continental slope submarine mass movements and proposes a conceptual model of slope failure. This provides a conceptual thread running through the remainder of the thesis. The chapter is largely based on work published by Owen et al. (2007). As well as providing a review of submarine mass movement theory, this chapter provides a brief investigation into the relationships between North Atlantic sector submarine mass movements and climate indicators (such as the GISP2 methane and sea-level records).

Chapter three reviews literature from the Barra Fan study site, neighbouring Rockall Trough and Hebrides Shelf: providing context for the application of the conceptual model of slope failure presented in chapter two, as well as foundations for the geophysical and geological investigation chapters that follow.

The geophysical component of the thesis is presented in chapter four. Through techniques of multibeam bathymetry, sub-bottom profiling and side-scan sonar the

Peach region of the Barra Fan is mapped and the extents and morphology of the Peach 4 debrite determined.

Chapter five focuses on geological investigation within the Barra Fan, specifically analysis of sediment core BGS CS 56/-10/239, which is located in the headwall area of Peach 4. Through analysis of this core, this thesis attempts to achieve its objective of refining the understanding the event's timing. To this end the chapter presents a detailed and comprehensive sedimentological and geochemical analysis of BGS CS 56/-10/239. A selection of the data and interpretation presented in this chapter was published by Owen et al. (2010). This thesis presents more data and an updated interpretation, reflecting the AMS ^{14}C dates obtained after paper publication.

Chapter six presents a synthesis of the combined geophysical and geological data, with an emphasis on the processes controlling mass movement on the Barra Fan. The discussion is widened to include previous work in the area, particularly work by Kroon et al. (1997; 2000 and their analysis of sediment core BGS CS 56/-10/36) and others concerned with the climatic and glacial history of the northwest British continental margin (for example Selby, 1989), as well as sedimentation on the Barra Fan (Howe, 1996; Holmes et al., 1998; Armishaw, 1999; Knutz et al., 2001; Knutz et al., 2002). This chapter refers to chapters two and three in order to explain why the northern flank of the Barra Fan is susceptible to large scale submarine sediment failures.

Chapter seven presents the key conclusions of this thesis as well as recommendations for future work in the Barra Fan region and in the field of continental slope submarine mass movements.

2. A review of the occurrence and cause of submarine mass movements and their relation to climate

2.1. Introduction to chapter

The following chapter is a development of work published in Quaternary Science Reviews by Owen et al. (2007). The intention is to provide a global review of the mechanical and geologic control of continental slope mass movements. In so doing the chapter seeks to answer two main questions. First, what is the current consensus on the factors that control the occurrence of submarine mass movement? Second, what evidence regarding cause have previous surveys of mass movement deposits/scars found? This work leads to the development of a conceptual model of continental slope failure, which is applied in later chapters of the thesis.

Additionally, recent (post 45 ka cal BP) North Atlantic sector submarine mass movements are analysed in relation to timing, sea-level variation and atmospheric methane concentrations. This review is based on a database of North Atlantic sector mass movements that has been developed from Owen (2000), Maslin et al. (2004) and finally Owen et al. (2007) as a part of this PhD project. Initially this approach sought to test whether their was a relationship between submarine mass movement and climate (i.e. Kennet et al.'s (2003) Clathrate Gun Hypothesis). However, as discussed later in this chapter it is felt that the data does not exist that would allow this relationship to be properly tested.

Although initial work, particularly with regard to compiling the database of submarine mass movements, was carried out prior to this thesis the vast majority of the work presented here was carried out during the PhD project. In particular, work on susceptibility of slopes to failure and the detailed analysis of individual mass movements' characteristics was undertaken entirely within the PhD (as demonstrated by the theoretical development between Maslin et al. (2004) and Owen et al. (2007)).

2.2. Occurrence of submarine mass movements

Before discussing regional and temporal occurrence of submarine mass movements it is necessary to briefly review the engineering and mechanical properties of marine sediments.

2.2.1. Physical properties of soil and the mechanics of sediment failure

In this section the term soil is used rather than sediment, reflecting the geological and engineering nomenclature with respect to physical properties and stability.

2.2.1.1. Physical properties of soil

A soil may be defined as being an unconsolidated assemblage of solid particles between which are voids (Bell, 1992). As such, when considering a soil's properties it is useful to consider the individual grains, the voids and the structure as a whole.

It is important to distinguish between cohesive soils, like clays and fine silts, and non-cohesive soils like coarser silts, sand, gravels and larger particles. The former are attracted to one and other by electro-chemical bonds and respond to stress as a matrix, whereas the coarser particles act individually and in this case the soil strength comes from inter-particle friction (Frossard, 1979).

The ratio of voids to particles in a given volume of soil equates to porosity, which in turn influences soil density (along with particle density). Porosity is determined by degree of consolidation, with more consolidated soils having lower porosities than looser packed, less consolidated soils. The connectivity of voids, or pores, determines the soil's permeability, or the ease with which water may pass through: the hydraulic conductivity.

Generally speaking, finer particles, such as clays, have lower permeabilities than coarser particles (Bell, 1992; Laberg and Vorren, 2000; Strout and Tjelta, 2005). However, permeability is also influenced by packing and size distribution, with loose well sorted soils having the greatest porosity values (Graton and Fraser, 1935).

2.2.1.2. Consistency of cohesive soils

Consistency of cohesive soil is determined by clay mineral composition and moisture content. The lower the moisture content, the stronger the attraction between particles and the more brittle the material. Based on the Atterberg tests a clay deposit may be defined as being: solid, semi-solid, plastic or liquid (Haigh et al., 2013). Plastic limit, and liquid limit define the water content required for the material to act as a plastic or liquid (Bell, 1992).

As consistency is largely governed by moisture content, greater consolidation is associated with solid, more brittle consistency and generally increases with depth in the sedimentary column. Conversely, less consolidated clays tend to show greater plasticity or liquidity and are located shallower in the sedimentary column. However, erosion may lead to overconsolidated materials being present in shallow locations (Bryn et al., 2005a).

2.2.1.3. Stress, strength and the role of pore fluid

Shear strength of a soil may be defined as being the maximum resistance to shear stress and when this maximum is reached the soil is regarded as having failed (Bell, 1992). The Coulomb criterion may be used to calculate resistance on a plane.

$$\tau = c + \sigma_n \tan \phi$$

Equation 2.1: Coulomb failure criterion.

Where τ is the shear stress acting along plane; c is cohesion; σ_n is the normal stress (acting perpendicular to the plane); and ϕ is the angle of shearing resistance. The resultant value of resistance is equal to the stress and the strength.

Stress that controls changes in volume and strength of a soil is known as effective stress (σ') and equates to the intergranular pressure that develops when a soil resists an applied load. An important role is played by the soil pore water, as this offers no resistance to the shear. Therefore, the total stress (σ) is equal to the pore water pressure (u) plus the effective stress; the Coulomb criterion is modified to the Mohr-Coulomb criterion in order to account for this.

$$\tau = c' + (\sigma - u) \tan \phi'$$

Equation 2.2: Mohr-Coulomb failure criterion.

Where c' is the effective cohesion and ϕ' is the effective friction angle. Hence, in saturated soils increased shear stress may be carried by the pore water, causing an increase in pore pressure and reduction in shear strength (Savage and Baum, 2005).

When a soil is loaded the void ratio decreases and settlement occurs. However, in the case of saturated soils the presence of pore water means that loading is accompanied by a equal increase in pore pressure (in excess to hydrostatic pressure); which dissipates with time in permeable soils. The rate at which this dissipation occurs is governed by Darcy's Law.

$$v = ki$$

Equation 2.3: Darcy's Law.

Where v is the rate of flow, k is the permeability coefficient and i the gradient of the potential head (measured in the direction of flow). When considered in a stratigraphic context this means that upwards fluid dissipation may generate excess pore pressure

(associated with a reduction in shear strength) below a layer with a lower permeability coefficient (Biscontin et al., 2004).

As water flows through a soil energy is transferred to the particles past which it flows, exerting a drag effect known as seepage force (Orange and Breen, 1992). If water flows toward the surface the effect is counter to gravity and reduces the effective stress. In areas where fissuring has occurred this can produce erosion as water moves preferentially through cracks in the soil removing sediments.

2.2.1.4. Mechanics of failure

A soil will fail when downslope (shear stress) force exceeds the resisting (shear strength) force. Sediments deposited in a state where shear strength exceeds shear stress will be stable. However, an alteration of this state, through either a reduction in shear strength or through an increase in shear stress operating on that sediment, can lead to failure (Biscontin et al., 2004).

Different materials respond to failure in different ways. Loose soils will contract, whereas dense soils will dilate in response to shearing. Liquefaction may occur when saturated, loosely packed soils experience increased excess pore pressure that reduces the intergranular forces: causing the material to act like a viscous liquid.

Cohesive soils may undergo strain-softening, that is to say excess pore pressure and reduction in strength (Kvalstad et al., 2005). Increased water content from excess pore pressure will influence the soil's consistency, potentially passing the plastic or liquid limit (see section 2.2.1.2) causing collapse of the overlying sedimentary column.

2.2.2. Controls on slope failure: susceptibility to failure and triggering of failure

Stability of a slope is determined by the balance of the destabilising forces (downslope component of gravity, seepage forces, pore fluid pressure) and the stabilising forces (slope – normal component of gravity × friction coefficient, cohesion). The balance between these is in engineering terms the factor of safety (F, the ratio of the two sets of opposing forces). As F decreases the susceptibility to failure increases as the additional, transient seismic or fluid pressure force needed to produce failure decreases (see also Sultan et al., 2004 for discussion of factor of safety).

From a geological perspective, this thesis distinguishes two categories of process that combine to produce the change in state from stable slope to failure and mass movement. These categories are susceptibility to failure and triggering mechanisms (susceptibility may be considered analogous to pre-conditioning as outlined by Masson et al. (2006)).

For a slope to fail, it must first be susceptible to failure when subjected to a triggering process (see section 2.2.2.2). This is a product of geological history and local environmental conditions. For example the development of a low permeability layer, in an otherwise relatively permeable environment, will lead to an increase in susceptibility to failure through prevention of pore water expulsion and the development of overpressure (see section 2.2.1.3; Dugan and Flemings, 2000; Volpi et al., 2003; Biscontin et al., 2004). Sedimentation patterns, glacial history and geological uplift are all factors that may influence a slope's susceptibility to fail without actually triggering a mass movement, or failure, event.

Trigger mechanisms tend to be identifiable events with clear temporal constraints. For instance an earthquake, or rapid destabilisation of a gas hydrate reservoir. This trigger will then influence the slope's geometry or sedimentological properties causing it to fail. For example, earthquake seismic shaking leads to vertical and horizontal movement which increases the gravimetric forces operating on the sediments and the pore pressure: reducing the sediment shear strength allowing failure to occur (see Wright and Rathje, 2003; Martel, 2004; Strout and Tjelta, 2005).

Climate change and mass movement may, therefore, interact in the first instance through the effect of climate upon susceptibility to failure of sedimented slopes, or through the effect of climate upon the occurrence and intensity of triggering events. The effect upon climate of the slope failures then has the potential to act either as a positive or as a negative feedback upon the primary (climate driven) interaction.

2.2.2.1. Susceptibility factors

Susceptibility factors are those which influence the long-term ($>10^2$ years) likelihood of a slope to fail.

In high latitudes the advance and retreat of large ice sheets influences the adjacent continental slopes' susceptibility to failure through a variety of mechanisms.

For example isostatic uplift, of the continental side of the slope, coupled with the flooding of the ocean basins (by rising sea level) leading to basin subsidence, causes slope steepening (Van Weering et al., 1998). A steeper slope increases the downslope gravimetric force (the shear stress) increasing the likelihood of failure. Depending on sediment type and overpressure conditions, submarine landslides can originate on nearly flat surfaces. Slope angles on the Mississippi delta are generally <0.4°, in this area mudslides caused by Hurricane Camille (1969) destroyed two platforms (Bea et al., 1983) and have been documented on angles of 0.01° (see Hampton et al., 1996 and references cited therein; Coleman et al., 1998; Walsh et al., 2006). A change in

slope angle of <1° can be very significant in terms of a slope's engineering safety factor and its susceptibility to fail.

Rapid sedimentation, and variation in sedimentation type as associated with the glacial cycles leaves a distinct sedimentary column. During interglacials pelagic sedimentation tends to dominate. This produces silts and muds: sediments associated with high water content. During glacials and particularly during deglaciation, glaciogenic sedimentation dominates. This is associated with a very rapid input of clay rich terrigenous sediments (see Dowdeswell and Elverhøi, 2002). Deposited on top of soft pelagic muds, the glaciogenic sediment will compact them and force the pore fluids out of the pore spaces and into migration. However, upon reaching the less permeable glaciogenic sediment, overpressure will build up causing a reduction in sediment shear strength and the development of a weak layer (see Orange and Breen, 1992; Dugan and Flemings, 2000; Volpi et al., 2003; Biscontin et al., 2004; Strout and Tjelta, 2005). A contrast must be drawn, on glaciated margins, between sedimentary fan locations and inter-fan locations. Work on the Svalbard margin by Dowdeswell and Elverhøi (2002) demonstrates that the fan areas are characterised by major sedimentary input during full glacial conditions. Interfan areas, however, receive high rates of sedimentation with the glacial advance, very low sedimentation during the last glacial maximum (LGM) and then a rapid increase in sedimentation rates during the deglaciation. Return to interglacial conditions during the Holocene is associated with low rates of sedimentation.

It is also important to consider sequences of units. Multiple glacial – interglacial cycles build up alternating undercompacted units and low-permeability layers. Periglacial outwash deposits (silts and sands) tend to have high-permeability and porosity, the rapid rates of deposition lead to inefficient compaction. The muds and hemipelagic sediments, which follow, will tend to have a lower permeability (due to lower rates of deposition and smaller particle size) and more efficient compaction. Owing to the lofting of buoyant meltwater (once coarser sediment has settled into lower levels of the flow) there is the potential for developing thick, highly permeable and porous units immediately below interglacial muds (Hesse et al., 2004). Sediments deposited away from ice-proximal regions may lack fine-grained fraction. Once these units are loaded by sediment deposition in the next glacial cycle there is a potential for development of excess pore pressure at the boundary between glacial sands and inter-glacial muds.

On the Norwegian margin contouritic sediments are important in determining the susceptibility of the slope to future failure. Infill drift contourites are deposited in existing slide scars, such as Storegga (Bryn et al., 2005b) and Trænadjupet (Laberg and

Vorren, 2000). They smooth the rough seabed created by the mass wasting processes and produce thick sediment bodies with high water content, which generate excess pore pressure when rapidly loaded by glaciogenic sediment. Bryn et al. (2005b) conclude that the distribution of contourite drifts will influence the position of the next generation of slides.

In order to understand a slope's susceptibility to failure it is important to consider the slope and its sediments at the granular level. According to Orange and Breen (1992) the forces acting at this scale are: gravity, seepage force and the frictional and cohesive strength of the material.

Sedimentation and alteration to the biogeochemcial properties of the sediments can increase the values of seepage force (and fluid migration), frictional strength of the material and pore pressure. Total stresses can be changed via sedimentological processes also.

As outlined in section 2.2.1.3, increased pore pressure reduces the capacity of sediments to resist shear stresses and increases the likelihood of failure (Biscontin et al., 2004; Savage and Baum, 2005; Strout and Tjelta, 2005). Several environmental changes may lead to excess pore pressure through rapid sedimentation: pelagic, contouritic and glaciogenic (Dugan and Flemings, 2000; Bryn et al., 2005b; Strout and Tjelta, 2005). Therefore, a slope may be susceptible to failure, due to excess pore pressure, because of its sedimentation history.
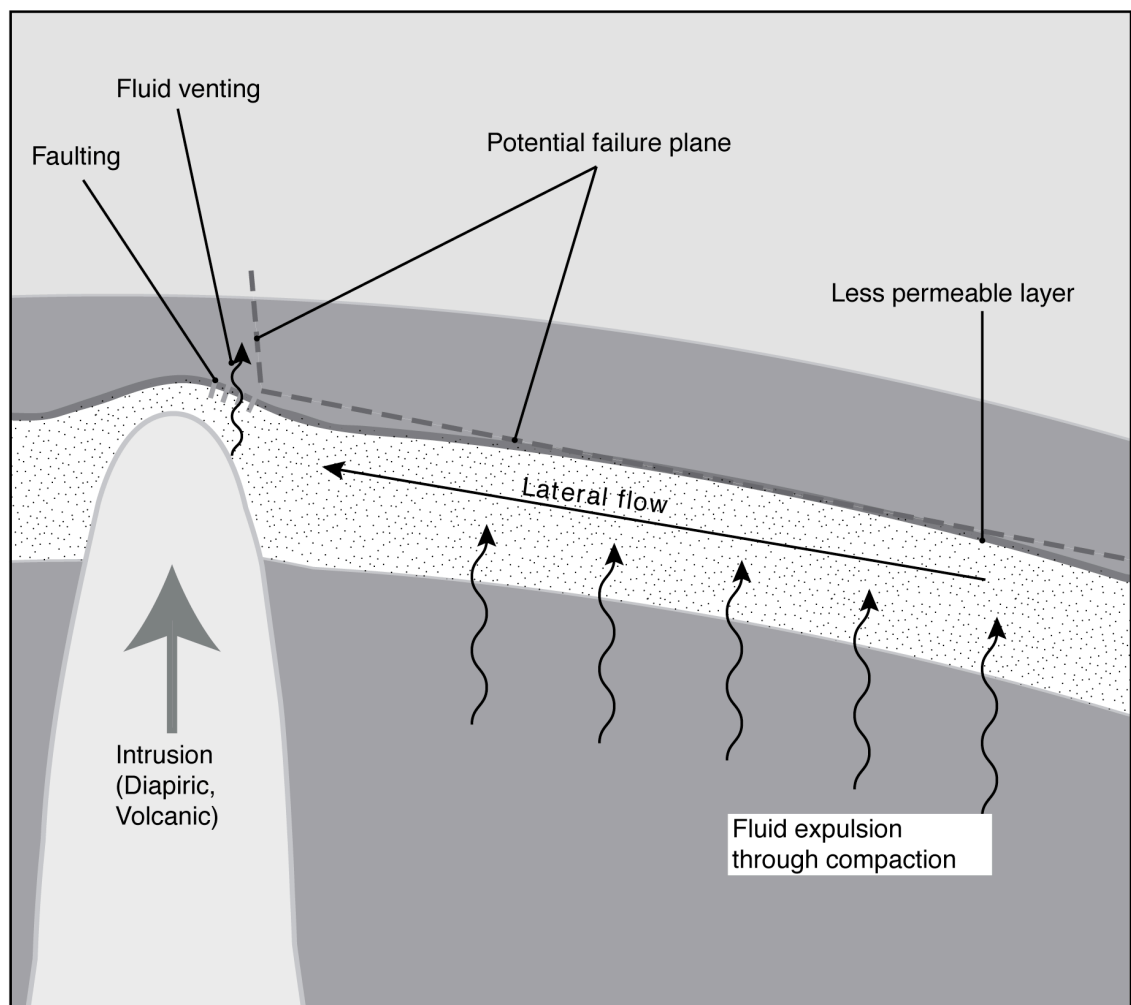
Figure 2.1: Development of a failure plane through overpressure, permeability variation and fluid flow.

Under the conditions associated with a homogeneous sedimentary column, deposited at a constant rate with constant porosity the sediments will compact, due to increased gravity loading, and the pore fluids will migrate up the column. However, the presence of faults and less permeable layers will alter the migration. Faults channel fluid flow (see Volpi et al., 2003). Less permeable layers initially prevent vertical passage, create overpressure beneath the cap and then potentially channel the flow beneath the cap creating lateral flow until a weakness in the overlying layer is found, when vertical migration can recommence (see Figure 2.1; Orange and Breen, 1992; Dugan and Flemings, 2000; Volpi et al., 2003).

Diagenetic modification of sediments may also increase susceptibility to failure, as demonstrated by the work of Volpi et al. (2003) investigating biogenic silica compaction. The transformation of Opal-A to Opal-CT is associated with a porosity reduction of ~20%, consequently a layer of excess pore pressure occurs beneath this diagenetic front. Seismic profiles provide evidence of fluid vents rising from this boundary, in addition to evidence of surface layer creep (Volpi et al., 2003). Pliocene

and early Pleistocene failures in the Storegga area may also be associated with Opal diagenesis (Lawrence and Cartwright, 2009).

Bacteria generate methane (biogenic) from the breakdown of organic rich sediments deep in the sedimentary column, this can migrate upwards to form clathrates, forming methane hydrate (Mienert et al., 1998; Dickens, 2003). Thermogenic methane may also migrate upwards in the sedimentary column. The clathrates strengthen the sediments but free gas (a reservoir of which may form beneath the hydrate layer) will significantly weaken the sediments increasing the likelihood of failure (Haq, 1998; Mienert et al., 1998; Sultan et al., 2004). Gas hydrates may only occur in high pressure and/ or low temperature regimes, an increase in temperature or a reduction in pressure can cause the hydrate bonds to destabilise, releasing the caged-gas molecules (Mienert et al., 1998; see Dickens, 2003) and reducing the strength of the sediment. Hence the development of gas hydrates will increase the susceptibility of a slope to fail especially after long periods of free gas accumulation beneath the hydrate layer and when environmental conditions change to destabilise the hydrate layer.

As well as the micro-scale (granular) it is also necessary to consider the meso- and macro-scales (regional). Throughout the Cenozoic era the northwest Eurasian plate, and northwest European continental margin, has been subject to periods of uplift (see chapter three; Praeg et al., 2005; Stoker et al., 2010). This, as well as the increased continental denudation associated with the Plio-Pleistocene glacial cycles, led to the development of many fan complexes including the Bear Island, North Sea and Barra Fans (Wilson et al., 2004; see Bryn et al., 2005b; Dahlgren et al., 2005). It can be argued that the most important factor in a slope's susceptibility to failure is a supply of sediment to fail. As such in the case of the northwest European margin shelf front fans continental uplift and the onset of Pleistocene glacial cycles (with the associated increase in sedimentation) could be said to be the primary influence of susceptibility. Volcanic uplift would exert a similar, more localised, effect.

From whichever source it is derived, uplift will increase the angle and the gravimetric forces acting on a slope: further increasing failure susceptibility.

In low latitudes continental slope susceptibility to failure is primarily governed by sediment supply: through changes in deposition rates and centres. Sedimentation rate, on the continental shelf and slope in low latitudes, is influenced strongly by onshore climate and marine productivity. For example in the South China Sea glacial stages are marked by an increase in the aridity over northern Asia and a strong aeolian sediment input; while interglacials are associated with a stronger summer monsoon (with enhanced precipitation) resulting in greater physical erosion and chemical weathering

(Boulay et al., 2005). Marine productivity influences the rates of pelagic sedimentation, and in the tropics is primarily governed by nutrient availability. This can be increased through intensified upwelling (see Little et al., 1997), as observed during the LGM on the Benguela margin or increased supply of terrigenous sediment (see Von Rad and Tahir, 1997), as observed on the Indus shelf during the early Holocene.

Changes in sediment deposition centres will also effect low latitude continental slope susceptibility to failure through both changing slope angle and influencing pore pressure and fluid migration. During lowstands river fan systems tend to bypass deltas and deposit fluvial, silty, clays directly onto the upper slope (see Amazon fan (Maslin et al., 1998), Indus fan (Von Rad and Tahir, 1997), Bengal fan (Weber et al., 2003) and Pearl River fan (Boulay et al., 2005)). These clays may act as a less permeable layer and a barrier to pore fluid migration. The fans are also subject to erosion, or aggradation, at different times. The Indus fan, for instance, was subject to massive erosion during the LGM, when there was extensive turbidite and slumping activity, during the Younger Dryas it aggraded and since the Holocene there has been relatively little activity (Von Rad and Tahir, 1997).

2.2.2.2. Triggers of slope failure

An event that initiates failure is termed a trigger.

Expansion and contraction of the cyrosphere affects seisimicity in high latitudes. The removal of the ice-mass releases stresses accumulated through long-term tectonic deformation: glaciation tends to be associated with aseismicity and the deglaciation with a pulse of seismic activity (Bungum et al., 2005 and references cited therein).

In the deglacial and postglacial environment, the largest earthquakes are likely to be found around the margins of the rebound dome, in the case of Fennoscandia: in the northwest quadrant of the former forebulge (Muir-Wood, 2000). Work by Fjeldskaar et al. (2000) reinforces this. They predict the transition zone between uplift and subsidence to be located just offshore western Norway, as they note, the location where bending stress of the crust will be greatest. Increased seismicity is associated with faults that have been reactivated by sediment loading, for example beneath shelf-front fans (Bungum et al., 2010).

Seismic triggers are defined as a cyclic or vibrational motion of the earth (Wright and Rathje, 2003; Biscontin et al., 2004). Acceleration-induced sliding occurs when strong seismic motions subject the sediments to horizontal and vertical accelerations, however, liquefaction-induced sliding occurs when cyclic shearing weakens non-cohesive sediments (Wright and Rathje, 2003). Seismic shaking will generate excess

pore pressure and it is possible for upward migrating pore fluid to cause an instability beneath a region with a lower fluid dissipation rate (Biscontin et al., 2004). Slope failure may occur several months after the seismic event because the time required to reach critical conditions may range from minutes to months according to the corresponding consolidation and hydraulic conductivity of different soil profiles, which will influence the fluid dissipation rate (Wright and Rathje, 2003; Biscontin et al., 2004).

Storm wave, or tsunami, loading may also trigger failures. Water waves generate adjacent zones of high and low pressure beneath crests and troughs, and shear stress is generated between these zones (Hampton et al., 1996; Locat and Lee, 2005). Tsunami wave fronts are capable of generating large hydrodynamic pressures on the seafloor with the potential to lead to failure (see Wright and Rathje, 2003). An example is demonstrated by the work of Bea et al. (1983) in the Gulf of Mexico. Storm waves produced during the passage of Hurricane Camille (August 1969) triggered sediment failure to a depth of 30 m and lateral movement exceeded 1000 m (see Bea et al., 1983). More recently waves generated by hurricanes Katrina and Ivan triggered mudslides that damaged pipelines (Gilbert et al., 2007). Storm occurrence is controlled temporally by climate: in high latitudes by the movement of the polar front and in low latitudes by the development of high-altitude zonal winds that tend to shear off hurricane systems.

Rapid drawdown of water, for instance by the approach of a tsunami, removes the resisting forces exerted by the water and induces undrained loading conditions, potentially causing failure (see Wright and Rathje, 2003). The Skagway slide and fjord tsunami in Alaska (1994) may have been initiated by an exceptionally low tide (see Rabinovich et al., 1999).

Gas hydrate destabilisation can trigger slope failure. Distribution and stability of hydrates are controlled by: temperature, pore pressure, gas composition and pore water salinity (Kvenvolden, 1993; 1998). Any change in these parameters may lead to the conversion of hydrate into free gas plus water (Sultan et al., 2004). This conversion reduces cohesive strength by removing hydrate cement and raising pore pressure. There are two ways that changes in the oceans may lead to gas hydrate destabilisation. Firstly, a reduction in pressure through a drop in sea level: it has frequently been argued that the sea level lowstand, associated with glacial conditions, could result in gas hydrate destabilisation, with the associated free gas release (Nisbet, 1990; Haq, 1998; Kennett, 2003). Secondly, through an increase in ocean temperatures (as associated with the deglaciation or warm interstadials) causing destabilisation of the hydrate sediments (see Kennett, 2003; Mienert et al., 2005).

However, due to the diffusive flow of heat through sediments there will be a delay between ocean warming and dissociation of hydrates located below seabed (Yamano et al., 1982; Phrampus and Hornbach, 2012). In either case methane gas is released from the oxygen-hydrogen bonds creating a weak layer in the sedimentary column.

Failure may also be triggered by rapid sediment deposition and the associated development of excess pore pressure. For instance: vertical fluid migration is initiated by sediment consolidation, a less permeable layer is encountered leading to high excess pore pressure, eventually this fluid may be expelled by venting (Volpi et al., 2003). This loading process has produced a potential failure plane of reduced shear strength. As the downslope force gradually increases failure could be triggered, by the very gravimetric loading that has created the failure surface, at the moment when the driving downslope force exceeds the resisting shear strength (see Hampton et al., 1996).

Differences in patterns of triggering events can be seen between the high and low latitudes. There is a relative absence of post-glacial seismicity in lower latitudes compared to abundance in higher latitudes. In lower latitudes hurricane frequency and alterations in sedimentation patterns are more significant trigger control mechanisms.

Cyclic variation in frequency and/or severity of triggering events may in itself produce particularly large failure events. A low-triggering period allows time for build up of susceptible sediment sequences that are then subjected to a period of high triggering event activity. This may explain the comparative absence of large-scale mass movement events on highly active margins, and locations (such as the Makran Margin of southwest Pakistan (see Prins and Postma, 2000)), and the greater frequency of such events in less active locations (such as the Sindh margin, the northwest European margin and the Amazon fan).

2.2.2.3. Continuum of susceptibility and triggering

As outlined above, some processes (for example sedimentation and the presence of gas hydrates) may act as susceptibility factors and trigger mechanisms. In some cases there may be no clear distinction between the categories and as such a continuum can be considered. For example, in the case of overburden development via sediment consolidation and excess pore pressure the environmental process (sedimentation) operates on a long timescale but, theoretically, when a critical condition is reached failure occurs instantaneously (Bell, 1992).

Conversely an earthquake may occur over a very short timescale, but generate excess pore pressures over a period of months to years (Biscontin et al., 2004). In this case a trigger mechanism is extremely difficult to identify and acts to increase susceptibility.

2.3. Impacts of submarine mass movements

In addition to the creation of slump and slide scars on continental margins, and turbidite sands on the abyssal plains, submarine mass movements have three potentially major consequences: damage to seabed infrastructure; gas hydrate release; and tsunami generation.

2.3.1. Damage to infrastructure

There is a large amount of infrastructure installed on the seabed, with cables (electrical and communications) and oil and gas infrastructure (wellheads, templates and pipelines) the most prevalent. As the amount of seabed infrastructure increases so does the potential exposure and likelihood of submarine mass movement induced damage: both economic and environmental.

The first known instance of submarine mass movement induced damage to seabed infrastructure occurred in 1929 when the Grand Banks turbidite broke transatlantic communications cables (Piper and Asku, 1987; Piper et al., 1999a). More recently damage has been caused to offshore oil and gas platforms (e.g. Mudflows triggered during Hurricane Camille in 1969 (Bea et al., 1983)) and pipelines (e.g. Mudflows triggered during Hurricane Ivan in 2004 (Gilbert et al., 2007)).

Rising fossil fuel prices, and reduced reserves, pushes hydrocarbon exploration into deeper waters beyond the continental shelf break (e.g. Ormen Lange, Norwegian continental margin; West of Shetland, British continental margin; Campos Basin, southeastern Brazilian margin; and Lower Congo Basin, Angolan continental margin (Khain and Polyakova, 2004)). In so doing infrastructure is exposed to greater risks of slope failure and submarine mass movement due to steeper slopes. Even if wellheads and templates are not located in high risk areas, connecting infrastructure (pipelines, cables and umbilicals) may have to traverse these areas. The volume of research undertaken on the Ormen Lange gas field (western Norwegian margin), situated in the headwall scar from the Storegga landslide, demonstrates how seriously these risks are taken (see Solheim et al., 2005).

The rapid growth of digital data (global Internet Protocol traffic has increased fivefold over the last five years (CISCO, 2011)), offshore renewable energy and calls to connect national electrical power grids has led to a large increase in the number and

length of subsea cables (BERR, 2008). The vast majority of transcontinental data is transmitted via seabed fibre optic cable (as opposed to satellite) and damage to cables may disrupt parts of this communication network for months (e.g. Aiwen, 2009).

As these assets have to make landfall, and at times cross ocean basins, they are exposed to potential risk from a number of hazards. Some of the greatest risks are posed by anthropogenic activities such as fishing (e.g. trawling) and ship anchors (BERR, 2008), however, natural hazards including earthquakes (Aiwen, 2009) and submarine mass movements also cause disruption to the seabed cable network. Several examples of submarine mass movement induced cable breaks exist, from the 1929 Grand Banks event (Piper and Asku, 1987; Piper et al., 1999a) to the 2006 event associated with the Pingtung earthquake off southwest Taiwan (Hsu et al., 2008).

2.3.2. Tsunami generation

Tsunamis occur as a result of water displacement, which may be caused by a number of mechanisms including earthquake (the most common), volcanic eruption, submarine mass movement, sub-aerial landslide and bolide impact (Dawson and Stewart, 2007; Tappin, 2010).

During the twentieth century tsunamis generated by submarine mass movement have been linked to 27 fatalities in Newfoundland (see Locat, 2001) and 2000 fatalities in Papua New Guinea (Tappin et al., 2001; Tappin et al., 2008). Peat deposits from the early Holocene provide evidence of a tsunami, triggered by the Storegga landslide, that produced run-ups of between 20 m and 5 m around the North Sea basin (Bondevik et al., 1997; Bondevik et al., 2005).

The magnitude of a tsunami generated by a submarine mass movement is dependent on the initial volume of the mass movement, seafloor geometry, the cohesion of the displaced mass, acceleration and velocity of the mass movement (Locat et al., 2004). The sediment type and rheology are also important considerations: stiff clays will convert more of the mass movement's energy into tsunami energy, and are thus more likely to produce a tsunami than less dense, less compacted and more heterogeneous sediments (Tappin et al., 2001; Gisler et al., 2010).

As with gas hydrate release (see section 2.3.3), whether or not the mass movement is disintegrative or cohesive is an important factor in tsunami generation. The more disintegrative the mass movement the less efficient it will be at displacing water and generating a wave front. However, a cohesive slide mass may not travel as fast as a disintegrative one. There is a tradeoff between cohesion of the sliding block and its basal friction, hence the velocity that it can attain. The true impact of the tsunami will

not simply be a function of its size, but also of the region where it impacts. A large tsunami impacting on an uninhabited coastline will have a less severe impact than a smaller tsunami impacting on a densely inhabited coastline. Mentioned previously, tsunamis may have the additional effect of triggering submarine slope failures, and potentially generating more tsunamis.

2.3.3. Gas Hydrate release

A consequence of a mass movement occurring within, or adjacent to, clathrate bearing sediments is the possible release of gas hydrates. Release of this gas (commonly CH_4 or CO_2) into the atmosphere could have had significant impact on past global climate, for example the K/T event (Day and Maslin, 2005), the PETM (Norris and Röhl, 1999; Zachos et al., 2001; Dunkley Jones et al., 2010; Maslin et al., 2010) and abrupt termination of the Pleistocene glaciations (Paull et al., 1991).

The specific mechanisms of failure triggering are also important in localising the failure plane above, within or below the zone of gas hydrate stability. They may also determine whether the developing failure becomes disintegrative, producing a disaggregated mass of sediment, or whether much of the sediment remains as slabs of coherent sediment. Gas hydrate embedded within the latter is carried down into deeper water and thus in general further into the stability field of solid gas hydrate.

The principal mechanism of hydrocarbon release from such failures is therefore not from the cohesive sediment masses themselves, but from uncapped reservoirs of free gas in the sediments below the failure plane and to a lesser extent from decompressed gas hydrates also originally located below the failure plane (known as the champagne cork effect (see Maslin et al., 2010)).

In contrast, disintegrative slope failures (Hampton et al., 1996) typically develop into large-volume turbidity currents or grain flows. In such cases, while dense lithic grains settle out as ocean floor deposits, low-density, buoyant hydrate clasts will tend to rise in the water column and ultimately float upwards through the low-pressure limit of hydrate stability and there decompose releasing methane to the surface layers of the ocean or even directly to the atmosphere. On a small-scale, such floating may involve individual gas hydrate grains or nodules as demonstrated experimentally by Paull et al. (2003). On a larger scale in turbidity currents, buoyant gas hydrate grains would tend to rise in the turbidity currents and perhaps even produce convective lift-off of the turbidity current once a sufficiently high fraction of the sediment grains had settled out, in the reverse process to the rapid sinking of dense sediment laden plumes (Carey, 1997).

Large-scale lift-off of buoyant plumes from turbidity currents, equivalent to the buoyant rise of hot ash clouds from pyroclastic flows (Sparks et al., 1993), have been inferred from the characteristics of graded hemipelagic mud layers associated with the giant freshwater turbidites produced by meltwater discharge 'Heinrich' events from the Laurentian ice sheet (Hesse et al., 2004). Knutz et al. (2002) interpret a similar mechanism on the Barra Fan to account for their B1 lithofacies (which consists of sharp based sand layers and muddy beds). Association of such layers with disintegrative continental slope sediment failures would provide direct evidence of escape of buoyant plumes from such failures and, due to the requirement of lower density freshwater, plausible evidence for gas hydrate release.

2.4. Review of late Pleistocene and Holocene North Atlantic sector submarine mass movements

This section is based on an extensive review of scientific evidence for the timing and causes of submarine mass movements. The first stage was the development of a database of well dated North Atlantic sector large-scale submarine mass movements for the last 45 ka (presented previously by Owen (2000), Maslin et al. (2004) and in updated, expanded form as part of this PhD project by Owen et al. (2007)).

2.4.1. Database methodology and uncertainty

Several fields are incorporated in the database and Table 2.1 summarises these and the reason for their inclusion.

Field	Reason for inclusion
Ocean/sea location	In order to allow an appreciation of geographical patterns and to locate the event
Specific Location	As above
Latitude	As above, but specifically to allow a glacial component to be considered
Event Name	To simplify discussion and general comprehension
Mass movement type	Being a mass movement database it contain many varieties of deposits (landslides, turbidites, and so on) and it is important to understand these differences and realise that different triggers may cause different types of failure
Radiocarbon age	The majority of timing estimations for this period (0 – 45 ka) have used ^{14}C dating
Calendar age	Dates may be in ^{14}C years but ice core and sea-level data are expressed in calendar years. Conversion was performed using Calib4.3 (Stuiver and Reimer, 1993)
Dating method	Despite the dominance of ^{14}C dating other techniques, with different reliabilities and assumptions, are used and it is important to be aware of these
Reliability index	Reflecting the difficulty in dating mass movements accurately. Some are easier to date than others, the more reliable the date, the more analytical weight which can be placed upon it (see text and Table 2.2)
Volume	Simply demonstrating the different magnitudes of events
Mass	As above, but this field also allows a consideration of quantity of carbon release
Reference	Major reference providing information regarding event location, dimensions (with volume) and timing
Author(s) ascribed cause	Adding to potential cause and effect analysis as well as providing some insight into the initial author(s) findings
Notes	Cataloguing the work undertaken in database construction, such as assumptions, extrapolations and any other information used (including reference)

Table 2.1: Explanation of mass movement database fields.

The dataset produced using these methods consists, at its most basic, of timing and volume/mass of mass movements during the past 45 ka. Exact age determination is vital; an error of a thousand years may make the difference between rising and falling sea level, or a CH_4 peak or trough.

2.4.1.1. Reliability of mass movement ages

A recent study by Urlaub et al. (2013) presents a database of submarine mass movements with age error bars. This thesis employs a reliability index to account for the potential errors associated with the date of mass movements. This more qualitative approach reflects the number of different sources of dating error beyond those present

within a sediment core sample. It also acknowledges the uncertainty associated with analytically sound ^{14}C dates, for example the marine reservoir effect (Bard et al., 1994; Austin et al., 2011) and uncertainties associated with multiple debris lobes within a 'single' event (Evans et al., 1996; Haflidason et al., 2005). Errors are not produced for the events within this database, but it is anticipated that associated error will be shorter for events indexed as 1 or 2 and longer for those indexed 4 or 5. Equally, uncertainty concerning the ascribed date will be greater for events indexed 4 and 5 with a possibility of these dates being significantly changed by more detailed research.

Reliability index score	Factors for inclusion	Example events
1 - Excellent Reliability	Timing of event determined by multiple well placed core samples combined with a detailed geophysical survey.	Grand Banks Turbidite, Storegga Slide
	Historical observation of event.	
2 - Good Reliability	Timing of event determined by core samples with a geophysical survey.	Amazon Fan Western Debris Flow, Herodotus Basin Megaturbidite
	Where multiple core samples are used location may be subject to sedimentary hiatuses that reduce dating confidence.	
	Where single core sample is used it will be located in a basin plain with known sedimentation history.	
3 - Average Reliability	Timing of event determined by cores samples with a geophysical survey.	Cape Fear Slide, Trænadjupet Slide
	Where estimation of age is from a single core sample it is supported by geophysical data.	
	Where age estimation is from multiple core samples these dates may have a relatively large range.	
4 - Mediocre Reliability	Timing of event will be based on a core sample, but assumptions may have been made about sedimentation rates in order to interpolate between date markers.	Canadian Abyssal Plain Turbidites, Faeroe Slide
	Where interpolation was not necessary, the environment will have reduced dating certainty (e.g. seabed erosion).	
5 - Poor Reliability	Timing is determined by loosely constrained seismostratigraphy.	Peach debrite 2, Andøya Slide
	Core sample provides evidence of timing from nearby event, not within it.	

Table 2.2: Determination of reliability index.

The reliability index is not attempting to grade the research, rather it reflects the level of difficulty of dating a particular mass movement emplacement. For example dating a megaturbidite, in a basin plain where sedimentation rates are known, is a great deal

more straightforward to date than a debris flow in a river fan system that has been subjected to erosion during periods in its history. The reliability index is a five point scale as follows: 1 Excellent reliability; 2 Good reliability; 3 Average reliability; 4 Mediocre reliability; 5 Poor reliability. Some published dates have simply not been used due to doubt over their validity and more recent work, for example the omission of the Embley (1982) date for the Saharan sediment slide because of more recent research published by Gee et al. (1999). Table 2.2 provides an overview of the index.

2.4.1.2. Potential bias within the database

Bias within the database may be considered in terms of geography and chronology. In general terms it is expected that this database is biased towards populated coastlines, especially those with significant oil and gas reserves. Locations that are remote and/or hazardous (e.g. Arctic) are anticipated to be under-represented and locations with significant hydrocarbon reserves (e.g. Norway) may be over-represented.

The database may also be biased towards more recent events. These are more easily identifiable on bathymetry and may also erode or obscure older events, particularly when events reoccur in the same location (e.g. AFEN slide (Wilson et al., 2004), Storegga Slide (Evans et al., 1996; Bryn et al., 2005a)). It is also generally more straight-forward to date events that have occurred more recently due to the length of core samples that are obtainable. Only rarely, for example on the Amazon Fan (Maslin et al., 1998), are events sampled via drilling. Shorter samples acquired via gravity- (<3 m length), vibro- (<5 m length) or piston-corers (<30 m) are more commonly used to sample mass movement deposits and as noted by Urlaub et al. (2013) this will tend to bias the analysis in favour of more recent events.

This thesis acknowledges the presence of these biases and considers them when discussing distribution and timing of mass movement.

2.4.1.3. Further complications when dating mass movement events

Many problems are encountered when dating submarine mass movements, as demonstrated in Figure 2.2. The most reliable method for determining emplacement dates, during the last 45 ka, is AMS ^{14}C dating pelagic sediment immediately above the deposit, as this should have been deposited immediately after emplacement. Material below the deposit will include reworked older material and the deposit itself will consist of sediment deposited prior to failure. It is not always possible to obtain dates from immediately above the deposit. In some instances timings are ascertained through extrapolations from sedimentation rates; but it should be noted that these are not always continuous. Moreover, the hemipelagic sedimentation above the slide may be

so rapid as to not contain enough dateable "pelagic" material. Alternatively, where a mass movement from shallow water is emplaced in much deeper water it may be preferable to pick abyssal-depth dwelling benthic foraminifera to date, in order to eliminate contamination of the dated samples from slide material (which should not contain the abyssal dwelling species).
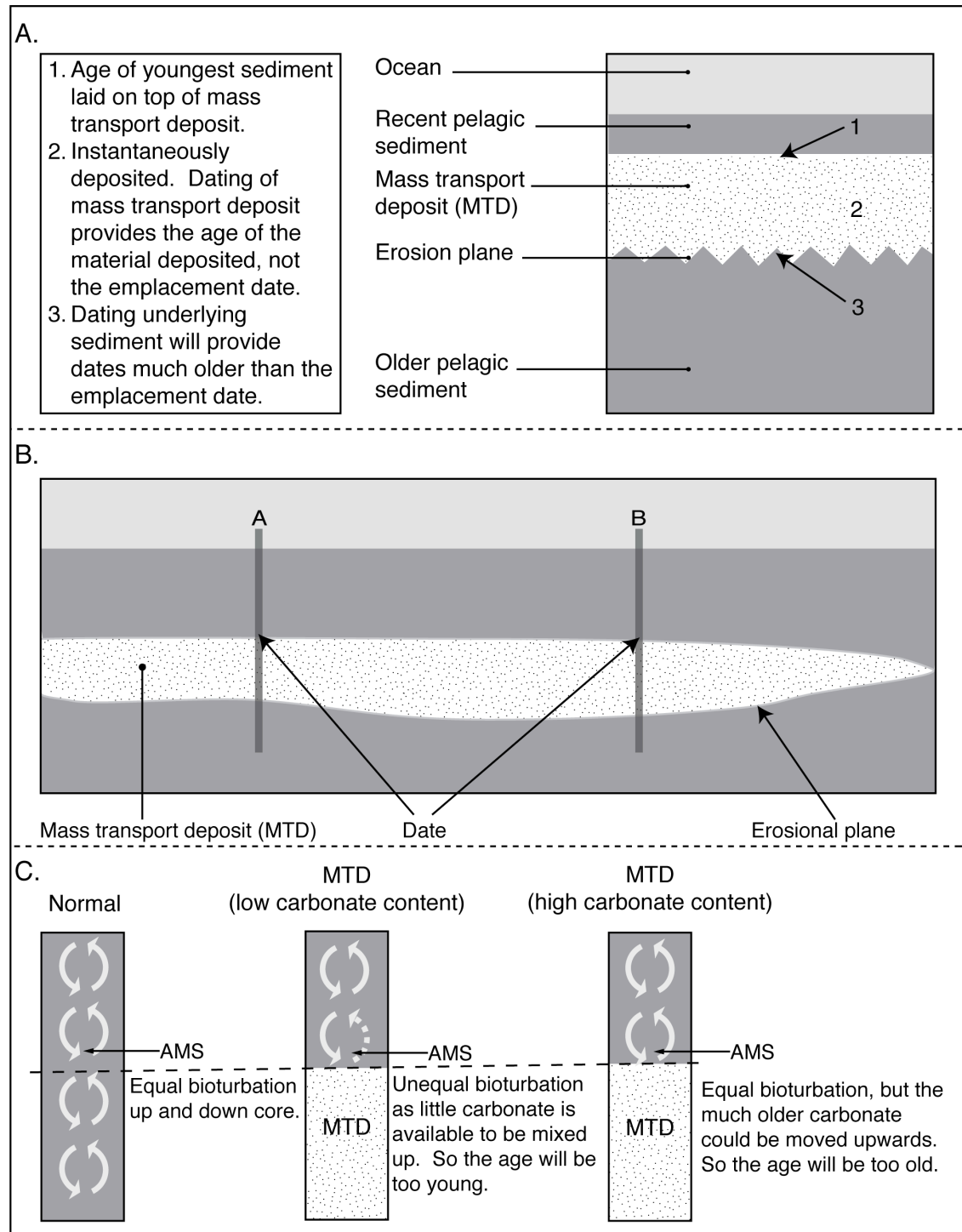
Figure 2.2: Dating submarine mass movements. A. Sedimentary column variation. B. Ideal locations of AMS dates. C. Effect of bioturbation.

The effect of bioturbation on AMS ^{14}C dates can lead to substantial error. Benthic organisms are known to burrow up to 10 cm into the ocean sediments (Loubere et al., 1995), this means that sediments of different ages can be mixed and in areas of low sedimentation rates, dating accuracy greatly reduced. Where a mass transport deposit has a low carbonate content there will be unequal bioturbation, as little carbonate is available to be mixed upwards and this younger material will be preferentially moved downwards, so AMS ^{14}C dating will under-represent the age of the event. Where the mass transport deposit has high carbonate content there may be equal bioturbation, but older carbonate will be bioturbated upwards making the age of the slump too old (see Figure 2.2.C). Published ^{14}C dates, although acquired through sound research, may be inherently inaccurate. Unfortunately, it is impossible to include standard error for mass movement timing due to a lack of metadata.

Volume/mass of mass movements are also an important component of the database, although not of this particular analysis (see Maslin et al., 2004). Relevant data has been taken from articles concerning the event in question. In some cases (notably the Cape Fear slide, Andøya slide, and Canadian Arctic turbidites) assumptions and extrapolations have been made. Specific instances shall be discussed in more detail later, however, whenever assumptions have been made or extrapolation performed this has been justified on a scientific basis.

2.4.2. Database results

Table 2.3 is an abbreviated version of the mass movement database (the full database is included as Appendix A); deposits are listed in chronological order. Figure 2.3 shows the geographical location of events and their chronological distribution in relation to the assigned reliability index. Though included in the table and figure the Canary debris flow and the Madeira abyssal plain 'b' turbidite will not form a part of the further analysis. This is because they have a volcanic, subareal, trigger (see Masson et al., 1998) and they are controlled by different factors than the other events listed.

Urlaub et al. (2013) test the relationship between submarine mass movements and global climate change statistically and do not demonstrate a statistically significant relationship. As noted by the authors, there are a number of possible reasons for this, including: that there is no relationship; the database is too small; heterogeneity between margins resulting in different phase signals; and mass movement age constraint not being sufficiently robust.

This thesis does not seek to test whether there is a relationship between submarine mass movements and climate change; as due to age uncertainty, local sea levels and

the time taken to trap bubbles in ice (outlined in Maslin et al. (2010)), it seems the data does not exist to allow a rigorous test. Instead, this thesis briefly examines the relationships between occurrence of mass movements and climate proxies before a detailed analysis of the local factors that are interpreted to have contributed to the occurrence of individual mass movement events.

The latitudinal distribution of these events through time, shown in Figure 2.4.A, shows a clear trend. Prior to 12 ka cal BP most events are mid to low latitude, after 12 ka cal BP high latitude events dominate. Figure 2.4.B shows the occurrence of mass movements in relation to a global mean sea level curve. This graph shows a relatively sparse grouping of events from 45 to 23 ka cal BP. From 23 to 14 ka cal BP there is a cluster of events associated with the sea level lowstand and Termination 1B. There is a further cluster of events after Termination 1A, followed by a steady grouping of Holocene events.

Name	Location	Latitude (°N)	Type	Age (cal years BP)	Reliability	Volume (km³)	Author(s) ascribed cause	Selected key references
Grand Banks Turbidite	Sohm Abyssal Plain	45	Turbidite	70	1	185	Earthquake	Piper and Asku (1987)
Canadian Abyssal Plain Turbidite 3a	Canadian Abyssal Plain	71	Turbidite	3100	4	240	Earthquake	Grantz et al. (1996)
Canadian Abyssal Plain Turbidite 2	Canadian Abyssal Plain	71	Turbidite	2400	4	80	Earthquake	Grantz et al. (1996)
Canadian Abyssal Plain Turbidite 1	Canadian Abyssal Plain	71	Turbidite	1300	4	80	Earthquake	Grantz et al. (1996)
Canadian Abyssal Plain Turbidite 4	Canadian Abyssal Plain	71	Turbidite	8200	4	80	Earthquake	Grantz et al. (1996)
Traenadjupet	North Norwegian Continental Margin	68	Slide	4000	3	900	Earthquake, -post-glacial	Laberg et al. (2000), Laberg et al. (2002)
Canadian Abyssal Plain Turbidite 3b	Canadian Abyssal Plain	71	Turbidite	6000	4	160	Earthquake	Grantz et al. (1996)
Storegga	West Norwegian Continental Margin	66	Slide	8100	1	2800	Earthquake, sedimentary overburdening, pore fluid migration	Jansen et al. (1987), Haflidason et al. (2004), Bryn et al. (2005)
Peach Debrite 4	Northwest British Margin	57	Debrite	11500 (see caption note)	3	135	Earthquake	Holmes et al. (1998), Armishaw (1999), Knutz et al. (2002) and this study
Faeroe Slide	Northeast Faeroe Margin	64	Slide	10300	4	158	Slope steepening and increased sedimentation	Van Weering et al. (1998)
Andoya	North Norwegian Continental Margin	70	Slide	10000	5	180	Earthquake -post-glacial	Laberg et al. (2000)
Baltimore Slide Complex	Northeast American Margin	38	Slide complex	9400	5	200	Earthquakes, undercutting	Embley (1980, 1982)
Eastern Debris Flow	Amazon Fan	4	Debris Flow	14500	2	1500	Increased sedimentation and changing sea-level	Maslin et al. (1998, 2005), Piper et al. (1997)
Madeira Abyssal Plain 'b' Turbidite	Madeira Abyssal Plain	31	Turbidite	15000	2	125	Volcanic	Weaver and Rothwell (1987)
Canary Debris Flow	Canary Island Margin	28	Debris Flow	15000	2	400	Volcanic	Masson et al. (1998)
Cape Fear Slide	Blake Ridge	33	Slide	16800	3	1700	Gas Hydrate, Salt Dapir intrusion and Earthquakes	Popenoe et al. (1991), Paull et al. (1996), Hornbach et al. (2007)
H13 Turbidite	Horseshoe Abyssal Plain	36	Turbidite	17700	4	33	Earthquake and sea-level change	Lebreiro et al. (1997)
BIG '95	Western Mediterranean	40	Debris Flow	11500	4	26	Increased sedimentation and Earthquake	Lastras et al. (2002)
Western Debris Flow	Amazon Fan	4	Debris Flow	13000	2	2000	Increased sedimentation and changing sea-level	Maslin et al. (1998, 2005), Piper et al. (1997)
Black Shell Turbidite	Hatteras Abyssal Plain	31	Turbidite	18300	4	100	Increased sedimentation and Earthquake	Elmore et al. (1979)
Peach Debrite 3	Northwest British Margin	57	Debrite	21000	3	199	Earthquake	Holmes et al. (1998), Knutz et al. (2001)
Balearic Abyssal Plain Megaturbidite	Western Mediterranean	40	Turbidite	22000	1	500	Earthquake, Clathrate release and increased sedimentation	Rothwell et al. (1998)
Herodotus Basin Megaturbidite	Southeast Mediterranean	33	Turbidite	27125	2	400	Tectonic steepening, lowered sea-level and seismic trigger	Reeder et al. (2000)
Hinlopen/Yermak Megaslide	Northern Svalbard Continental Margin	81	Slide	30000	2	1300	Tectonically induced shelf collapse during rapid onset of glaciation	Vanneste et al. (2006), Winkelmann and Stein (2007), Winkelmann et al. (2008)
Deep Eastern MTD	Amazon Fan	4	Debris Flow	35000	2	610	Gas Hydrate destabilisation	Maslin et al. (1998), Piper et al. (1997)
Peach Debrite 2	Northwest British Margin	57	Debrite	36500	5	673	Earthquake	Holmes et al. (1998), Knutz et al. (2001)
Deep Western MTD	Amazon Fan	4	Debris Flow	43500	2	360	Gas Hydrate destabilisation	Maslin et al. (1998), Piper et al. (1997)

Table 2.3: North Atlantic Sector Late Pleistocene - Holocene submarine mass movements. Selectted key references listed. NOTE - 11.5 ka cal BP date for Peach 4 is based on work conducted in later chapters of this thesis.
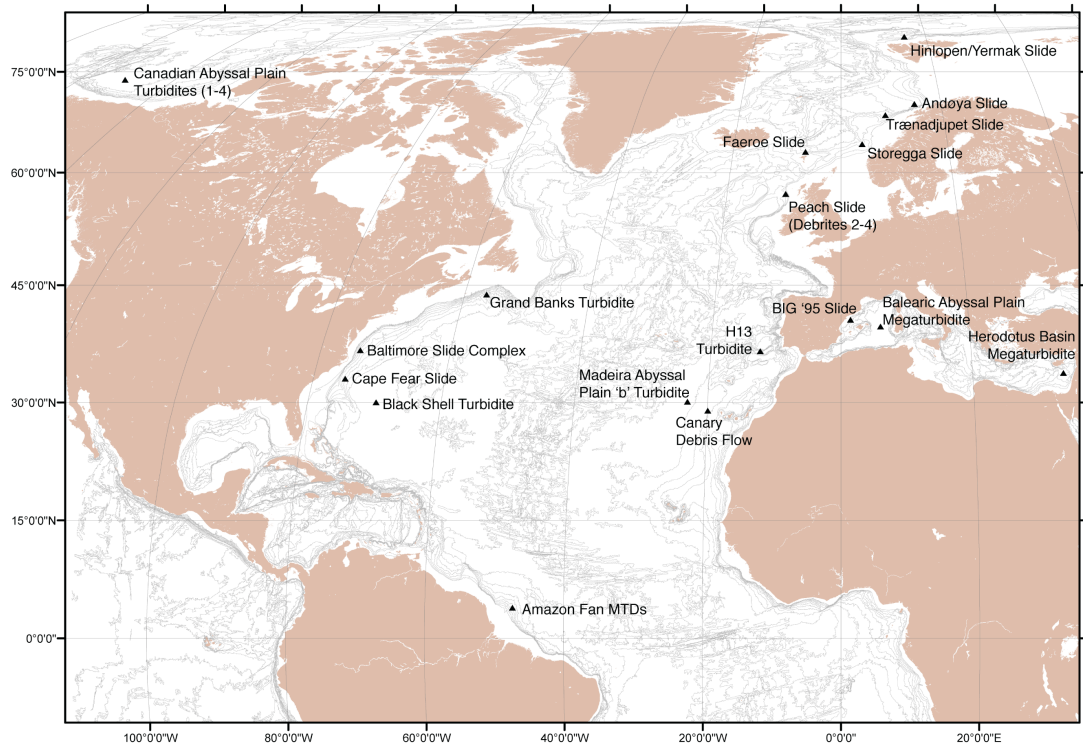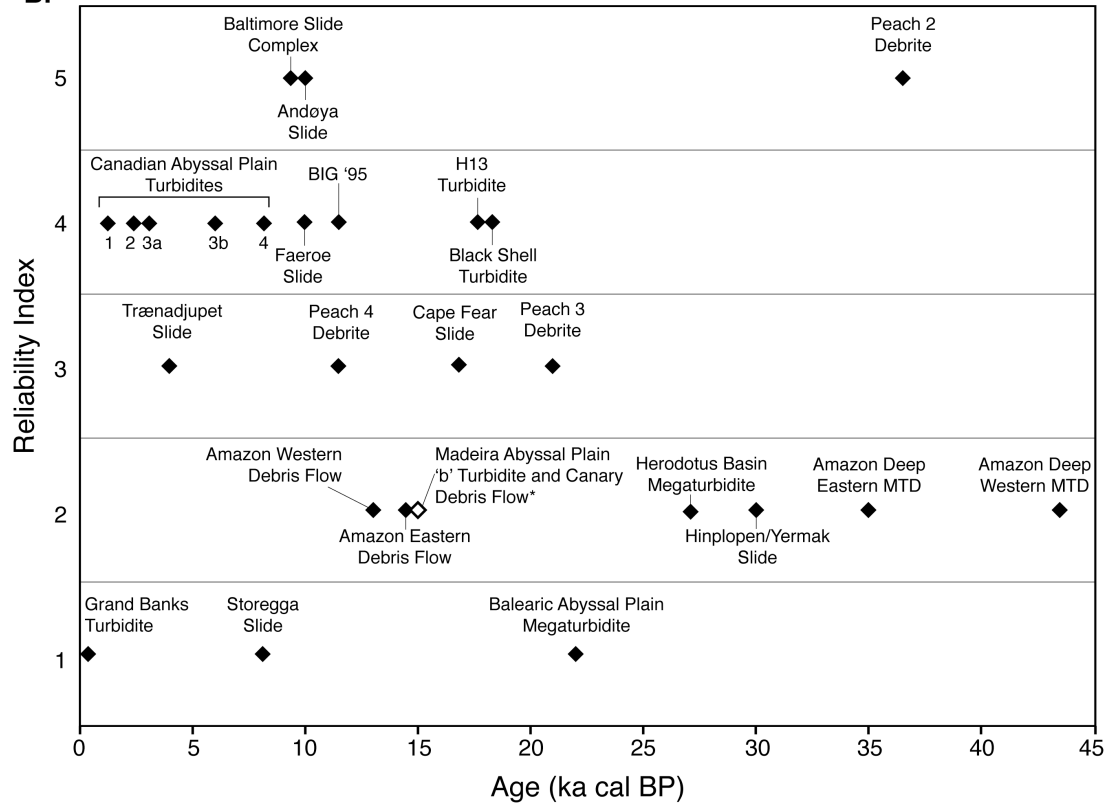
Figure 2.3: Distribution of late Pleistocene and Holocene North Atlantic sector submarine mass movements. A. Geographical distribution. B. Chronological distribution, with estimated reliability of date (1 = excellent reliability to 5 = poor reliability). *Madeira Abyssal Plain Turbidite and Canary Debris Flow shown, but excluded from further analysis due to volcanic origin.
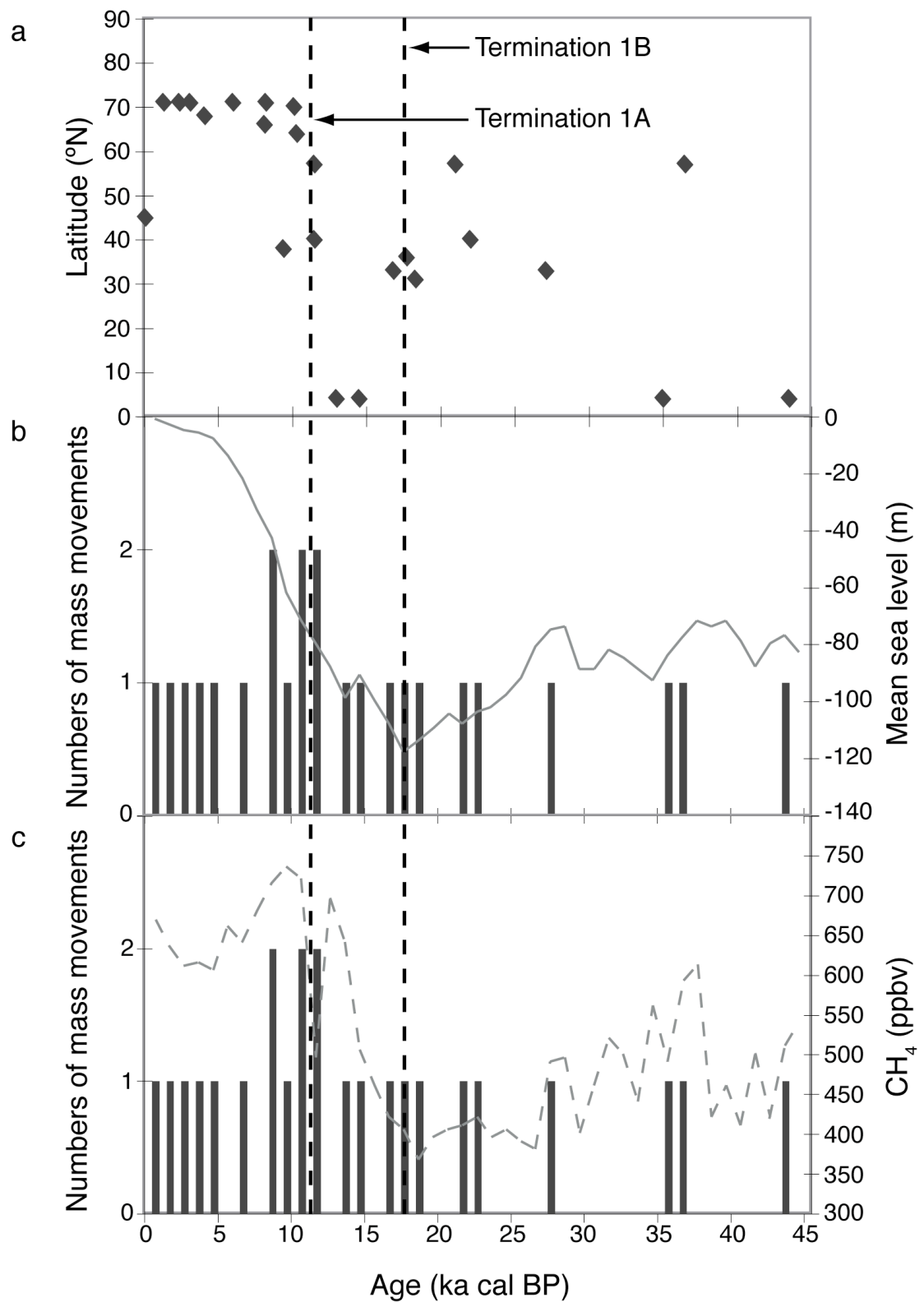
Figure 2.4: Latitudinal distribution (A) and timing of submarine mass movements compared with mean global sea level (B) and GISP2 CH_4 (C). NOTE - events with a volcanic cause are excluded from this analysis.

Figure 2.4.C shows the relationship between mass movements and Greenland ice core GISP2 CH_4. From 45 to 23 ka cal BP mass movements show no clear link with CH_4 peaks. Two events: the Amazon Deep Eastern Mass Transport deposit of the Amazon Fan and the Herodotus Basin Megaturbidite may coincide with CH_4 peaks. However, a further two: the Amazon Deep Western Mass Transport Deposit and the Peach 2 debrite seem to coincide with a CH_4 trough. Following Termination 1B there is a cluster of events associated with the increase of CH_4, however, they are not associated with the Pre-Boreal CH_4 peak. Following the Younger Dryas and Termination 1A there is a second cluster of three events, which coincide with the early Holocene CH_4 peak. These links between continental slope failure and climate are examined in more detail in section 2.5.

2.5. Discussion of susceptibility factors and triggering mechanisms affecting the key deposits in the database.

As the main objective of this chapter is to develop a conceptual model of continental slope failure that may be tested against the Barra Fan and Peach slide, low latitude events (including Mediterranean, southern European, northwest African and Amazon Fan) are excluded from the following discussion. Low latitude events are discussed in detail by Owen et al. (2007).

These deposits have reasonably well constrained dates of emplacement, an estimation of volume and they are all large scale (> 25 km^3). The following section is ordered by geographical location.

2.5.1. Northwest European margin

2.5.1.1. Hinlopen/Yermak

On the continental margin north of Spitsbergen, the Hinlopen/Yermak megaslide is a large, multiphase, retrogressive translational slide with a volume estimate of 1250 - 1350 km^3 (Vanneste et al., 2006; Winkelmann et al., 2008). It is situated at the seaward limit of the Hinlopen trough on the associated trough mouth fan (Vanneste et al., 2006; Winkelmann and Stein, 2007; Winkelmann et al., 2008). The event is marked by headwalls up to 1600 m high (Winkelmann et al., 2008) and rafted blocks up to 450 m high (Vanneste et al., 2006). These extreme headwall heights, mark this event as something of a unique case.

AMS ^{14}C analysis of *Neogloboquadrina pachyderma* date the slide to 30 ka cal BP (Winkelmann et al., 2008). Winkelmann and Stein (2007) consider triggers and conclude that the slide was a result of the rapid onset of glaciation, asymmetric ice-

loading and forebulge development leading to enhanced tectonics. Gas hydrate dissociation is considered unlikely as a primary cause owing to the relatively shallow depth of the modelled hydrate stability zone in relation to the original failure plane; however, dissociation may have contributed to instability in the upper slope (Winkelmann and Stein, 2007). Contemporary evidence of methane hydrates on the Spitsbergen margin (Westbrook et al., 2009) provides some support for a contributory role for hydrate dissociation.

2.5.1.2. Andøya

In the northeastern Norwegian-Greenland Sea on the Norwegian continental margin proximal to the Lofoten Basin Andøya is a translational slide (Laberg et al., 2000). The slide deposits cover 9,700 km^2 and the scar area is approximately 3,600 km^2 (Laberg et al., 2000). No precise volume estimates of this slide have been found. However, taking a conservative estimate of 50 m for the headwall scarp (inferred from Laberg et al., 2000 pp. 263) a figure of 180 km^3 is obtained (Scar area (3600 km^2) × headwall height (0.05 km)). Precise timing of the Andøya slide is not known. 3.5 kHz profiles indicate that there is little or no overlying sediment and the bathymetry reveals a very uneven seafloor (Laberg et al., 2000). This implies that the event is recent. At 4 m depth, in a sediment core from the nearby Andøya Canyon, *Neogloboquadrina pachyderma* offer a ^{14}C date of 8,940 ± 150 (corresponding to a calendar date of 10 ka BP), after which pelagic sedimentation dominates (Laberg et al., 2000). This has been taken to represent the age of the event as shock from the Andøya slide would have caused mass movement in the canyon. The event occurred in the early Holocene after the major part of the deglaciation, shortly after 10 ka cal BP most of the Fennoscandinavian ice had retreated (Svendsen and Mangerud, 1987). Susceptibility to mass movement would have been increased by high sedimentation rates during the deglaciation and slope steepening due to isostasy. Vorren et al. (1998) note that Andøya is situated on the steepest part of the eastern Norwegian-Greenland sea continental margin (5 - 18˚). An earthquake, associated with the post-glacial uplift of Fennoscandinavia, is cited as the most probable trigger due to the events location in an area of comparatively high seismic risk (Laberg et al., 2000).

2.5.1.3. Trænadjupet

On the continental slope east and northeast of the Vøring plateau in the Norwegian-Greenland Sea Trænadjupet is a large translational slide (Laberg and Vorren, 2000). Slide scar area is approximately 5,000 km^2 and the deposits have been estimated at 900 km^3, assuming an average thickness of 100 m (Laberg et al., 2002b). Timing of the

event is based on AMS ^{14}C dates from two cores taken from within the scar. Sampling of *Neogloboquadrina pachyderma* indicates that pelagic sedimentation resumed in the slide scar from 4 ka ^{14}C BP (Laberg et al., 2002b). This indicates that the event occurred immediately prior to this time, post deglaciation during the mid-Holocene (corresponding to a calendar date of 4 ka BP). From the presence of large blocks and rafts of sediment Laberg and Vorren (2000) argue that failure occurred along surfaces of weakness: most likely interglacial, contouritic, muds possessing relatively high water content and low undrained shear strength. High clay and organic content could lead to excess pore pressure and methane (Laberg and Vorren, 2000). Through geotechnical tests Sultan et al. (Sultan et al., 2004) established that the contouritic sediments, in which the main failure occurred (Laberg et al., 2003), were particularly weak in undrained conditions appropriate to cohesive failure. Sediment stability would be reduced along these bedding planes and potential for failure increased. Trænadjupet is situated in an area of rapid post-glacial Fennoscandinavian uplift and high intraplate seismicity (Fjeldskaar et al., 2000; Laberg and Vorren, 2000; Laberg et al., 2000). Martinussen's (1961) Andøya sea level curve (see Figure 2.4A and Figure 2.5) demonstrates that rebound is occurring at time of failure. An earthquake, or succession of small earthquakes, is cited by Laberg and Vorren (Laberg and Vorren, 2000) as the most likely trigger mechanism. Deglacial sedimentation and isostatic slope steepening would have made the slope more susceptible to failure, an earthquake would have increased the sediment shear stress causing it to fail along the planes of weakness.

2.5.1.4. Storegga

On the Norwegian continental margin south of the Vøring plateau Storegga is a retrogressive, translational slide (Jansen et al., 1987; Bugge et al., 1988; Evans et al., 1996; Haflidason et al., 2004; Bryn et al., 2005b; Haflidason et al., 2005). The slide scar area is 50,000 km^2 and the slide volume has been estimated as between 2,400 km^3 and 3,200 km^3 (Haflidason et al., 2004). It was initially thought that the slide consisted of three separate events: Storegga I (50 - 30 ka), Storegga II (8 – 5 ka) and Storegga III (5 ka) (Jansen et al., 1987; see Bugge et al., 1988; Evans et al., 1996). However, it is now believed that all three events occurred simultaneously (Haflidason et al., 2004; Haflidason et al., 2005). Tsunami deposits have been observed in lake, bog and peat sediments in Norway, Faeroe, Shetland and mainland Scotland (Bondevik et al., 1997; Smith et al., 2004; Bondevik et al., 2005). AMS ^{14}C dating of these deposits provides consistent figures of between 7.0 and 7.3 ka ^{14}C BP (Bondevik et al., 2005) . Additionally Haflidason et al. (2004) date the slide scar at 7,250 ± 250 AMS ^{14}C BP. This corresponds to a calendar age of 8.1 ka BP.

Initial discussion of triggers focused on the role of earthquakes, with a possible facilitating role from gas hydrates (see Bugge et al., 1988; Evans et al., 1996). With the discovery and subsequent development of the Ormen Lange gas field this area has been subject to intense research. The role of gas hydrates is viewed, at most, as a secondary process: no sign of clathrates have been found in the area's boreholes though some BSRs have been identified (Kvalstad et al., 2005; Mienert et al., 2005). A greater emphasis is placed on the role of glacial sediment loading of the North Sea Fan and pore fluid migration to, and sediment swelling of contouritic marine clays in the distal regions of the Storegga slide (see Bryn et al., 2005b; Kvalstad et al., 2005). An earthquake is widely regarded as the most likely initial trigger. Research on onshore post-glacial faults indicates a magnitude 7 earthquake approximately every 1.1 ka (Bungum et al., 2005). The event occurred post deglaciation during a period of massive rebound (see Figure 2.5) and it is likely that rapid sedimentation and isostatic slope steepening would have increased susceptibility to failure. This region could also be subject to enhanced seismicity from a deglacial seismic pulse migrating from the former forebulge of the Fennoscandian ice sheet (see Fjeldskaar et al., 2000).

In many ways, as noted by Urlaub et al. (2013), analysis of Storegga may be viewed as a cautionary tale where initial interpretations have been overturned. In this case due to a massive survey campaign at a cost of many millions of euro. Timing has been constrained by analysis of 89 core samples (Haflidason et al., 2005) and correlation to tsunami deposits in peat (Bondevik et al., 2005). Despite this vast analysis there is still debate surrounding the event's timing relative to the 8.2 ka event (Dawson et al., 2011; Urlaub et al., 2013) and there is limited direct evidence of cause.

This raises the question as to how likely are we to be able to identify causes of events, equally as complex as Storegga, with a fraction of the resources?

2.5.1.5. Faeroe slide

Large scale sliding has occurred on the northeast Faeroe margin, south of the Norwegian basin (Van Weering et al., 1998). No precise volume estimates have been found for this slide. For the purpose of this thesis a rough calculation of 158 km^3 has been made (0.2625 km [slump scar height] × (60 km [slump scar width] × 10 km [slump runout])) from the dimensions described by Van Weering et al. (1998). A single AMS ^{14}C date, 9,850 ± 140, was obtained at the foot of the main slump scar on top of compacted and deformed sediments (Van Weering et al., 1998). Multiple sliding events are proposed by Van Weering et al. (1998). The most recent sliding event's early Holocene date, coupled with Van Weering et al. (1998) proposed cause, suggests that the events may have occurred within a relatively short time span. For the purpose of

this chapter (precise volumes not being the most important factor) the entire 158 km^3 of displaced sediment shall be ascribed the 9,850 ± 140 ^{14}C BP (corresponding to a calendar date of 10.3 ka BP), post deglaciation, date. Van Weering et al. (1998) focus on a combination of subsidence of the Norwegian basin - leading to slope steepening, increased glaciogenic sedimentation from the Faeroese margin and increased sediment supply from contourite currents following the resumption of deep water circulation. These are factors that would have dramatically increased the slope's susceptibility to fail.

2.5.1.6. Peach slide (debrites 4, 3 and 2)

Chapters four to six of this thesis focus on the Peach slide. This section presents a brief review of the published understanding of these events prior to this research.

The Peach slide situated on the northern flank of the Barra Fan, west of Northern Britain, consists of four major debrite units: debrite 4 (135 km^3), debrite 3 (199 km^3), debrite 2 (673 km^3) and debrite 1 (823 km^3) (Holmes et al., 1998). Age of debrite 1 is very loosely constrained using seismic stratigraphy and is believed to pre-date shelf edge glaciation at 0.44 Ma (Holmes et al., 1998). Maslin et al. (2004) employed the age/depth profile of the Barra Fan constructed by Knutz et al. (2001) to estimate debrite ages. From this work the following ages were calculated: Debrite 2 at 36.5 ka cal BP, debrite 3 at 21 ka cal BP and debrite 4 10.5 ka cal BP (Maslin et al., 2004). Debrite 2 occurred during the build-up of the British ice sheet, when there was intermittent IRD prior to 30 ka in the Barra Fan (Knutz et al., 2001; Scourse et al., 2009; Hibbert et al., 2010). Knutz et al. (2001) state that between 21 and 12 ka there were high rates of fine clastic sedimentation and that the glacial ice extended to the outer shelf until 16 – 17 ka. Debrite 3 occurred just after the British ice sheet LGM (Scourse et al., 2009) during a period of lowered sea-level and high sedimentation that would have increased the slope's susceptibility to failure. Debrite 4 occurred after the deglaciation in a period when isostatic seismicity would have been high. Holmes et al. (1998) cite earthquakes, based on a historical database, as the most likely trigger of the mass movement.

In a region with such a complex morphology, oceanography and sedimentology this seems a somewhat simplistic view. Subsequent chapters of this thesis refine the age of Peach 4 to between 11 and 12 ka cal BP, susceptibility factors and possible triggers are discussed in greater detail in chapter six.

2.5.2. Canadian Arctic

2.5.2.1. Canadian abyssal plain turbidites 1, 2, 3a, 3b and 4

Grantz et al. (1996) show a turbidite sequence in the Canadian abyssal plain (Arctic ocean), these turbidites originated on, or from the front of, the Mackenzie delta. Volume has been estimated by multiplying the thickness of the turbidite units by the area of the abyssal plain (200 km × 400 km = 80,000 km^2). This is believed to be valid due to the distal positioning of the core in relation to the turbidite source area. Volume estimates for turbidites 1, 2, 3a, 3b and 4 are 80 km^3, 80 km^3, 240 km^3, 160 km^3 and 80 km^3 respectively. Grantz et al. (1996) present an age profile of the turbidite sequence based on AMS ^{14}C dating of *Neogloboquadrina pachyderma*. It is limited by low sedimentation rates and some bioturbation; however, this profile can be used to date the turbidites with relative accuracy. Emplacement dates for turbidites 1, 2, 3a, 3b and 4 as interpreted from the age profile in Grantz et al. (1996) are 1.3, 2.4, 3.1, 6.0 and 8.2 ka cal BP respectively. Earthquakes are cited as the most likely trigger of the turbidites, a statement supported by a zone of active seismicity existing beneath the Mackenzie delta and the upper Mackenzie cone (Grantz et al., 1996). During the Holocene (particularly during the early Holocene) the Mackenzie delta would have been subjected to isostatic forces influencing slope steepness and seisimicity. The deglaciation would have deposited large amounts of sediment increasing the likelihood of overburdening and susceptibility to failure.

2.5.3. Northeast American margin

The northeast American continental margin shows an interesting change of geological processes from north to south. Glaciers reached the shelf-edge on the Nova Scotian margin, on the New England margin rivers transported glacial sediments to shelf-edge deltas and south from the middle Atlantic margin there is little glacial influence (Twichell et al., 2009).

2.5.3.1. Grand Banks turbidite

The Grand Banks turbidite is situated in the Sohm abyssal plain off the northeastern American continental margin. The Laurentian Fan, on the upper continental slope, off St.Pierre Bank, has been identified as the source area (Piper and Asku, 1987; Piper et al., 1999a). Piper and Asku (1987) estimated the total volume of the event as 184 km^3. The event broke transatlantic communications cables; this gives us an accurate date of 18th of November 1929 AD, and ties it to a tsunami on the same date (Piper and Asku, 1987; Piper et al., 1999a). The trigger mechanism for the event was a magnitude 7.2 earthquake, which led to widespread slumping of the top 20 – 25 m of sediment and

generated the turbidity current (Piper et al., 1999a). Piper and Asku (1987) identified coarse grained sediment, deposited during the deglaciation, in the turbidite deposit. Increased sedimentation, via the Lawrence River during the Holocene may also have increased the continental slope's susceptibility to failure.

2.5.3.2. Baltimore canyon slide complex

This slide complex is just south of Baltimore canyon on the eastern United States' continental margin (Embley, 1980). It covers an area of 4,000 km^2 and affects the top 50 to 100 m of sediment (Embley, 1980; Embley, 1982). Assuming a depth of 50 m volume can be estimated, crudely, as 200 km^3. Two sediment cores with AMS ^{14}C dates have been acquired from the head of the slide complex. Two dates of 10,080 and 7,285 ^{14}C BP were obtained from clays above the deformed sediment (Embley, 1980). A sample of the slide deposit matrix at the top of the flow yields a AMS ^{14}C date of 11,820 ± 340 BP (Embley, 1980), indicating that mass movement occurred after this time. The slide complex may have developed over a substantial period of time in a series of discreet events. For the purpose of this paper the mean age of the overlying sediment, 8,683 ^{14}C BP (corresponding to a calendar date of 9.4 ka BP), will be taken to represent the age of the slide complex, a date which is post deglaciation. Trigger mechanisms are discussed by Embley (1982), roles played by earthquakes, gas hydrates and undercutting are all proposed. Occurring after the deglaciation rapid sedimentation would have increased the slope's failure susceptibility through potential overburdening and increased pore pressure.

2.5.3.3. Black Shell turbidite

The Black Shell turbidite is situated in the Hatteras abyssal plain, off the southeastern United States' continental margin (Elmore et al., 1979). The volume is at least 100 km^3 (Elmore et al., 1979). Coarse shell material within the deposit has been dated using AMS ^{14}C. The youngest age from this sample was 15,855 ± 260 ^{14}C BP (Elmore et al., 1979). This is the maximum age of the event and for the purpose of this paper this date will be taken to represent the age of the event, placing it just after the LGM. Elmore et al. (1979) suggest that the coalesced deltas of the Susquehanna, Potomac and Neuse rivers failed, initiating a turbidity current. Deglaciation would have increased sedimentation on the deltas and increased failure susceptibility. Elmore et al. (1979) discuss slope oversteepening, which is the factor increasing the susceptibility of the slope to failure, with either a tectonic event or a spring flood acting as the final trigger.

2.5.3.4. Cape Fear slide

The Cape Fear landslide is situated on the continental margin of the southeastern United States, off Cape Fear, North Carolina (Popenoe et al., 1991; Schmuck and Paull, 1993; Hornbach et al., 2007). The headwall scarp is over 50 km long and 120 m high, the deposits extend 400 km downslope (Popenoe et al., 1991). Popenoe et al. (1991) give dimensions for the upper 70 km of the slide, an approximate volume of 300 km^3 can be calculated for this portion. Extrapolated for the entire 400 km length this yields a volume of 1,700 km^3. Hornbach et al. (2007) suggest that at least five separate slide events have occurred during the past 30 ka cal BP, so it is likely that a number of events contribute to the 1700 km^3 value.

Samples taken from above an unconformity at 0.5 to 2.0 m depth within the slide scar yielded ages from 9.0 to 14.5 AMS ^{14}C ka BP (Paull et al., 1996). If one assumes that pelagic sedimentation resumed just after the event, and that the unconformity represents the top of the slide deposit, then the oldest AMS ^{14}C date is the same age as the youngest episode of the Cape Fear slide. Corresponding to a calendar date of 16.8 ka BP, placing the event just after the LGM. A number of likely contributing factors are discussed by Popenoe et al. (1991) including: decomposition of gas hydrate, salt diapir intrusion and earthquakes. Hornbach et al. (2007) interpret a normal fault and suggest that displacement along this led to upward migration of salt and slope steepening.

The slide deposit is in an area rich in gas hydrates, the combination of the salt diapirs acting as free gas traps and the event occurring during a period of lower sea levels may have weakened the sediments sufficiently for an earthquake to trigger the slide. Recent work (Phrampus and Hornbach, 2012) investigating changes to the Gulf Stream suggests that warming temperatures are destabilising hydrates in the region. A similar process could have occurred in the post-glacial ocean.

2.6. Discussion of timing of mass movements relative to changes in sea level and climate.

The sea level curve shown in Figure 2.4.B is derived from Barbados and Pacific data (see McGuire et al., 1997 and references cited therein). It is more appropriate to use this curve with reference to lower latitude events. This is because high latitude regions may have been glaciated and their relative sea level is a function of both isostatic and eustatic factors. The Fennoscandian mass movement events are compared with local relative sea level to demonstrate this.
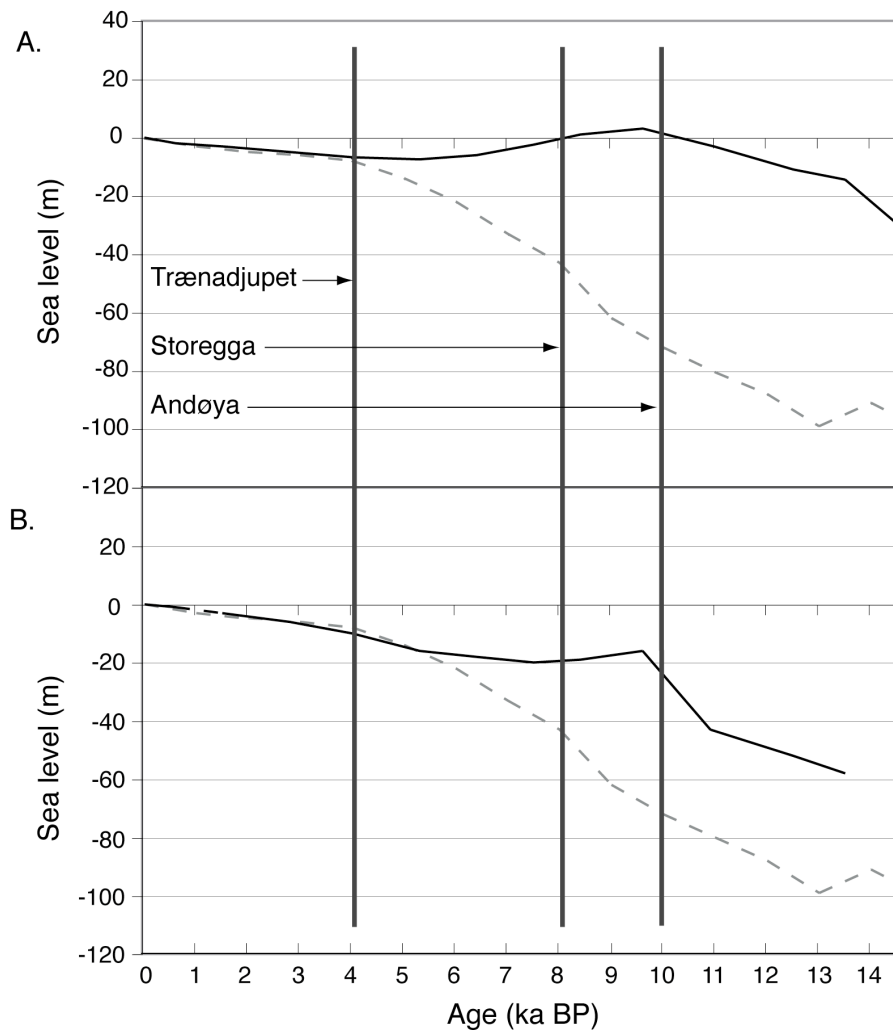
Figure 2.5: Comparison of local sea level curves (solid) with mean global sea level (dashed). Norwegian event timing also shown. A. Martinussen's (1961) Andøya curve (~72°N). B. Svendsen and Mangerud's (1987) Frøya curve (~66°N. Global mean sea level from McGuire et al. (1997) and references cited therein.

Figures 2.5.A and B show local relative sea level curves for the last 14.5 ka at Andøya and Frøya, on the west coast of Norway. Figure 2.6 shows the approximated rate of Isostatic movement (rebound or depression), calculated by subtracting the rate of global sea level change (from McGuire et al., 1997) from the rate of local sea level change (from Martinussen, 1961; Svendsen and Mangerud, 1987), at these locations.

At Andøya (see Martinussen, 1961) there is a rise in sea level until ~10 ka cal BP, between 10 and 5 ka cal BP local sea level falls and from 5 ka cal BP a slight rise in sea level occurs as the eustatic rise dominates the local sea level. This pattern is explained by the isostatic curve in figure 2.6. At ~11 ka cal BP Isostatic change appears to be very low, possibly a result of the Younger Dryas re-glaciation. The rate increases to ~7 m ka^{-1} at 10 ka cal BP. Isostatic uplift peaks in the period 8 – 9 ka cal BP at ~21 m ka^{-1}, a result of rapid rebound shortly after the final deglaciation. At 7 – 8 ka cal BP there is a reduction in the rate of rebound, though it remains at ~13 m ka^{-1}. Between 6

and 7 ka cal BP the rate increases slightly, to ~15 m ka^{-1}, after which the rate decreases steadily until 3 ka cal BP when it reaches late Holocene values of ~1 m ka^{-1}.

At Frøya (see Svendsen and Mangerud, 1987) sea level rises steadily until 11 ka cal BP, the rate of rise then increases until shortly after 10 ka cal BP. There then follows a period of declining sea level until ~7.5 ka cal BP, from which point there is a slow rise in sea levels to the present. Figure 2.6 shows a decline in the rate of isostatic rise from 12.5 ka cal BP. Between 11.5 and 9.5 ka cal BP this decline becomes a pronounced negative spike (to -19 m ka^{-1}). It is suspected that this is a false value, resulting in an age offset between the local and global sea level data displayed. From 9.5 ka cal BP the figure is more reliable. The peak rate of uplift occurs between 8 and 9 ka cal BP at ~22 m ka^{-1}, by 7 ka cal BP this has reduced to ~10 m ka^{-1}. From 4 ka cal BP rates of uplift are relatively constant at the low late Holocene levels.

The Andøya slide, at 10 ka cal BP, occurs during the Fennoscandian ice sheet's final stage of retreat (Svendsen and Mangerud, 1987; Bungum et al., 2005). As Figure 2.6 demonstrates, this is a period of increasing isostatic uplift. This fact gives backing to Laberg et al.'s (2000) view that the Andøya slide was most likely caused by an isostatic induced earthquake. During periods of ice retreat sedimentation rates tend to be much higher due to melt-water discharge, ice-rafting and ice-streams (see Dowdeswell and Elverhøi, 2002). This sedimentation could lead to overburdening and pore fluid migration (Dugan and Flemings, 2000; Biscontin et al., 2004; Strout and Tjelta, 2005). Bungum et al. (2005) argue that a pulse of increased seismicity followed immediately from the deglaciation (from 10 ka cal BP), most likely with M_w (moment magnitude) 7+ earthquakes. Situated offshore Norway, on the boundary between the ice sheet and the forebulge region, during the deglaciation and the early Holocene the area would be subject to high rates of crustal stresses and increased seismic activity (Fjeldskaar et al., 2000; Muir-Wood, 2000). It seems likely that, occurring at this time in this location, the Andøya mass movement was caused by the continental slopes being overloaded by sediment during the deglaciation and the triggering of this unstable mass by an isostatic earthquake in a period of, post-deglaciation, heightened seismic activity. Faulting of the continental margin due to continental rebound is also a possible cause (Andøya is situated on the steepest section of the Norwegian-Greenland sea margin with current angles between 5˚ and 18˚ (Vorren et al., 1998)). However, a fall in local relative sea level coupled with a rise in sea water temperature of 5 ˚C (Birks and Koç, 2002) would have made free gas release from hydrates more probable and it is possible that they played a role.
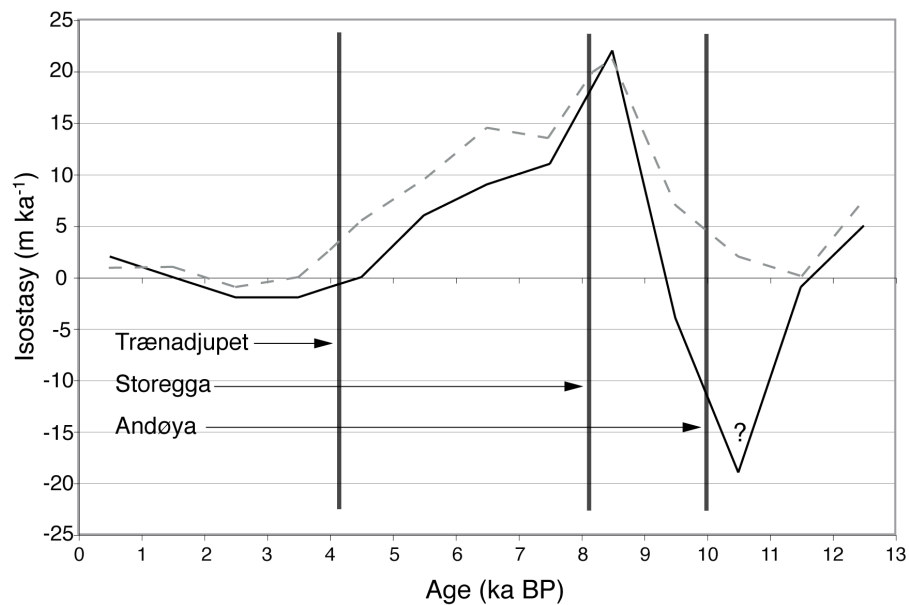
Figure 2.6: Approximation of isostatic change of sea level at Frøya (solid) and Andøya (dashed) for the past 12.5ka. West Norwegian margin mass movements also shown. Isostatic change derived from Martinussen (1961), Svendsen and Mangerud (1987) and McGuire et al. (1997). Value shown is the amount of change for the preceding ka.

This isostatic data, combined with the research conducted on the Ormen Lange field, presents an even stronger argument for an earthquake or some form of crustal warping, related faulting, triggering Storegga. The failure occurred at 8.1 ka cal BP (Haflidason et al., 2004; Haflidason et al., 2005), Figure 2.6 demonstrates that this is immediately after the period with the greatest rate of uplift (>20 m ka^{-1}), at this time uplift is still >10 m ka^{-1} at Frøya, close to the Storegga slide scar. The event's occurrence would seem to be related to post-glacial environmental change: rapid sedimentation on the North Sea Fan associated with the disintegration of the Fennoscandinavian ice sheet, resulted in pore fluid migration north to the Storegga region, an increase in seismic activity, isostatic induced slope steepening (Bryn et al., 2005a). Any role of clathrate destabilisation, through warming ocean temperatures, is a secondary factor.

Trænadjupet occurs, after the local eustatic rise resumes, at 4 ka cal BP. Isostatic rebound was still taking place, as noted by Laberg and Vorren (2000) but, as shown in Figure 2.6, at a reduced rate. This event is possibly an example of a slope made susceptible to failure during the deglacial environment and then triggered several ka later. It has been argued, based on studies of onshore faults and historical records (see Bungum et al., 2005), that the recurrence time of a M_w 7 earthquake on the Norwegian margin is currently approximately 1.1 ka. If such an event occurred in close proximity to the slide area it is quite probable that it would have triggered the event if the slopes were already loaded with unstable sediments. Whilst there is no direct evidence of

seismicity occurring offshore Norway during the deglaciation and early Holocene, work by Mörner et al. (2000) and Bungum et al. (2005) document suspected M_w 8 earthquakes in the scandinavian region, as well as several other M_w 7 and M_w 8 events occurring in the deglaciation and Holocene, indicating that during this period Fennoscandia was seismically active.

Providing an exception to the deglacial focus, the Hinlopen/Yermack megaslide (on the north Spitsbergen margin) has been dated at 30 ka cal BP during the onset of the LGM (Winkelmann et al., 2008). Winkelmann and Stein (2007) propose that the slide was a consequence of the rapid onset of glaciation, including asymmetrical ice-loading and rapid drawdown of water. This case study demonstrates the potential destabilising effects of glacial onset.

When predicting future mass movements on the deglaciating margins of Greenland and Antarctica it is inappropriate to do so with reference to global sea level. Figure 2.5 and Figure 2.6 demonstrate very clearly the need to consider local factors such as relative sea level and local sedimentation patterns.
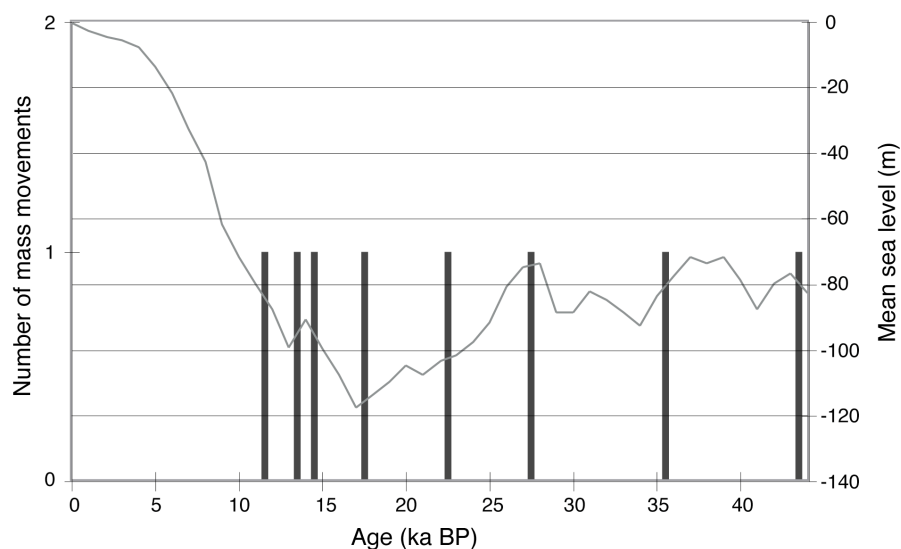
Figure 2.7: Low latitude, non-glaciated margin mass movements and mean global sea level curve (from McGuire et al., 1997) for the past 45 ka.

At lower latitude, non-glaciated, margins the McGuire et al. (1997) sea level curve (derived from Barbados coral (Fairbanks, 1989) and Pacific core data (Shackleton, 1987)) is appropriate. Figure 2.7 shows mass movements associated with such margins, mass movements from the northeastern American margin have been omitted because of the influence of the Laurentian ice sheet. Three events are associated with the deglaciation between 15 and 11.5 ka cal BP. Four events occur at regular intervals between 22 and 43.5 ka cal BP. The other event occurs either at, or just after, the LGM.

Due to the large volume of work conducted on them and their relatively robust age constraint (see Figure 2.3), the Amazon Fan events provide a good case study of the low latitude situation (see Maslin and Mikkelsen, 1997; Piper et al., 1997; Maslin et al., 1998; Maslin and Burns, 2000; Maslin et al., 2005). The western and eastern debris flows occurred during the deglaciation (Maslin et al., 1998; 2005). Deglaciation of the Andes and increased continental wetness caused a massive increase in Amazon sediment discharge (Maslin et al., 1998; Maslin and Burns, 2000; Maslin et al., 2005) (Maslin et al., 1998; Maslin and Burns, 2000; 2005). The rising sea level shifted the deposition centre towards the upper continental slope and the Amazon fan, possibly causing overburdening and failure (Maslin et al., 1998; 2005). The deep events occurred earlier during periods of rapidly falling sea level (15 - 25 m ka^{-1}). This lower sea level would have increased the susceptibility of the slope to failure. Destabilisation of gas hydrates and dissociation of clathrates is the trigger proposed by Maslin et al. (1998; 2005).

2.7. Latitude effects upon susceptibility factors and triggers - a conceptual model of high latitude continental slope failure

Different causal factors operate at different latitudes. These are driven by the movement of water between the ocean basins and the continental ice sheets; and the associated changes in susceptibility and triggering mechanisms that this causes. These different feedbacks are illustrated in Figure 2.8.

2.7.1. High latitude glaciated margins

During the glaciation (Figure 2.8.A) high latitude regions experience an increase in ice-mass. This influences sediment deposition (shift from pelagic to glaciogenic), eustatic sea level (falling), isostatics (depression of continental crust due to ice-mass), seismicity (reduced incidence of earthquakes due to weighting of the continental shelf) and ocean temperatures (cooling). In turn these factors influence the trigger mechanisms. In this instance gas hydrates are destabilised by the falling eustasy but stabilised by the falling ocean temperature. The combined effects of isostasy and eustasy influence local sea level, which affects gas hydrates, sediment deposition and erosion. Stochastic factors (such as non-isostatic earthquakes) may trigger slope failures at any time.
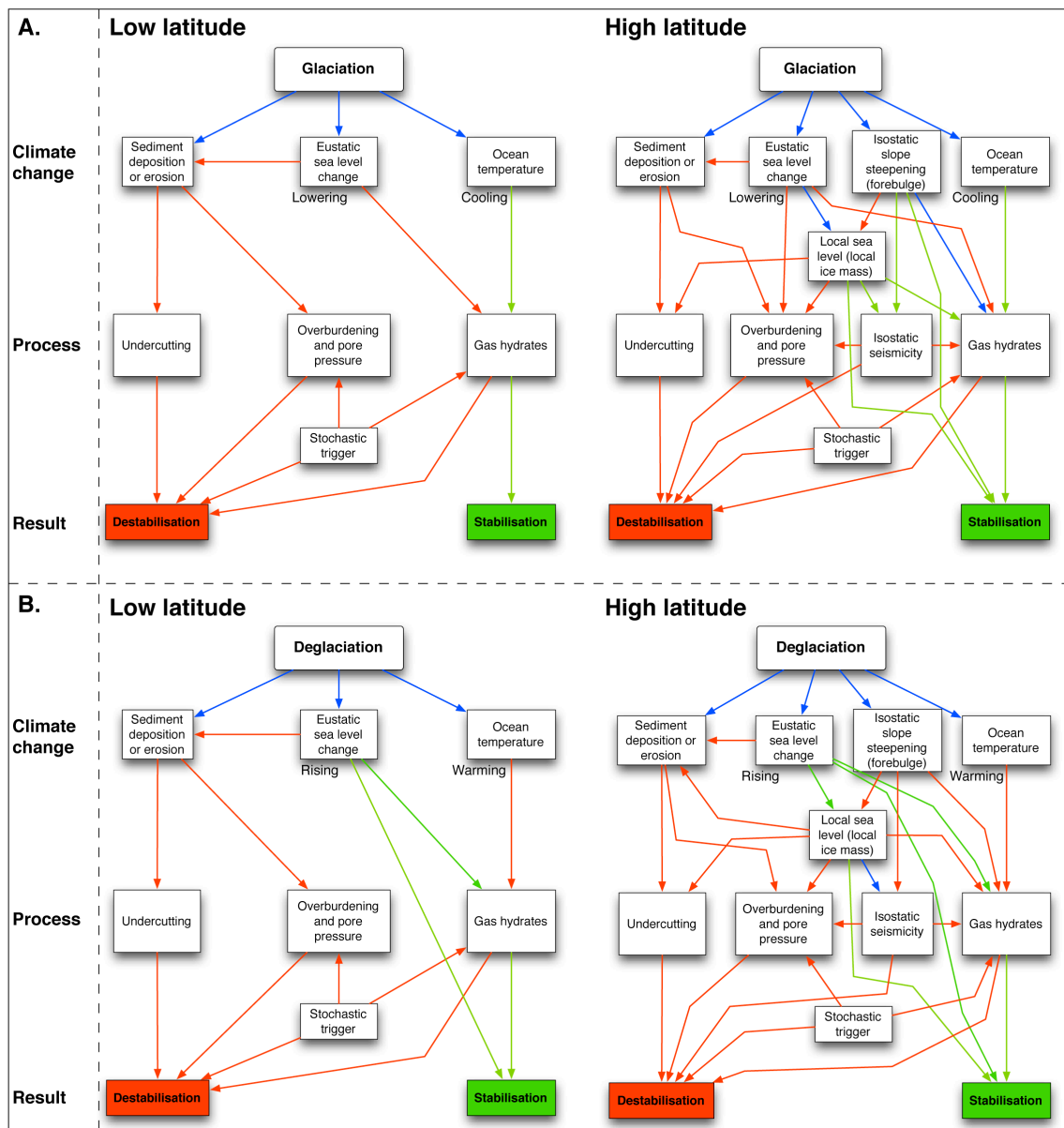
Figure 2.8: Flow diagram demonstrating climate change driven mass movement cause variation during glacial (A.) and deglacial (B.) periods. Processes illustrated for low and high latitudes. Red lines indicate destabilising, green indicate stabilising and blue indicate potentially stabilising or destabilising factors.

During the deglaciation (Figure 2.8.B) high latitude regions experience the collapse of the continental ice-mass. This influences sediment deposition (huge, rapid increase in glaciogenic followed by a return to pelagic (see Dowdeswell and Elverhøi, 2002)), eustatic sea level (rising), isostatics (rebound of depressed continental crust), seismics (pulse of high seismicity in the forebulge region (Fjeldskaar et al., 2000; Muir-Wood, 2000; Bungum et al., 2005)) and an increase in ocean temperatures (~5°C in the Eastern Norwegian sea during the Holocene transition (Birks and Koç, 2002)). The rate of isostatic uplift experienced on some of these margins means that depth of water (and hence pressure) does not increase at the same rate as seawater temperature.

This increases the likelihood of destabilised gas hydrates, however, with a time lag due to diffusive heat flow through sediments (Yamano et al., 1982).

The timing of these deglacial driven processes is region dependent: as different ice sheets melted at different times. For example, Knutz et al. (2002) place the British Ice sheet LGM between 31 and 21 ka cal BP, with a first stable onshore position dated between 17.9 and 15.5 ka cal BP (Everest et al., 2006). Evidence from the Vøring margin provides a 19 ka cal BP date for the Fennoscandian ice sheet LGM, with decreasing ice influence by 18 ka cal BP and an onshore position prior to 14.5 ka cal BP (Dahlgren and Vorren, 2003). Meltwater outflow into the Gulf of Mexico is dated at 15.7 ka cal BP (Broecker et al. (1988) ^{14}C dates Fairbanks et al. (2005) calibration), providing a different age for the Laurentian ice sheet deglaciation.

Rapid sedimentation, release of isostatic forces, an upsurge of seismicity and gas release from hydrates increase stresses operating on the continental margins. High latitude margins are relatively stable during the glaciation and relatively unstable during deglaciation. Supporting this view, Lee (2009) suggests that mass movements on the northeast American margin are less likely, by a factor of 1.7 to 3.5, to occur during the present interglacial than they were during the last glacial. Urlaub et al.'s (2013) study demonstrate no statistically significant relationship between submarine mass movements and climate change, however, they do suggest that mass movements are most frequent after the LGM. In high latitudes during deglaciation local relative sea level will bare little resemblance to mean global relative sea level (see Figure 2.5) and, therefore, the timing of processes influencing slope stability may change from region to region.

2.7.2. Low latitude non-glaciated margins

During the glaciation (see Figure 2.8.A) low latitude regions experience a fall in ocean temperature and relative sea level: influencing sediment deposition (change of deposition centre, see Maslin et al. (1998; 2005)). Trigger mechanisms are also influenced. Gas hydrates are destabilised by falling sea level but stabilised by cooling temperatures, although temperatures are not reduced to the same degree as in the higher latitudes. A difference in sea surface temperatures of 1.2°C between the glacial and Holocene is reconstructed by Billups and Spero (1996) for the western equatorial Atlantic Ocean. The gas hydrate stability zone will be reduced during glacial periods in low latitudes. Change in sediment deposition can lead to overburdening through increasing pore pressures (Dugan and Flemings, 2000; Biscontin et al., 2004; Strout and Tjelta, 2005).

During the deglaciation (see Figure 2.8.B) low latitude regions experience a eustatic rise in relative global sea levels due to the melting of the high latitude ice-mass, sediment deposition will increase due to melting of glaciers in mountains (e.g. Andes and Himalaya) and increased continental wetness (see Maslin et al., 1998; Maslin and Burns, 2000). Gas hydrates will be destabilised by increasing ocean temperatures but stabilised by rising eustatic sea level. Sediment failure is likely to occur due to sediment overburdening resulting from increased rates of sedimentation and shifting deposition centres. Low latitude continental margin slopes will be more susceptible to failures triggered by earthquakes during deglacial periods due to the rapid build up of sediment resulting from the return of interglacial conditions.

2.8. Chapter summary

This chapter demonstrates that Late Pleistocene North Atlantic submarine mass movements have been influenced by climatic change through a combination of isostatic and sedimentary processes associated with the oscillating relative sea level. Certain slopes are predisposed to failure because of their sedimentary structure and geological history.

A latitudinal zoning exists in the causes of submarine mass movements through the past 45 ka. In the high latitudes predominantly during deglaciations, through increased sedimentation, increased ocean temperatures and the release of isostatic energy: increasing the susceptibility of slopes to failure due to isostatic/seismic triggers. In the low latitudes lowered sea relative levels during the glacial increase the probability of failure due to clathrate destabilisation and free gas release (Nisbet, 1990; Haq, 1998; Kennett, 2003) and during the deglacial increased sedimentation and changes in deposition centres increase the likelihood of failure due to overburdening of the sedimentary column (Maslin et al., 1998; 2005). Deglacial submarine mass movements are associated with the early Holocene methane peak.

Climate driven environmental change (with associated changes in local and global relative sea level, sedimentation and isostatic seismicity) is likely to initiate submarine mass movement in the same way as it has in the past. Glacial retreat in Antarctica (see Cook et al., 2005) and Greenland (see Howat et al., 2005; Velicogna and Wahr, 2006) will increase the likelihood of sedimentary failure and mass movements (with their associated impacts of tsunamis and CH_4 release) occurring in these locations.

2.8.1. Implications for the Barra Fan and Peach debrites

Section 2.5.1.6 outlined the published understanding of susceptibility factors and trigger mechanisms of the Peach debrites prior to this thesis. The chapters that follow

investigate the northwest British continental margin, focusing on the Barra Fan and Peach slide in more detail. In particular, as already demonstrated important for Storegga (Bryn et al., 2005b) and Trænadjupet (Laberg and Vorren, 2000), the role of glaciogenic and contouritic sedimentation will be examined.

As such chapter three provides an overview of the geologic and oceanographic context of the Rockall Trough and Barra Fan.

3. Geologic and oceanographic development of the Barra Fan and northwest British continental margin

3.1. Introduction to chapter

This chapter provides a geologic and oceanographic framework for the region and the Barra Fan study site based on a review of previous research. This provides a context (including oceanographic, sedimentological and cryospheric influences) within which to discuss submarine mass movement on the Barra Fan; and also provides the foundations for the application of chapter two's conceptual model of slope failure to this region in later chapters.

The main question that this chapter seeks to answer is: how has the margin evolved over geological time to provide the current setting? This question may not have a succinct answer, but knowledge of these factors will be essential when discussing the sedimentary processes operating on the margin in later chapters of this thesis.

3.2. Development of the northwest British continental margin

The Cenozoic evolution of the northwest British continental margin has been a function of igneous, tectonic and epeirogenic activity; and subsequent impact on oceanographic and sedimentary processes.

3.2.1. Palaeocene igneous activity

The northeast Atlantic was formed by the separation of Greenland and Europe by tectonic rifting at approximately 55 Ma (Storey et al., 2007; Anell et al., 2009). This coincided with intense activity of the North Atlantic Igneous Province (NAIP), which included large scale eruptions in Baffin Island, East and West Greenland, Faeroes, British Isles and the seaward dipping reflectors to the rifted margin (Carter et al., 1979; Kent and Fitton, 2000; Storey et al., 2007; Anell et al., 2009). The bulk of Cenozoic volcanism in the British Isles occurred between 61 and 59 Ma, though late-stage dyke emplacement continued till ~58 Ma (Kent and Fitton, 2000). It is during this period that the seamounts of the Rockall Trough (Rosemary Bank, Anton Dohrn and Hebrides Terrace; see figure 3.2) were formed. Age constraints for the offshore intrusions are not so well defined as for onshore (Kent and Fitton, 2000; Anell et al., 2009); however, the Hebrides Terrace intrusion is believed to have been formed prior to 60 Ma (Omran (1990), cited in Stoker et al., 1993).

3.2.2. Post-rift tectonic margin evolution

Following the Palaeocene rifting of the northeast Atlantic the northwest European margin, and adjacent deep-water basins, have undergone a structural evolution

encompassing uplift and subsidence during different periods (Japsen and Chalmers, 2000; Stoker et al., 2002; Dahlgren et al., 2005; Praeg et al., 2005; Stoker et al., 2005a; Anell et al., 2009; Stoker et al., 2010).

A variety of methodologies (including geomorphological analysis, seismic stratigraphic interpretation, Vitrinite reflectance and Apatite fission track analysis (AFTA)) have been used to reconstruct Cenozoic uplift and subsidence of the northwest European margin (see Japsen and Chalmers, 2000; Praeg et al., 2005; Anell et al., 2009). Praeg et al. (2005) identify three major periods of relative uplift of the northwest European continental margin during the Cenozoic: late-Palaeocene to early-Eocene margin uplift (~60 - 50 Ma); Eocene offshore subsidence (~35 - 25 Ma); and early-Pliocene to present margin and shelf uplift (4 ± 0.5 Ma to present). With some discrepancy, the timings of these uplift episodes are supported by work by Anell et al. (2009) and Stoker et al. (2010).

The late-Palaeocene to early-Eocene episode is believed to have involved primary upwelling, from the Palaeo-Iceland-plume, with associated underplating of the lithosphere with less dense magma (Saunders et al., 2007; Anell et al., 2009). Saunders et al. (2007) present evidence supporting uplift of the British Isles occurring between 56.5 and 54 Ma during this episode.

The Eocene is marked by subsidence of the offshore basins and the deepening of the Faeroe Conduit, the Fram Strait and subsidence of the Greenland-Scotland Ridge (Stoker et al., 2002; Praeg et al., 2005; Stoker et al., 2005a; Stoker et al., 2010). These bathymetric changes resulted in an early-Miocene southern gateway for thermohaline circulation and allowed the strengthening of bottom current circulation in the Rockall Trough (Praeg et al., 2005; Stoker et al., 2005a; Stoker et al., 2010).

The most recent uplift episode, late-Pliocene to present, is associated with the development of prograding shelf-front wedges (including the Barra Fan), the age of which pre-date the onset of northern hemispheric glaciation by ~1 Ma (Stoker et al., 2002; Dahlgren et al., 2005; Praeg et al., 2005; Stoker et al., 2005b; Stoker et al., 2010). Intriguingly, the timing of this uplift episode is approximately coeval with the proposed shoaling of the Panama seaway to within 100 m of sea-level (4.6 Ma); an event that is proposed to have intensified North Atlantic thermohaline circulation and increased moisture supply to the high northern latitudes (Haug and Tiedemann, 1998; Bartoli et al., 2005). It is likely that increased precipitation, combined with uplift, would have resulted in the continental and shelf denudation required to initiate growth of shelf-front wedges.

There is some disagreement concerning the cause of uplift with one school favouring the role of upper mantle convection (e.g. Japsen and Chalmers, 2000; Kent and Fitton, 2000; Saunders et al., 2007) and another that of plate boundary reorganisation (e.g. Stoker et al., 2005b; Stoker et al., 2010). It seems probable that both processes may have played roles during the Cenozoic, however, mantle convection associated with the Iceland-plume seems likely to have been confined to the late-Palaeocene uplift episode (Stoker et al., 2010). Equally, Praeg et al. (2005) note that plate reorganisation may be driven by mantle convection, as such periods of enhanced mantle upwelling may coincide with periods of plate reorganisation.

3.2.3. Sedimentation process response to margin evolution

The tectonic changes associated with the Cenozoic evolution of the northwest European margin had a profound effect on shelf-margin and deep-water sedimentation on the British continental margin and in the Rockall Trough.

Five key regional unconformities are identified in the Rockall Trough (and northwest European margin more generally): late-Eocene, base Neogene, intra-Miocene, intra-Pliocene (or base Upper Neogene) and intra-Pleistocene (or Glacial) (Stoker et al., 2002; Dahlgren et al., 2005; Laberg et al., 2005; Praeg et al., 2005; Stoker et al., 2005b). These unconformities bound sediment units that reflect particular sedimentary regimes and often represent erosional surfaces indicating a change in regime.

There is some evidence supporting bottom current activity (likely sourced from Tethyan Outflow Water) and associated contouritic sedimentation from the late-Eocene or early-Oligocene (Laberg et al., 2005; Stoker et al., 2005b). However, a significant expansion of bottom current activity and associated contourite sedimentation is not observed in the Rockall Trough until after the intra-Miocene unconformity ~15 Ma (Laberg et al., 2005). This unconformity is the stratigraphic signature of an erosive event believed to have been the consequence of increased bottom current vigour following the deepening of the Faeroe conduit during a tectonic inversion that changed the geometry of the Wyville-Thomson Ridge Complex (Stoker et al., 2002; Stoker et al., 2005b). The regional extent of the unconformity, north and south of the Greenland-Scotland Ridge, supports this view (Laberg et al., 2005). Contourite sedimentation dominates the successions of the northwest European margin from the intra-Miocene to intra-Pliocene unconformities, reflected in the characteristics of the RPb (Rockall and Porcupine Basins), FSN-2a (Faeroe-Shetland area) and Kai (North Sea Fan, Møre and Vøring Margins) formations (Bryn et al., 2005b; Stoker et al., 2005b).
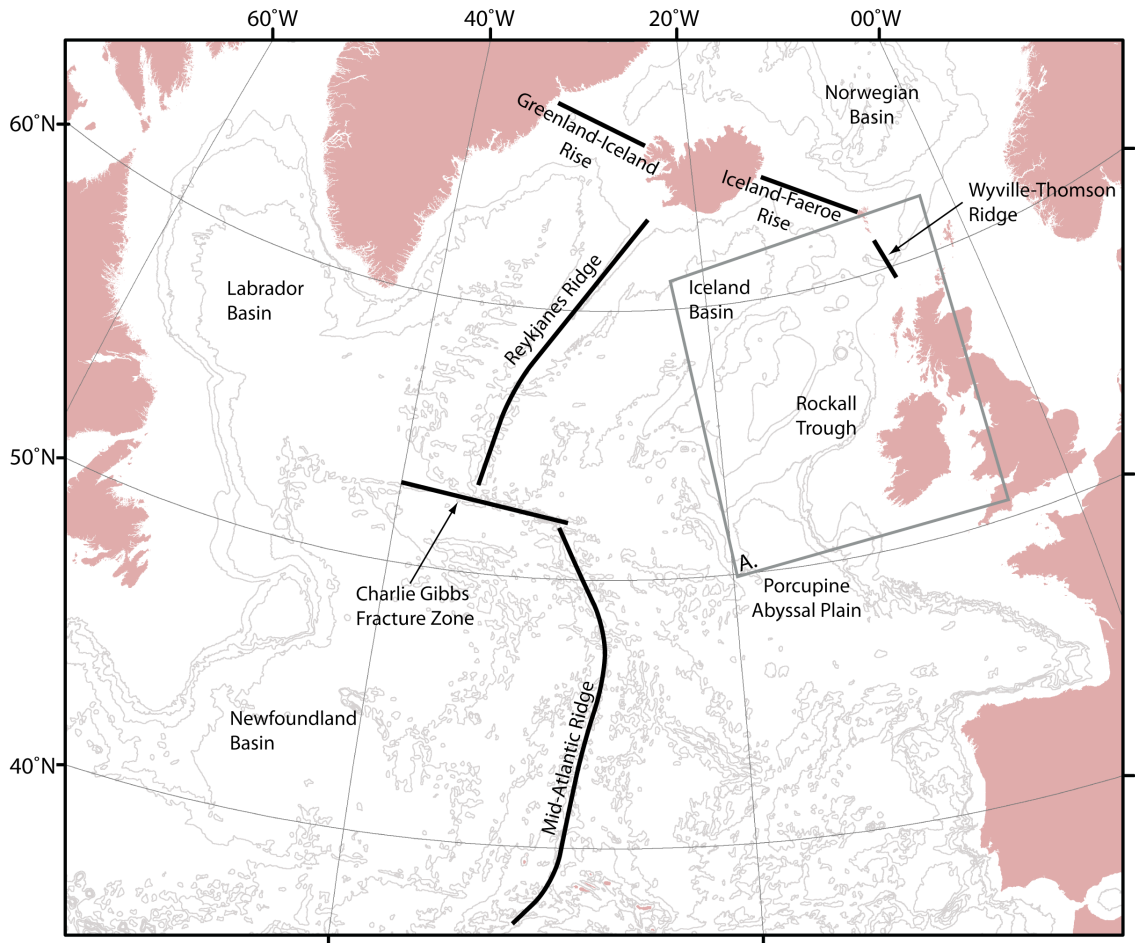
Figure 3.1: Contemporary North Atlantic overview. Contours indicate 1000 m intervals, thick black lines indicate oceanographically significant bathymetric features, major basins are indicated. Approximate location of figure 3.4 shown by inset box A.

Dated at 4 ± 0.5 Ma, the intra-Pliocene unconformity marks the commencement of increased downslope sediment transport and forms the base of the large European shelf-front wedges (Stoker et al., 2002; Dahlgren et al., 2005; Stoker et al., 2005b). This unconformity has been linked to an erosive event driven by uplift of the continent and shelf as well as bottom current activity (Stoker et al., 2002). Accounting for this most recent uplift episode, Praeg et al. (2005) propose a epeirogenic tilting hypothesis. This view is supported by Japsen and Chalmers (2000) who propose a domal uplift and subsidence model; and by Stoker et al. (2005b) who note that the 4 Ma age of the unconformity is compatible with timing of late Neogene plate reorganisations in the Atlantic and Pacific.

Growth of shelf-front wedges, including the Barra Fan, pre-dated northern hemispheric glaciation by ~1 Ma (Stoker et al., 2002; Dahlgren et al., 2005; Praeg et al., 2005; Stoker et al., 2005b) and initiation of growth appears to have been a consequence of increased continental denudation via uplift and increased runoff due to increased moisture following the shoaling of the Panama seaway at 4.6 Ma (Haug and Tiedemann, 1998). The glaciogenic component of the shelf-front wedges was

deposited post 2.5 Ma and the bulk of this post 0.44 Ma (Stoker et al., 1994; Dahlgren et al., 2005). The earliest ice-rafted debris in the Rockall Trough has been dated to 2.48 Ma (Stoker, 1995), however, the intra-Pleistocene (or Glacial) unconformity is dated to 0.44 Ma on the Hebrides slope: marking the onset of Pleistocene shelf-wide glaciation (Stoker et al., 1994).

3.3. Barra Fan during the Pleistocene and Holocene

Shown in Figure 3.2, the Barra Fan is situated on the northwest British continental margin. A prograding slope front fan, it is located on the continental slope between the Hebrides Shelf and the Rockall Trough (Stoker, 1995; Armishaw et al., 1998; Stoker, 1998). At the shelfbreak water depth varies between 150 m and 200 m, towards the toe of the fan it is in excess of 2000 m (Stoker, 1995).

To the north of the Barra Fan is the Hebrides slope and the extremely steep (up to 26°) Giekie escarpment. To the south are the Hebrides Terrace Seamount (HTS) and the Donegal Fan. The Barra and Donegal Fans are frequently referred to as a single fan complex (Armishaw et al., 1998). Taken as such the Barra-Donegal fan complex covers 6,300 km^2 and has a thickness of ~650 m (Armishaw et al., 1998; Holmes et al., 1998). As this thesis is concerned with sedimentation affecting the northern, Barra, sector of the complex the name Barra Fan shall be used throughout. The main regional faults are shown in Figure 3.2.B, these are all pre-Tertiary (Stoker et al., 1993). The region experiences a low level of seismic activity at the present time (HSE, 2002), though it is anticipated that this level increases during deglacial periods and for some millennia after (Bungum et al., 2005; Bungum et al., 2010).

Though the Sula Sgeir Fan (see Figure 3.2.A), the Rona and Foula wedges situated further to the north, are major glaciogenic deposits (Stoker, 1995; Stoker et al., 2009) the Barra Fan is the largest deposit of glaciogenic sediment on the western British continental margin (Armishaw et al., 1998). It is also the most southerly of the glaciogenic prograding fans (features also referred to as Trough Mouth Fans) on the western European continental margin (Dahlgren et al., 2005; O'Reilly et al., 2007).
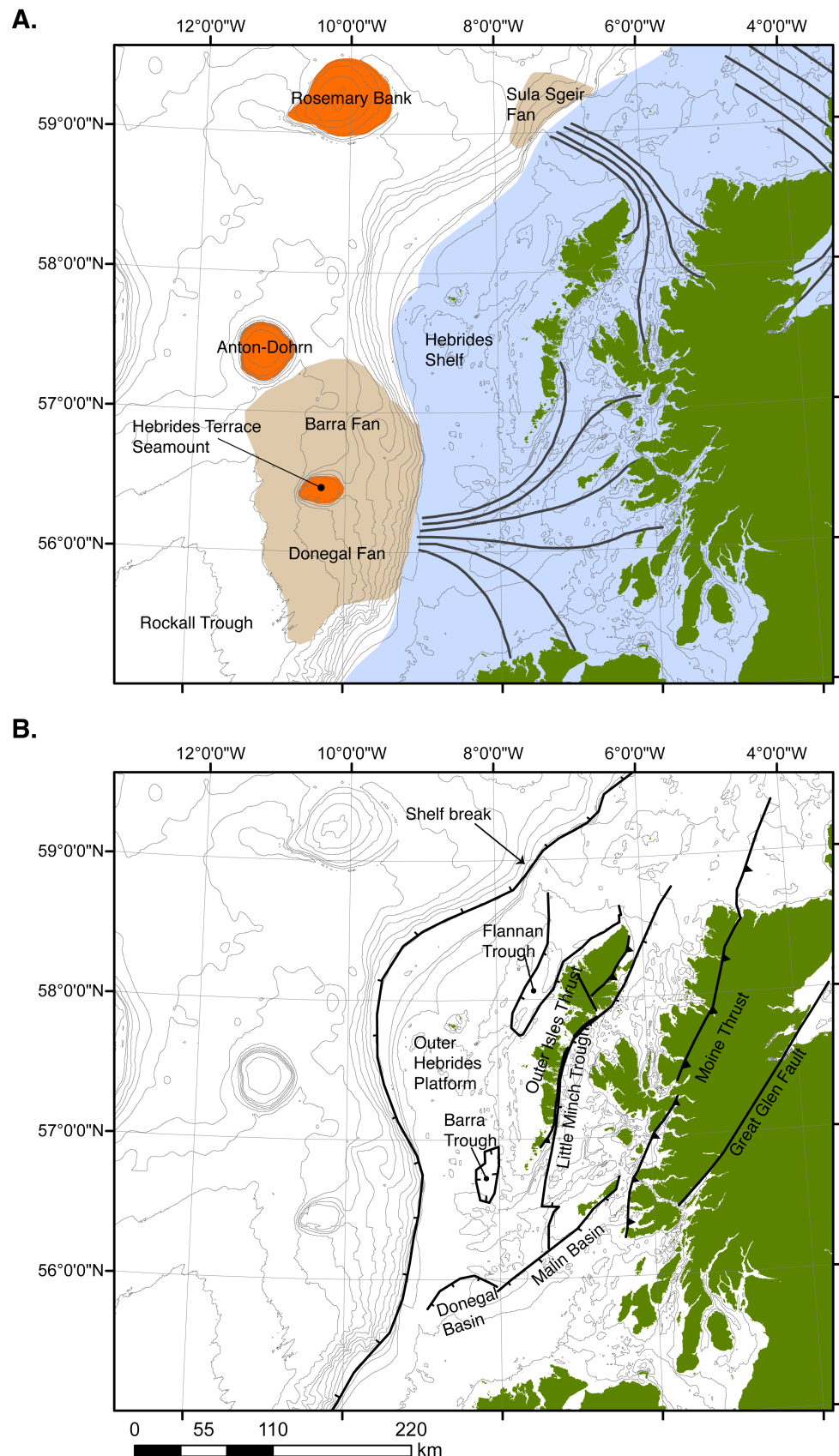
Figure 3.2: Overview of northwest British continental shelf and adjacent Rockall Trough. A. Glacial features, light blue shows maximum ice sheet extents and thick grey lines approximate major ice-stream locations (from Bradwell et al., 2008). B. Main regional faults (from Stoker et al. (1993)), tick indicates downthrow side, for thrust faults barb is on upthrow side. Contour intervals 50 m between 0 and 250 m water depth; and 250 m for depths greater than 250 m.

The base of the Barra Fan is defined by the intra-Pliocene unconformity and linked to continental uplift (see Section 3.1.3 and Stoker et al., 2002; Dahlgren et al., 2005; Stoker et al., 2005b). Ice rafted debris (IRD) evidence from the Rockall Plateau indicates that the margin has accumulated glacially derived sediment since ~2.48 Ma (Stoker, 1995). Though widespread glaciation of the Hebrides Shelf did not occur until the mid-Pleistocene, when there was a major change in the inner margin sedimentation style. According to Stoker (1998) grounded ice sheets have reached the shelf edge at least twice in the last 0.5 Ma. Evidence from Tertiary basalt IRD supports a Hebrides shelf-grounded ice sheet during the Wolstonian glaciation, between 173 and 128 ka (Hibbert et al., 2010). The slope front glaciogenic (post 0.44 Ma) deposits are termed the Upper Macleod sequence and consist of mid- to late-Pleistocene muds. These overlie the pre-glacial shallow marine sands of the Pliocene to early- to mid-Pleistocene Lower Macleod sequence (Stoker et al., 1993; Stoker, 1995). The uppermost unit on the Barra Fan is the Gwaelo Sequence, which overlies glacial debris flows (Stoker et al., 1993).

3.3.1. Relationships between the Barra Fan and the British ice sheet during the late Pleistocene (Devensian)

The British ice sheet (BIS) is the Barra Fan's primary sediment source, and so glacial and deglacial periods represent key intervals with regards to fan sediment accumulation. Therefore, when considering slope stability on the fan it is necessary to consider the extent of ice-cover as well as timings, and nature, of advance and retreat of the BIS.

Globally, in terms of relative sea level, the last glacial maximum (LGM) is believed to have occurred over a period of 6 - 7 ka sometime prior to 21 ka cal BP (Peltier and Fairbanks, 2007). The precise timing and extent of the BIS's LGM is subject to debate, though there is consensus in the first shelf edge ice-grounding occurring between 0.5 - 0.4 Ma (Stoker et al., 1994). Extensive evidence supports this view, including moraines (Selby, 1989; Stoker et al., 1994; Dunlop et al., 2010) and large scale lineations (Graham et al., 2007). Major growth of the BIS is thought to have occurred, after Heinrich event 4, from 38 ka cal BP (Peters et al., 2008; Scourse et al., 2009). A detailed study by Clark et al. (2012), presents the period 27 - 26 ka cal BP as that of maximum ice extent, or the British LGM. Figure 3.2.A, shows the shelf-edge northwestern extent of the BIS as mapped by recent work (Bradwell et al., 2008; Clark et al., 2012).

The relative stability of the BIS within the Devensian (the period in which the BIS was last present) is hotly debated. Conflicting views are expressed by Hall et al. (2003) and

Bowen et al. (2002), with the former also considering a much more extensive LGM BIS likely.

Marine data, based on core samples from the Rockall Trough and its environs, are broadly consistent. British ice sheet lithic deposition is limited prior to Heinrich event 4 (Peters et al., 2008; Hibbert et al., 2010), at approximately 38 ka (Hemming, 2004). An increase in BIS IRD between 28 and 30 ka until 20 - 18 ka is noted by a number of studies (Knutz et al., 2002; Knutz et al., 2007; Peck et al., 2007; Scourse et al., 2009; Hibbert et al., 2010; Hall et al., 2011), reflecting a probable shelf-edge advance and subsequent collapse. Evidence of a number of meltwater pulses within this period is presented by Knutz et al. (2007), Peck et al. (2007; 2008) and Hibbert et al. (2010) demonstrating the existence of localised, ice sheet disintegration. Heinrich-type events that would also be associated with rapid sediment deposition.

The Barra Fan itself consists primarily of sediments sourced from either western Scotland or northwest Ireland (Knutz et al., 2001; Bradwell et al., 2008; Peters et al., 2008; Howe et al., 2012). The Hebrides Shelf is incised by a number of deep trough features (i.e. North, Central and South Stanton Deeps and the Malin Deep, see James (1992)), believed to be eroded by palaeo-ice-streams (Stoker et al., 1994; Armishaw et al., 1998; Bradwell et al., 2008; Scourse et al., 2009; Dunlop et al., 2010). Recent work by Howe et al. (2012) provides evidence of a Hebrides ice-stream that flowed southwards through the Little Minch. Figure 3.2 presents 50 m contour intervals on the continental shelf, indicating deeps that may have been eroded by moving ice, the generalised interpreted ice-stream locations from Bradwell et al. (2008) are also shown. These features act as conduits for sediment transported from the continent, onto the fan and into the Rockall Trough and their location demonstrates the primary inputs toward the south of the fan complex, focused on the Donegal Fan area.

3.3.1.1. Chronology of the LGM and deglaciation at the Barra Fan

Ice rafted debris evidence in the North east Atlantic supports maximum glaciation occurring at approximately 27 to 24 ka cal BP (Peck et al., 2007; Hibbert et al., 2010; Hall et al., 2011), corresponding well with data from the Barra Fan: which places the period of maximum ice advance at between 31 and 21 ka cal BP (Knutz et al., 2002). The age of the deglaciation, calculated from decline in IRD concentrations, is estimated at 18.4 - 17.2 ka cal BP (Peck et al., 2007) and 19 - 16 ka cal BP (Knutz et al., 2007). These ages correspond well with terrestrial data: evidence from cosmogenic [10]Be dating of moraines in northwestern Scotland provide an age of 17.9 to 15.5 ka cal BP for the first stable onshore position of the BIS (Everest et al., 2006). A stable onshore ice sheet does not preclude the possibility of an active shelf-edge ice-stream, Scourse

et al. (2009) suggest that iceberg calving took place on the Barra Fan shelf-edge during the Younger Dryas.

Based on sea surface temperatures, reconstructed from planktonic foraminiferal assemblages, Kroon et al. (2000) place the Bølling period slightly after 14.6 ka cal BP, the Younger Dryas slightly after 13.5 ka cal BP and state that the Holocene was fully established by 10.9 ka cal BP (Kroon et al. (2000) AMS ^{14}C dates converted using Fairbanks et al. (2005) radiocarbon calibration).

3.3.1.2. Local sea level and isostatic rebound

As discussed for the Norwegian margin, in section 2.6, because of the presence of a local ice sheet, during the late-glacial and early Holocene changes to local sea level on the west coast of Scotland would have been significantly different to the mean global sea level. Several studies have investigated raised shorelines on the Scottish mainland and the Hebrides (Jordan et al., 2010; Smith et al., 2012). However, these terrestrial studies are confined to the Holocene.

Lambeck (1995) presents a modeled sea level curve, for a location to the south of St Kilda (based on the model presented by Lambeck (1993)) that extends to 22 ka cal BP. This model is based on relatively conservative ice sheet parameters (not extensive expansion onto the Hebrides Shelf and 400 m thick ice on the Hebrides) and a rebound component based on lithospheric thickness and mantle viscosity. The mean of Lambeck's (1995) modeled data is presented in Figure 3.3.A. The data is supported by palaeoenvironmental core data presented by Peacock et al. (1992) and is similar to other reconstructions from the region (Jordan et al., 2010).

Modeled local sea level data should be regarded as a generalised view. Local ice sheet and lithospheric variation will result in different magnitudes and velocities of crustal adjustment (see Lambeck, 1993). As such the data presented in Figure 3.3 should be regarded as an approximate view.

Considering the above caveat, it is possible to estimate the isostatic component of the local sea level by subtracting the eustatic (global sea level) component, shown in Figure 3.3.B. As noted by Lambeck (1995) and observed in palaeoenvironmental data by Peacock et al. (1992) the lack of a local response to the rapid eustatic sea level rise between 17 and 14 ka cal BP is significant. This may be explained by a substantial isostatic uplift event west of the Hebrides at this time, estimated data in Figure 3.3.B shows rates of 10.25 m ka^{-1}. The significant negative isostatic event shown at 13 ka may result from generalisation in the local model or a significant crustal depression caused by expanding ice-mass. As the timing is prior to the Younger Dryas (as

modeled by Lambeck (1993)) generalisation appears the more likely. The positive rebound episodes shown during the Holocene are broadly in agreement with shoreline observations in the region (Jordan et al., 2010; Smith et al., 2012).
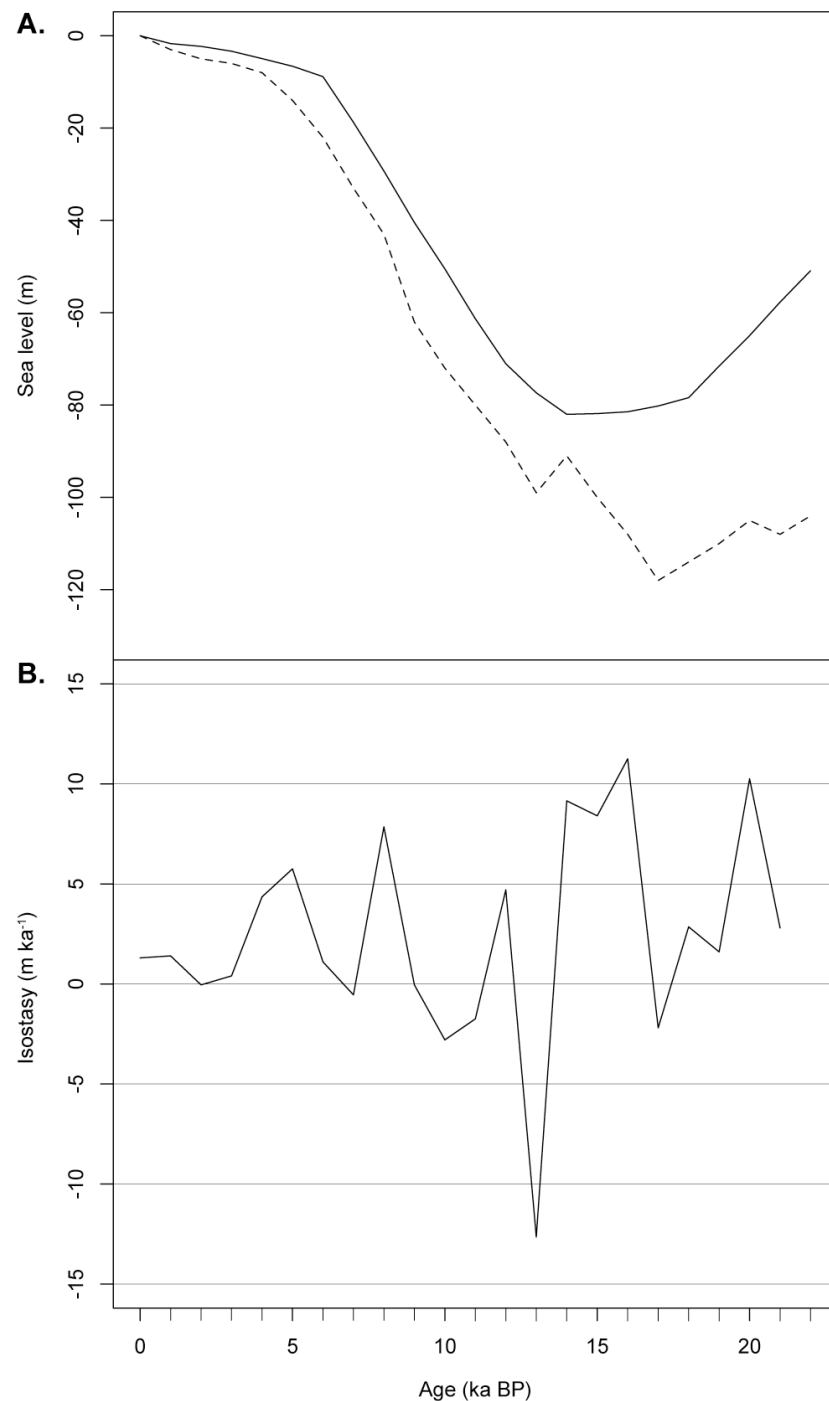
Figure 3.3: Local sea level and estimated isostatic rebound for the Hebrides Shelf. A. Local sea level (solid line, from Lambeck, 1995) compared against global sea level (dashed line, from McGuire et al., 1997 and references cited therein). B. Rate of isostatic change, value shown is the amount of change for the preceding ka.

3.3.2. Oceanographic setting of the Rockall Trough and Barra Fan
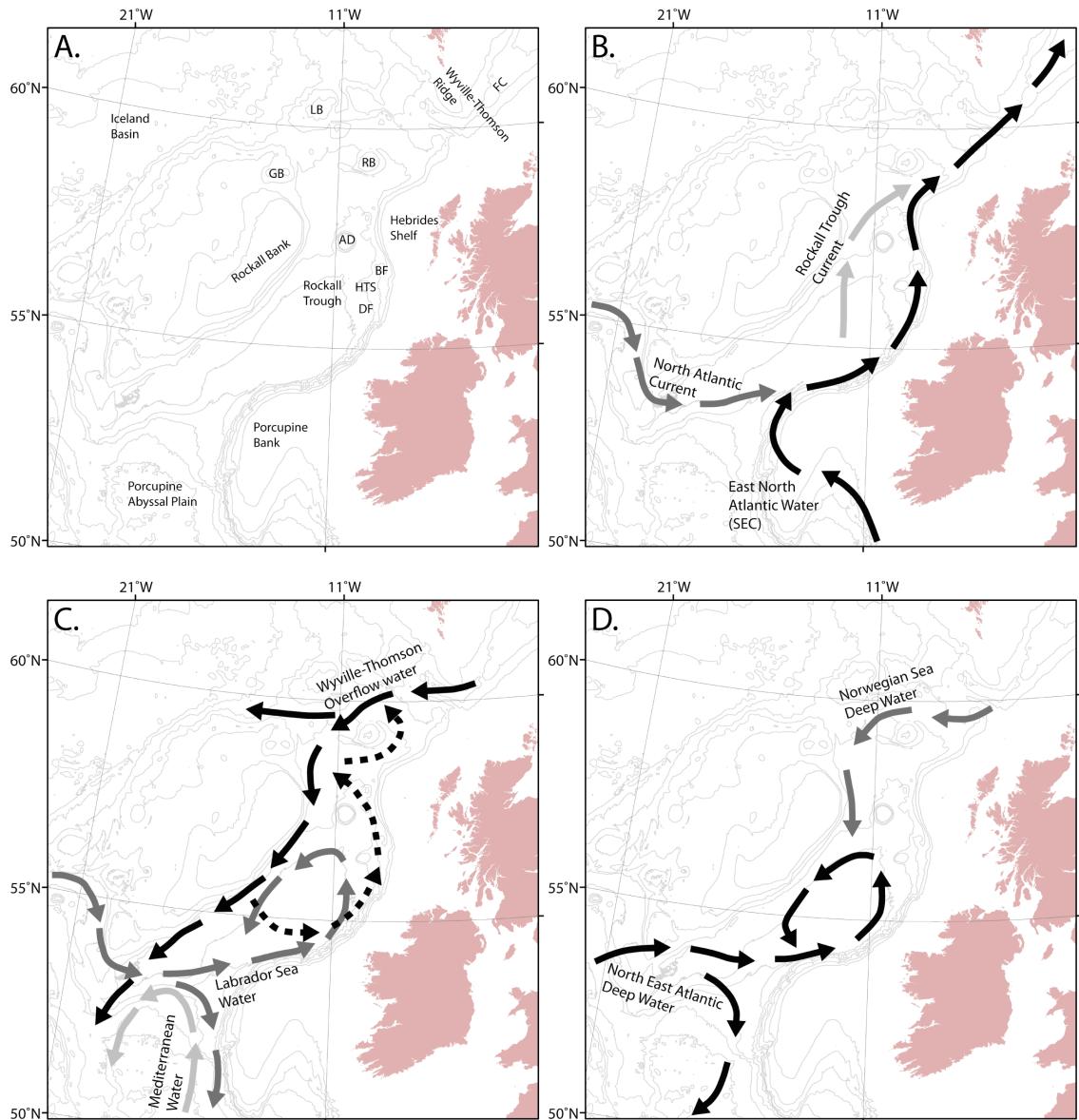
Figure 3.4: Contemporary oceanographic setting of the Rockall Trough and Barra Fan, contours indicate 500 m intervals. A. Shows major bathymetric features: AD - Anton Dohrn Seamount, BF - Barra Fan, DF - Donegal Fan, FC - Faeroe Conduit, GB - George Bligh Bank, HTS - Hebrides Terrace Seamount, LB - Lousy Bank, RB - Rosemary Bank. B. Upper water mass circulation (from Holliday et al., 2000; New and Smythe-Wright, 2001). C. Intermediate water mass circulation, dashed lines indicate inferred flow (from Johnson et al., 2010; Ullgren and White, 2010). D. Deep water mass circulation (from New and Smythe-Wright, 2001).

As Figure 3.4.A shows, the Rockall Trough is located west of the British and Irish continental margin, bounded by Rockall Bank in the west and the Wyville-Thomson Ridge in the north. Water depth increases from 1200 m in the north to 4500 m in the south, where the trough borders the Porcupine Abyssal Plain (Øvrebø et al., 2006). Water masses in the Rockall Trough display an anti-clockwise cyclonic gyre, with many eddies around banks and seamounts (Holliday et al., 2000), a function of the Corriolis Effect acting within a semi-enclosed, northern hemispheric basin.

3.3.2.1. Contemporary circulation

Situated in the northeast Atlantic the Rockall Trough, in a generalised view, is located within Atlantic Meridional Overturning system, with warm, saline water travelling northwards from the Caribbean and Gulf of Mexico, as the North Atlantic Current, and sinking in the Nordic Seas, before returning south as North Atlantic Deep Water (NADW) (Holliday et al., 2000; McManus et al., 2004). However, looking at the Rockall Trough on a local level the picture is more complicated and operates at a number of different bathymetric levels. Figure 3.4 outlines the present understanding of contemporary circulation in the Rockall Trough for upper (3.4.B), intermediate (3.4.C) and deep (3.4.D) water masses.

The majority of water masses that enter the Rockall Trough do so from the south. In the upper layers (see Figure 3.4.B) East North Atlantic Water (ENAW) is the major current, transported polewards with the Shelf Edge Current (SEC), contributing an average of 3.0 Sv of the mean upper water northerly flow of 3.7 Sv (Holliday et al., 2000; Øvrebø et al., 2006). The SEC typically displays flow speeds of 15 - 30 cm s^{-1} and is associated with the upper 400 - 500 m of the water column (New and Smythe-Wright, 2001; Johnson et al., 2010). Supporting this, Armishaw et al. (1998) document scour features, on the upper slopes of the Barra Fan, indicative of velocities of between 12 and 25 cm s^{-1}. The Rockall Trough Current separates from the main SEC flow and flows to the west of Anton Dohrn, before rejoining the main flow passing over the Wyville-Thomson Ridge into the Nordic Seas (New and Smythe-Wright, 2001).

The situation for intermediate water masses is shown in Figure 3.4.C. The presence or absence of Mediterranean Water (MW) in the Rockall Trough, has been subject to considerable debate. However, recent work by Johnson et al. (2010) and Øvrebø et al. (2006) appears to show this water mass to be absent north of 52° - 54°N. Ullgren and White (2010) identify the MW salinity maxima at 1000 m depth and evidence for its presence to 53°N, at Porcupine Bank. The key intermediate water mass entering from the south is the cold and relatively fresh Labrador Sea Water (LSW), which flows via the Charlie Gibbs Fracture Zone (see Figure 3.1) and occupies depths between approximately 1100 and 2200 m (New and Smythe-Wright, 2001; Johnson et al., 2010; Ullgren and White, 2010). The depth of LSW varies, with Johnson et al. (2010) mapping the mass between 1100 and 1800 m water depth east of Anton Dohrn, but New and Smythe-Wright (2001) describing LSW as present between 1700 and 2200 m in a cyclonic gyre following the 2500 m contour. Wyville-Thomson Overflow Water (WTOW) enters from the north of the Rockall Trough, is present at 600 - 1200 m depth and can be traced to at least 55°N (Johnson et al., 2010).
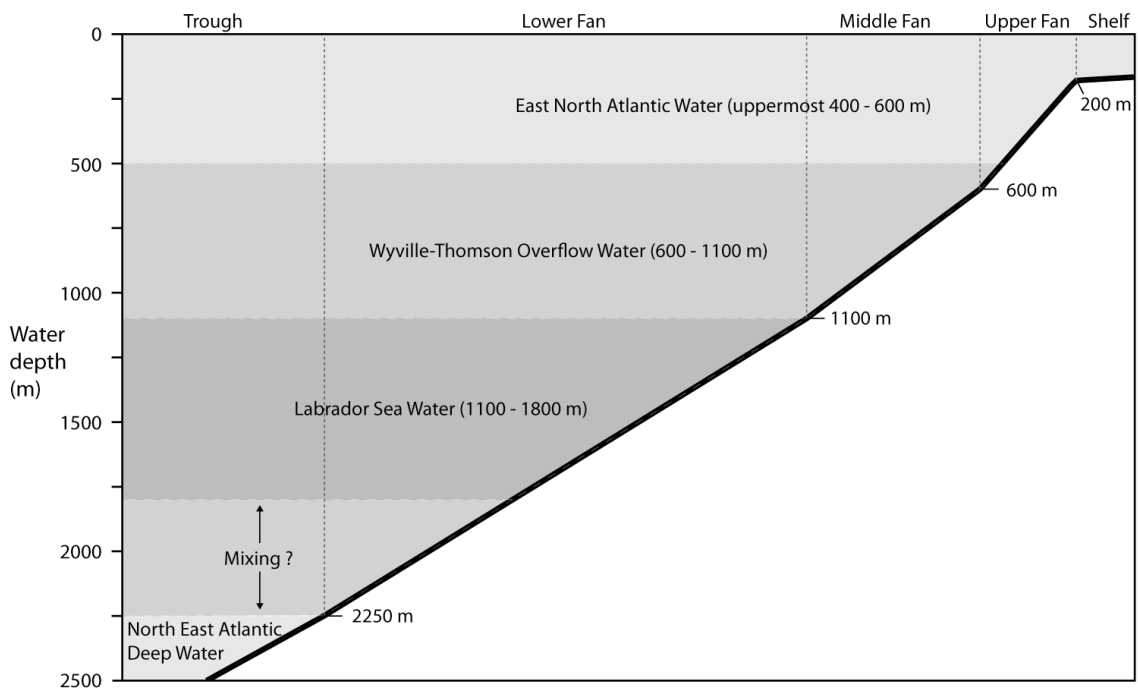
Figure 3.5: Contemporary water masses bathing the Barra Fan, lower, middle and upper fan divisions from Armishaw et al. (2000), water mass divisions from New and Smythe-Wright (2001) and Johnson et al. (2010). A degree of mixing is likely to occur at all boundaries.

Figure 3.4.D shows circulation patterns for deep water masses within the Rockall Trough. The deepest water mass present in the Rockall Trough, though not shown in Figure 3.4, is Antarctic Bottom Water (AABW), which may extend to 56°N (New and Smythe-Wright, 2001; Johnson et al., 2010). The dense Norwegian Sea Deep Water (NSDW) enters the Rockall Trough via the Faeroe conduit (section 3.2.2) and over the Wyville-Thomson Ridge (New and Smythe-Wright, 2001). As a consequence of mixing with surrounding water masses a salinity maximum is formed at 2300 - 2500 m water depth, this is associated with North East Atlantic Deep Water (NEADW) (Øvrebø et al., 2006). As with upper and intermediate water masses, deep water masses in the Rockall Trough display a cyclonic gyre and frequent eddies. High current speeds may be associated with these water masses, Dickson and McCave (1986) record velocities of up to 29 cm s^{-1} at 2500 m water depth in the southern Rockall Trough.

3.3.2.2. Circulation patterns during glacial periods

Driven by temperature and salinity gradients, it has been argued that freshening of the North Atlantic during deglaciations leads to a weakening of thermohaline circulation (Bond et al., 1993). In the North Atlantic, glacials are also associated with a reduction in deep convection and overflows from the Nordic Seas (McManus et al., 2004; Lynch-Stieglitz et al., 2007). Decreased deep ocean ventilation has also been observed at the onset of the Younger Dryas (Thornalley et al., 2010).

However, ocean circulation may not simply have been more sluggish. Work by Negre et al. (2010) using an Atlantic [231]Pa/[230]Th gradient points to reversed deep water flow during the LGM, with a southern sourced water mass flowing northward at a rate half the average of the southern flowing Holocene NADW. This change in flow direction would result in a switching of the contemporary Rockall Trough's anti-clockwise gyre to clockwise; a change that would have profound effects on deep water drift sedimentation.

Analysis of the sortable silt fraction in the Rockall Trough by McCave et al. (1995) indicates vigorous intermediate water circulation during the last glacial, but more sluggish bottom water circulation. Further sedimentological evidence, supports the view of reduced bottom current flow in the Rockall Trough during glacials and stadials. Øvrebø et al. (2006), Knutz et al. (2002) and Armishaw et al. (2000) document a predominance of sandy contourite deposits (indicative of high current flow speeds) during the Holocene and of muddy contourites (indicative of low current flow speeds) during the glacial period.

The consequence of these variations in circulation patterns and vigour, with regards to sedimentation on the Barra Fan, is that there will be distinct differences between glacial and interglacial periods with regards to the permeability and water content of the sediments. The finer grained, clay rich, glacial layers acting as barriers to fluid migration from contourite sediments deposited during inter-stadials (see Section 2.2.2.1).

3.3.3. <u>Sedimentary processes on the Barra Fan</u>

Sedimentation off northwest Britain in general, and on the Barra Fan in particular, is governed by a combination of down-slope and across-slope mechanisms. The down-slope component is driven by the delivery of terrigenous material from the continent to the ocean basin, via glaciogenic and mass movement processes (Howe, 1995; Holmes et al., 1998; Armishaw et al., 2000; Knutz et al., 2001; Knutz et al., 2002). Across-slope sedimentary processes are driven by ocean circulation and often manifest as contourite deposits (Knutz et al., 2002; Øvrebø et al., 2006). The characteristics of these deposits are defined by the flow speed of the water they are deposited in. High current speeds, where fine particles remain in suspension, result in sandy or gravel-lag contourites and lower speeds allow more muddy deposits to form (Faugères and Stow, 1993).

3.3.3.1. Across-slope sedimentation

As stated in section 3.2.3 there is evidence supporting vigorous bottom current activity in the Rockall Trough since the intra-Miocene unconformity, at approximately 15 Ma. These large scale currents resulted in the formation of the Feni Ridge, a large sediment drift in the south of the Rockall Trough (Stoker, 1998; Laberg et al., 2005), as well as smaller drifts on the Barra Fan itself. A number of studies have shown evidence (both geological and geophysical) of widespread contourite sedimentation on the Barra Fan (Howe, 1996; Armishaw et al., 1998; Armishaw, 1999; Armishaw et al., 2000; Knutz et al., 2001; Knutz et al., 2002). For example, the Barra Fan Drift, which consists of sediment waves, the crest-to-crest length of which is ~3 km and the height of which are 15 - 30 m (Howe, 1996; Knutz et al., 2002). Bottom currents on the Barra Fan follow seabed topography and this drift is forming in the lee of an old slope failure lobe, potentially associated with reduced current velocity (Howe, 1996; Knutz et al., 2002). In deeper water, on the fan, sediment waves are aligned parallel to along-slope bottom currents that are interpreted to have formed them (Armishaw et al., 1998).

As the characteristics of contourites are defined by the water masses that deposit them, a change in circulation will lead to a change in lithology. In the case of the Barra Fan, this means that the sediment lithology changes with water depth, reflecting the different water masses that bathe the fan at different depths (see Figures 3.5 and 3.6). This is perhaps illustrated most clearly by the mudline location, representing the boundary between sandy contourites (zone of current erosion) and clay rich sediments (zone of deposition), at 1500 m (Armishaw, 1999). As circulation patterns also change with time, particularly during glacial to interglacial transitions (see section 3.2.1.2), so too will the sedimentation that results from this circulation. Hence, circulation changes may be an additional reason why there is a marked difference between glacial and interglacial sedimentation on the Barra Fan (see Armishaw et al., 2000; Knutz et al., 2002).
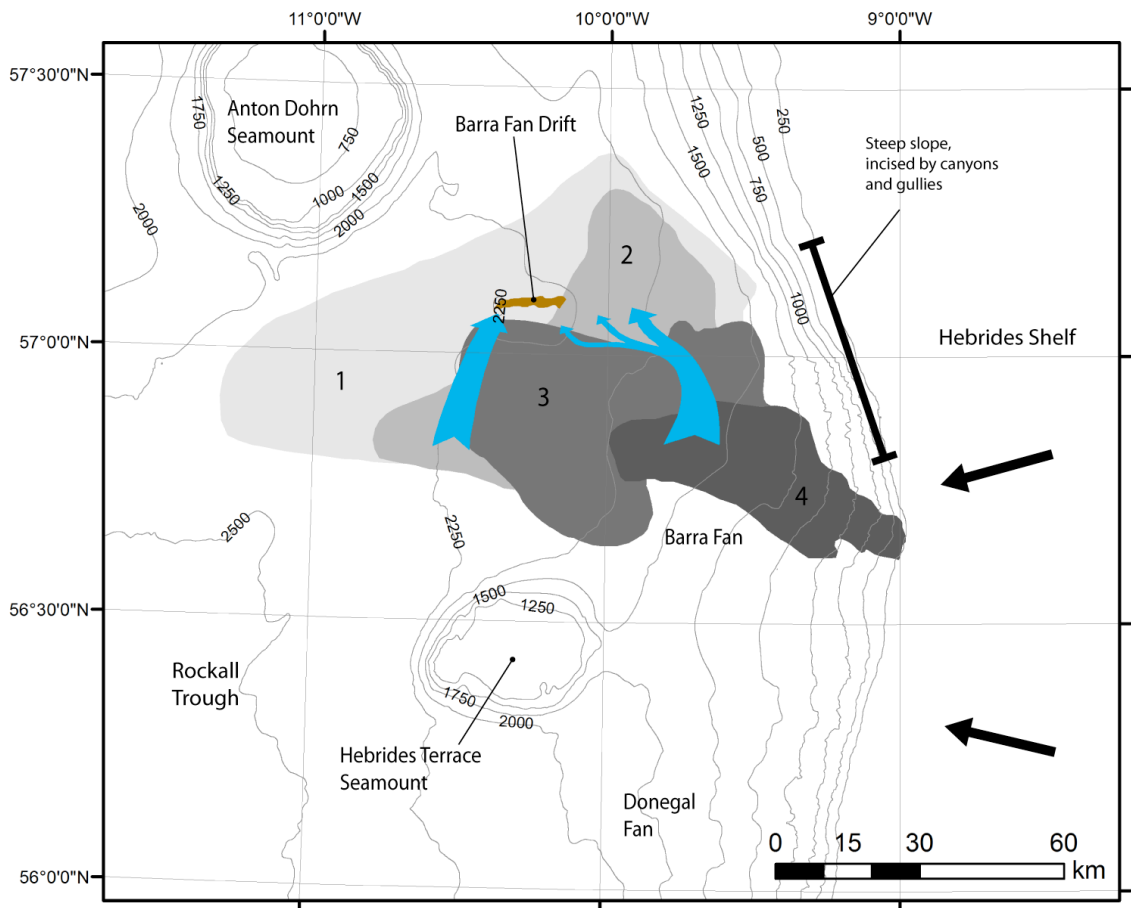
Figure 3.6: Overview of sedimentary processes on the Barra Fan. Shaded grey areas represent Peach Debrites 1 to 4 (from Holmes et al., 1998), blue arrows indicate interpreted bottom current flow paths (from Knutz et al., 2002), black arrows represent approximate locations of palaeo-ice-streams.

3.3.3.2. Down-slope sedimentation

A further reason why there is a difference between glacial and interglacial sedimentation is change in sediment supply: with glacial (and deglacial) periods marked by a large increase in terrigenous sedimentation (Armishaw, 1999; Armishaw et al., 2000; Knutz et al., 2001; Knutz et al., 2002). This terrigenous sediment is transported to the shelf break via ice-streams originating in western Scotland and northern Ireland (Bradwell et al., 2008; Dunlop et al., 2010; Howe et al., 2012). Morainal ridges are visible adjacent to the continental shelf break, providing evidence of glaciogenic sedimentation as the ice retreated (Selby, 1989).

This terrigenous input contributed towards extremely rapid rates of sedimentation, especially during the last deglacial. For this period, Knutz et al. (2001) calculate sedimentation rates of up to 2 m ka^{-1} on the northwestern margin of the fan, whereas Kroon et al. (1997; 2000) record rates of >1 m ka^{-1} towards the centre of the fan. Rapid

deposition on the steep upper slopes of the Barra Fan resulted in unstable sediments that were transported downslope as debris flows or turbidites (see chapter 2 for a discussion of mass movement processes) to the gentler slopes of the middle and lower fan (Armishaw, 1999; Armishaw et al., 2000).

A number of down-slope transport mechanisms are known to operate on the Barra Fan. Sandy turbidites have been identified in numerous core samples from the region (Howe, 1996; Kroon et al., 1997; Knutz et al., 2001; Knutz et al., 2002). However, Armishaw et al. (2000) find no evidence of turbidite deposits: they propose that their relatively short core samples failed to reach sufficient depth to sample such material. Glaciogenic debris lobes are present on the fan, with lobate terminations often coinciding with the gradient change associated with the upper- to mid-slope boundary (Armishaw et al., 1998; Armishaw, 1999). North of the fan, the continental slope is steep and incised with canyons and gullies that are proposed to have acted as conduits for sandy debris flows and turbidites to reach the lower slopes of the fan (Armishaw et al., 1998; Holmes et al., 1998; Armishaw, 1999). The Peach slide, is located in an embayment to the north of the fan (see Figure 3.5; Holmes et al., 1998).

As Figure 3.6 shows, and as originally presented by Holmes et al. (1998), the Peach slide has developed during the Pleistocene and consists of four major debrite units: debrite 1 (823 km^3), debrite 2 (673 km^3), debrite 3 (199 km^3) and debrite 4 (135 km^3). The complex covers an area of ~1600 km^2 and is associated with steep scarp margins and debris blocks, flows and lobes (Armishaw et al., 1998; Armishaw, 1999). Using an age/depth profile of the Barra Fan (constructed by Knutz et al., 2001) Maslin et al. (2004) determined the age of the three most recent debrites: 2, 3 and 4 as 36.5, 21 and 10.5 ka cal BP respectively.

However, it is felt that this age estimate is relatively imprecise and this thesis aims to improve the precision by use of geochemical and sedimentological analysis of samples located in the slide headwall area.

There may not be a clear distinction between hemipelagite deposition and downslope transport. Armishaw et al. (2000) interpret a glaciomarine dumpstone facies, clay-rich material with pebble clasts: they speculate that the unit may result from rapid dumping of sediment (potentially from an overturning ice-berg) and that the deposition may involve a degree of downslope transport. Similarly, Howe (1996) interprets a hemiturbidite unit, which he states shares some of the characteristics of both hemipelagic and turbiditic sediments. As Armishaw et al. (2000) argue, in their proposed model of fan sedimentation, it seems that processes do not operate in isolation but as an interaction. Indeed, a combination of down-slope and across-slope

processes may be involved in the development of sediment waves associated with the Barra Fan Drift (Howe, 1996; Knutz et al., 2002).

3.4. Chapter summary: differences between sedimentation in glacial and interglacial periods

As previously discussed in this chapter, there are marked differences in the Barra Fan's oceanographic and sedimentary regimes during glacial and interglacial intervals. In turn, these differences manifest themselves via changes in sedimentology.

In the contemporary ocean circulation (see Figures 3.4 and 3.5), the upper slopes are exposed to the relatively high velocity SEC and sediments dominated by sandy contourites (Armishaw et al., 2000; Knutz et al., 2002; Øvrebø et al., 2006). Deposition of finer sediment occurs when there is a reduction in current velocity, for instance in the lee of escarpments (Knutz et al., 2002) due to turbulence caused by bathymetry (Øvrebø et al., 2006).

The glacial Rockall Trough was subject to different circulation and much greater terrigenous sediment input. Whereas bottom current circulation may have been reduced in vigour (McManus et al., 2004; Lynch-Stieglitz et al., 2007; Thornalley et al., 2010), or even reversed (Negre et al., 2010), there is evidence of an active intermediate water mass regime (McCave et al., 1995). As such, across-slope sedimentation processes are likely to have been significant, even though the down-slope (both glaciogenic and mass transport) component would have dominated during these intervals (Howe, 1996; Armishaw et al., 2000; Knutz et al., 2001; Knutz et al., 2002). The deglacial period was marked by extremely high sedimentation rates, caused by terrigenous inputs from the disintegrating BIS (Kroon et al., 1997; Kroon et al., 2000; Knutz et al., 2001). Larger scale down-slope transport processes such as via debris flows, slumps and landslides have been inferred to have occurred in this period (Armishaw et al., 1998; Holmes et al., 1998; Armishaw et al., 2000).

Chapter four will now analyse the regional morphology and acoustic facies: with the objective of improving the understanding of sedimentological processes operating in the study area.

4. Surface and shallow-subsurface morphology of the Peach slide region of the Barra Fan

4.1. Introduction to chapter

4.1.1. Objectives

The principal objective of this chapter is to map the surface and shallow-subsurface morphology of the Barra Fan and Peach slide. An improved understanding of this morphology will, in conjunction with the oceanographic and geologic framework presented in chapter three, inform analysis in chapter five and further discussion in chapter six.

This chapter asks a number of questions. First, what seismic units present in the shallow sub-surface of the Barra Fan? Second, can these units be defined in terms of sedimentary process? Third, what evidence of submarine mass movement is present in the region?

This chapter also tackles some of the specific objectives outlined in section 1.3; namely mapping the different acoustic facies associated with submarine mass movements and making full use of GIS software to improve interpretation and analysis of the Barra Fan environment.

4.1.2. Previous geophysical studies

The major published geophysical studies of the Barra Fan are those of Armishaw (1999), Armishaw et al. (1998, indeed this reference is presented as a chapter in Armishaw, 1999) and Holmes et al. (1998). Additional, less extensive, geophysical investigations are undertaken by Howe (1996) and Knutz et al. (2002). Selby (1989) presents an investigation of the Hebrides margin. In addition to these published studies UCL (Wild, 1985) and BP Exploration (Cook, 1989) produced unpublished reports documenting slope failure in the region.

Armishaw (1999) interprets surface morphology and maps seismic echo character using MBE (multibeam bathymetric echosounder), SSS (sidescan sonar) and SBP (sub-bottom profiler) data. Holmes et al. (1998), present a description of the Peach debrite complex using a combination of MBE, SSS and SBP data to locate the mass movement events.

This study focuses on the surface and shallow-subsurface geology and provides more detail than previous work by extracting more information from the available data. This is primarily achieved through the use of computer software developments that have occurred during the intervening decade. Firstly, scanned images of seismic profiles are

converted into SEGY data files (using a methodology similar to that of Miles et al., 2007) and then interpreted using seismic processing software. Secondly, GIS software is used to analyse datasets (such as MBE, SSS and interpreted SBP) both independently and jointly.

In practical terms, this means that where Armishaw (1999) mapped echo character types, this thesis presents a shallow-seismic stratigraphy within which it is possible to consider facies associations, similar to those presented by Jenner et al. (2007) on the Nova Scotian margin. With regards to MBE data, whereas Armishaw (1999) and Holmes et al. (1998) used these data to identify scars and debris lobes, this thesis analyses these data for slope angle, and correlates bathymetric changes directly with the sub-surface interpretation (using a similar methodology to Leat et al., 2010). This process allows more detailed interpretation in this chapter and discussion of sediment transport mechanics in chapter six.

Datum parameters WGS 84	
Spheroid	WGS 84
Semi-Major Axis	6 378 137.000 m
Semi Minor Axis	6 356 752.314 m
Flattening	1/298.257223563
Projection parameters UTM zone 29N	
Projection	Universal Transverse Mercator
Zone	29 North
Latitude of Origin	0°
Longitude of Origin / Central Meridian	9° West
Scale Factor on Central Meridian	0.9996
False Easting	500 000
False Northing	0
Unit	International Metres

Table 4.1: WGS 84 datum parameters and UTM Zone 29N projection parameters.

4.1.3. Geophysical data from the Peach region of the Barra Fan

A number of geophysical surveys have been performed on the Barra Fan, notably BGS regional surveys, AFEN (Atlantic Frontiers Environmental Network) tranches 19-22 and the LOIS SES (Land-Ocean Interaction Study Shelf Edge Study) survey.

These surveys have provided an archive of sub-bottom profiler, sidescan sonar and multibeam bathymetric data that are used in this thesis.

4.2. Methods

4.2.1. GIS construction and geodetic system

GIS analysis for this thesis was performed using ESRI ArcGIS 10.1.

All horizontal data are referenced to the WGS '84 datum and grid coordinates are referenced to UTM Zone 29N. This zone is suitable for use between 6º W and 12º W. Table 4.1 outlines the projection parameters of UTM Zone 29N, this projection uses metres as the horizontal unit (as opposed to degrees of latitude or longitude). Using metres for x, y and z dimensions makes a number of analytical tasks, such as measuring distance, area and volume; and calculating gradients much more straightforward.

4.2.2. Multibeam bathymetry

The primary bathymetric data source used by this thesis is the LOIS SES 3" bathymetric grid (BODC, 1999).

The original dataset is a grid of tide corrected bathymetric depths spaced at 3" longitude by 3" latitude between 56° N and 57° N; and 9° 25' W and 8° 55' W. The data were collected between 02/03/1995 and 22/03/1995, poor weather conditions resulted in a number of gaps in the data (BODC, 1999).

BODC ASCII data were converted into ESRI ASCII format and converted to raster data within ArcGIS. LOIS SES 3" geographical grid corresponds to a grid resolution of 92 m north to south and 51 m east to west between 56° N and 57° N in UTM grid coordinates.

Detailed analysis of bathymetry (including gradients) is based solely on the LOIS SES dataset. In order to aid regional interpretation (as well as to provide a seabed reference for sub-surface interpretation), gaps in LOIS SES data have been infilled with the SRTM30 bathymetric data (see Becker et al., 2009). The method employed to infill these gaps is outlined in section 4.2.2.1.

SRTM30 bathymetry is based on gravimetric data that are calibrated using vessel soundings (Becker et al., 2009) and appears to be higher quality than the GEBCO 08 grid in the Barra Fan locality. The SRTM30 grid has a 30" spacing, corresponding to a grid resolution of 920 m north to south and 510 m east to west in the Barra Fan study area. The data are lower resolution and less reliable than the LOIS SES bathymetry and as such are used to provide regional context, not for interpretation.

4.2.2.1. Combining bathymetric datasets
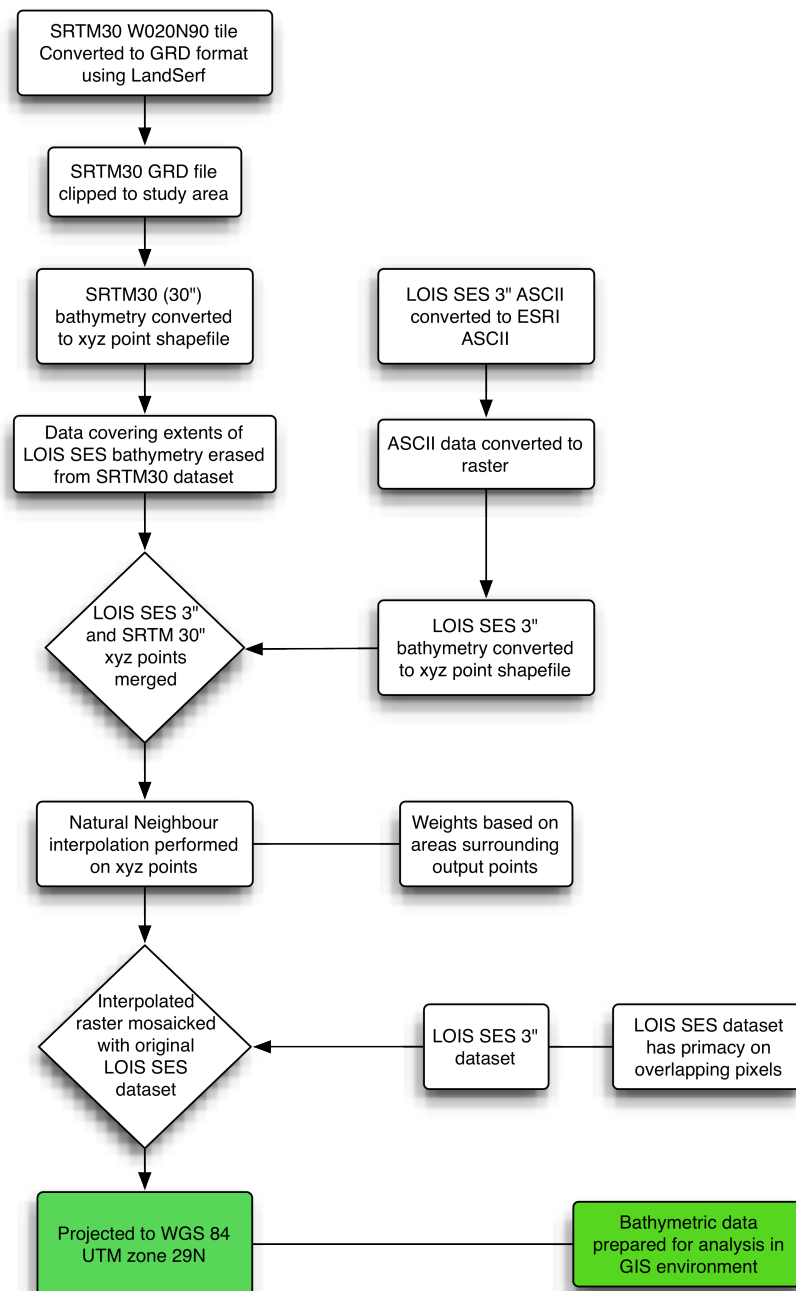
Figure 4.1: Bathymetry conversion workflow.

Figure 4.1 outlines the methodology used to combine the SRTM30 and LOIS SES bathymetry datasets. LOIS and SRTM30 datasets were converted to xyz points and merged, with the LOIS SES data extents erased from the SRTM30 dataset. Natural neighbour interpolation was used to grid the data to 15" resolution. The natural neighbour interpolation technique calculates output raster weights based on areas and has been demonstrated to be effective with bathymetric data (see Merwade et al., 2006; Coleman et al., 2011).

Once regridded the 15" bathymetry was mosaicked with the original LOIS SES 3" dataset, the higher resolution data having primacy on overlapping pixels. This method interpolates the SRTM30 data values to the more reliable LOIS SES multibeam bathymetry values at the boundary of the two datasets. The resultant bathymetry is more reliable than the SRTM30 data and has less severe discrepancies between datasets.

4.2.3. Sidescan sonar

TOBI sidescan sonar data were acquired from the AFEN CD-ROM (see AFEN, 1998). AFEN tranches 19-22 are in the location of the Barra Fan. The TOBI survey was performed on the R.V. Colonel Templer between 12/06/1998 and 14/06/1998 (AFEN, 1998; Masson and Jacobs, 1998). PDF format charted data, gridded at 6 m, were converted to TIFF files and then Geo-referenced in ArcGIS using the charted positional annotation as reference points.
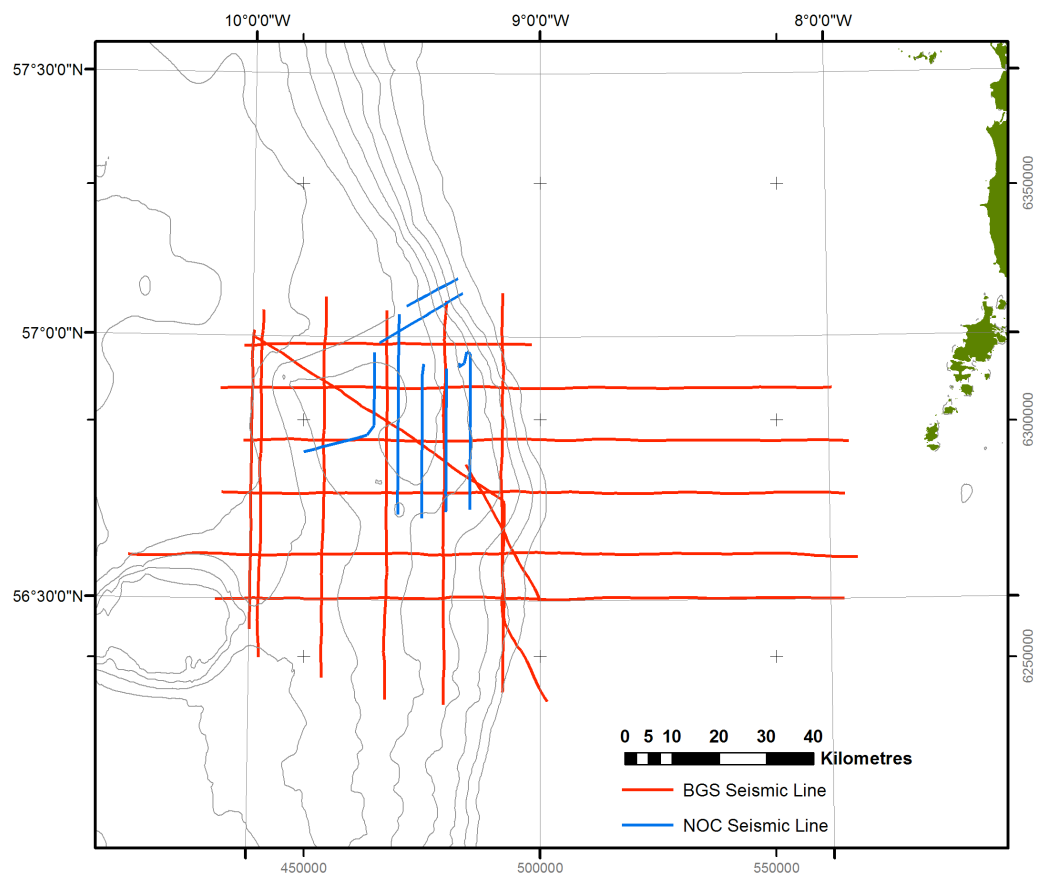
Figure 4.2: Overview of BGS and NOC seismic data analysed in this thesis. Contours are every 250 m from SRTM30 data.

4.2.4. Sub-bottom profiles

This thesis analyses high frequency pinger data, not sparker or airgun. This is because of the focus on processes within the upper sedimentary column. Analysis of deeper records would add to the study and is recommended for future work (see chapter seven).

4.2.4.1. Data analysed

Line name	Latitude Start (D.D)	Longitude Start (D.D)	Latitude End (D.D)	Longitude End (D.D)	Record Type	Length (km)
BGS_1985_6_1	57.0494	-9.9629	56.3884	-9.9647	3.5 kHz Pinger	73.67
BGS_1985_6_12	57.0751	-9.7452	56.3516	-9.7484	3.5 kHz Pinger	80.60
BGS_1985_6_13	56.3107	-9.5310	57.0497	-9.5333	3.5 kHz Pinger	82.31
BGS_1985_6_14	56.8997	-10.1093	56.9019	-7.9874	3.5 kHz Pinger	129.30
BGS_1985_6_15	56.799	-7.9307	56.8006	-10.0261	3.5 kHz Pinger	128.05
BGS_1985_6_16	56.7016	-10.0999	56.7000	-7.9455	3.5 kHz Pinger	132.02
BGS_1985_6_17	56.5792	-7.9047	56.5813	-10.4180	3.5 kHz Pinger	154.53
BGS_1985_6_18	56.4992	-10.1167	56.5000	-7.9532	3.5 kHz Pinger	133.27
BGS_1985_6_22	57.0686	-9.3250	56.3016	-9.3311	3.5 kHz Pinger	85.45
BGS_1985_6_23	56.3251	-9.1282	57.0838	-9.1303	3.5 kHz Pinger	84.53
BGS_1985_6_27	56.308	-8.9748	56.9973	-9.9920	3.5 kHz Pinger	107.90
BGS_1985_6_28	57.0109	-9.9947	56.4416	-9.9982	3.5 kHz Pinger	63.42
BGS_1985_6_2	56.98079	-10.02902	56.9858	-9.0274	3.5 kHz Pinger	60.91
BGS_1985_7_1	56.4992	-8.9988	56.7580	-9.2568	Deep Towed Boomer	32.92
Length of BGS records:						**1348.9**
NOC_AFEN_49	56.9509	-9.2792	56.6723	-9.2413	3.5 kHz Pinger	38.64
NOC_AFEN_50	56.6679	-9.3249	56.9398	-9.3249	3.5 kHz Pinger	30.27
NOC_AFEN_51	56.9488	-9.4037	56.6558	-9.4077	3.5 kHz Pinger	32.63
NOC_AFEN_52	56.6623	-9.4907	57.0432	-9.4907	3.5 kHz Pinger	42.40
NOC_AFEN_53	57.0582	-9.4646	57.1116	-9.2860	3.5 kHz Pinger	12.35
NOC_AFEN_54	57.0836	-9.2692	56.9883	-9.5583	3.5 kHz Pinger	20.50
NOC_AFEN_55	56.9700	-9.5747	56.7800	-9.8181	3.5 kHz Pinger	31.81
Length of NOC records:						**208.6**
Total Length of records analysed:						**1557.5**

Table 4.2: Overview of acoustic data analysed in this thesis.

As Figure 4.2 shows, the BGS regional survey lines are generally spaced at 10 km intervals. This thesis analyses six east to west lines and five north to south orientated lines. BGS 1985 6 27 and BGS 1985 7 1 are run southeast to northwest. The NOC AFEN survey lines tend to bisect the space between the BGS survey lines, giving a greater density of survey lines in the Peach region of the Barra Fan.

As Table 4.2 shows, the sub-bottom data interpreted is high frequency. As such they are suitable for relatively high resolution (potentially < 1 m), shallow (upper 50 m of sedimentary column) investigations into the sedimentary facies of the Barra Fan.

Deep towed Boomer line BGS 1985 7-1 provides high quality data, but is not analysed (though it was cross-referenced to aid interpretation). This is for two reasons: first, the towed nature of the data provided difficulty in ascertaining the correct position; second, the track is very similar to pinger line BGS 1985 6-27.

4.2.4.2. Conversion of paper seismic records into digital seismic files

Seismic records   **Navigation data**

```
┌─────────────────────┐    ┌──────────────────┐    ┌──────────────────┐
│ BGS and NOC paper   │    │ BGS navigation   │    │ NOC              │
│ seismic records     │    │ supplied per 10  │    │ navigational     │
│ obtained and drum-  │    │ minute fix in    │    │ fixes not        │
│ scanned to TIFF     │    │ XLS format.      │    │ available.       │
│ format              │    └──────────────────┘    └──────────────────┘
└─────────────────────┘             │                       │
          │                         ▼                       ▼
          │               ┌──────────────────┐    ┌──────────────────┐
          ▼               │ BGS navigational │    │ Extract          │
┌─────────────────────┐   │ fixes assigned   │    │ navigation data  │
│ TIFF files cropped  │   │ an arbitrary     │    │ from recorded    │
│ to portions of      │   │ timestamp.       │    │ vessel track     │
│ equal print delay   │   │                  │    │ chart (PDF), as  │
│ and sweep, with     │   │ Increasing 10    │    │ supplied by NOC. │
│ navigational fixes  │   │ minutes          │    │                  │
│ at start and end of │   │ incrementally in │    │ Positions        │
│ cropped section.    │   │ a rightwards     │    │ extracted at 15  │
└─────────────────────┘   │ direction as     │    │ minute intervals │
          │               │ ImageToSEGY      │    │ marked on chart. │
          │               │ requires time to │    └──────────────────┘
          │               │ increase left to │
          │               │ right.           │
          │               └──────────────────┘
          │                         │                       │
          │                         ▼                       ▼
          │               ┌──────────────────────────────────┐
          ▼               │ Navigation applied to marked     │
┌─────────────────────┐◄──│ fixes.                           │
│ ImageToSEGY used to │   │                                  │
│ convert TIFF files  │   │ Delay and sweep specified.       │
│ to SEGY files       │   └──────────────────────────────────┘
└─────────────────────┘
          │
          ▼
┌─────────────────────┐
│ SEGY files          │
│ converted to COD    │
│ format using Coda   │
│ File Utilities      │
└─────────────────────┘
          │
          ▼
┌─────────────────────┐
│ COD file imported   │
│ to Seismic+ for     │
│ interpretation      │
└─────────────────────┘
```

Figure 4.3: Flowchart demonstrating the process used to convert paper seismic records into digital seismic data files.

Figure 4.3 outlines the process by which BGS and NOC paper seismic records were converted into seismic data files using Chesapeake Technology's ImageToSEGY™ application. This conversion allows the seismic data to be interpreted digitally and analysed alongside other digital data (bathymetry and sidescan sonar) in a GIS environment. Export of interpretation, to xyz data, is also much less time consuming and more precise than manual interpretation of paper records. However, accuracy is only as good as the seismic records and navigation data used to create the seismic data files.

ImageToSEGY performs the conversion based on start and end navigation (to the left and right of the TIFF file) and top and bottom time (to the top and bottom of the TIFF

file) of the scanned image and then interpolating these specified data to the intervening pixels. Illustrating this, a screen grab from ImageToSEGY is shown in Figure 4.4.

There are two potentially significant sources of error in the conversion process. First, the navigation data is itself subject to error. Second, interpolating between fixes assumes a straight line course, constant vessel speed over ground and ping rate.

This thesis now considers potential navigation error from interpolation and then performs position checks on prominent bathymetric features.
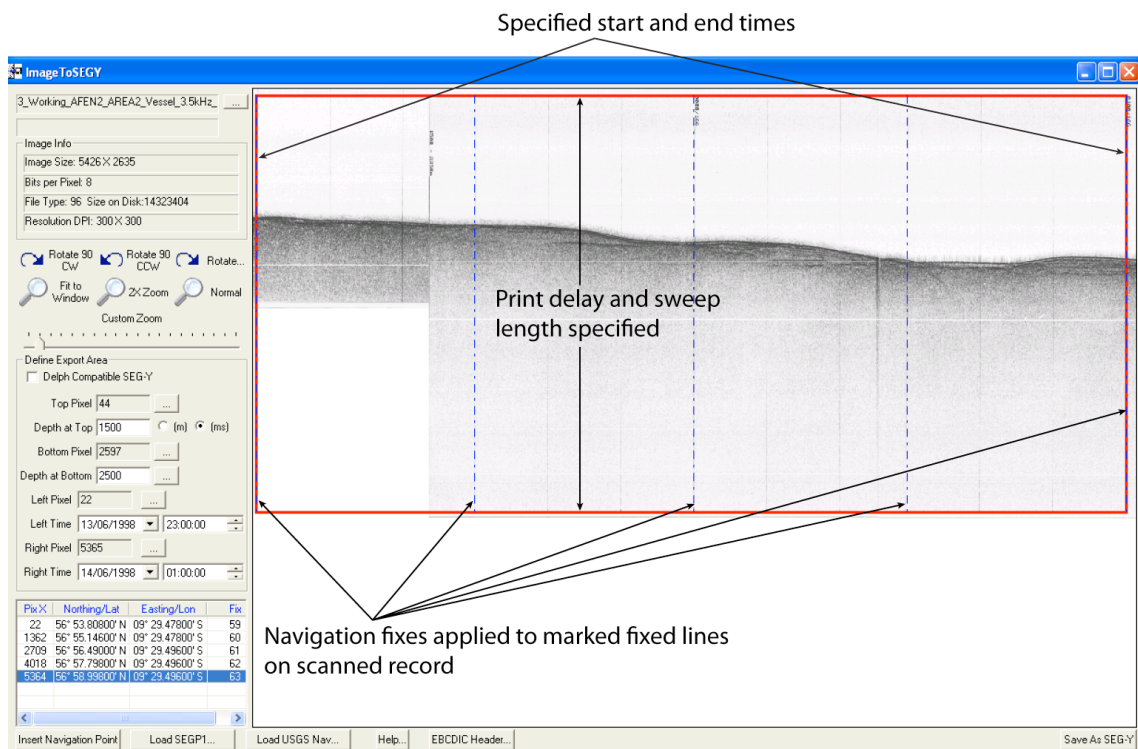
Figure 4.4: Annotated screen grab from the ImageToSEGY application. Data example shown is NOC AFEN 3.5 kHz pinger.

4.2.4.3. Navigation sources for sub-bottom profile data

BGS data, acquired in 1985 on the RRS Charles Darwin, was part of the initial phase of GPS roll-out and would have used a Trimble 4000 receiver, there could have been periods of an hour or more with no satellite coverage (Pers Comm Knight, 2012).

Navigational fixes, expressed in geographical coordinates, at 10 minute intervals were obtained from BGS in XLS format.

NOC AFEN data was acquired in 1998 on the RV Colonel Templer, using a Racal Skyfix DGPS logging at 30 s intervals (Masson and Jacobs, 1998). Such a system is

accurate to the order of 1 m. Unfortunately this navigation data was not available for the conversion of scanned paper records to digital seismic files.

In order to provide navigation, positions were extracted from a PDF chart of the vessel's track, supplied by NOC. Thirty minute intervals were marked on the chart and positions extracted for these locations using the ruler tool in Adobe Acrobat. Distances measured in mm to two decimal places on the pdf and converted to decimal degrees (507.661 mm per degree latitude and 278.299 mm per degree longitude). Measuring to two decimal places provides a conversion precision of 0.129", or approximately 4 m. The actual accuracy will be less than this, however, the major error associated with this navigation will due to interpolation between fixes.

Once prepared navigation fixes were inserted onto the equivalent marked fixes visible on TIFF scans in ImageToSEGY (see Figure 4.4).

4.2.4.4. Potential error due to interpolation

When interpolating navigation between fixes, ImageToSEGY calculates the heading and distance between fixes, divides the distance by the intervening number of pixels and adds the resultant value incrementally per pixel until the next navigation fix is reached. This method assumes a constant heading, ping rate and speed over ground (SOG). These assumptions are not always correct and there is a potential error associated with increased distance from a fix (as Figure 4.5 demonstrates).

As the sole navigation used in the conversion process are the fix locations, heading is assumed to be constant between these points. However, as Figure 4.5 illustrates, in all probability, this will not be the case with slight changes in heading occurring as the vessel is steered to remain on course. These changes in heading will also lead to an across track positional error, as the vessel veers off the designed survey line. No information is available to take this into account. However, as the data were collected during summer in an area that is not subject to strong tidal currents it is assumed that the across track error is minimal.

Firing rates for BGS pinger data analysed were between 0.5 s in shallow water and 2 s in deep water. However, firing rates are altered to avoid the pinger pulse inferring with data (i.e. producing a thick band of noise at 0.5 s, 1.0 s, 1.5 s TWTT and so on). In practical terms this means that a change in bathymetry in the order of 350 m will require a change in firing rate of approximately 0.1 s in order to move the interference away from the sweep. When this happens it alters the number of pings between fixes, more for increased firing rates and less for reduced firing rates: leading to error in

horizontal interpolation. This thesis does not attempt to correct for changes in firing rate for the following reasons.

i. BGS navigation fixes are every 10 minutes, and will correct for any firing rate induced error after a relatively short distance.

ii. There is no information on NOC firing rate changes, so it would be impossible to correct this data.

iii. Changes are on steep ground where signal penetration and, therefore, interpretation will be minimal.

iv. To do so would be extremely time consuming.
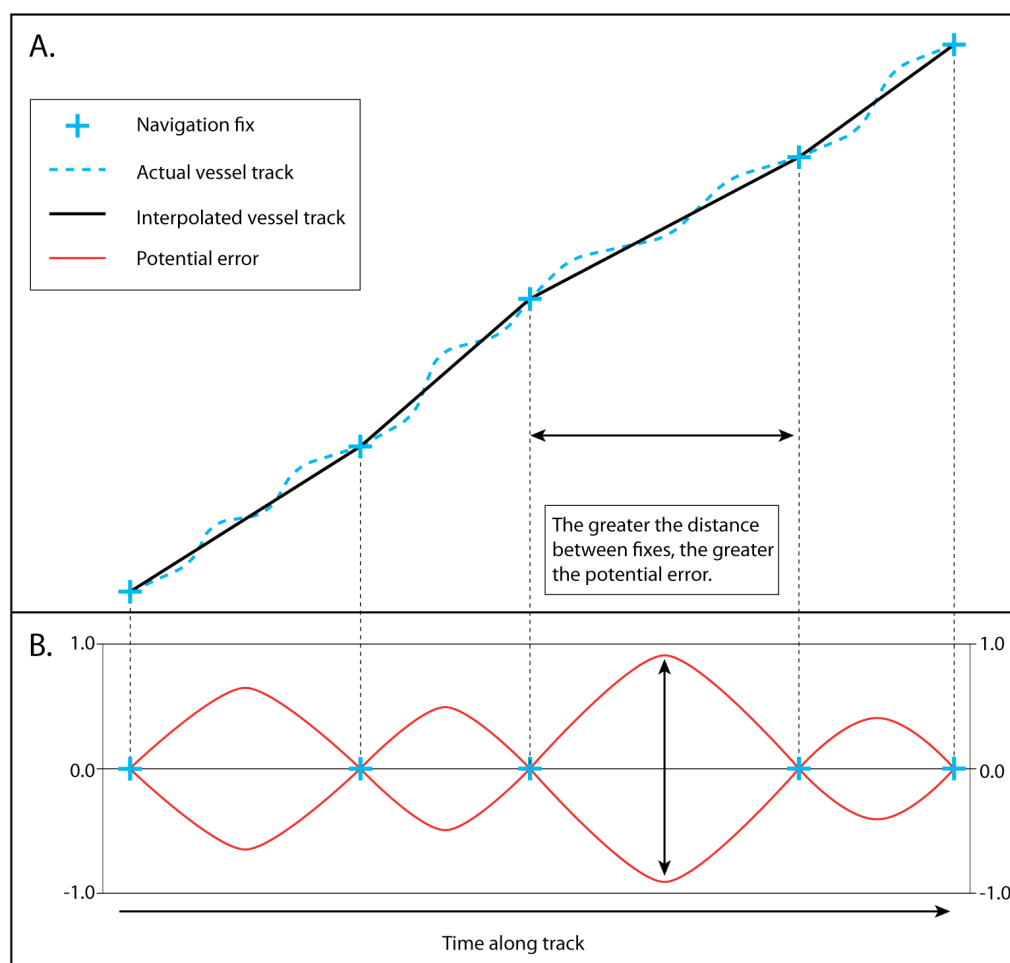
Figure 4.5: Potential error associated with navigation interpolation. A. Plan view of vessel track, with fixes and interpolated track. B. Potential positional error associated with interpolation between fixes (see Table 4.5 for calculated potential error based on acoustic data analysed in this thesis).

In order to estimate the potential error associated with interpolated navigation, this thesis examines distance and time between fixes and calculates variation in vessel SOG during a survey line. These calculations are presented in Appendix B.

Analysis of distance between fixes for BGS and NOC data reveals that BGS data has a mean distance of 1520.5 m between fixes. Therefore, it follows that over the course of the survey lines, the mean furthest distance of ping to fix (i.e. the interpolation mid-point) is 760.3 m. For NOC data the values are 2331.9 m and 1165.9 m respectively (see Table B.1).

Using distance and time between fixes (600 s for BGS data and 1800 s for NOC data) it is possible to calculate vessel SOG (shown in Table B.2). Minimum, mean and maximum SOG are calculated based on the shortest, mean and longest distance between fixes on the survey lines. This calculation shows that BGS survey lines were generally run at a faster speed (2.05 - 2.92 m s^{-1}) than the NOC survey lines (0.99 - 1.54 m s^{-1}). A difference that is explained by considering that the NOC AFEN lines were run whilst towing a TOBI system over steep terrain.

An attempt is made to provide an estimate of the potential for along track positional error due to navigation interpolation. Table B.3 presents calculations of potential errors (expressed in distance) resulting from the difference between maximum and minimum SOG during a survey line (which varies between 0.85 m s^{-1} and 0.10 m s^{-1}, shown in Table B.2) at the mid-point between navigation fixes.

It is unlikely that the full range of SOG would occur between neighbouring fixes, as such the value used as the best estimate of potential error is that calculated by subtracting the potential error resulting from minimum SOG from that resulting from maximum SOG and dividing the result by two (see column six, Table B.3). Mean values are 130.61 m for BGS data and 250.88 m for NOC data. There is significant variation, with the potential error for BGS data ranging between 66.54 m and 366.22 m; and NOC data between 34.17 m and 531.53 m.

These values represent the potential for error: the greater the distance between fixes, with the greater variation in SOG, the greater the potential for error.

However, it may be more useful to estimate error by cross referencing the different geophysical data types and measuring the positional difference of prominent features.

4.2.4.5. Positional error assessment from geophysical data

Figures 4.6 and 4.7 show comparisons between LOIS SES multibeam bathymetry, AFEN sidescan sonar and BGS and NOC sub-bottom profile data. A summary of the results is shown in Table 4.3.

	Data Type	Easting	Northing	Positional differences - data type	Difference (m)
Positional check based on ridge crest at 1180 m below mean sea level.	NOC AFEN 49 3.5 kHz Pinger	485284.8	6306520.4	Pinger - Bathymetry	**23.7**
	LOIS SES bathymetry	485285.2	6306544.1	Pinger - Sidescan Sonar	**50.0**
See Figure 4.6.	AFEN SSS	485278.0	6306570.4	Bathymetry - Sidescan Sonar	**26.3**
Comment:	A broad crest of ~90 m length visible in pinger data. Timestamp for pinger position is 18:15:33.				
Positional check based on slide scarp at 635 m below mean sea level.	BGS 1985 6 27 3.5 kHz Pinger	492306.9	6274107.5	Pinger - Bathymetry	**39.9**
	LOIS SES bathymetry	492304.9	6274067.6		
See Figure 4.7	AFEN SSS	Beyond extents of data			
Comment:	Slope break occurs over ~50 m in pinger data. Timestamp for pinger position is 09:30:27.				

Table 4.3: Positional check summary. Positions are WGS 84 UTM zone 29N.

Figure 4.6 shows excellent agreement between all three data types, with differences not exceeding 50 m despite the bathymetric depth of 1180 m. On bathymetric data, the crest of the ridge is located within 25 m of the pinger position (i.e. well within the 3" resolution of the bathymetric data). It is difficult to make a precise comparison with the AFEN sidescan sonar, as the data is noisy and the crest of the ridge is not so pronounced, however, the feature aligns to resolution of the data. It is particularly encouraging to note that the pinger timestamp for this point is 18:15:33, the point furthest from navigation fixes and potentially subject to the greatest interpolation error.
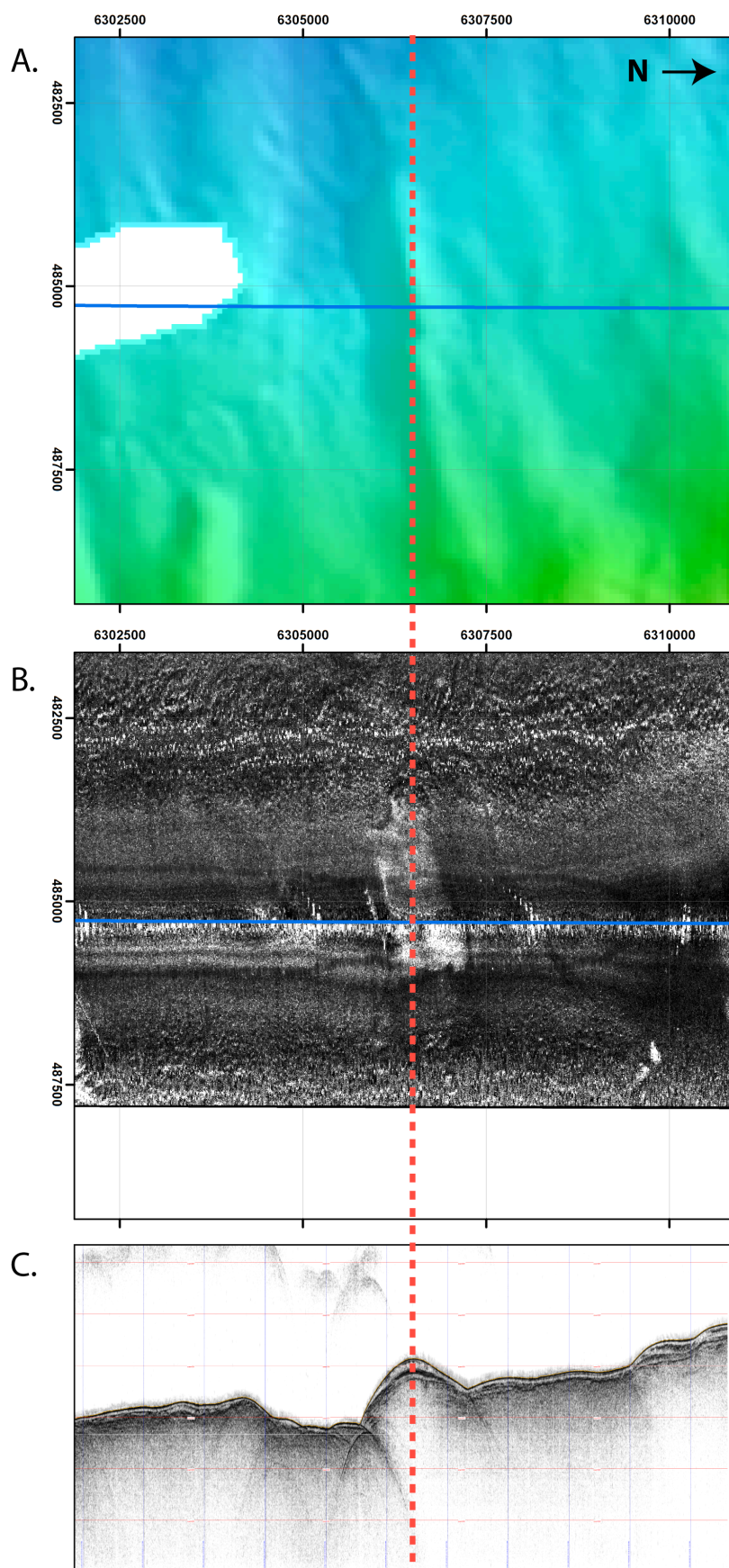
Figure 4.6: Positional accuracy check for bathymetry (A), sidescan sonar (B) and NOC AFEN vessel pinger data (C). Blue line indicates location of line NOC AFEN 49. Dashed red line indicating alignment of spur between the three data types.
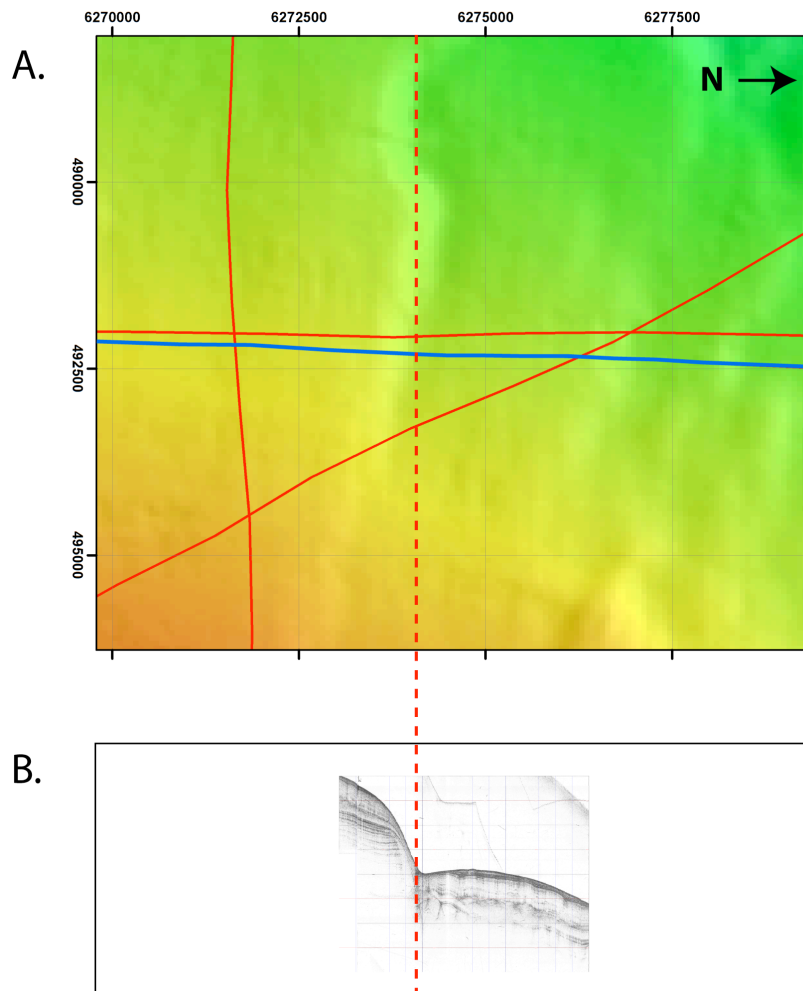
Figure 4.7: Positional accuracy check for bathymetry (A) and BGS pinger data (B). Blue line indicates location of line BGS 1985 6 27, solid red lines other BGS survey lines. Dashed red line indicating alignment of base of scarp between the two data types. Note - AFEN sidescan data does not cover this area.

Figure 4.7 presents a comparison of LOIS SES bathymetry and BGS pinger line 1985 6 27 at the location of the southern margin of the Peach slide scarp. Measured from the slope break, the distance between pinger and bathymetry positions is 39.9 m. This distance is less than the resolution of the LOIS SES. This pinger position is located 27 s from a navigation fix and, therefore, provides a reasonable assessment of the maximum accuracy of the data.

4.2.4.6. Lateral and vertical data resolution

Generally, the lateral resolution of sub-bottom acoustic data is determined by the firing rate and Fresnel zone. Acoustic data analysed in this thesis have firing rates of between 2 and 0.5 pings per second, as section 4.2.4.4 shows: SOG varied between 1

and 3 m s^{-1}. Based on these values, ping rates varied between one ping per 6 m and one ping per 0.5 m travelled over ground.

The Fresnel zone may be defined as the area of constructive reflection accumulation surrounding the ray theory reflection point (Lindsey, 1989). That is to say the area from which waves are reflected back to the acoustic signal receiver. Based on the equations presented by Sheriff (1980), the Fresnel zone diameter from a 3.5 kHz pinger at the seabed (assuming 1500 m s^{-1} acoustic velocity through water) would be 29.3 m and 41.4 m at 1000 m and 2000 m water depth respectively. This means that for acoustic data analysed in this thesis, lateral resolution is limited by the Fresnel zone. The Fresnel zone increases with depth and velocity, as such it is more of a concern for reflectors deeper in the sedimentary column (Widess, 1982; Lindsey, 1989).

Vertical data resolution may be considered in two ways: the resolution of the raw data and the resolution of the scanned paper record.

BGS and NOC pinger data analysed in this thesis were both acquired using a 3.5 kHz system. Using the Rayleigh criterion, theoretical resolution of acoustic data is $\lambda/4$ (where λ = wavelength) (O'Brien and Lerche, 1988). Using an assumed acoustic velocity of 1650 m s^{-1} (as employed by Holmes et al., 1998) it is possible to calculate the sediment thickness that equates to $\lambda/4$ as follows:

$$\lambda = \frac{\text{Sediment acoustic velocity (m s}^{-1})}{\text{Acoustic wave frequency (Hz)}}$$

$$\lambda = \frac{1650}{3500}$$

$$\lambda = 0.47\,\text{m}$$

$$\lambda/4 = 0.118\ \text{m}$$

Equation 4.1: Wavelength and theoretical resolution of pinger data.

Practical data resolution is dependent on the signal to noise ratio, the form and duration of the incident wavelet and the reflector distribution (Widess, 1973; 1982). When reflectors are located in close proximity (in relation to the acoustic wavelength) higher acoustic impedance contrasts cause reverberation in the sub-bottom record, which reduces the vertical resolution. Dense, coarser sediments will have this effect: reducing the resolution to 0.5 m or more. However, finer, softer sediments such as silts will have very little reverberation and display a greater resolution, closer to the 0.12 m theoretical limit.

It is possible to calculate the resolution of the scanned paper records by comparing their sweep length (Two Way Travel Time (TWTT)) with the number of vertical pixels.

Record source	Width of paper record (cm)	Sweep length (ms)	Number of pixels in sweep	TWTT per pixel (ms)	Thickness of sediment per pixel (m), assuming acoustic velocity of 1525 m s^{-1}
BGS	48.8	250 - 500	5800	0.04 - 0.09	0.05 - 0.12
NOC AFEN	21.6	1000	2550	0.39	0.51

Table 4.4: Data resolution of scanned pinger records.

As Table 4.4 demonstrates, owing to the shorter sweep lengths and greater number of pixels, BGS pinger scanned records have a greater resolution than the NOC records. This is not due to lower quality acquisition, in fact NOC AFEN data recorded 4980 samples per second (Masson and Jacobs, 1998), but due to the conversion from paper record. Whereas NOC records have 3 pixels per m, BGS has up to 20 pixels per m. In practical terms this means that it proves very difficult to interpret NOC pinger data at less than 1 m resolution, whereas when the acoustic properties of the sediments allow, it is possible to interpret BGS data at sub 0.5 m resolution.

As well as interpolating horizontally, ImageToSEGY also interpolates vertically: assigning each pixel a TWTT value. It is possible to introduce error at this stage by inaccurate cropping (commonly a result of slight warping of the paper record during the scanning process). However, the interpolation is accurate: measured distance between paper record scale lines (digitised during the conversion process) show errors of <0.5% as compared to the digital scale lines within Seismic+™ (i.e. 50 ms scale lines from paper records measured at 49.8 ms in Seismic+).

4.3. Surface geology data analysis and results

4.3.1. LOIS SES and SRTM30 bathymetry

4.3.1.1. Bathymetric overview

As Figure 4.8 shows, in the study area the Hebrides Shelf margin is located between 9°
and 9° 30' W. To the east the Hebrides Shelf displays depths of less than 200 m, with
the Stanton and Malin Deeps the areas of greatest depth. Between these areas, the
Stanton Banks reach to within 50 m below mean sea level.
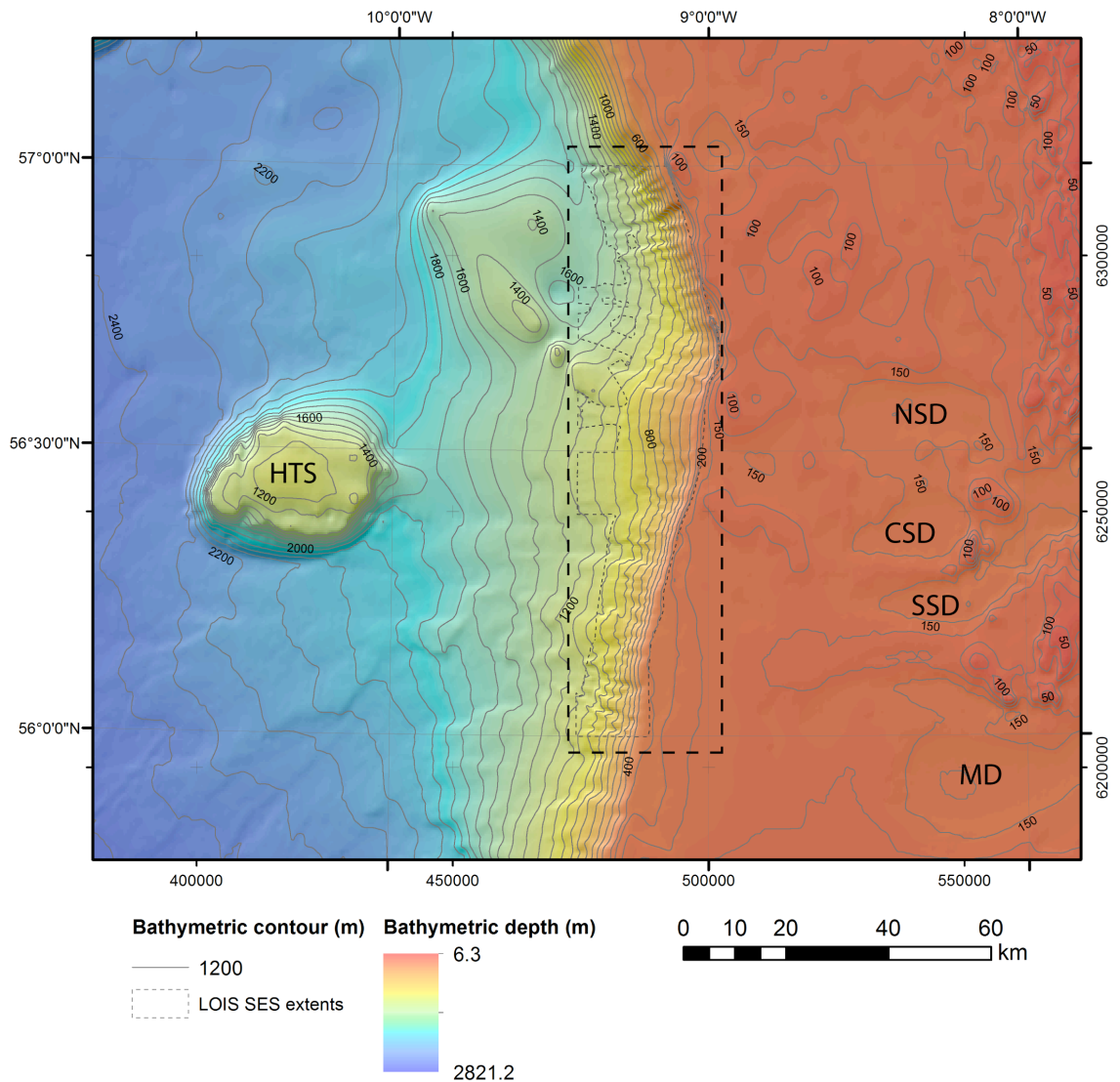
*Figure 4.8: Bathymetry overview of Barra Fan and neighbouring regions. Dashed box shows
extents of Figure 4.11. HTS: Hebrides Terrace Seamount, NSD: North Stanton Deep, CSD:
Central Stanton Deep, SSD: South Stanton Deep, MD: Malin Deep. Bathymetric contours at 25
m intervals for the shallowest 200m and at 100 m intervals below.*
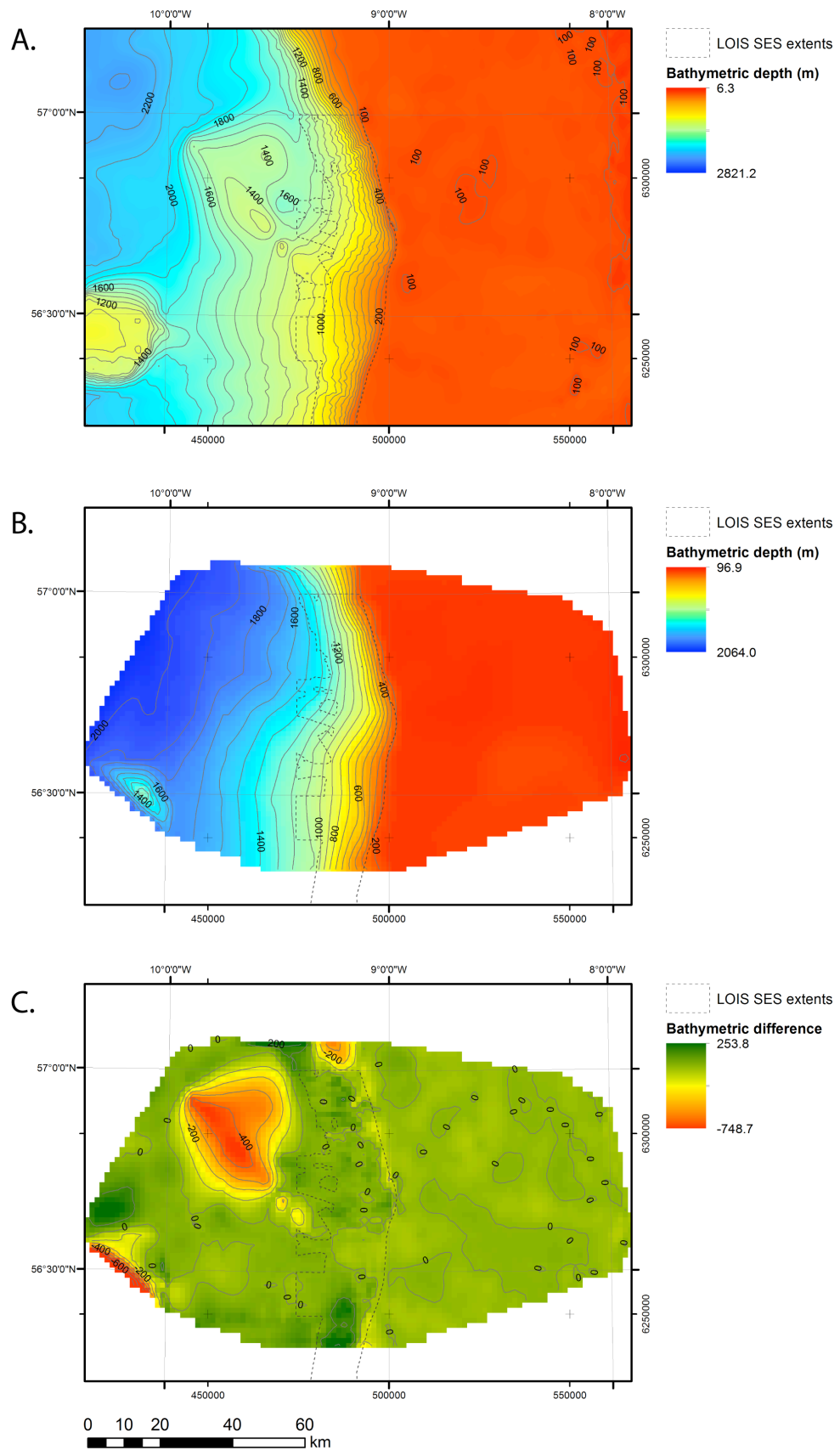
Figure 4.9: Artefact in SRTM30 data. A. Combined SRTM30 and LOIS SES bathymetry. B. Interpolated bathymetry from BGS seismic fixes. C. Difference between SRTM30 and LOIS dataset and BGS seismic fix dataset. Note - extreme values at the perimeter of panel C are due to interpolation over steep slopes on the Hebrides Terrace Seamount and continental margin.

To the west of the continental margin is the Rockall Trough, which achieves depths of 2000 m below sea level within 50 km of the Hebrides Shelf. Depths of > 4000 m are achieved further south in the Rockall Trough, as documented in chapter three. Situated around 56º 30' N 10º 15' W, the Hebrides Terrace seamount is a major bathymetric high located 50 km from the shelf break. As Figure 4.8 shows, this feature rises from 1700 m to 1010 m below mean sea level on the eastern flank and from 2000 m on the western flank. This feature is a large igneous intrusion (see chapter three and Stoker et al., 1993), with a diameter of some 20 km at its summit.

Widely spaced contours between the Hebrides Terrace Seamount and the continental margin indicate the central location of the sedimentary fan, which engulfs the seamount, with the Barra Fan to the north and the Donegal Fan to the south (see chapter three).

An embayment is apparent at the northern limits of the Barra Fan, with a negative relief of some 400 m relative to mounded sedimentary fan build-up to the west. This mounded build-up, that is present in both SRTM30 and GEBCO '08 datasets, is an artefact. Figure 4.9 shows an interpolated bathymetry (panel B), based on single beam echosounder values at BGS seismic fix locations, that is subtracted from the combined LOIS SES and SRTM30 data (panel A). The resultant values are shown in panel C.

The interpolated bathymetry shown in panel B is based on tide corrected depth values at each navigational fix from the BGS 1985 data (see Table 4.2). As such, the input points are fairly widely spaced, with survey lines run at 10 km spacing, although there are numerous crossings and a diagonal line running across the apparent high (see Figure 4.2). The data were interpolated using Natural Neighbour and gridded to 60" resolution.

Overall there is good agreement between the interpolated BGS fix bathymetry and the combined LOIS SES and SRTM30 data. Due to a scarcity of data points, the interpolated BGS fix bathymetry is less reliable at its margins. As such, the large discrepancy in the southwest of Figure 4.9 panel C, on the steep slopes of the Hebrides Terrace seamount is easily explained. Similarly, differences of 200 m at the north and south on the continental margin may be explained by interpolation over steep slopes. However, the large >400 m (and two smaller >100 m) difference located on the north of the Barra Fan appears to be due to incorrect SRTM30 bathymetry data as this area is crossed by five BGS survey lines, none of which show the feature.

This artefact has been communicated to GEBCO, who have confirmed that the original GEBCO '08 dataset appears to contain erroneous data (Pers Comm Weatherall, 2012)

and that the next update will include this finding. This artefact is removed (arithmetically, using the values displayed in Figure 4.9.C) from the bathymetry discussed in the remainder of this thesis.

Figure 4.10 shows more detailed imagery of the LOIS SES bathymetry between 56º N and 57º N, this dataset covers the continental slope in this location.
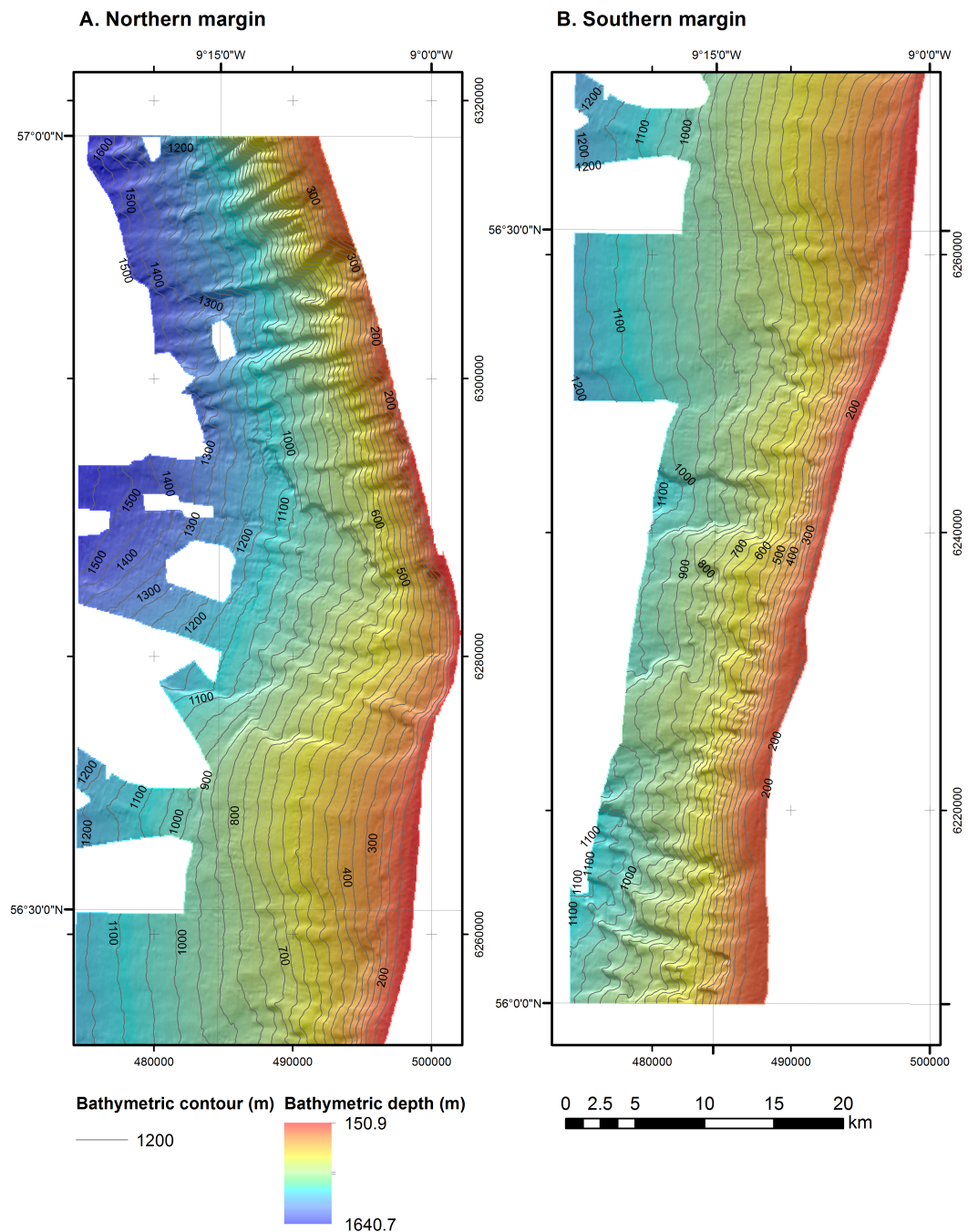
Figure 4.10: LOIS SES bathymetry. A. 57º 5' N to 56º 25' N. B. 56º 20' N to 56º 0' N. Contours at 50 m intervals.

The main features apparent in the dataset are: gullies in the north; a landslide scar between these gullies and the smooth surfaced sediment fan to the south; and in the far south of the data set: broad, deep gullies.

4.3.1.2. Slope gradients

A. Northern margin

B. Southern margin

Angle (°)

0.0 - 1.01
1.01 - 2.0
2.01 - 3.0
3.01 - 4.0
4.01 - 5.0
5.01 - 7.5
7.51 - 10.0
10.01 - 12.5
12.51 - 25.6
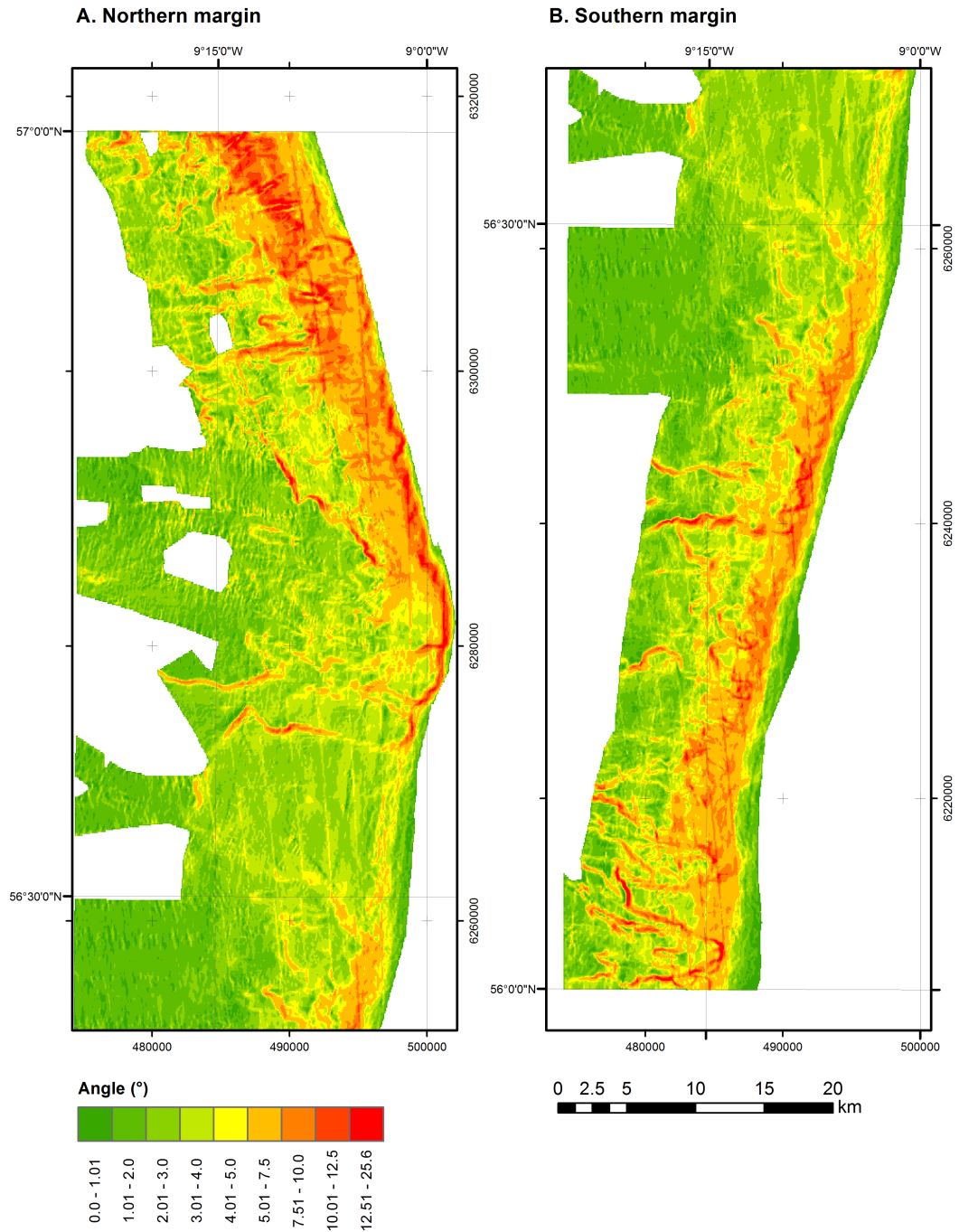
Figure 4.11: Gradients calculated from LOIS SES bathymetry. A. 57º 5' N to 56º 25' N. B. 56º 20' N to 56º 0' N.

Gradients, calculated in ArcGIS using the LOIS SES bathymetry, display values ranging from close to 0 to 25.6º. Regionally, the steepest gradients are located in the north of the LOIS SES bathymetry, where extensive areas display angles >10º. Steep slopes are also observed over extensive areas in the south of the dataset, with angles

>7.5º common. The gentlest slopes are located on the lower slope in the central fan area, where they are generally <2º.

Locally the steepest slope angles are associated with the side walls of gullies and landslide scarps. In the northern gullied area angles reach 20º, whereas on the landslide scarp slopes they are commonly between 10º and 17º. The steepest slopes, of almost 26º, are associated with a complex landslide or gully feature in the far south of the LOIS SES bathymetry.

Figure 4.11.A also reveals a number of hummocky, undulations within the lower slopes of the slide amphitheatre. Further linearly distributed narrow bands of undulating slope angles appear visible perpendicular to the slope, on the lower slopes of the fan. If real, these features may be associated with downslope sediment transport. However, in some cases they may be caused by artefacts within the data. These features are discussed further in chapter six.

4.3.1.3. Landslide scar

The LOIS SES bathymetry provides complete coverage for the large landslide scar within depths less than 1100 m below mean sea level. This covers the portion of the scar within the upper continental slope, which is envisaged to be a good proportion of the zone of evacuation.
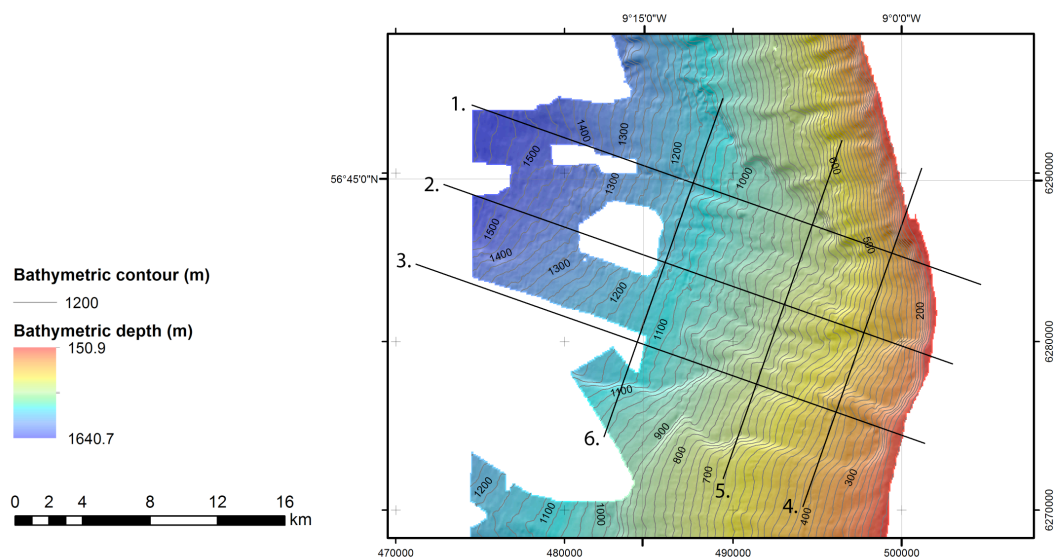
Figure 4.12: Map of landslide scar. Numbered lines indicate cross-sections displayed in Figure 4.13. Contours at 25 m intervals.

As Figure 4.12 shows, the scar extends eastward, cutting back into the Hebrides Shelf creating an embayment within the continental margin. A smaller scar is visible upslope from the main slide scar and a number of lobes extend within the main scar. The scar

area, at depths shallower that 1100 m below mean sea level is 210 km^2. In this upper region the maximum width of the evacuated area is 17.8 km.

Figure 4.13 displays bathymetric profiles for the numbered lines in Figure 4.12. Profiles 1 to 3 demonstrate the transition from steep upper slopes (angles commonly 11º) to gentler angles on the middle (3º) and lower (<2º) slopes. Relief is considerable: profile 6 shows scarp heights of 73 m and 46 m in the north and south respectively; and section 5 shows relief of 40 m within the landslide scar, associated with mounded deposits.

Slope angles associated with the scarp slopes are between 6º and 9º in the south and between 10º and 17º in the north (see Figure 4.11). The southern scarps in particular are often associated with moats, as shown in Figure 4.13 profile 5. There is no obvious join between the southern and northern scarps; an area of some 131 km^2 between the 900 m contour in the south (56º 38' 52" N 9º 11' 19" W) and the 650 m contour in the north (56º 42' 58" N 9º 3' 3" W) is obscured by downslope deposits from the upper slope.

These flows appear to originate from three upper scars, which reach the 200 m contour. The largest, and most pronounced, of these is the southernmost, which has an area of 36 km^2 and maximum scarp height of 80 m. This feature is 3.3 km wide and displays an evacuation zone of 3.5 km length and a depositional lobe of some 5 km length, with 20 m to 30 m elevation.
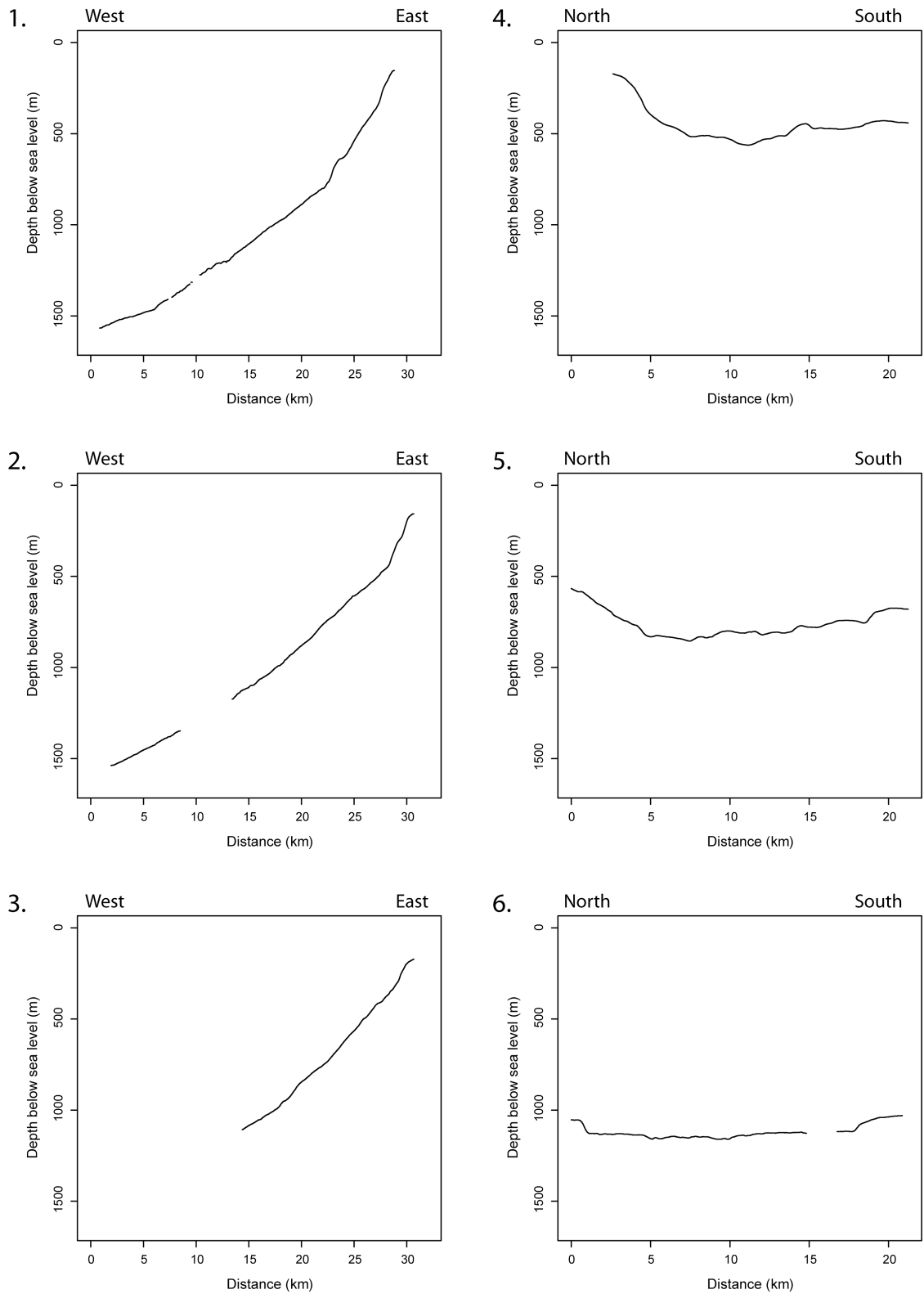
Figure 4.13: Profiles across landslide scar marked in Figure 4.12. Downslope sections displayed west to east and across slope sections north to south.

4.3.1.4. Gullies

The continental margin in the far north and south of the study area is incised by numerous gullies. Figure 4.14 shows bathymetry from areas of gullies in the north and south of the LOIS SES dataset, bathymetric sections from these areas are displayed in Figure 4.15. Data coverage is less extensive in the south, with the lower limit close to the 1100 m contour, compared with below the 1500 m contour in the north.
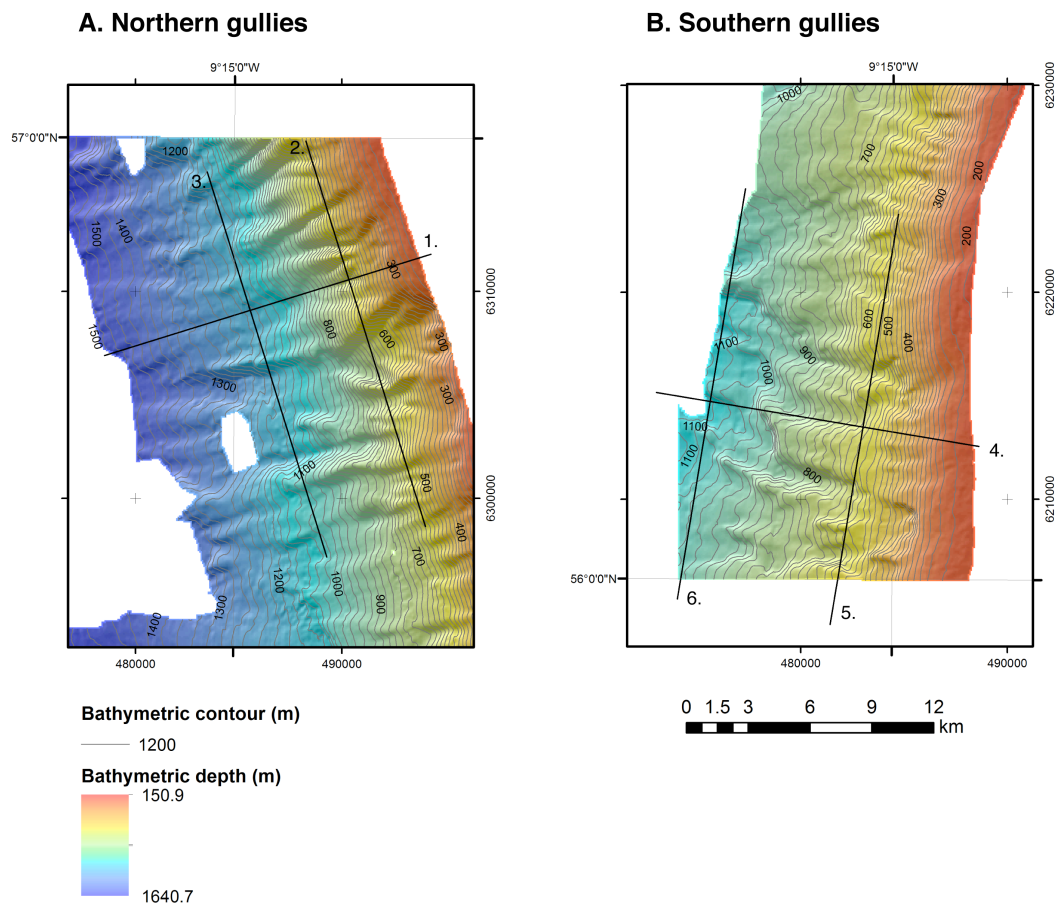
Figure 4.14: Map of gullies in north (A) and south (B) of LOIS SES bathymetry. Numbered lines indicate cross-sections displayed in Figure 4.15. Contours at 25 m intervals.

The morphology of the northern gullies is displayed in Figures 4.14.A and 4.15.A. They originate at depths of 300 m and extend to beyond the LOIS SES data limit; although in much less pronounced form. Figure 4.15 profile 2 is crossed by 12 individual gullies, which appear to coalesce to seven major features further downslope in profile 3. These gullies are steep sided and V-shaped, they display a maximum incision of 150 m, although 50 m is a more common value. Figure 4.15 profile 3 is crossed by seven individual gullies, which are generally less pronounced with less steeply angled walls and reduced incision.

A. Northern gullies
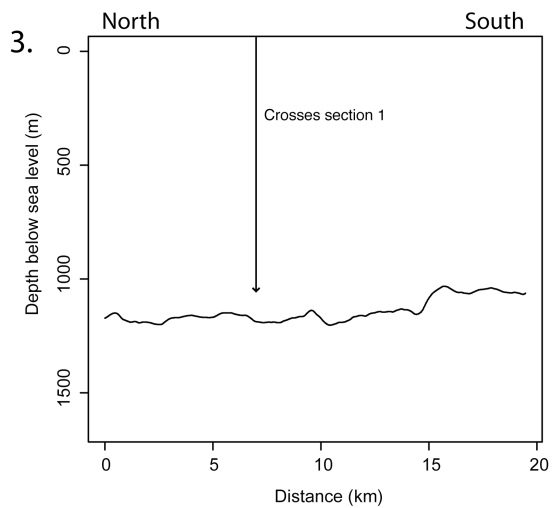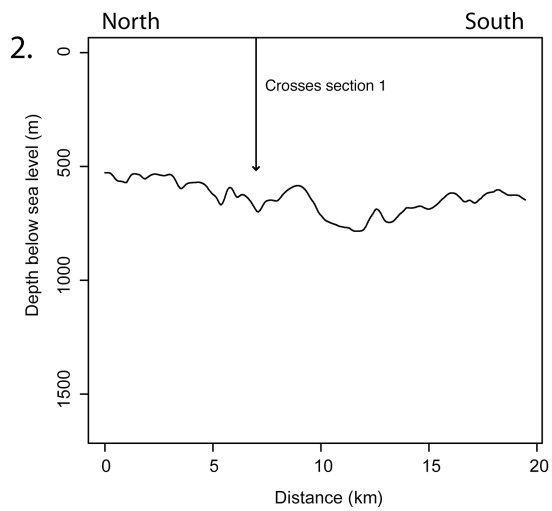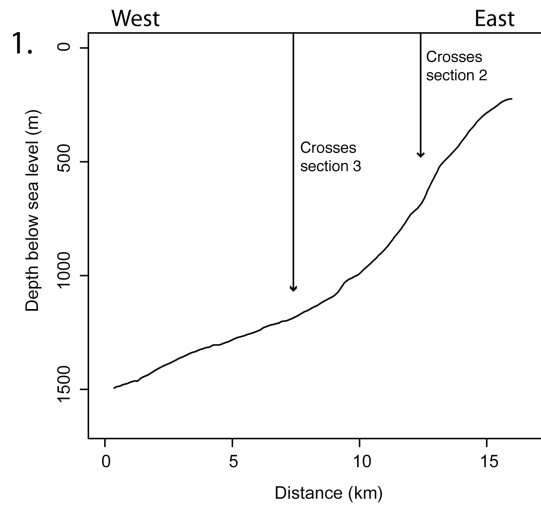
B. Southern gullies
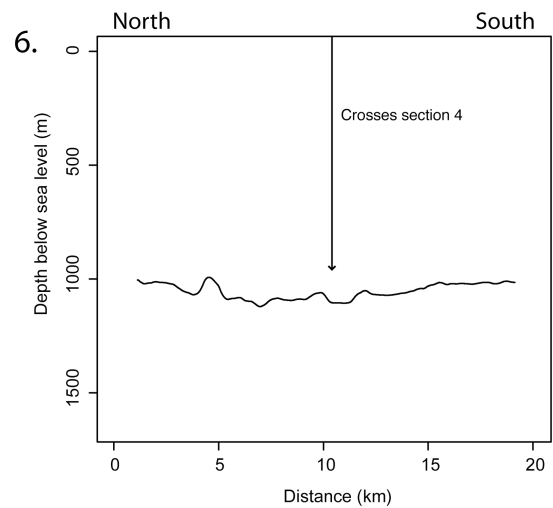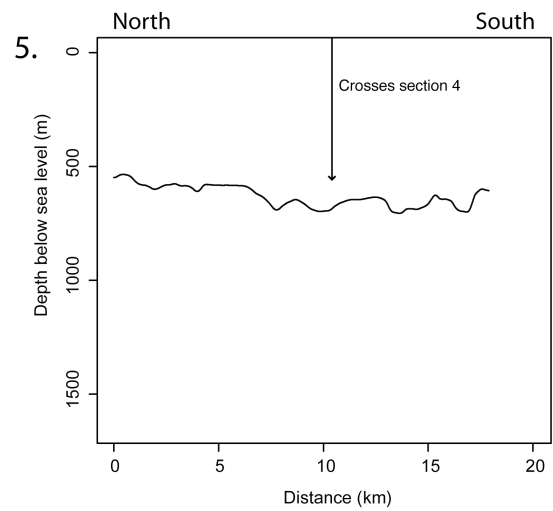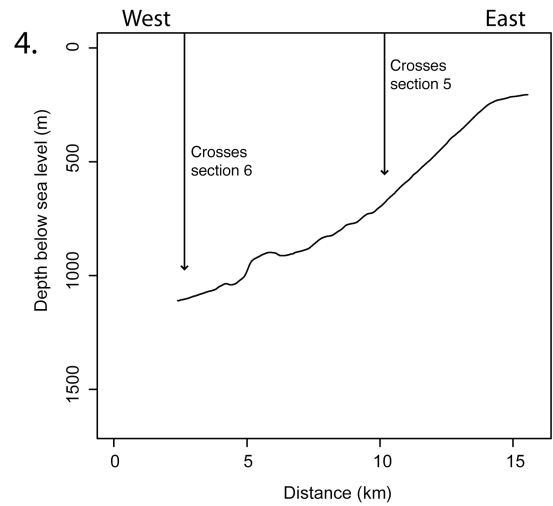
Figure 4.15: Profiles through gullied areas indicated in Figure 4.14. Downslope profiles displayed west to east and across slope sections north to south.

The convex lower slope and reduced number of individual gullies reflects the confluence of these at depths below 1100 m below mean sea level. A large bowl shaped depression is crossed by Figure 4.15 profile 2 at 12 km along section, it is clearly visible in Figure 4.14.A. Three feeder channels enter this feature from the upper slope, the LOIS SES data does not show their upper sections. So close to the shelf break, it is tempting to infer that these feeder channels originate at or near to the Hebrides Shelf.

Figures 4.14.B and 4.15.B display the morphology of the southern gullies. They originate at depths of 300 m and extend to beyond the LOIS SES data limit, although in much less pronounced form. In this location the LOIS SES data only extends to the 1100 m contour, as such much of the lower slope is not visible. The pronounced mound feature visible in Figure 4.15 profile 4 appears to be a buttress eroded from the surrounding material.

Figure 4.15 profiles 5 and 6 demonstrate that six upper slope gullies coalesce to form three gullies further downslope. These gullies are very steep sided and U-shaped. Maximum incision is 100 m, with 50 m a more commonly observed value. Confluence of gullies appears to occur from depths of 1000 m. The southern gullies are appreciably wider than those in the north and have steeper walls (angles up to 25.6º), which act to leave freestanding buttresses between neighbouring channels (see Figure 4.14.B).

These gullies are discussed briefly in chapter six.

4.3.2. AFEN TOBI sidescan sonar

4.3.2.1. Sidescan sonar overview
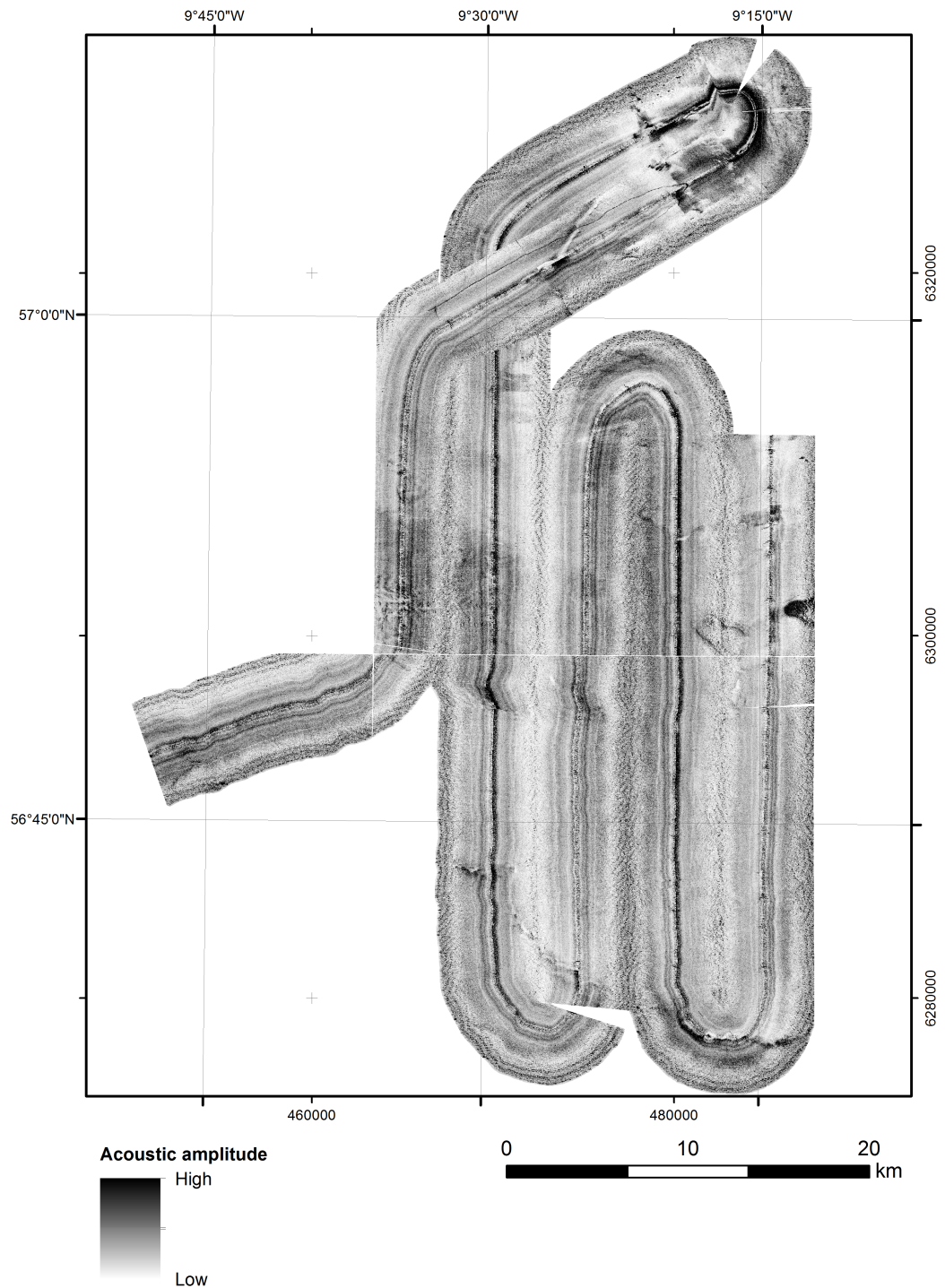
Figure 4.16: Raw AFEN TOBI sidescan sonar data. Track parallel striping is an artefact.

Sidescan data presented in in Figure 4.16 are the unprocessed data provided on the AFEN CD-ROM (AFEN, 1998). A number of artefacts are present in the data and these limit the degree of interpretation that is possible. A limited interpretation is presented in Figure 4.17, however, the interpretation is combined with bathymetry and sub-surface

results for the interpretation presented in section 4.5. Major features such as landslide scarps and debris deposits are clearly visible within the sidescan data: extending the seabed interpretation beyond the limits of the LOIS SES dataset.
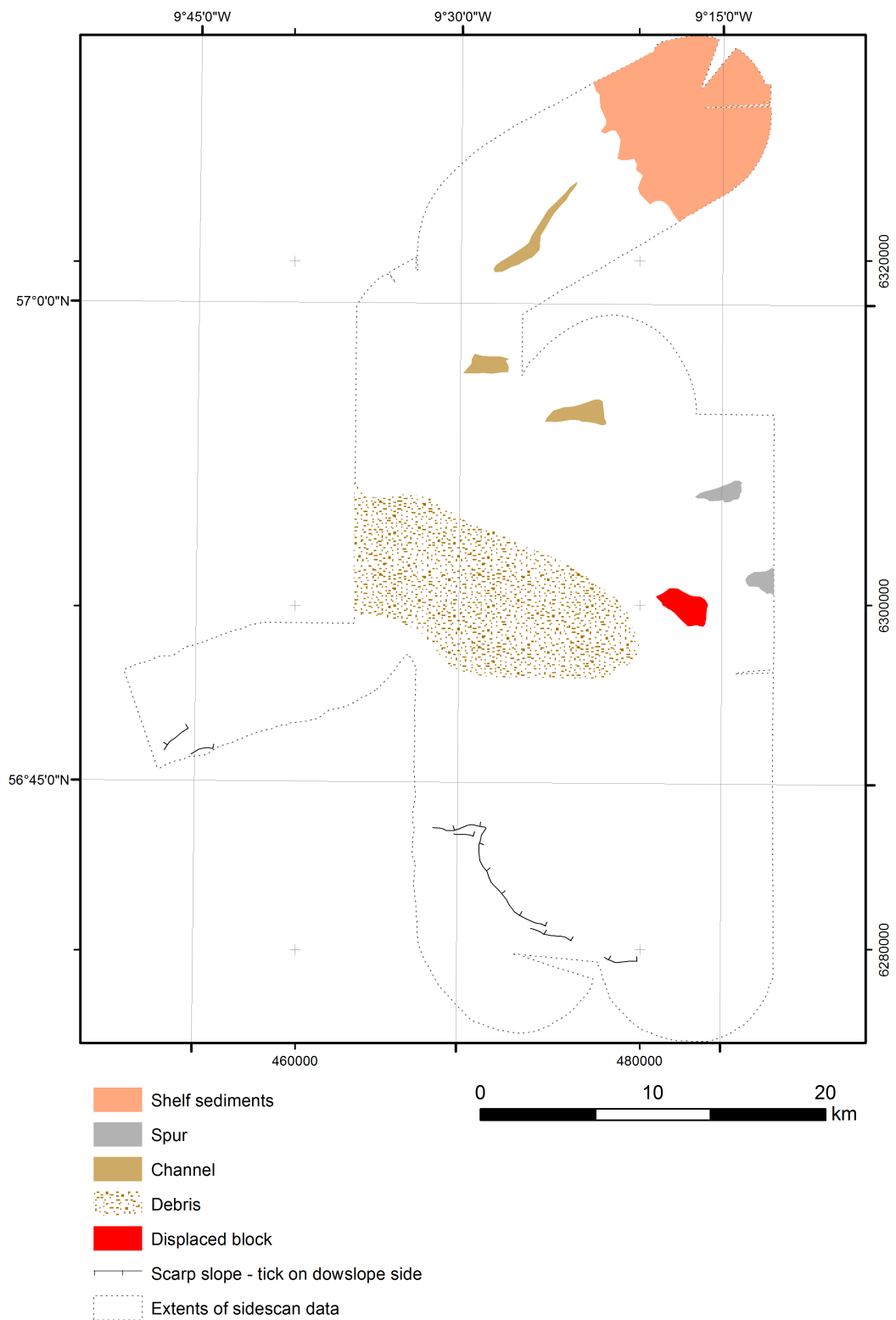
Figure 4.17: Major features interpreted from AFEN TOBI sidescan sonar. Interpretation was completed with the aid of bathymetric and sub-bottom profiler data.

4.4. Sub-surface geology data analysis and results

4.4.1. Sub-surface geology overview

This thesis interprets seven different acoustic facies from BGS and NOC pinger records, building on previous interpretations from Howe (1996), Armishaw et al. (1998), Armishaw (1999) and Knutz et al. (2002) on the Barra Fan. Work by Tripsanas et al. (2007; 2008) on the Nova Scotia margin informs the criteria used to differentiate debris flow facies. Table 4.5 presents an overview of this interpretation.

Acoustic record interpretation is based on the reflectivity of the seabed and sub-seabed. Relative size of reflected amplitudes is dependent on the differences in acoustic impedance of the material on either side of the interface, where acoustic impedance is calculated by multiplying a unit's P-wave velocity by its density (Gadallah and Fisher, 2009). The reflection co-efficient, and therefore the magnitude and polarity of the reflector, is the ratio of the reflected ray to the incident ray (Gadallah and Fisher, 2009). As outlined by Piper et al. (1999b), facies are interpreted on the basis of: presence or absence of reflection; relative amplitude of reflection; reflector geometry; and the relative amplitude of backscatter in the absence of reflectors.

This interpretation is concerned solely with the uppermost sedimentary column as imaged by the high resolution, low penetration, pinger records (with cross reference to one deep-towed boomer record). Surface sediments will be influenced by deep processes. This deeper geology may be investigated using longer wavelength, higher amplitude, acoustic (such pulses more commonly referred to as seismic) sources such as sparker or airgun. However, in the study area, these data sources are limited in amount and quality (the paper BGS paper records are very compressed and do not lend themselves to the SEGY conversion process) and were not analysed. Some details of the deeper geology of the Barra Fan are shown by James and Hitchen (1992) and Holmes et al. (1998).

Acoustic facies interpreted here may be considered components of the Gwaelo and Macleod sequences, interpreted in BGS Peach Quaternary chart (James, 1992) and discussed by Howe (1996).

Appendix C presents the sub-surface interpretation log.

Facies	Characteristics visible in acoustic record	Interpretation	Evidential support
Ia	Uppermost unit - Low-amplitude and transparent	Muddy contourite	Sampled by BGS core samples and interpreted by Armishaw (1999), Armishaw et al. (2000), Kroon et al. (1997; 2000) and Knutz et al. (2002).
Ib	Uppermost unit - High-amplitude	Sandy contourite	
IIa	Parallel reflectors draping underlying units	Hemipelagic sedimentation, consisting of varying contributions from hemipelagic, contouritic, glaciogenic and turbiditic sources	Corresponds to the Gwaleo sequence (Stoker et al., 1993). Lack of ground truthing prevents differentiation of sources, which Howe (1996), Kroon et al. (2000) and Knutz et al. (2002) demonstrates are mixed.
IIb	Unit of parallel reflectors underlaying chaotic or high-amplitude facies	Hemipelagic sedimentation, separate facies to simplify analysis.	FIIb represents interpretation of Upper Macleod sequence.
III	High-amplitude unit	Unit consisting of coarser sediments, which may be sandy contourite or turbidite when ponded	Coarser material provides higher amplitude returns and literature (Howe, 1996; Knutz et al., 2002) supports presence of contourites and turbidites.
IVa	Chaotic, semi-transparent unit with hyperbolae; displaying mounded morphology at upper boundary	High viscosity cohesive debris flow	Chaotic, semi-transparent to transparent facies indicative of debris flow deposits (numerous studies, including Canals et al., 2004; Tripsanas et al., 2007).
IVb	Chaotic, semi-transparent unit displaying flat to concave upper boundary	Low viscosity cohesive debris flow	Higher viscosity results in deposits displaying positive relief, low viscosity materials act more like liquids and infill resulting in zero or negative relief (Tripsanas et al., 2007).
IVc	Prominent reflector within chaotic, semi-transparent unit	Indicating multistage event	
V	High-amplitude, irregular, hyperbolic return	Hard debris	Indication of rugged terrain, noted by numerous studies, including Armishaw et al. (1998), since Damuth et al. (1983).
VIa	Acoustic blanking within sedimentary column - diffuse	Diffuse fluid escape	Documented on Sula Sgeir Fan by Baltzer et al. (1998).
VIb	Acoustic blanking within sedimentary column - associated fault	Fluid escape associated with polygonal fault	As documented in the Faroe-Shetland Channel (Bulat and Long, 2001) and Norwegian Margin (Reiche et al., 2011).
VII	Marked reflector displacement or high-amplitude vertical reflections below depression	Fault	Diameter of Fresnel zone (see Lindsey, 1989) may obscure detail in deep water and faults are visible as high-amplitude, linear, near-vertical features.

Table 4.5: Overview of interpreted acoustic facies.

4.4.2. Identifying characteristics and interpreted origin of acoustic facies

4.4.2.1. Acoustic facies I - Uppermost sedimentary unit

Acoustic facies I is interpreted where the uppermost unit in the sedimentary column clearly drapes the underlying units and has a clear basal reflector that differentiates it from the units below. This prominent reflector indicates a change in acoustic impedance and sedimentation process. As shown in Figure 4.18, this unit may overlie acoustic facies II, which it is differentiated from by a lack of laminations.
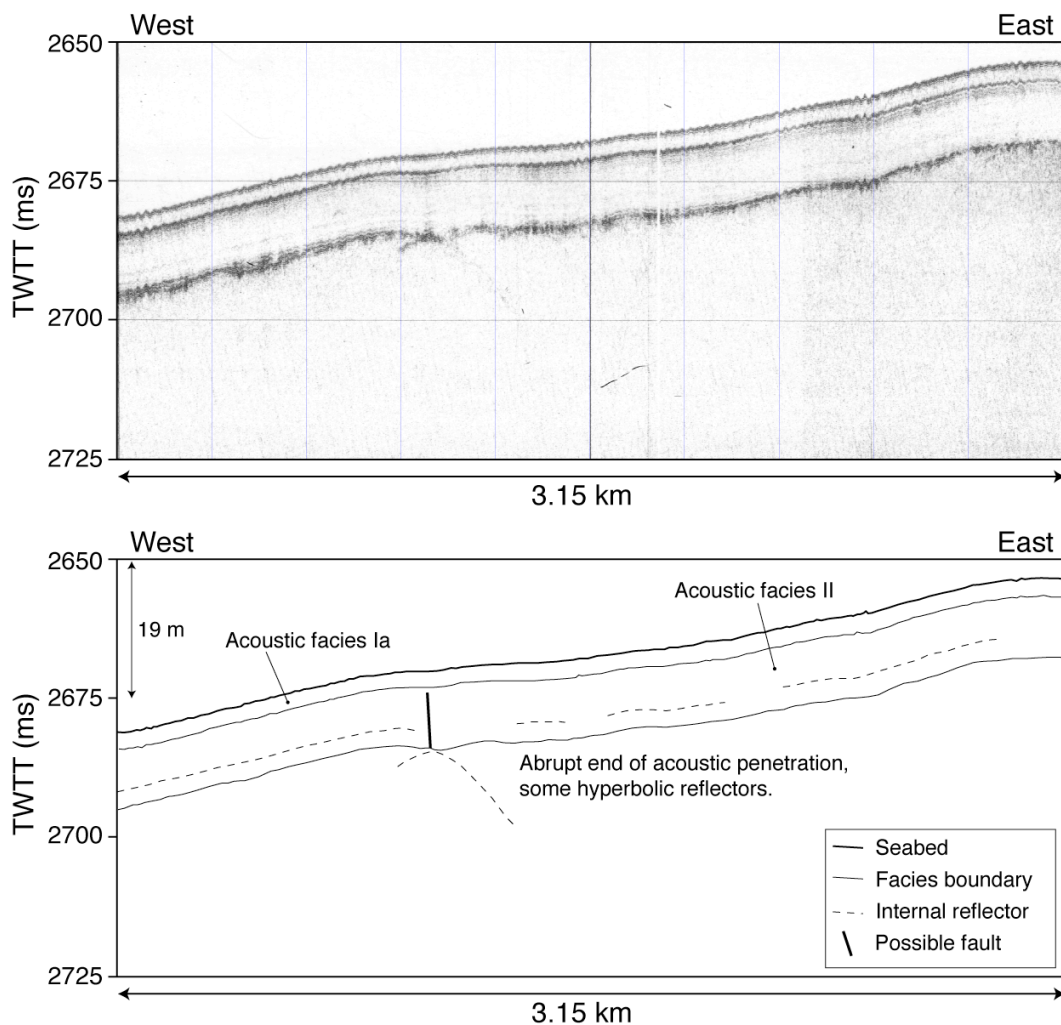
Figure 4.18: Example of muddy contourite, facies Ia; and hemipelagic sediments, facies II from BGS pinger record 1985 6-16. Approximately 25 times vertical exaggeration.

Acoustic facies I is generally <4 ms TWTT thick and not always present. When there is no clear acoustic difference between the uppermost unit and underlying drape (as shown in Figure 4.21) FI is not interpreted. This unit may display low (largely transparent) or high amplitudes. As such this thesis interprets acoustic facies Ia and Ib (as shown in Figure 4.19), low and high amplitudes respectively.

Ground truthing of this unit is attempted via the published core sample records from the region. Armishaw et al. (2000) present 24 core logs from the Barra Fan and Peach slide that document a thin (< 0.5 m) uppermost sandy contourite unit, which overlies muddier sediments (contouritic, hemipelagic or glaciogenic). At the northern edge of the Barra Fan, Howe (1996) shows seven core logs that indicate the presence of a 0.1 - 0.4 m thick, poorly sorted, foraminiferal rich sand layer overlying muddier sediments (hemipelagic and hemiturbidite). Knutz et al. (2002) describe piston core MD95-2006, recovered from 2130 m water depth at the northwest margin of the Barra Fan; they describe a silty-muddy contourite unit, ~1.5 m thick, overlying a 4 m thick sequence of hemipelagic muds grading into muddy contourites. The prominent reflector that defines the unit's base may indicate a period of increased current velocity, resulting in sediment winnowing and development of lag deposits, or deposition of coarse sediments via turbidity currents.

On the basis of the sediment core interpretations described above acoustic FIa and FIb are interpreted as muddy and sandy contourites respectively. The distinction between these two facies sub-types is not always clear on the acoustic record, reflecting the likely presence of more varied lithology including the muddy sand, and sandy mud indicated on the BGS Peach Sea Bed Sediments chart (James and Wright, 1990).

In some locations the facies thickens and in these instances consideration was given as to whether the facies could indicate debrite deposition. Characteristic wavy reflectors are not visible within the unit, though in a muddy contourite the low internal reflection co-efficient (see section 4..4.1, Gadallah and Fisher (2009)) results in an acoustically transparent facies (Rebesco and Stow, 2001; Stow and Faugères, 2008). A lack of ponding and pinch out (characteristics associated with debris flows (Amy et al., 2005; Iverson et al., 2010)) would also appear to support the contourite interpretation.

Outlined in chapter three, the Barra Fan is bathed by a number of different bottom currents and scour and drift features are apparent in both the bathymetric and acoustic data. These are discussed in more detail in chapter six.

Table 4.6 presents the evidence for and against different interpretations of FI.

Hemipelagite	Debrite	Contourite
Evidence for:		
The uppermost unit generally occurs as a drape.	Transparent acoustic facies can be indicative of debrite facies (Piper et al., 1999b; Tripsanas et al., 2007).	Strong evidence of across slope current (e.g. erosional and depositional moats and drifts visible in acoustic and bathymetric data).
Sediment core analysis shows a high terrigeneous content.	Thickness varies, possibly indicating locations of thicker accumulation via mass transport.	Asymmetry of upper unit is visible at times (see Figures 4.28 and 4.32).
		Transparent unit is typical of muddy contourite deposited under a low energy regime (Stow and Faugères, 2008).
		Previous studies in the region (Howe, 1996; Armishaw, 1999; Armishaw et al., 2000; Knutz et al., 2002) document contourite in the upper units.
Evidence against:		
In some instances there is a clear asymmetry.	Ponding and pinch-out is not apparent in the acoustic data.	Asymmetry is not always apparent.
Erosional features, indicative of bottom current action, are noted on the Barra Fan and on the margins of the slide scar.	There are no hyperbolae visible in the unit.	Wavy reflectors are not visible in the acoustic data.
	There is no internal structure visible in the unit.	
	Regional core samples do not provide evidence of mass movement facies in the uppermost section of the sedimentary column.	

Table 4.6: Evidence for and against different interpretations of acoustic facies I.

This thesis concludes that the most probable interpretation is that of contourite. However, as discussed by Armishaw et al. (2000), the sedimentation process is likely to be mixed, with downslope and across slope sources acting in tandem. It is considered likely that FI will consist of sediments derived from a number of sources (hemipelagic, glaciogenic and resuspended eroded material) and transport mechanisms, which are modified by slope parallel currents. This multi-process view reflects the hemiturbidite interpretation by Howe (1996).

4.4.2.2. Acoustic facies II - Parallel reflectors draping underlying units
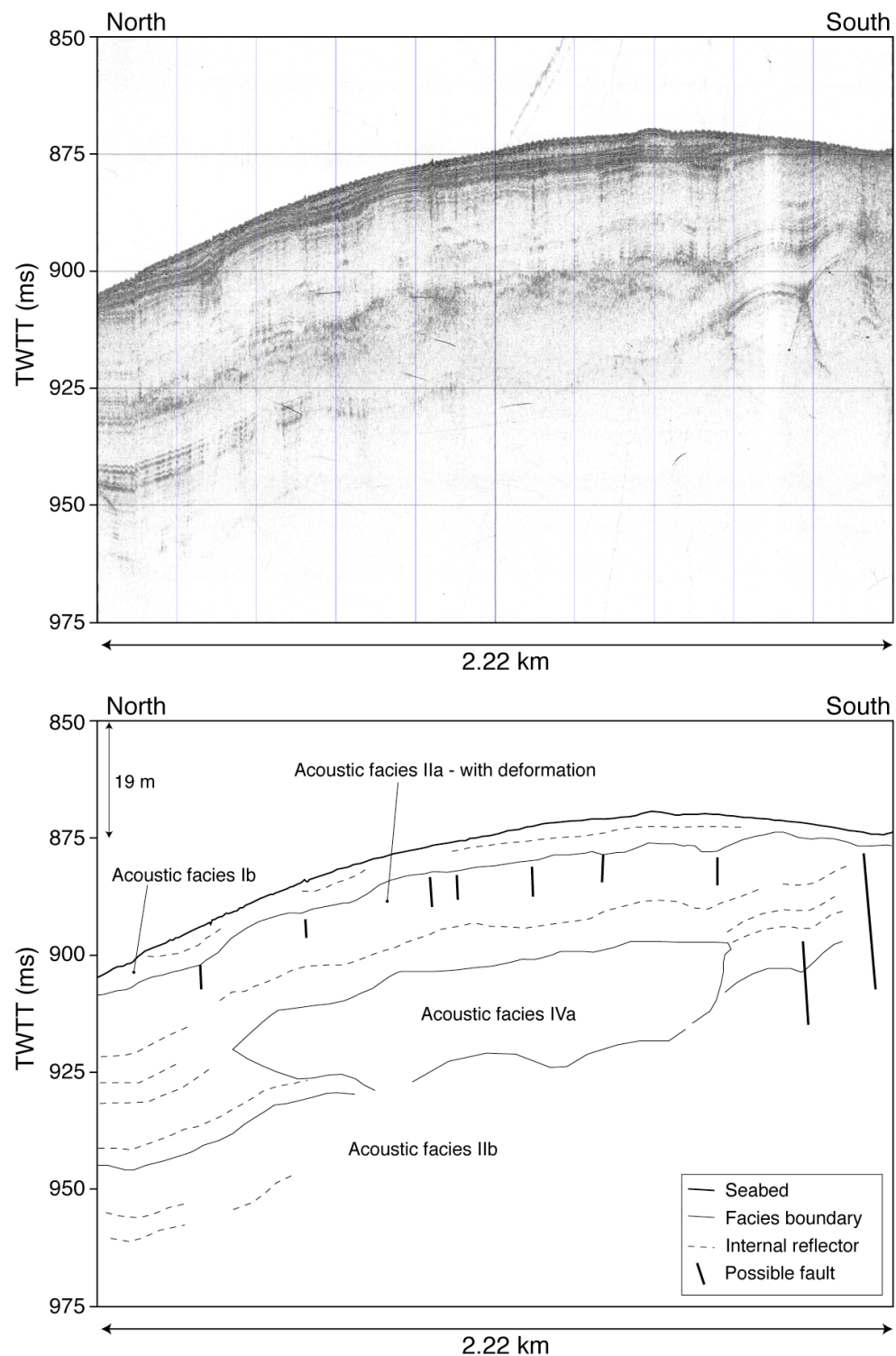
Figure 4.19: Example of sandy contourite, facies Ib, from BGS pinger record 1985 6-27. Uppermost reflectors are truncated indicating possible current scour. Sediment deformation is apparent in deeper units, where acoustic facies II, IVa and VII are interpreted. Approximately 17 times vertical exaggeration.

This facies is present in the upper sedimentary column, is of relatively low acoustic amplitude and drapes underlying units with parallel reflectors. Where present, this facies is generally between 10 and 50 ms TWTT thick, though thickness is generally

~25 ms TWTT. Displaying a draped morphology this unit is probably hemipelagic in origin.

Generally underlying acoustic FI, ground truthing of FII is rare due to the low number of core samples >2.5 m length. Piston core MD95-2006, presented by Knutz et al. (2002), penetrates a unit that is equivalent to FII. Knutz et al.'s (2002) Seismic unit IA is a stratified drape and consists of glacimarine clays merging upwards into contourites (tied seismic and core interpretation from Knutz et al. (2002) is presented and discussed further in chapter six). Further north, on the Hebrides slope, Stoker et al. (Stoker et al., 1994) present a seismic stratigraphy interpreted with borehole 88/7.7A. According to Stoker et al. (1994), the upper 20 m of the sedimentary column is dominated by sedimentation during the Devensian.

Borehole 88/7.7A is located several hundred kilometres further north on the continental margin from the Barra Fan and will be subject to different sedimentation rates and patterns. However, it does provide useful insight due to the similarity of the seismic record shown by Stoker et al. (1994) to the pinger records from the Barra Fan; suggesting that acoustic facies II may consist of sediments deposited during the last glacial transition, in other words the Gwaelo sequence (see Stoker et al., 1993). This is consistent with the chronology presented by Knutz et al. (2002).

At times acoustic FII displays a higher amplitude lower unit below a lower amplitude upper unit. This may reflect the change from glaciogenic to contouritic sedimentation demonstrated by Knutz et al. (2002). Where a further occurrence of parallel reflectors is apparent below another facies this is interpreted as FIIb. If FIIa corresponds to the Gwaelo sequence, it seems likely that FIIb the topmost part of the Upper Macleod sequence.

Interpreting this unit as hemipelagic, this thesis acknowledges it will consist of a mixture of glaciogenic, contouritic, hemipelagic and turbiditic sediments (as documented by Howe (1996), Knutz et al. (2002) and Armishaw et al. (2000)). However, a lack of data (extent and resolution) and ground truthing renders a more detailed interpretation impossible.

4.4.2.3. Acoustic facies III - High amplitude unit

A high amplitude unit acoustic facies III is interpreted to consist of coarser sediments. An example from the upper sedimentary column is shown in Figure 4.20.

On the Barra Fan coarser sediments are most likely deposited via sandy contourites or turbidites. It is extremely difficult to distinguish between these two types without ground truthing via core samples, therefore, this thesis does not generally attempt to do this.
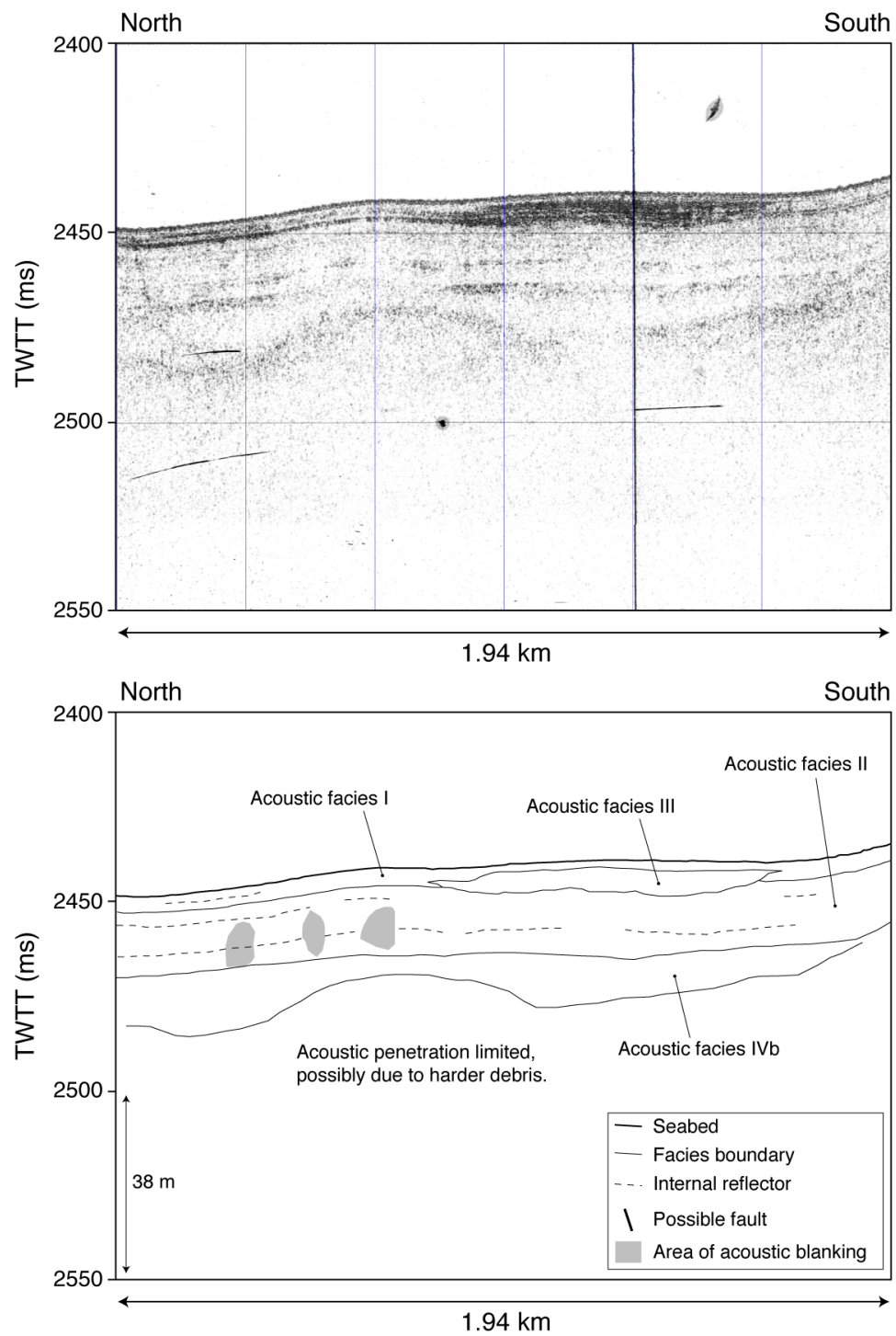
Figure 4.20: Example of low viscosity debris flow deposit, facies IVb, from BGS pinger record 1985 6-14. Acoustic facies I, II and III are also interpreted. Vertical exaggeration times 13.

It is possible to differentiate turbidites and contourites via morphology (see Faugères et al., 1999), with turbidites often ponded and contourites developing into drifts. To the north of the Barra Fan, where Howe (1996) and Knutz et al. (2002) have identified the Barra Fan drift (see section 3.2.3.1) it is possible to identify contourite drift deposits. Equally, chapter six shall attempt to use the seabed morphology to inform interpretation

with a view to identifying sedimentation process. However, with an acoustic line spacing of commonly 10 km the data resolution is not normally sufficient to distinguish between these two sediment types.

4.4.2.4. Acoustic facies IV - Chaotic semi-transparent
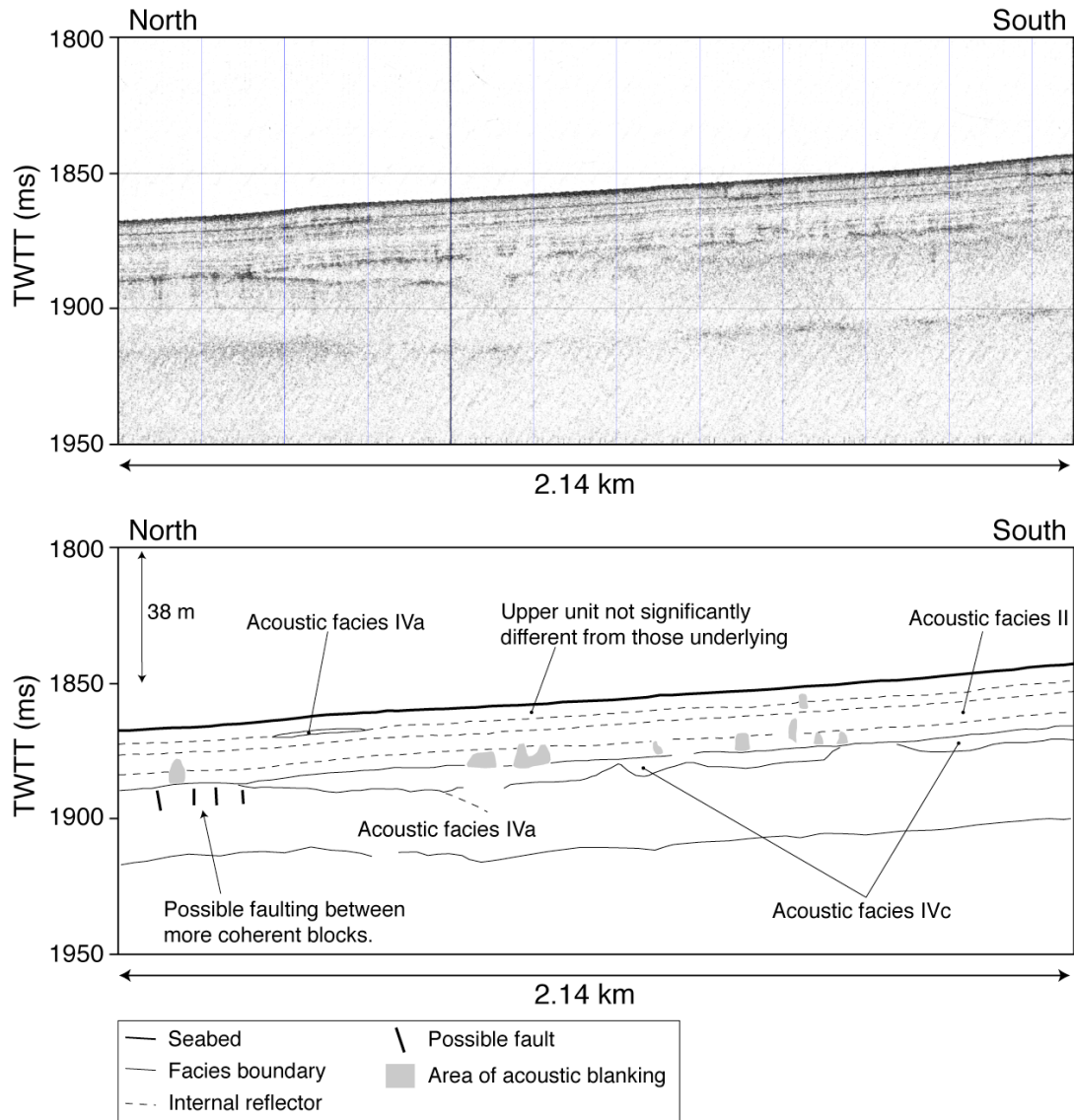
Figure 4.21: Example of high viscosity debris flow deposit, facies IVa; with prominent internal unit, facies IVc, from BGS pinger record 1985 6-13. Acoustic facies II and VIa are also interpreted. Approximately 8 times vertical exaggeration.

Acoustic facies IV, which is divided into three sub-facies, consists of chaotic semi-transparent facies; of which examples are shown in Figures 4.19, 4.20 and 4.21. Thickness of this facies varies from 1 - 2 ms TWTT to 50 ms TWTT or more. Often this facies extends beyond the limit of the pinger record's acoustic penetration. Morphology of the facies varies from ponded with slightly concave upper boundaries (see Figure 4.20) to mounded forms with convex upper boundaries (See Figure 4.21). From the

basis of the acoustic characteristics this unit is interpreted as being a debris flow deposit.

No existing core samples penetrate this facies, therefore ground truthing is not possible. However, referral to the mass transport facies literature allows more precise interpretation.

Numerous continental margin studies have demonstrated that chaotic, semi-transparent to transparent, acoustic facies are indicative of debris flow deposits (see Piper et al., 1999b; Laberg et al., 2002b; Canals et al., 2004). From interpreting acoustic characteristics of these facies in more detail it is possible to further refine the debris flow interpretation.

For example, mass transport deposits on the Nova Scotian margin have been investigated in great detail using acoustic data and core samples (Jenner et al., 2007; Tripsanas et al., 2007; Tripsanas et al., 2008). Using sediment core analysis it is possible to identify a large number of mass transport lithofacies, which may be used to inform the geophysical classification of debris flow deposits. Tripsanas et al. (2007) differentiate between low and high viscosity cohesive debris flows; which they distinguish on the acoustic record with low viscosity flows displaying flat to concave upper surfaces and high viscosity flows exhibiting slightly convex upper surfaces and hyperbolae.

Based on the acoustic characteristics observed in the Barra Fan data, and insights from the acoustic facies literature, this thesis interprets three sub-classes of chaotic semi-transparent facies. Acoustic facies IVa and IVb are interpreted as high viscosity cohesive debris flows and low viscosity cohesive debris flows respectively, they are differentiated on the basis of upper surface morphology (convex to concave) and presence of hyperbolae. A further acoustic facies, IVc, is interpreted to identify prominent internal reflectors within the debris flow units.

4.4.2.5. Acoustic facies V - High amplitude hyperbolic

Acoustic facies V displays high amplitude, irregular hyperbolic returns. The facies is observed on the seabed (as shown in Figure 4.22) as well as within the sedimentary column. Presence of this facies normally prevents any further acoustic penetration.

The presence of irregular hyperbolic reflectors in the acoustic record is generally an indication of blocks within the sediment or rugged terrain (Damuth, 1978; Damuth et al., 1983). These blocks may consist of individual boulders or rafted sediment blocks (Tripsanas et al., 2007). Investigating the morphology of the Barra Fan, Armishaw et al.
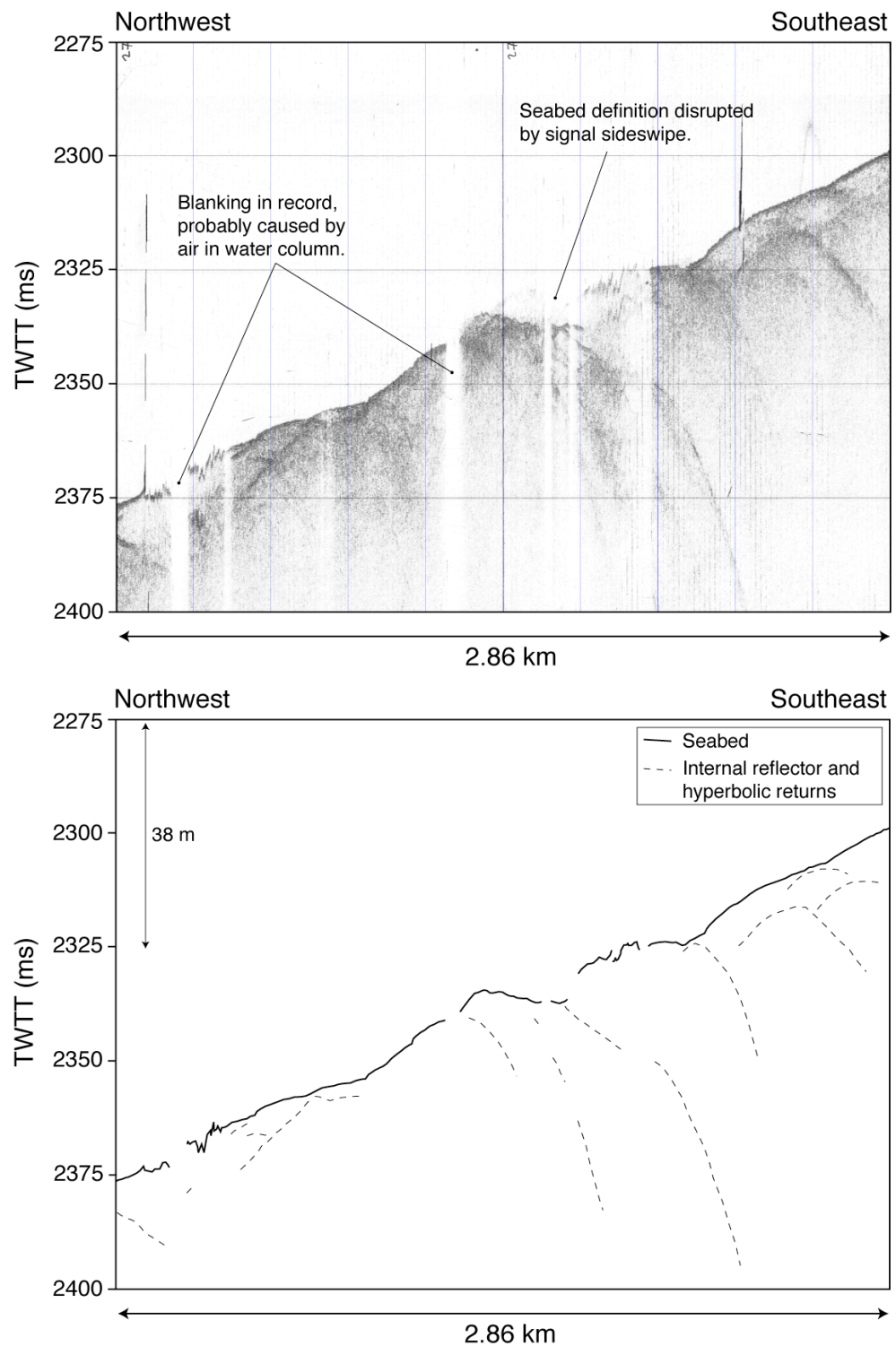
Figure 4.22: Example of hard debris deposits, facies V, from BGS pinger record 1985 6-27. The record displays some disruption from sideswipe as well as possible water column noise. Approximately 22 times vertical exaggeration.

(1998) interpret irregular hyperbolic returns as slump or slide masses. In the setting of the Barra Fan, where sediments are commonly dominated by clays, this interpretation is sensible as rugged terrain is likely to result from mass movement, either via erosion or deposition.

This thesis interprets these irregular hyperbolic returns as acoustic facies V, hard debris. This is different from Armishaw et al. (1998), and acknowledges the variety of downslope processes (from translation slides to debris avalanches) that can result in the deposition of debris and the creation of rugged terrain.

4.4.2.6. Acoustic facies VI - Acoustic blanking within sedimentary column
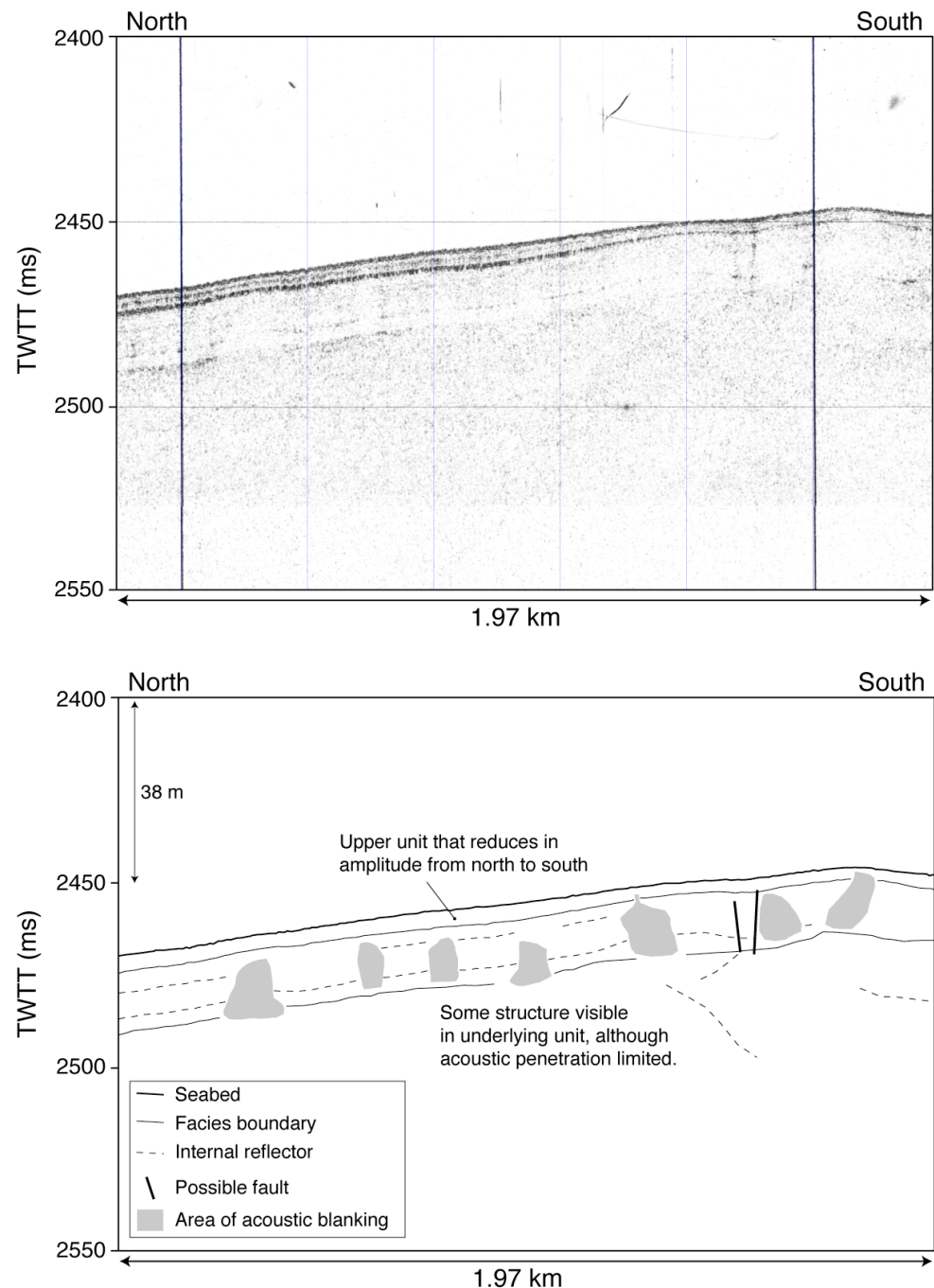
Figure 4.23: Example of diffuse acoustic blanking from BGS pinger record 1985 6-14. Approximately 12 times vertical exaggeration.

Acoustic blanking within the sedimentary column (as opposed to vertical blanking down the entire acoustic record, which is commonly caused by air in the water column effecting the transducer or hydrophone) is caused by by two primary reasons: high amplitude reflection units (potentially rock, salt intrusion, coarse sediments or free gas) resulting in reduced signal strength below them in the sedimentary column; and fluid reducing the reflectivity of host sediments.
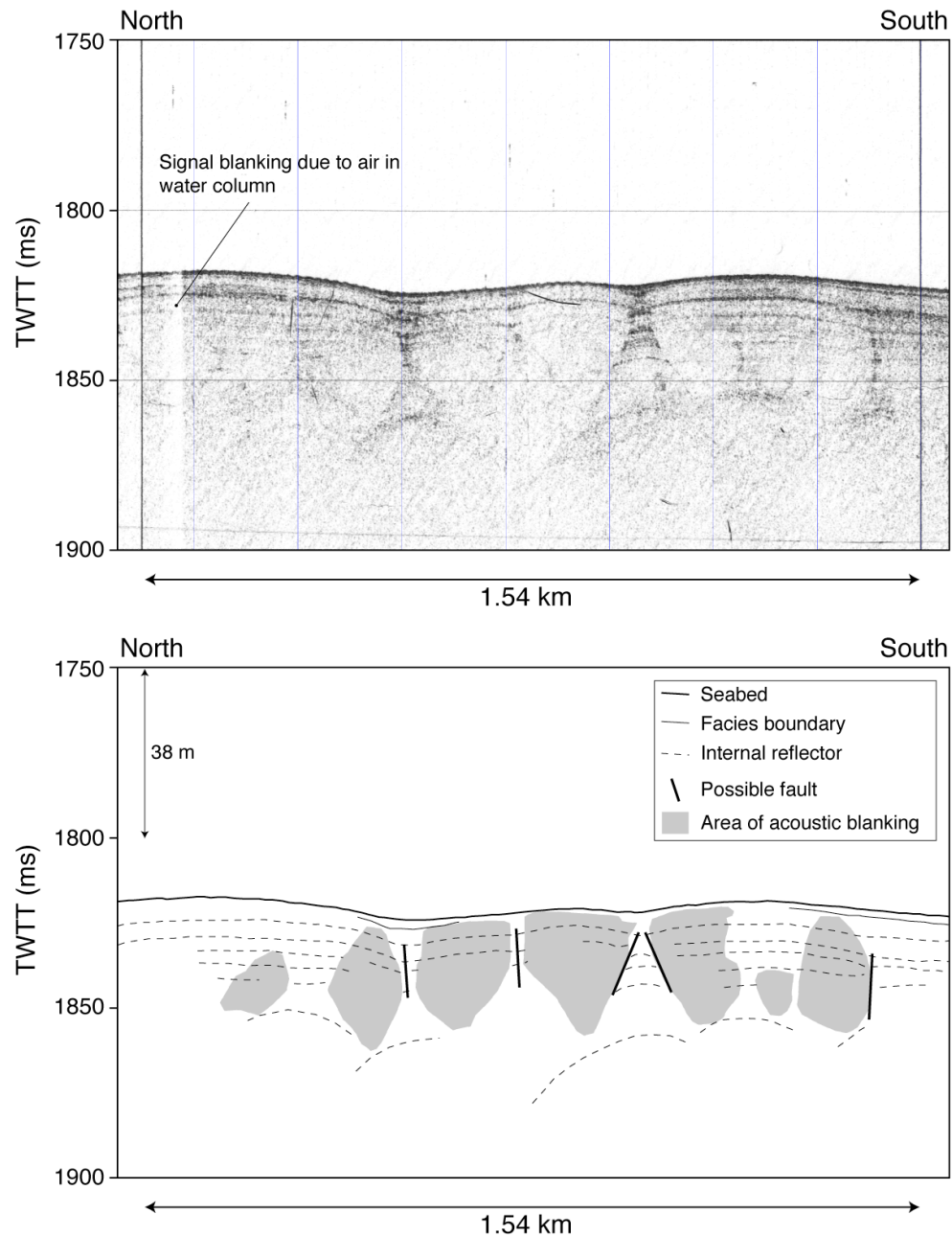
Figure 4.24: Example of acoustic blanking associated with faulting from BGS pinger record 1985 6-13. Approximately 9 times vertical exaggeration.

Acoustic facies VI is interpreted from the pinger record where acoustic blanking is interpreted to have been caused by fluid in the sedimentary column. Pore fluid explusion and upward fluid migration is linked to sediment overpressurisation (Paull et

al., 2008) and has previously been observed on the northwest British continental margin (Selby, 1989; Baltzer et al., 1998); as well as further north on the northwest European margin (Bryn et al., 2005b; Reiche et al., 2011). Fluid migration may occur diffusely in the sedimentary column or it may be channeled by faults (see Gay et al., 2007; Reiche et al., 2011; Talukder, 2012).

As such, this thesis interprets acoustic facies VIa (see Figure 4.23) as diffuse fluid expulsion; and acoustic facies VIb (see Figure 4.24) as fluid expulsion associated with faulting. The relationship between fluid expulsion and faulting on the Barra Fan is discussed in more detail in section 4.4.5.3 and chapter six.

4.4.2.7. Acoustic facies VII - Marked reflector displacement or high-amplitude vertical reflections below depression

Acoustic facies VII is interpreted where high-amplitude reflectors are aligned near-vertical in the sedimentary column (as shown in Figures 4.19, 4.21, 4.23 and 4.24).

A combination of deep water and the Fresnel zone diameter (see Lindsey, 1989) results in a relatively large ping footprint, and therefore reduced lateral resolution. Reduced lateral resolution means that faults with relatively low throw are unlikely to appear as clear displacements on pinger records. However, they may show a vertical signature and seabed morphology may indicate their presence.

These features are observed as linear, vertically aligned zones of high reflectivity below seabed depressions. These features are interpreted as shallow faults, which may originate from a number of mechanisms, including: soil creep resulting in extensional faulting and tear faults (see Yang and Davies, 2013); and dewatering of clays resulting in polygonal faulting as observed in the Faeroe-Shetland Channel (Bulat and Long, 2001) and offshore Norway (Bryn et al., 2005b).

Sediment deformation caused during downslope transport may also lead to faulting between blocks of sediment as well as at the side and headwalls of slides and slumps.

4.4.3. Importing sub-surface interpretation in a GIS environment

Sub-surface interpretation was performed in Seismic+ from autumn 2012 to early 2013 and subsequently imported into ArcGIS for more detailed analysis.

Within Seismic+ the seabed was tracked and each interpreted facies was assigned an interpretation type, which was placed manually on the top of the basal reflector at regular intervals. At times, with some facies, the basal reflector extended beyond the limit of acoustic signal penetration. Data quality was variable and exerted an influence over the detail of interpretation possible. Table 4.7 provides a data quality summary.

Line name	Quality statement	Comment regarding interpretation
NOC_AFEN_49	Good	Data quality is high, but low data resolution compared to BGS pinger lines reduces amount of interpretation possible.
NOC_AFEN_50	Good	In some circumstances crossing BGS pinger line allows more detailed interpretation due to cross-referencing.
NOC_AFEN_51	Good	
NOC_AFEN_52	Good	
NOC_AFEN_53	Good	
NOC_AFEN_54	Good	
NOC_AFEN_55	Good	
BGS_1985_6_1	Very poor	Compressed nature of the printed record meant no interpretation was possible
BGS_1985_6_12	Very good	Data quality is high detailed interpretation possible.
BGS_1985_6_13	Good	Data quality is generally high and detailed interpretation possible. Some areas of reduced data quality.
BGS_1985_6_14	Mixed	Varying data quality.
BGS_1985_6_15	Mixed	Data quality generally poor in deep water, however, sub-surface features visible and quality improves as water depth reduces.
BGS_1985_6_16	Good	Data quality is generally high and detailed interpretation possible. Some areas of reduced data quality.
BGS_1985_6_17	Poor to mixed	Data quality generally poor in deep water, however, sub-surface features visible and quality improves as water depth reduces.
BGS_1985_6_18	Mixed to good	
BGS_1985_6_22	Mixed	Quality generally very poor in the north, but improves in the south.
BGS_1985_6_23	Good	Data quality is generally high and detailed interpretation possible. Some areas of reduced data quality.
BGS_1985_6_27	Good	
BGS_1985_6_28	Poor	Some interference apparent, weak return signal. Interpretation possible with reference to crossing lines.
BGS_1985_6_2	Mixed to good	Some interference and noise apparent, but detailed interpretation possible at times.

Table 4.7: Summary of pinger line data quality.

Exported interpretation from Seismic+ consisted of a CSV file containing UTM grid position, depth below seabed (ms TWTT) and the survey line name. This interpretation was then formatted in a spreadsheet for import into ArcGIS.

4.4.3.1. Assumed seismic velocity

A vital consideration when converting interpreted depths from ms TWTT into metres is the velocity at which the seismic wave propagates through the sub-surface. Velocity is primarily dependent on material density, with denser materials having a faster velocity

than less dense. For example crustal material may have velocities in excess of 7000 m s^{-1} (Holbrook et al., 1994), whereas shallow muds have velocities between 1650 and 1500 m s^{-1} (Knutz et al., 2002; Nordfjord et al., 2009) dependent on water content. Between these extremes a range of velocities are encountered.

In a previous study of the Peach slide Holmes et al. (1998) employ an assumed velocity of 1650 m s^{-1}. For the deeper, denser sediments associated with the earlier phases of the Peach slide this velocity may be appropriate. However, as this thesis is concerned with the shallow subsurface morphology of the Barra Fan a uniform velocity of 1525 m s^{-1} is assumed. This is based on the measured velocity of units in core sample MD95-2006 and presented by Knutz et al. (2002).

It is acknowledged that some error will result in estimating thicknesses of all interpreted facies from a single velocity. For example, it is envisaged that FIVa will have a greater velocity than FIVb and FIIa. However, as interpretation is within the uppermost 70 ms TWTT of the sedimentary column the resultant error is likely to be low. For example a difference in velocity of 150 m s^{-1} over 70 or 30 ms TWTT is associated with metre depth differences of 5 and 2 m respectively. Equally errors would also be generated by assuming different velocities without strong supporting evidence.

4.4.3.2. Interpretation import method

Interpretation for the base of each acoustic facies was exported from Seismic+ in CSV format, imported to ArcGIS and converted to a point shapefile. Raster surfaces were created for each acoustic facies using inverse distance weighting (IDW) interpolation. For horizons, surfaces were created based on a 25 m grid and a 100 m fixed search radius (reflecting the possible distance between interpreted nodes). Fluid, debris and fault interpretation was gridded to 10 m resolution using a 25 m fixed search radius (reflecting the isolated nature of these facies).

Creation of surfaces is associated with a degree of smoothing and associated loss of detail. However, as the IDW interpolation is based on a search zone with a fixed radius of 100 m and the calculated value of the resultant raster is strongly weighted in favour of interpretation at the centre, it is felt that loss of detail should be minimal.

Pinger survey polyline shapefiles were converted to point a shapefile with nodes spaced every 10 m along the lines (resulting in more than 150,000 nodes). Bathymetric depths and depth below seabed of interpreted facies were extracted to these nodes using ArcGIS Spatial Analyst.

4.4.3.3. Sub-surface data analysis method

Converting interpretation into raster surfaces and extracting this information to evenly spaced points allows calculation of unit thicknesses and analysis of the distribution of different facies (and associated grouped facies) throughout the study area.

Python logic functions were used to calculate thickness of different interpreted facies. These functions are simple. However, in order to ensure accurate calculation, thickness fields were calculated based on each observed sequence of units, with null values returned when sequences did not fulfill statement criteria. Equation 4.2 provides an example of a logic function used.

```
def Reclass(FIA, FIB, FIIA, FIIB, FIII, FIVA, FIVB, FIVC):
  if FIIA == 0:
    return 0
  elif FIIA > 0 and FIIA < min(FIA, FIB, FIIB, FIII, FIVA, FIVB, FIVC):
    return FIIA
  elif FIIA > max(FIA, FIB, FIIB, FIII, FIVA, FIVB, FIVC):
    return FIIA - max(FIA, FIB, FIIB, FIII, FIVA, FIVB, FIVC)
  elif FIIA > max(FIA, FIB) and FIIA < min(FIIB, FIII, FIVA, FIVB, FIVC):
    return FIIA - max(FIA, FIB)
  else:
    return 999
```

Equation 4.2: Python logic function example.

At each node maximum interpreted depth was compared to total interpreted thickness to ensure accurate calculation.

Thicknesses were also calculated for draping units (FIa, FIb, FIIa, FIIb) and contourite units (FIa, FIb). Due to the difficulty of determining whether FIII is associated with turbidite or contourite sedimentation in these calculations FIII was treated as neutral. When it was encountered within a draping sequence it is considered a draping facies. However, when located directly above mass movement facies it is considered a mass movement facies.

Once thicknesses were calculated analysis was performed on the data to determine lateral and vertical variability. Facies present at seabed were mapped to inform the seabed classification. Mass movement facies were mapped at different stratigraphic levels, determined by their position in relation to contourite and hemipelagite facies. Additionally, thicknesses of contourite facies were analysed in relation to bathymetric depth and geographical location.

4.4.4. Occurrence of interpreted facies

Facies	Maximum interpreted depth (m)	Thickness (m)			Comment regarding occurrence
		Max	Mean	Mode	
Ia	13.5	13.5	3.4	3.0	Widespread throughout the north of the study area, where it is commonly the uppermost sedimentary unit. Absent on large parts of the southern Barra Fan and from steepest slopes or where debris is located at the seabed.
Ib	10.3	10.3	2.1	1.1	Interpreted infrequently and generally found in shallower waters toward the shelf break. May form part of a lensed drift type deposit.
IIa	43.9	43.6	13.1	9.6	Interpreted over a large portion of the study area, although it is not observed on steep slopes and where debris and debris flows occur at or near the surface. At times, interpreted depth is limited by acoustic penetration.
IIb	58.1	42.6	19.8	25.3	Interpreted infrequently and in shallow water where slopes are gentle: excellent data quality is required to identify the unit. The lowermost reflector visible has been interpreted as basal for interpretation purposes.
III	24.6	16.6	3.3	1.7	Most commonly encountered to the north of the study area, least common on the central Barra Fan.
IVa	57.4	46.1	11.4	5.4	Observed throughout the study area and occurs throughout the imaged sedimentary column. The facies may be found near or at the seabed, other times it is located below FI and FIIa.
IVb	37.9	25.5	5.7	6.1	Observed over a large area on the southern Barra Fan, within the upper slopes of the landslide scar and sporadically in the north of the study area.
IVc	39.5	34.2	6.2	4.5	Occurs sporadically within larger instances of FIVa.
V	66.7	NA	NA	NA	Throughout the study area, shallow occurrences most common downslope from landslide scars in the centre and south of the study area. Deeper occurrences tend to be associated with FIVa.
VI	42.9	NA	NA	NA	Widespread occurrence, except on steep slopes and in areas of landsliding. Interpretation may be prevented in some locations by reduced data quality.
VII	40.2	NA	NA	NA	Interpreted sporadically throughout the study area. Most common in sediments deformed by downslope movement and when associated with fluid release.

Table 4.8: Summary of interpreted acoustic facies results. Depths and thicknesses calculated using an assumed acoustic velocity of 1525 m s^{-1} through sediments.

An overview of occurrence of interpreted facies is presented in Table 4.8. Interpretation is influenced by quality of data, as outlined in Table 4.7. Highest quality of data allows the most detailed interpretation, with many horizons and deep penetration. Reduced data quality, for example caused by increased seastate or direction of travel (in relation to slope), leads to less detailed interpretation. Additionally, such conditions as dense, harder, sediments and steeper slopes lead to reduced signal penetration below the seabed.

Appendix D presents detailed facies plots, showing thickness and depth below seabed. The following section outlines the major findings of the interpretation.

4.4.4.1. Facies I: occurrence, thickness and characteristics

When present FI is the uppermost unit in the sedimentary column. Attempts have been made to distinguish between muddy contourites (FIa) and sandy contourites (FIb) on the basis of reflective amplitude. On this basis FIa is much more common than FIb, the latter generally found in shallower waters. However, this distinction is problematic as apparent changes in facies amplitude may be caused by instrumental factors such as signal gain and general data quality. Additionally, data resolution suffers in deeper water: a factor that may explain the different acoustic characteristics observed at different depths.

There is a clear division between the north and south of the study area, with the facies common in the north and rare in the south. Where this facies is not present at seabed the absence may be explained for a number of reasons: data quality may not allow interpretation; FIIa or FIII may be interpreted as present with no clear upper contourite unit visible (though possibly present); FV (blocky debris) or FIV (debris flows) may be present at the seabed. The absence of this facies on the south of the Barra Fan in primarily due to the absence of a clear distinction from FIIa.

Table 4.8 shows that mean thickness of FIa and FIb are 3.4 m and 2.1 m respectively. Modal thickness is less, with values of 3.0 m observed for FIa and 1.1 m for FIb.

4.4.4.2. Facies II: occurrence, thickness and characteristics

Facies IIa is interpreted over large areas within the study area. However, it is interpreted as absent on steep slopes and where debris and debris flows occur at or near the surface, such as within landslide scars in the south and centre of the study area. At times, interpreted depth is limited by acoustic penetration. Maximum observed depth is 43.9 m, though the unit is more commonly 10 - 13 m thick.

This facies is often overlain by FI, providing a total draping sediment thickness of the sum of FI and FIIa. This is described in more detail in section 4.4.5. At times FIIa appears subject to internal deformation and faulting: these observations are discussed in chapter six.

When FIIa is underlain by chaotic facies, with stratified facies observed below the chaotic, the deeper stratified units are interpreted as FIIb. Facies IIb is interpreted over relatively small areas and in shallow water where slopes are gentle, perhaps reflecting the requirement of excellent data quality to identify this unit.

4.4.4.3. Facies III: occurrence, thickness and characteristics

Facies III is most commonly encountered in the centre and north of the study area, it is least common in the south on the Barra Fan proper. Thickness is generally 3 m or less and it is observed most often within 5 m of the seabed. However, the facies is occasionally observed at depths of > 20 m below seabed and in these instances it is associated with FIV and FV.

The distinction between FIII and FIb is not always clear. It is likely that some instance of FIII are sandy contourite, however, FIb is only interpreted when a contouritic morphology is apparent (see Faugères et al. (1999)).

4.4.4.4. Facies IV: occurrence, thickness and characteristics

Facies IV is observed throughout the study area and at a variety of depths within the sedimentary column. The base of this facies is interpreted to a maximum depth of 57.4 m below seabed and a maximum thickness of 46.1 m is observed. This facies is divided into IVa (high viscosity), IVb (low viscosity) and IVc (internal structure). Of these, the most commonly observed is FIVa. Facies IVb is less widespread, although there are notable occurrences in the south of the study area and within the upper slopes of the Barra Fan. Facies IVc is observed with instances of FIVa.

As Table 4.8 shows, these sub-facies have markedly different thicknesses with means of 11.4 m, 5.7 m and 6.2 m for FIVa, FIVb and FIVc respectively. Comparison of modal and mean thickness demonstrates the distinction between FIVa and FIVb. Mean thickness of IVa is significantly greater than the mode, whereas FIVb has similar values. This reflects the occasional extremely thick, mounded, occurrences of FIVa (up to 46.1 m), which have the effect of increasing the mean relative to the mode. Facies IVb has a maximum thickness of 25.5 m (where ponded) and is rarely greater than 10 m thick, reflecting the thinner deposition due to its less viscous nature.

Maximum interpreted depths of FIV tend to occur toward the south of the study area on the slopes of the Barra Fan. Within the Peach slide scar interpreted depths are often < 20 m (see Appendix D). This may reflect harder substrate reducing signal penetration within the landslide scar.

On the fan the largest observed instances of FIVa occur below FIIa. Individual instances of this facies are interpreted across slope for distances of > 10 km and downslope for distances of 25 km. A large area of FIVb is also observed on the southern slopes of the Barra Fan, where it is exposed on the seabed at times. Debris flow morphologies are discussed in more detail in section 4.6 and chapter six.

4.4.4.5. Facies V: occurrence and characteristics

This facies is found throughout the study area, at observed depths ranging from seabed to 56.9 m below seabed. Shallow occurrences are most common downslope from the landslide scars in the south and centre of the study area (although surficial occurrences are also found on the eastern flank of the Hebrides Terrace seamount), deeper occurrences tend to be associated with FIVa.

4.4.4.6. Facies VI: occurrence and characteristics

Facies VI is observed over large regions within the study area. The main exception to this is within the landslide scar, which has relatively few instances. Elsewhere, this facies is generally found within FIIa, at times where it overlays FIV.

An attempt has been made to distinguish between diffuse fluid expulsion, FVIa, and fluid expulsion focused along faults (FVIb). Facies FVII (faults) are also commonly associated with Facies VI, though their identification is complicated by data resolution. The significance of this association is discussed in more detail in chapter six.

4.4.4.7. Facies VII: occurrence and characteristics

Facies VII, faulting, is interpreted at a number of instances within the study area. As outlined in section 4.4.2.6 identification of faults is not easy using the available available data from surface deployed sources. As such, fault displacement is not often visible in the data. However, at times seabed depression and vertically aligned high amplitude signals provide possible evidence of faulting.

Association of faults with fluid is briefly described in section 4.4.5.3 and interpreted causes are discussed in more detail in chapter six.

4.4.5. Overview of sub-surface geology results

4.4.5.1. Facies present at seabed

Legend:

- FIa - Muddy contourite
- FIb - Sandy contourite
- FIIb - Deep layer of stratified sediment
- FIIa - Hemipelagic stratified sediments
- FIII - High amplitude unit
- FIVa - High viscosity debris flow
- FIVb - Low viscosity debris flow
- FIVc - Internal structure within FIV
- FV - Blocky debris

- Acoustic survey lines
- Bathymetric contour - 100 m interval
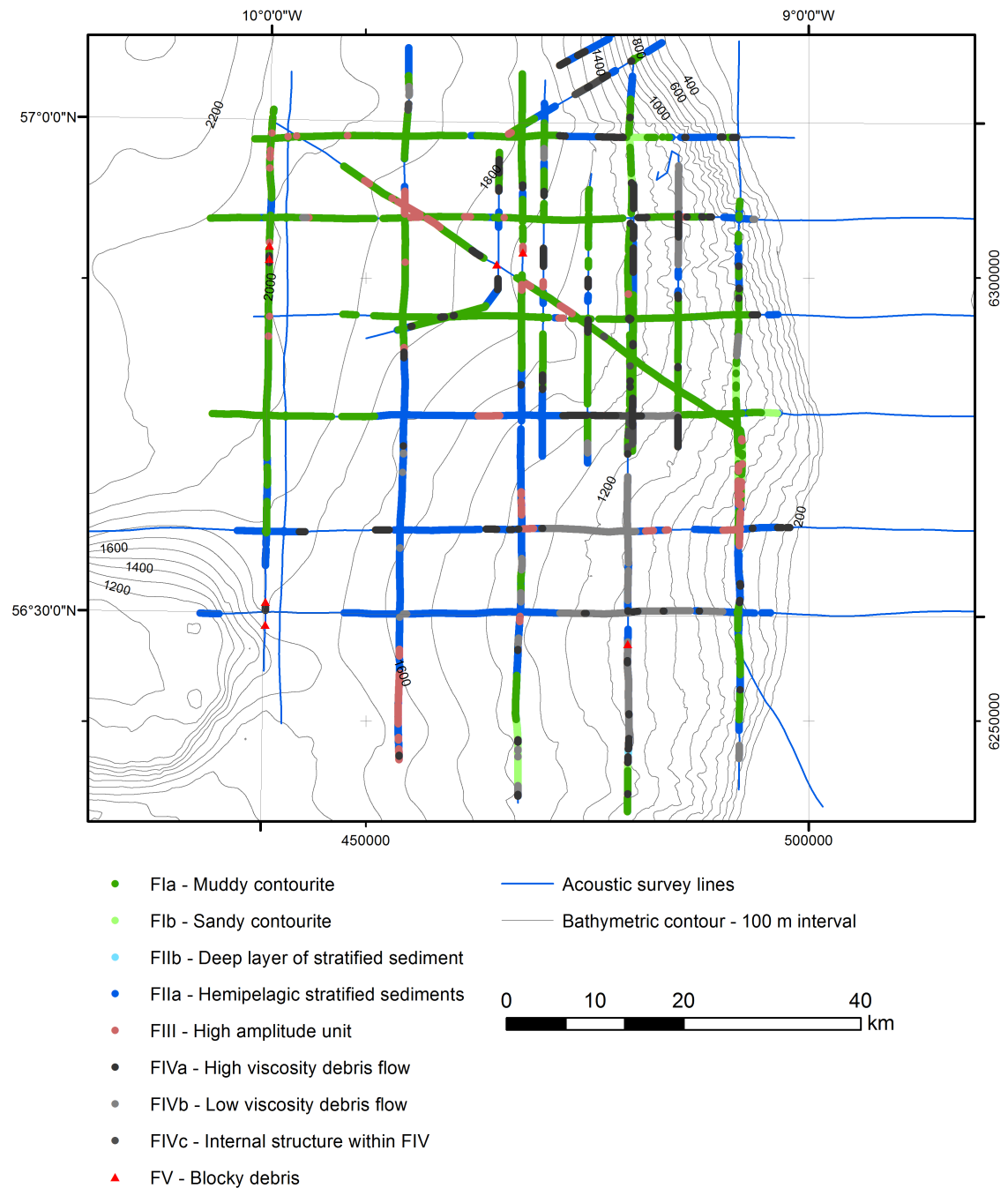
Figure 4.25: Acoustic facies present at seabed.

As Figure 4.25 demonstrates a variety of acoustic facies are interpreted as being present at the seabed from the pinger data, though FI and FIIa are most common. Facies III occurs in isolated patches, particularly on the upper slopes of the Barra Fan and in deeper water north of 56º 45' N. There are occurrences of FIV distributed throughout the study area, with FIVb most common on the slopes of the Barra Fan.

Facies V is occasionally present at the seabed, most commonly toward the western extents of the study area.

4.4.5.2. Thickness of draping sediments

By distinguishing between those facies that drape underlying units and those that do not it is possible to measure the thickness of sediment that overlies acoustic facies associated with deposition via mass movement processes. As such, Figure 4.26 presents the total thickness of sequences of draping acoustic facies (FIa, FIb, FIIa, FIIb) where they are present at the seabed.
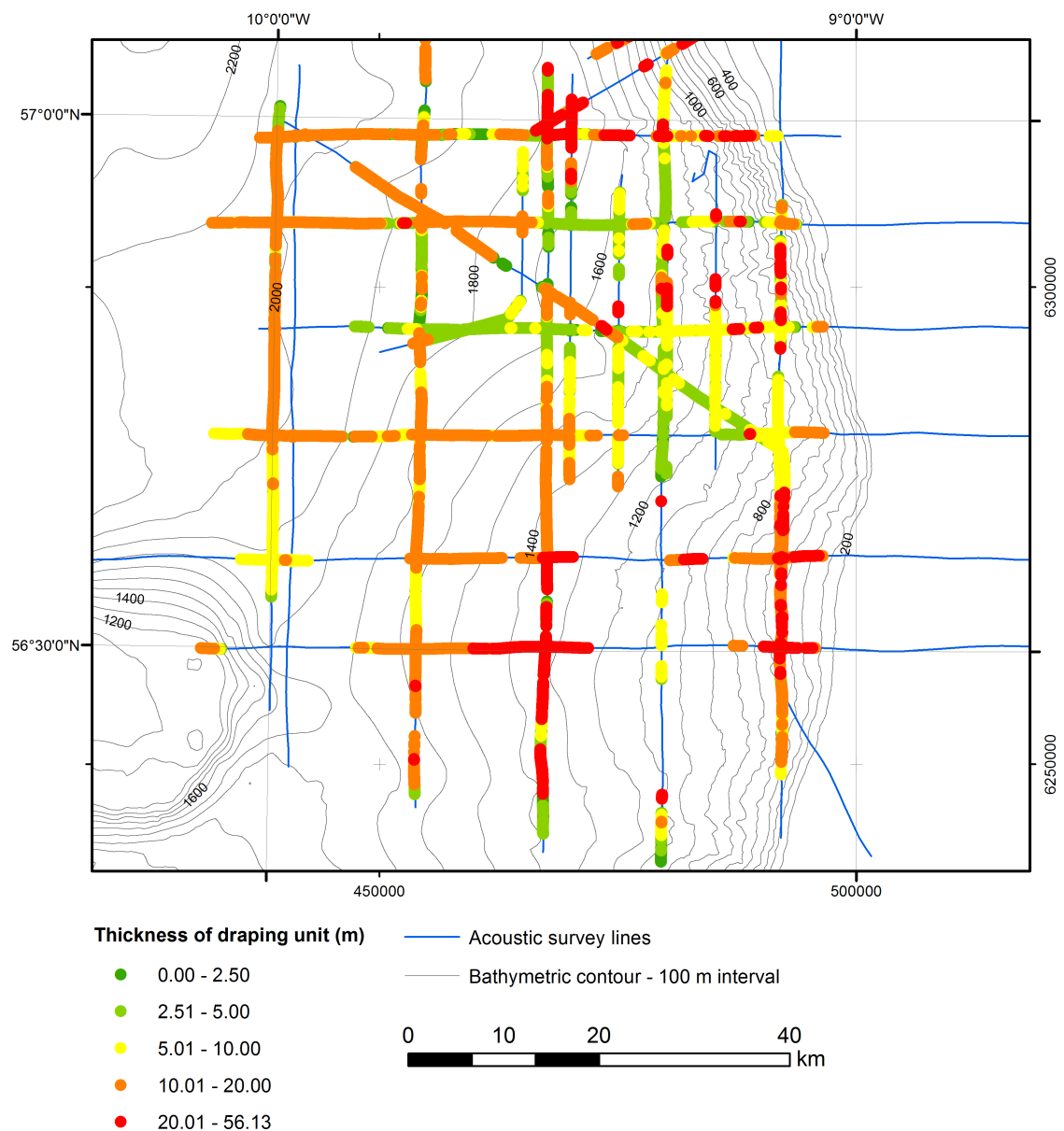
Figure 4.26: Thickness of draping sediment facies (FIa, FIb, FIIa, FIIb), where acoustic facies are interpreted.

Due to the large distances between pinger lines the data is presented as point thickness rather than as an isopach, as interpolation would remove the more detailed

variation. The plotted thickness displays only continuous draping sequence thickness. For instance, where FIV rests between FIa and FIIa the plotted value is that of FIa. As outlined in section 4.4.3.3, analysis treats FIII as neutral.

Where thicknesses are low this is either a result of an absence of interpretation below the upper unit or the presence of a mass movement associated facies below the upper unit. In the former case this is probably the result of denser sediments limiting signal penetration, potentially a result of a mass movement process not identifiable in the acoustic record. Maximum thicknesses exceed 50 m, in this cases the total thickness will exceed the pinger signal penetration.

The general pattern visible in Figure 4.26 is that of thicker sequences towards the centre of the Barra Fan and thinner sequences in the far south and central north of the study area.

4.4.5.3. Distribution of fluid and faults

Acoustic facies VI, fluid within the sedimentary column, is interpreted over a significant proportion of the study area, notably within draping sequences on the slopes of the Barra Fan. Lack of interpretation on west to east orientated lines, and some north to south lines (notably BGS 1985 6-22), is believed to be due to insufficient data quality (see Appendix C) as opposed to an absence of fluid.

As shown in Figure 4.27 fluid is largely absent from within the landslide area, with the exception of slumped hemipelagic sediments: where fluid release is observed. Fluid is often associated with faulting. In the case of slumped hemipelagic sedimentation it seems likely that downslope transport may act to fault and deform sediments, compacting them and forcing fluid from pore spaces. In the case of non-deformed sediments, as found on a large proportion of the Barra Fan alternate explanations are required. These are discussed further in chapter six.
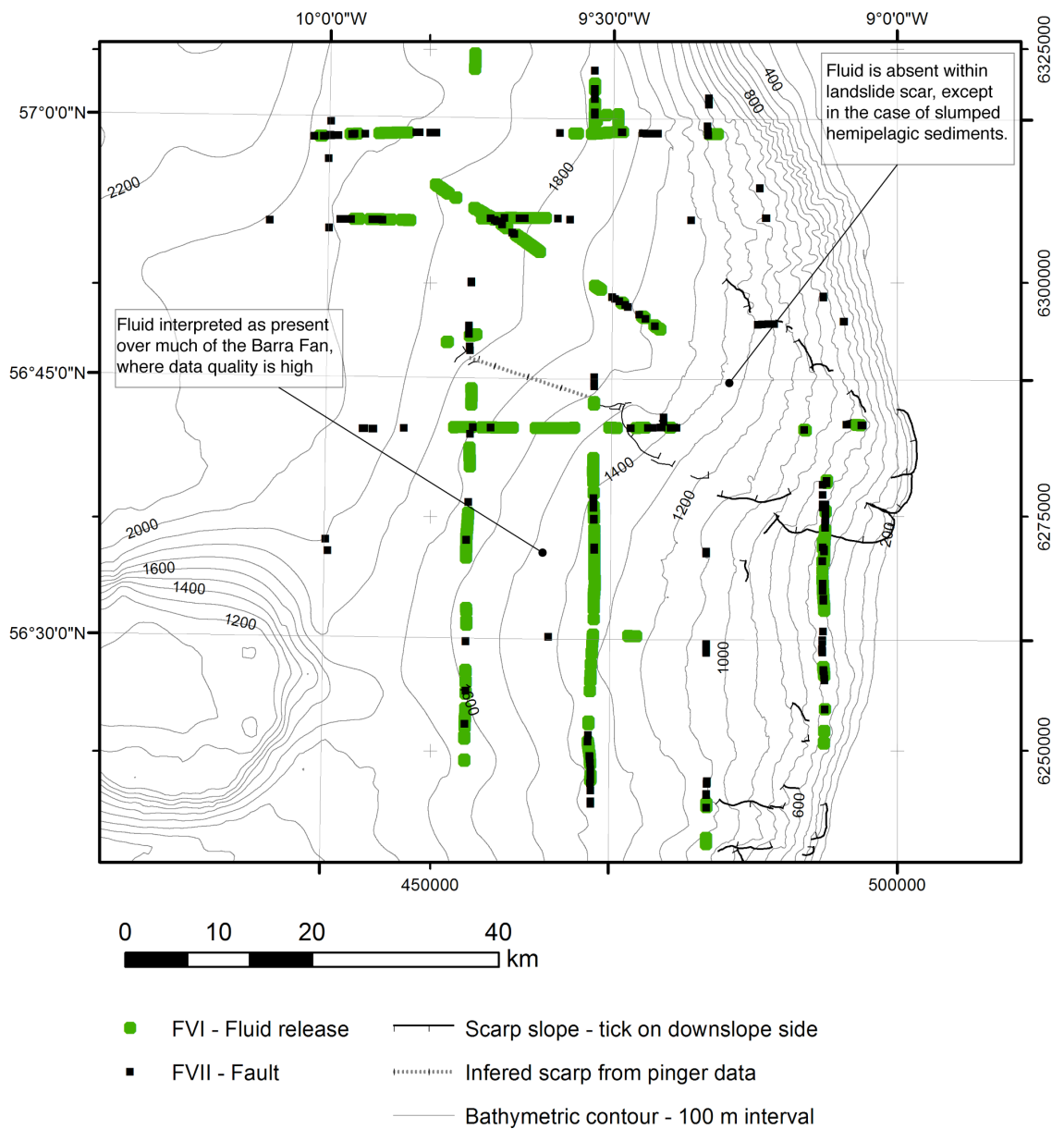
Figure 4.27: Location of fluid and faults interpreted from pinger data.

4.4.5.4. Sections across the study area

Figure 4.28 and 4.29 are interpreted sections, orientated north to south and west to east respectively, included to provide an overview of variation of acoustic facies within the sedimentary column.

Pinger line BGS 1985 6-12: Interpreted section

North

South

Fluid often observed
within hemipelagic unit

Debris and debris flow facies at or near seabed.
At times draped by a thin contourite unit

Debris and debris flow facies
located below hemipelagic unit

Depth below sea level (m)

Distance along survey line (km)

Legend:
- Seabed
- FIa - Muddy contourite
- FIb - Sandy contourite (not present on profile)
- FIIa - Hemipelagite
- FIIb - Deep layer of stratified sediments (not present on profile)
- FIII - High amplitude unit
- FIVa - High viscosity debris flow
- FIVb - Low viscosity debris flow
- FIVc - Internal structure within FIV
- FV - Blocky debris
- FVI - Fluid
- FVII - Fault

Figure 4.28: North to south orientated interpreted section from BGS pinger line 1985 6-12. Thickness of sediments based on an assumed acoustic velocity of 1525 m s⁻¹.

Shown in Figure 4.28, pinger line BGS 1985 6-12, runs north to south on 9º 45' W. In the far north of the line the sedimentary column is characterised by FIIa, with FVI. These facies rapidly give way to FIV, with FV located near the surface. Between KP (Kilometre Post: distance along survey line in km) 7 (57º 0' 40" N) and KP 20 (56º 53' 46" N) facies FIIa is present and is observed to 17 m below seabed, there are some instances of FVI. Facies V is occasionally present.

From KP 20 to KP 35 (56º 45' 46" N and indicated on the Figure) FV is present at the seabed and FIII is common. Facies IV and FIIa, which is subject to faulting (FVII) are also observed. Facies Ia is interpreted to drape the more chaotic and deformed facies to a thickness of 2 - 3 m.

Between KP 35 and KP 60 (56º 32' 2" N) the seabed shoals some 300 m. In this location FIIa is the most common seabed facies and is up to 20 m thick and commonly hosts FVI. Facies IV, with FV interpreted at the base, often underlies FIIa. Some instances of FVII are interpreted.

South of KP 60 there is a thick draping sequence apparent, which commonly achieves thicknesses of 20 m. Facies III and FVI are also interpreted within this sequence and FV and FIV are situated below the draping sequence. In the far south of BGS 1985 6-12 FIVa is located near the surface.

Figure 4.29 shows an interpreted section of pinger line BGS 1985 6-16, orientated west to east on 56º 42'N, from the Rockall Trough to the Hebrides Shelf. In the far west of the line, prior to KP 10 (9º 56' 4" W) FIIa is interpreted to depths of 10 m below seabed, overlying some instances of FV. Between KP 10 and KP 22 (9º 44' 9" W) FV and FIV are present below a draping unit consisting of FIIa. Facies VII is apparent at either end of this section. From KP 22 to KP 37 (9º 29' 25" W) a hemipelagic draping sequence of FIIa, containing FVI, of some 20 m thickness overlies FIV.

Between KP 37 and KP 55 (9º 11' 53" W) there is generally little acoustic penetration. Some FIIa is observed in the far west of this section, overlain by FIa. These instances of FIIa are subject to occurrences of FVII, otherwise the seabed facies are dominated by FV and FIV. From KP 55 to KP 65 (9º 2' 21" W) a well layered sequence, consisting of FIa, FIII, FIV and FV, up to 24 m thick is apparent. Immediately east of KP 65 an apparent slump block is observed, bordered by FVII at the base of the slope.

From KP 65 to KP 69 (8º 58' 42" W) the steep slopes of the continental slope are observed, leading to the Hebrides Shelf beyond. It was not possible to interpret acoustic facies on the slope.

Pinger line BGS 1985 6-16: Interpreted section

West

East

Depth below sea level (m)

Well layered sediment sequence downslope from apparent normal faulting and slump block

Dashed line indicates discrepancy between LOIS SES and SRTM30 datasets

Peach slide scar: debris, debris flows and faults observed at or near seabed

Distal debris deposits from Peach slide

Barra Fan: debris flows situated below hemipelagic drape.

Distance along survey line (km)

Legend:

— Seabed
— FIa - Muddy contourite
— FIb - Sandy contourite
— FIIa - Hemipelagite
— FIIb - Deep layer of stratified sediments (not present on profile)
— FIII - High amplitude unit
— FIVa - High viscosity debris flow
— FIVb - Low viscosity debris flow
— FIVc - Internal structure within FIV
• FV - Blocky debris
···· FVI - Fluid
▲ FVII - Fault

Figure 4.29: West to east orientated interpreted section from BGS pinger line 1985 6-16. Thickness of sediments based on an assumed acoustic velocity of 1525 m s⁻¹.

4.5. Overview of margin morphology

4.5.1. Surface Morphology

On the basis of seabed morphology, as interpreted from LOIS SES bathymetry, AFEN sidescan sonar and Pinger data, the study area between 57º N and 56º N may be subdivided into four categories (shown in Figure 4.30):
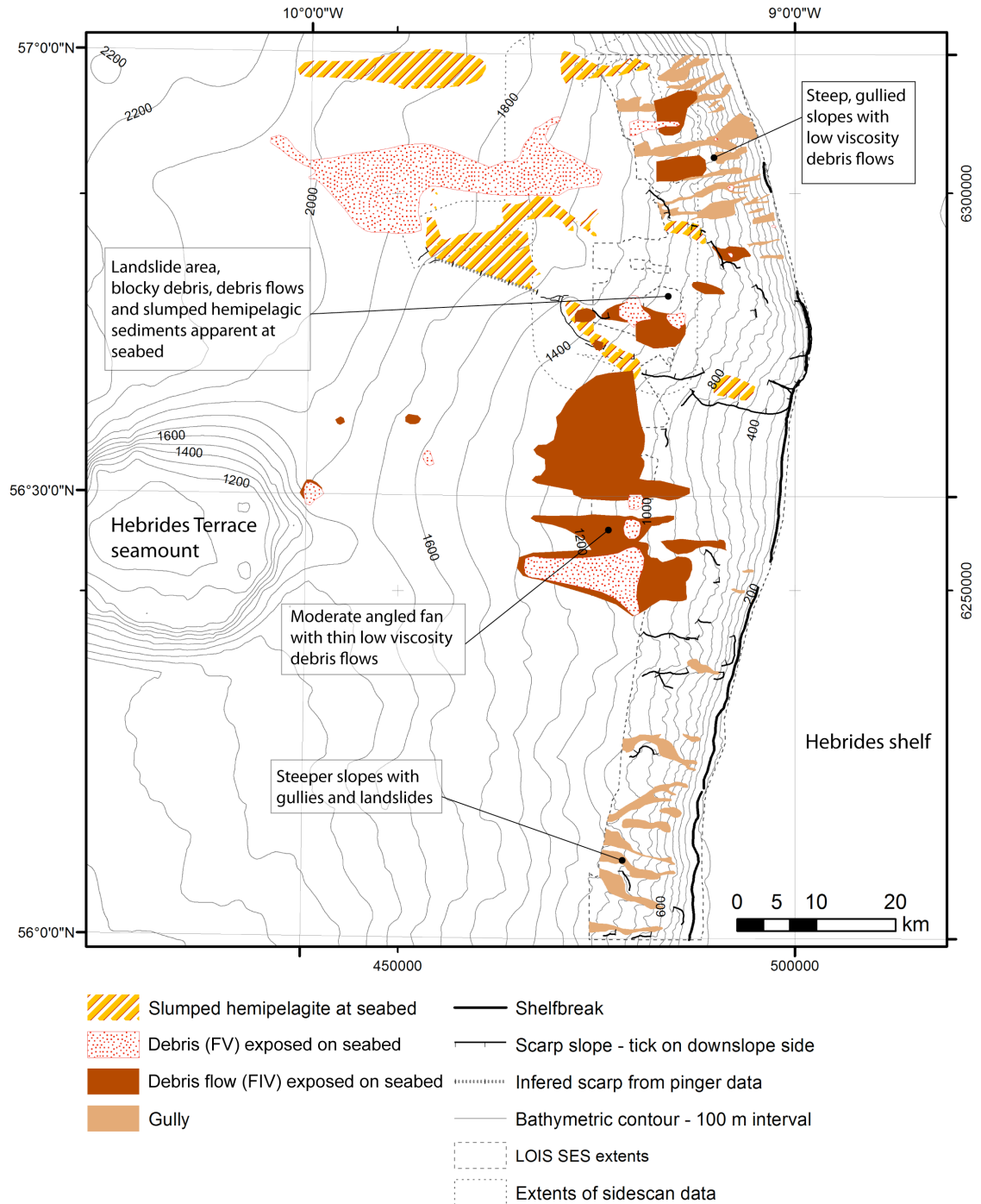
Figure 4.30: Seabed morphology interpreted from LOIS SES bathymetry, AFEN sidescan sonar and Pinger data supplied by BGS and NOC. Beyond the shelf break areas of uninterpreted seabed are expected to consist of hemipelagic or contouritic sediments.

i. A section of the continental margin dominated by steep slopes and gullies north of 56º 45' N.

ii. The large landslide, affecting an area of approximately 1300 km^2, which borders the steeply gullied area to the south and west. This area is characterised by debris and high viscosity debris flow facies, which are at times situated below a contourite unit. This slope failure is demarcated by the scarps shown in Figure 4.30 (also visible on bathymetry presented in Figure 4.10 and the interpreted section shown in Figure 4.28).

iii. To the south of this area the morphology is smooth and of gentler gradient, indicating a part of the upper and middle Barra Fan. Low viscosity debris flows are exposed on the seabed in this area.

iv. South again, to 56º N slopes steepen and are incised by a number of gullies and landslides.

In the south of the study area the LOIS bathymetry extends only 15 km past the shelf break, however, from looking at the SRTM 30 data it appears that some large canyons or surficial slope failures are present further downslope on the Donegal Fan.

4.5.2. Sub-surface morphology

4.5.2.1. Contourite (Facies I) thickness

On the basis of pinger data, widespread evidence of active bottom currents and with ground truthing from the region's core analyses (Howe, 1996; Armishaw et al., 2000; Knutz et al., 2002) this thesis has interpreted a contourite unit (Facies I) in the upper sedimentary column.
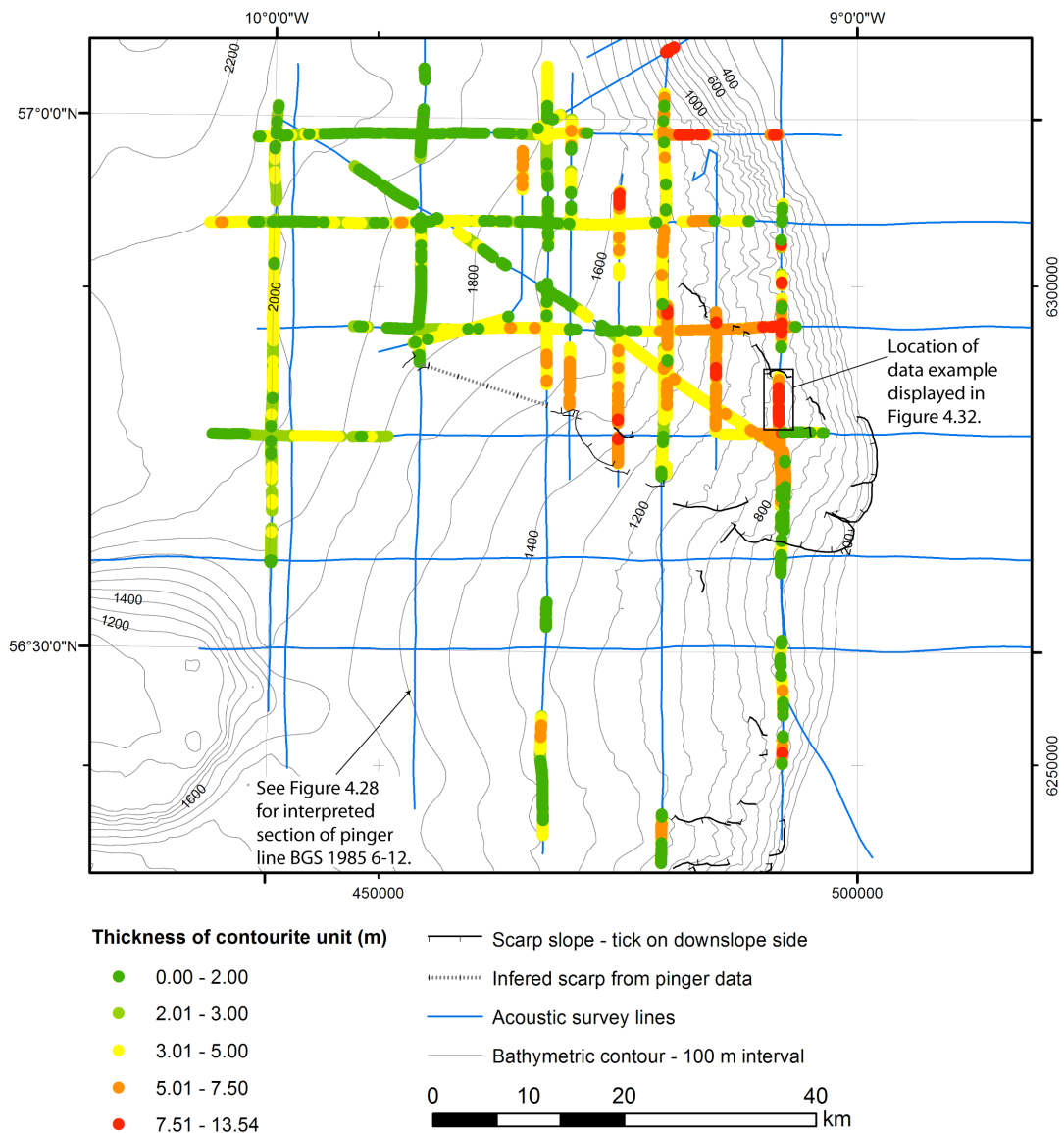
Figure 4.31: Contourite deposition in relation to surface morphology.

Figure 4.31 presents interpreted FI thicknesses in comparison to surface morphology. Facies I is largely absent from the southern slopes of the Barra Fan. As outlined in section 4.4.4.1, this is due to there being no clear distinction between this facies and FIIa. This lack of distinction signifies the absence of a sediment body, of significant thickness to appear in the acoustic record, deposited under different conditions to those that constitute FIIa.

Conversely, to the north of the Barra Fan FI is observed frequently and achieves significant thicknesses, particularly within the landslide scar. However, as demonstrated by Figure 4.31, there is variation with some areas having deposits > 10 m thick (see Figure 4.32) and other areas < 2 m thick or absent.
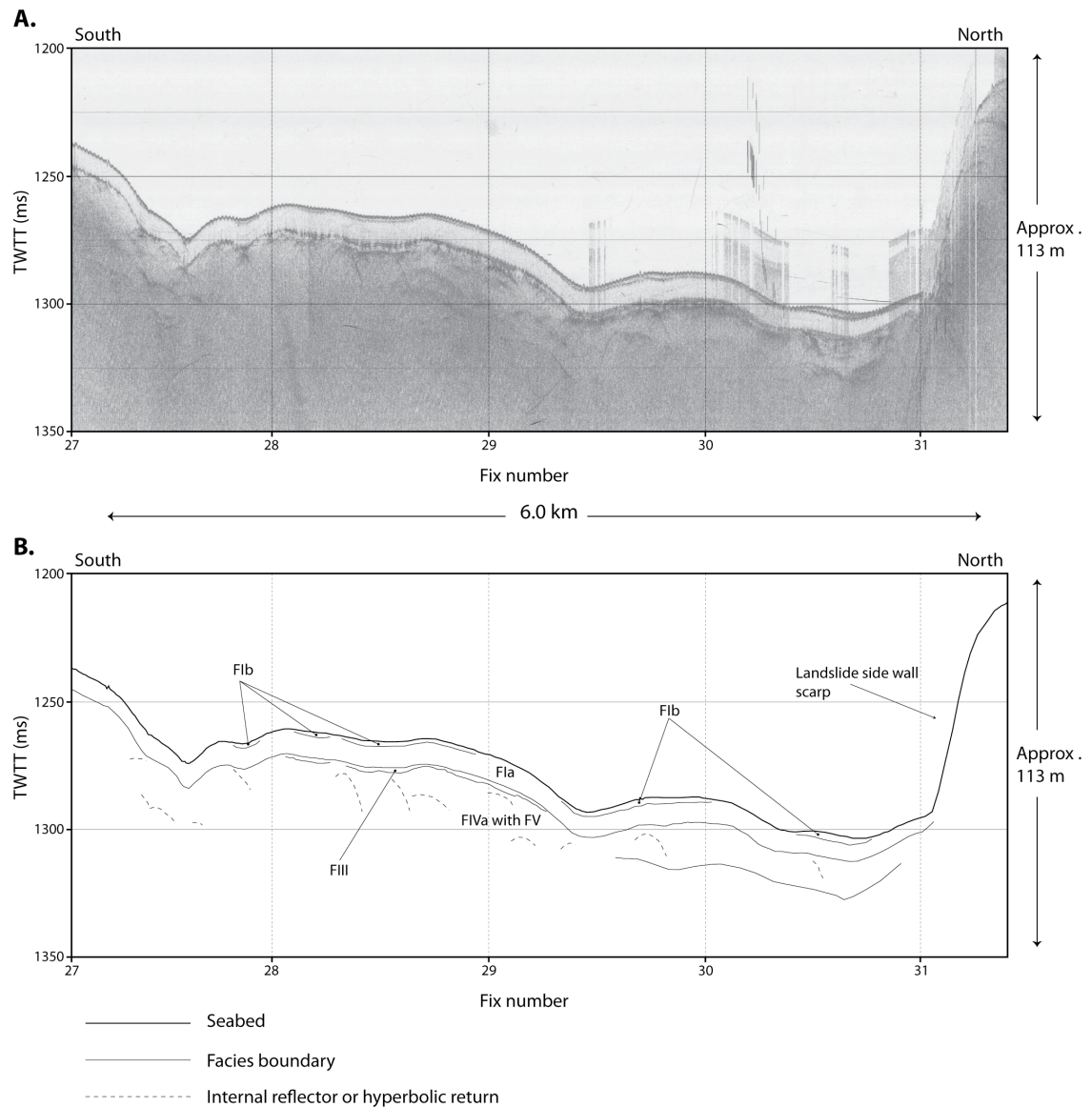
Figure 4.32: Pinger data example of contourites within the Peach slide scar. See Figure 4.31 for location.

Particularly within the landslide scar, consideration was given to whether a low viscosity cohesive or uncohesive debris flow interpretation was more appropriate (outlined in Table 4.6). However, the interpreted unit lacks characteristics associated with debris flows (see Amy et al., 2005; Iverson et al., 2010). For example, as Figure 4.32 demonstrates, ponding and pinch out or steep lateral margins are not apparent. Conversely, asymmetry of FI deposits in Figure 4.28 is similar to that described by Dorn and Werner (1993) for deposits on the Faeroe-Iceland Ridge; and the thinning of

the FI unit adjacent to the landslide scarp in Figure 4.32 bares marked similarity to erosional scour documented in the Sicily Channel by Marani et al. (1993). Additionally (shown in Figure 4.32), the interpreted FI facies, consisting of small scale drifts overlying a generally uniform drape, is strikingly different from the mounded debris flow facies (FIVa) below. This seabed morphology implies that sediments were deposited under the influence of bottom currents and as such are contourites (Stow et al., 2008).

It is recognised that sedimentation processes are often complex and that, as recognised by Armishaw et al. (2000) and Knutz et al. (2002), the Barra Fan is subject to downslope and across slope transport mechanisms. As such it is highly probable that sediments, interpreted as FI, within the slide scar originate from a number of sources and have been transported via a combination of processes. Along slope current driven sedimentation is discussed further in chapter six.

4.5.2.2. Occurrence of mass movement facies

Mass movement facies (FIVa, FIVb, FIVc and FV) are observed at varying depths within the stratigraphic column and in different geographical locations.

Figure 4.33.A displays the occurrence of mass movement facies that are exposed on the seabed. These include debris flows, blocky debris and slumped hemipelagic material. Debris flows observed at the seabed on the Barra Fan appear to pond in bathymetric depressions and often display a concave upper boundary, as such they are interpreted as low viscosity (FIVb). The debris flows located within the landslide scars in the south and central north of the study display greater relief, more hyperbolae and are interpreted as high viscosity (FIVa). A smaller area of debris and debris flows is observed on the east flank of the Hebrides Terrace seamount.

Mass movement facies underlying the surface contourite unit are shown in Figure 4.33.B. These consist of debris flows and blocky debris and are located in two main areas. First, in the centre and north of the study area, associated with the landslide area. Second, in the south of the study area, associated with and downslope from, the area of gullies and landslides.

Those debris and debris flow facies that underlie the hemipelagic unit are shown in Figure 4.33.C. These features move downslope from the upper slopes of the Barra Fan. They are absent from the upper slopes of the landslide area, but present on the lower slopes. Denser material will reduce pinger penetration and interpretation of these deeper units, from pinger data, within the landslide area will be impossible.

Mass movement facies occurrence is discussed in relation to chronology and sedimentology in chapter six

Blocky debris

🔴 Exposed on seabed
🟡 Below contourite
🟢 Below hemipelagite

Debris Flows

⬛ Exposed on seabed
🟧 Below contourite
🟩 Below hemipelagite
▨ Slumped hemipelagite at seabed
— Shelfbreak
⊣ Scarp slope - tick on downslope side
⋯ Infered scarp from pinger data
— Bathymetric contour - 100 m interval

0 10 20   40
km
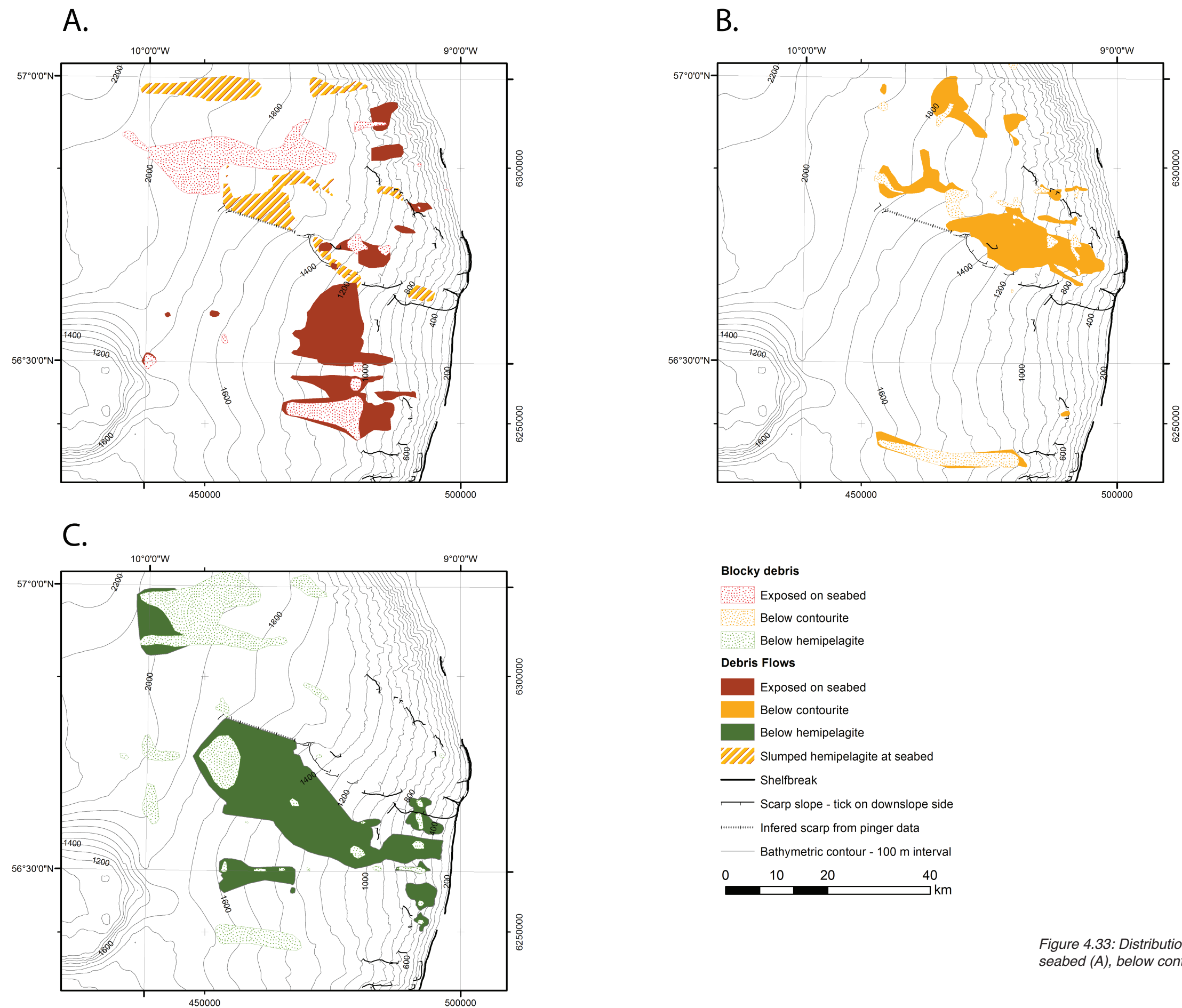
Figure 4.33: Distribution of mass movement associated facies. At seabed (A), below contourite (B) and below hemipelagite (C).

4.6. Chapter summary

This chapter has combined data spanning the paper and digital ages of marine geological exploration, and mapped the surface and shallow-subsurface geology of the British continental margin between 56º N and 57º N. Doing so in a GIS environment has allowed a much more detailed analysis of the region than has been achieved prior to this work.

A number of regions displaying distinct sedimentology have been identified. These include: an area of gullies in the north of the study area; a large landslide, containing slumped sediments at its southern margin and exposed debris in the west; the gently sloping Barra Fan, containing low viscosity cohesive debris flows on the surface and large buried debris flows; and a further area of wide, deeply cut gullies to the south of the study area.

A contourite unit is apparent in the north of the study area, as supported by ground truthing via the region's sediment cores (Howe, 1996; Kroon et al., 1997; Armishaw et al., 2000; Knutz et al., 2002). However, there is also regional heterogeneity with sedimentation patterns varying geographically and within the sedimentary column.

The presence of expelled fluid throughout the Barra Fan and its absence from the majority of the landslide area is noteworthy. Interpreted fluid is often associated with faulting: potentially signaling a role for excess pore pressure in the formation of faults and possibly slope failure.

The ideas and interpretation presented in this chapter are discussed alongside the regional context and a chronological framework in chapter six. Chapter five will focus the investigation on the region's mass movements through analysis of BGS gravity core 56/-10/239 and will attempt to improve the understanding of the chronology of slope failures in the area.

5. Sedimentology and geochemistry of 56/-10/239, a gravity core sample from the headwall area of the Peach slope failure

5.1. Introduction to chapter

5.1.1. Objectives

The key question in this chapter is: when did the Peach 4 debrite occur? As such, the primary objectives of the chapter are to select a sediment core from the Peach slope failure that contains failed material and to date this failure using AMS ^{14}C dating. When accomplished this will allow discussion of sediment failure in relation to the region's climatic and oceanographic context in chapter six.

Differentiation of down-slope and across-slope derived sediment is notoriously difficult (Stow, 1979). As such this chapter also attempts to provide information that can be used to develop methodologies to differentiate between contourite and turbidite sediments in chapter six. Some data presented in this chapter were published by Owen et al. (2010), however, that which follows is a more extensive, updated analysis and interpretation.

5.1.2. Previous sediment core studies from the region

The principal sediment core studies that have been undertaken in the Barra Fan and Peach slide region are those of Kroon et al. (1997; 2000), Armishaw et al. (2000) and Knutz et al. (2001; 2002). These studies have been concerned with the North Atlantic palaeoenvironment, via: investigations of ocean circulation and temperature; sedimentation on the Barra Fan; and British ice sheet variation.

One of the key aspects of this study, which differentiates it from previous work in the region, is that it ^{14}C dates material that overlies a mass movement deposit within a core sample. As such, this is the first study to provide a minimum age for the Peach 4 debrite.

5.2. Methods

5.2.1. Sediment core selection and sub-sampling

Logs of sediment cores acquired by the BGS were examined, alongside paper pinger records, at Murchison House, Edinburgh during September 2006. Cores were visually examined when: the log described facies indicative of mass movement (for example: slumped, sandy layer, chaotic); and/or BGS pinger records demonstrated sediments overlying failed material to be potentially less thick than the core sample length.

Table 5.1 provides details of the core samples that were inspected visually and Figure 5.1 displays the core locations with respect to the landslide scarp slope mapped in chapter four. This mapping was undertaken after core selection, which was based on more basic analysis of pinger records.

Core ID	Year collected	Latitude (D.D)	Longitude (D.D)	Water depth (m)	Core sample length (m)	Result of inspection
56/-10/35	1985	56.7792	-9.2215	1140	6.00	Quick visual inspection
56/-10/36	1985	56.7095	-9.3275	1290	5.46	Core already sampled down entire length
56/-10/37	1985	56.7877	-9.3733	1406	4.30	Quick visual inspection
56/-10/38	1985	56.9143	-9.3378	1452	1.63	Quick visual inspection
56/-10/40	1985	56.9902	-9.5443	1662	2.40	Quick visual inspection
56/-10/41	1985	56.9100	-9.5183	1663	2.15	Quick visual inspection
56/-10/42	1985	56.8007	-9.5028	1590	2.20	Core already sampled
56/-10/43	1985	56.7047	-9.5342	1514	1.94	Logged but not sampled
56/-10/51	1985	56.7018	-9.6742	1652	2.01	Quick visual inspection
56/-10/52	1985	56.8008	-9.7543	1850	2.00	Logged but not sampled
56/-10/162	1992	56.9997	-9.7492	1961	2.58	Quick visual inspection
56/-10/163	1992	56.8525	-9.9687	2003	2.54	Samples unavailable - taken by the Defense Research Agency (DRA).
56/-10/164	1992	56.8503	-9.7352	1850	3.61	
56/-10/175	1995	56.6265	-9.0282	331	2.13	Sample fell out of core barrel - logged by virtue that it was a duplicate of a core that was taken by the DRA. Unfortunate as BGS log contains reference to slumped material
56/-10/219	1996	56.6662	-9.1663	932	2.45	Logged but not sampled
56/-10/236	1996	56.7842	-9.0832	680	2.63	Logged but not sampled
56/-10/239	1996	56.7822	-9.1698	1030	2.50	Selected for sub-sampling due to suspected slumped material in lowermost 0.5 m

Table 5.1: Sediment cores inspected visually during September 2006.

Visual inspection determined that gravity core 56/-10/239 was most likely to achieve the study objectives, as it appeared to contain slumped material towards the core base. As Table 5.1 shows this core was acquired at 56.7822 N 9.1698 W in 1030 m water during 1996. The core was then sub-sampled.

Initial sub-sampling was performed at 2 cm intervals for the uppermost 2 m, with continuous 2 cm samples between 0.92 m - 0.98 m, 1.92 m - 1.98 m and 2.07 m - 2.13 m. Intervals of 2 cm were selected due to fears of low carbonate content (as noted by previous work, see Knutz et al. (2007)). Further sub-samples at 1 cm intervals, were

obtained during April 2008 for the lower most 0.5 m. Sub-samples were subsequently split for different analytical processes.
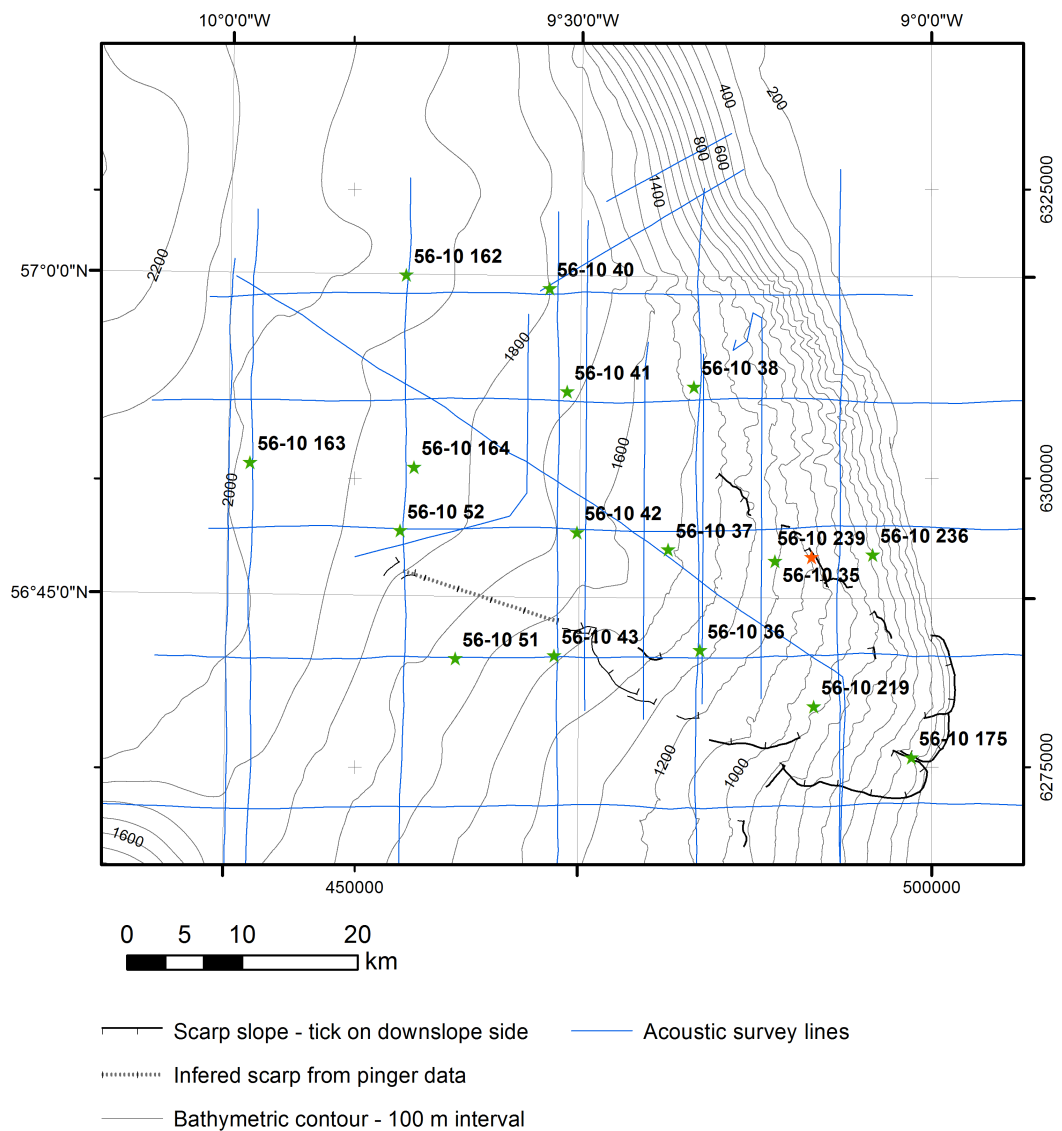
Figure 5.1: Locations of BGS sediment cores that were visually inspected prior to selection of BGS 56/-10/239 (red star) for sub-sampling. Landslide scarp slope from geophysical investigation in chapter four shown for reference.

5.2.2. Sediment analysis

Prior to analysis sub-samples were freeze-dried and ~4 g of dried sediment was retained for XRF analysis.

5.2.2.1. Particle size analysis

Particle size analysis was performed without prior removal of carbonate content by acid leaching. This is consistent with the methodology of Howe (1996) and Armishaw (1999). Sediments are anticipated to be carbonate poor and there is potential for

detrital limestone from Donegal within analysed sediments (Evans et al., 1983), which acid leaching would remove from the analysis.

Freeze-dried sub-samples were weighed and then wet-sieved, using deionised water, through apertures of 1000, 500, 250, 125 and 63 μm before analysis of <63 μm diameter fraction by SediGraph 5120. Sediments from the wet sieved >250 μm fraction were subsequently dry sieved up to the maximum particle diameter.

Fractions >63 μm were dried over the course of several days in a drying cupboard at ~ 40 ºC. Once fully dry samples were weighed and masses recorded. Mass of fractions were weighed and mass <63 μm fraction was calculated by subtracting the >63 μm fraction from total sub-sample dry weight.

Grain size			Size classification (as output from GRADISTAT - see Blott and Pye (2001))	Analytical technique used
Logarithmic (Phi)	Geometric size range	Geometric unit		
-3	16 - 8	mm	Medium gravel	Dry sieve
-2	8 - 4		Fine gravel	
-1	4 - 2		Very fine gravel	
0	2 - 1		Very coarse sand	
1	1 - 0.5		Coarse sand	Dry sieve after wet sieve
2	500 - 250	μm	Medium sand	
3	250 - 125		Fine sand	Wet sieve
4	125 - 63		Very fine sand	
5	63 - 32		Very coarse silt	Sedigraph
6	32 - 16		Coarse silt	
7	16 - 8		Medium silt	
8	8 - 4		Fine silt	
9	4 - 2		Very fine silt	
10	2 - 1		Clay	

Table 5.2: Particle size classification and analytical method.

Sub 63 μm fractions were covered and allowed to settle for four days, after which time excess water was pipetted away. Remaining sediment solution was split to 1 g - 2 g fractions in order to create a solution concentration of <3 % for SediGraph analysis (Coakley and Syvitski, 1991).

The SediGraph calculates particle size, based on the sedimentation principle and Stokes' Law. The law states that the terminal settling velocity of spherical particles is proportional to the square of the particle diameter: which means that coarse particles

settle more quickly than fine (Goossens, 2008). A collimated beam of X-ray is projected into an internal reservoir filled with sediment sample in liquid suspension (Webb, 2004). By monitoring, through X-ray attenuation, the rate at which particles settle and are removed from the monitored volume, an accurate measure of the cumulative sediment size distribution can be obtained (Jones et al., 1988; Coakley and Syvitski, 1991). As the method is based on Stokes' Law, the particle size obtained is the Equivalent Spherical Sedimentation Diameter (ESSD), also known as the Stokesian Diameter (Coakley and Syvitski, 1991).

Sedigraph samples were prepared and analysed during September and October 2008. Particle density was assumed to be that of silica, at 2.32 g cm^{-3}. A total of 358 analyses were performed, with up to eight repeats of each sub-sample. No sub-sample was analysed less than three times.

The GRADISTAT program (Blott and Pye, 2001) was used to calculate mean grain size, sorting, skewness and kurtosis.

5.2.2.2. Bulk sediment XRF geochemistry

The basis of XRF analysis is that secondary x-rays emitted by a sample, when stimulated by irradiation with appropriate primary photons, are characteristic of the source element (Boyle, 2000).

The sediment was finely ground using a pestle and mortar, placed in the appropriate containers (plastic with a tightly stretched polypropylene film base) and weighed. Analysis was performed under Helium gas flush on the UCL Geography department Spectro x-lab 2000 XRF analyser between late 2007 and May 2008, a minimum of two control samples were analysed in each batch (For further details of XRF analysis under Helium gas flush see Wien et al. (2007)). Standard deviation of repeat samples was low and full information is presented in Appendix E.

Major element proportions are expressed as percentages and trace element proportions are expressed as μg g^{-1}. Concentrations were calculated for the following elements: Na, Mg, Al, Si, P, S, Cl, K, Ca, Ti, V, Cr, Mn, Co, Ni, Cu, Zn, Ga, Ge, As, Se, Br, Rb, Sr, Y, Zr, Nb, Mo, Ag, Cd, In, Sn, Sb, Te, I, Cs, Ba, La, Ce, Hf, Ta, W, Hg, Tl, Pb, Bi, Th and U.

5.2.2.3. Total organic carbon

Total organic carbon (TOC) analysis was performed on sediment samples previously used for XRF analysis.

Approximately 2 g of dried sediment was weighed and soaked in 50 ml 5% hydrochloric acid (HCL) overnight in order to remove inorganic carbon ($CaCO_3$). As it is necessary to return the residue to a neutral pH, sediment and HCL residue is decanted into centrifuge containers with deionised water and centrifuged at 2000 rpm for eight minutes. The supernatant is removed and the contents agitated. This process was repeated at least four times. Finally the pH is tested using litmus paper: a level between 5 and 7 is regarded as acceptable. Excess supernatant was removed and the tubes placed in a drying cupboard until dry.

Total organic carbon analysis was performed on the inorganic carbon free residue sample using the UCL Wolfson LECO C/S analyser on the 16th of October and the 18th of November 2009. Approximately 0.25 g of sample is placed in a crucible and covered with a small quantity of accelerant (iron filings). The sample is then combusted via exposure to microwaves (see dry combustion technique outlined by Schumacher (2002)) and the percentage of carbon and sulphur calculated. Every twentieth sample a standard is analysed in order to determine instrument drift.

Percentage TOC is calculated for the entire sediment core sub-sample by multiplying the percentage of carbon as recorded by the LECO C/S analyser by the proportion of the inorganic carbon free residue of the whole sub-sample expressed as percent. For example when HCL soaking removes 28% of initial sample mass, leaving a residue representing 72% of the original sample and LECO C/S analyser calculates carbon content at 50% this represents TOC content of 36% (0.5 [LECO carbon] × 0.72 [residue percentage of original sample] = 0.36).

5.2.3. Stable isotope geochemistry

5.2.3.1. Fundamentals of foraminiferal $\delta^{18}O$ and $\delta^{13}C$ in palaeoceanographic studies

Foramininfera are single celled marine organisms that secrete $CaCO_3$ shells (tests), both planktonic and benthic species may be used to analyse the isotopic composition of oxygen and carbon.

Oxygen has three naturally occurring isotopes: ^{16}O, ^{17}O and ^{18}O. ^{16}O is the most abundant, representing 99.76% of the total, ^{18}O 0.20% and the least abundant ^{17}O contributing the remainder (Rohling and Cooke, 1999). Fractionation of oxygen during the hydrological cycle, on the principle that ^{16}O evaporates more readily and that ^{18}O precipitates more readily, means that the ratio of ^{18}O to ^{16}O ($\delta^{18}O$) is an extremely useful proxy in environmental and climate reconstruction.

The fractionation of oxygen, during the secretion of $CaCO_3$ from aqueous solution, is temperature dependent (Urey, 1947). This concept led to the calculation of palaeo-

temperatures from the $\delta^{18}O$ of carbonate (Urey et al., 1951) and foraminifera (Emiliani, 1955). However, from analysing benthic foraminifera Shackleton (1967) demonstrated that foraminiferal $\delta^{18}O$ was largely determined by the global ice-volume. Further work revealed the roles played by salinity (Duplessy et al., 1991) and carbonate ion concentration (Spero et al., 1997).

Hence, the $\delta^{18}O$ of seawater is a function of global ice volume, temperature and salinity (Emiliani, 1955; Shackleton, 1967; Shackleton, 1987; Duplessy et al., 1991). Organisms which secrete carbonate shells, such as foraminifera, may be used to reconstruct seawater $\delta^{18}O$, as the $\delta^{18}O$ of carbonate shells is a function of seawater $\delta^{18}O$, temperature and salinity (Shackleton, 1967; Duplessy et al., 1993) as well as species specific vital effects and carbonate ion concentration (Spero and Lea, 1996; Spero et al., 1997).

This ratio is expressed as deviation from a standard in per mille (‰), in the case of carbonates, VPDB (Vienna-belemnite shell). Equation 5.1 shows the standard calculation.

Carbon also has three naturally occurring isotopes: ^{12}C, ^{13}C and ^{14}C. Of these ^{12}C contributes approximately 98.9% of the total carbon compared to ^{13}C, which contributes about 1.1% (Rohling and Cooke, 1999). Both these isotopes are stable, whereas ^{14}C is radioactive and constitutes a negligible proportion of the global carbon reservoir.

The ratio of ^{13}C to ^{12}C ($\delta^{13}C$) is determined by the the carbon cycle and fractionation of carbon, primarily during photosynthesis (Jasper et al., 1994; Hayes et al., 1999). During photosynthesis planktonic foraminifera use $^{12}CO_2$ preferentially over $^{13}CO_2$, this depletes surface water ^{12}C and is reflected in planktonic foraminiferal tests that record surface water $\delta^{13}C$ (Curry et al., 1988) with effects from respired CO_2 and symbionts (Spero et al., 1991).

$$\delta^{18}O \text{ or } \delta^{13}C = 1000 \times \frac{\text{Isotopic ratio sample - Isotopic ratio standard}}{\text{Isotopic ratio standard}}$$

Equation 5.1: Calculating $\delta^{18}O$ and $\delta^{13}C$ V-PDB

When the planktonic foraminifera die and sink beyond the thermocline the organic carbon is remineralised, resulting in reduced deep water $\delta^{13}C$ that is recorded by the $\delta^{13}C$ of benthic foraminiferal tests, with effects from microhabitat and early diagenesis of organic matter (Loubere et al., 1995; Gehlen et al., 1999). The interaction of organic

and inorganic carbon, and planktonic and benthic dwelling species means that foraminiferal $\delta^{13}C$ may be used for a variety of studies, including: surface water $\sum CO_2$ (Spero, 1992), ocean productivity (Bertrand et al., 1996), deep water circulation (Oppo et al., 1995; Matsumoto and Lynch-Stieglitz, 1999) and estimates of gas hydrate release (Norris and Röhl, 1999; Dunkley Jones et al., 2010; Panieri et al., 2012).

Isotopic signal preservation is an important consideration as the $\delta^{18}O$ and $\delta^{13}C$ values of foraminiferal tests may be altered post-deposition via dissolution and diagenesis (Marshall, 1992; Mitchell et al., 1997). Of these factors, the carbonate compensation depth (CCD), below which carbonate dissolution exceeds carbonate supply, is amongst the most noteworthy. Controlled by hydrostatic pressure, temperature and carbonate ion concentration (Farrell and Prell, 1989; Archer, 1996) it is of huge importance to $CaCO_3$ preservation in the deep ocean. Contemporary North Atlantic CCD is calculated to be >4000 m (Archer, 1996).

Stable isotope analysis is performed on $CaCO_3$ tests from planktonic foraminiferal species *Globigerina bulloides* and *Neogloboquadrina pachyderma (sinistral)*.

5.2.3.2. Characteristics of Globigerina bulloides

Globigerina bulloides is a surface dwelling sub-polar to temperate foraminifera and calcifies in the uppermost 60 m of the water column *(Schiebel et al., 1997)*. It has been demonstrated that this species exhibits a progressive increase in $\delta^{18}O$ of up to 0.8‰ with test development, which may be due migration within the water column and the recommended size fraction is 270 to 320 µm *(Spero and Lea, 1996)*. *G. bulloides* $\delta^{18}O$ has been shown to decrease with increasing CO_3^{2-} *(Spero et al., 1997)*. Equation 5.2 shows equilibrium calibrations for *G. bulloides* from Spero and Lea *(1996)*, where x is the mean test size for chamber number.

$$\delta^{18}O_{equilibrium} = 1.21 - 0.0016x$$

$$\delta^{13}C_{\sum CO_2} = 0.000012x^2 - 0.011x + 3.97$$

Equation 5.2: Cold condition $\delta^{18}O$ and $\delta^{13}C$ equilibrium calibrations for Globigerina bulloides (Spero and Lea, 1996)

5.2.3.3. Characteristics of Neogloboquadrina pachyderma (sinistral)

Neogloboquadrina pachyderma (sinistral) is a sub-surface foraminifera that is common in polar and sub-polar water masses *(Kohfeld et al., 1996)*. Calcification depths have

been observed in the upper 200 m of the water column *(Kohfeld et al., 1996; Bauch et al., 1997)*. *N. pachyderma (s.)* $\delta^{13}C$ displays an offset of -1‰ in comparison to equilibrium calcite and displays $\delta^{18}O$ values consistent with water column values found between 80 m and 120 m *(Kohfeld et al., 1996)*. Peck et al. *(2008)* use a mean calcification depth of 150 m.

5.2.3.4. Planktonic foraminiferal $\delta^{18}O$ and $\delta^{13}C$ methodology

Foraminifera were picked between March 2008 and February 2009. Individuals were picked from the 250 μm to 500 μm fraction, however, when scarce *N. pachyderma (s.)* was also picked from the 250 μm to 125 μm fraction. Attempts were made to pick 30 individuals of each species per sample in order to achieve a $CaCO_3$ sample mass of 400 μg.

Foraminiferal $CaCO_3$ samples were analysed for $\delta^{18}O$ and $\delta^{13}C$ using the UCL BEIF gas bench facility between the 16th and 17th of February 2009.

5.2.4. Foraminiferal AMS ^{14}C dating

5.2.4.1. Overview of marine ^{14}C dating

As outlined in section 5.2.3.1, of the three naturally occurring isotopes of carbon, ^{14}C is radioactive. Once an organism dies it ceases to acquire any new carbon, therefore, if the ratio of carbon isotopes in nature is assumed to be constant and if the half-life of ^{14}C is known it is possible to calculate the age of a sample by the isotopic ratio.

Conventional ^{14}C dating methods measure the amount of β^- emissions from a particle, however, AMS ^{14}C has allowed the accurate ^{14}C dates from much smaller samples as individual ^{14}C particles are counted (Stafford et al., 1991). Radiocarbon decays with a half-life of 5730 ± 40 (Godwin, 1962) years. However, due to older ^{14}C dates being calculated from a previously calculated value of 5568 years (Libby, 1955) this is the agreed constant for radiocarbon dating (Mook, 1986).

Radiocarbon is produced by reaction between ^{14}N and cosmic ray neutrons in the atmosphere (Lingenfelter, 1963), the rate of production is not constant. For instance ^{14}C production has been correlated with sunspot activity (Stuiver, 1961) and the ratio of ^{14}C to ^{12}C has declined due to variation in the carbon cycle, for example via a degassing of ^{14}C depleted CO_2 during the last glacial transition (Edwards et al., 1993; Kitagawa and van der Plicht, 1998; Beck et al., 2001). Therefore, to allow comparison with other chronologies ^{14}C ages need to be calibrated. Such calibrations are performed using tree rings, varved sediments, speleothems and corals (Stuiver et al., 1998; Hughen et al., 2000; Hughen et al., 2004; Fairbanks et al., 2005).

As ^{14}C is produced in the atmosphere, marine ^{14}C dates are subject to a reservoir effect, where samples are depleted relative to the contemporaneous atmosphere (Ascough et al., 2007). This effect varies geographically and temporally and is most pronounced in the deep ocean, where low levels of water mixing mean that ^{14}C decays without replenishment. Present day North Atlantic surface water is calculated to have a reservoir effect of 400 years, whereas polar waters exhibit a reservoir effect of 800 - 1200 years (Bard et al., 1994; Austin et al., 1995; Ascough et al., 2005). Reflecting this regional variation, movement of the polar front is anticipated to influence the North Atlantic reservoir effect during glacial to interglacial transitions (Bard, 1988).

From reference to the Vedde ash layer (the age of which is constrained via terrestrial AMS ^{14}C dating), Austin et al. (1995) demonstrate a shift in reservoir age of British North Atlantic waters from the present day value of 400 years, to 700 years during the Younger Dryas. Previous studies investigating shallow sediments on the Barra Fan have used reservoir corrections of 400 years (Kroon et al., 2000; Knutz et al., 2001).

5.2.4.2. Planktonic foraminiferal AMS ^{14}C dating methodology

Funding was awarded for five foraminiferal $CaCO_3$ AMS ^{14}C dates under NERC allocation number 1441.1009, as outlined in Table 5.3. Insufficient $CaCO_3$ content meant that the samples below 2 m depth could not be submitted.

Sample number	Sample depth (cm)	Foraminiferal species	Comment
SUERC-28178	16 - 18	*N. pachyderma (s.)*	Analysed April 2010
SUERC-28179	156 - 158	*G. bulloides*	Analysed April 2010
SUERC-28180	196 - 198	*N. pachyderma (s.)*	Analysed April 2010
	207 - 213	*N. pachyderma (s.)*	Unable to submit sample due to insufficient $CaCO_3$ content
	240 - 250	*N. pachyderma (s.)*	
SUERC-30290	194 - 198	*N. pachyderma (s.)*	Analysed July 2010, after query regarding validity of SUERC-28180

Table 5.3: Overview of foraminiferal $CaCO_3$ AMS ^{14}C dates awarded under NERC allocation number 1441.1009

The three submitted samples were analysed at the NERC radiocarbon facility at East Kilbride during April 2010. Following a query by NERC staff that sample SUERC-28180 contained 4 mg C as opposed to the recommended 5 mg C a new sample was submitted and analysed during July 2010.

5.3. Results

Appendix E presents a selection of data in tabular form, all XRF data is included in digital form on the accompanying DVD.

5.3.1. Visual log
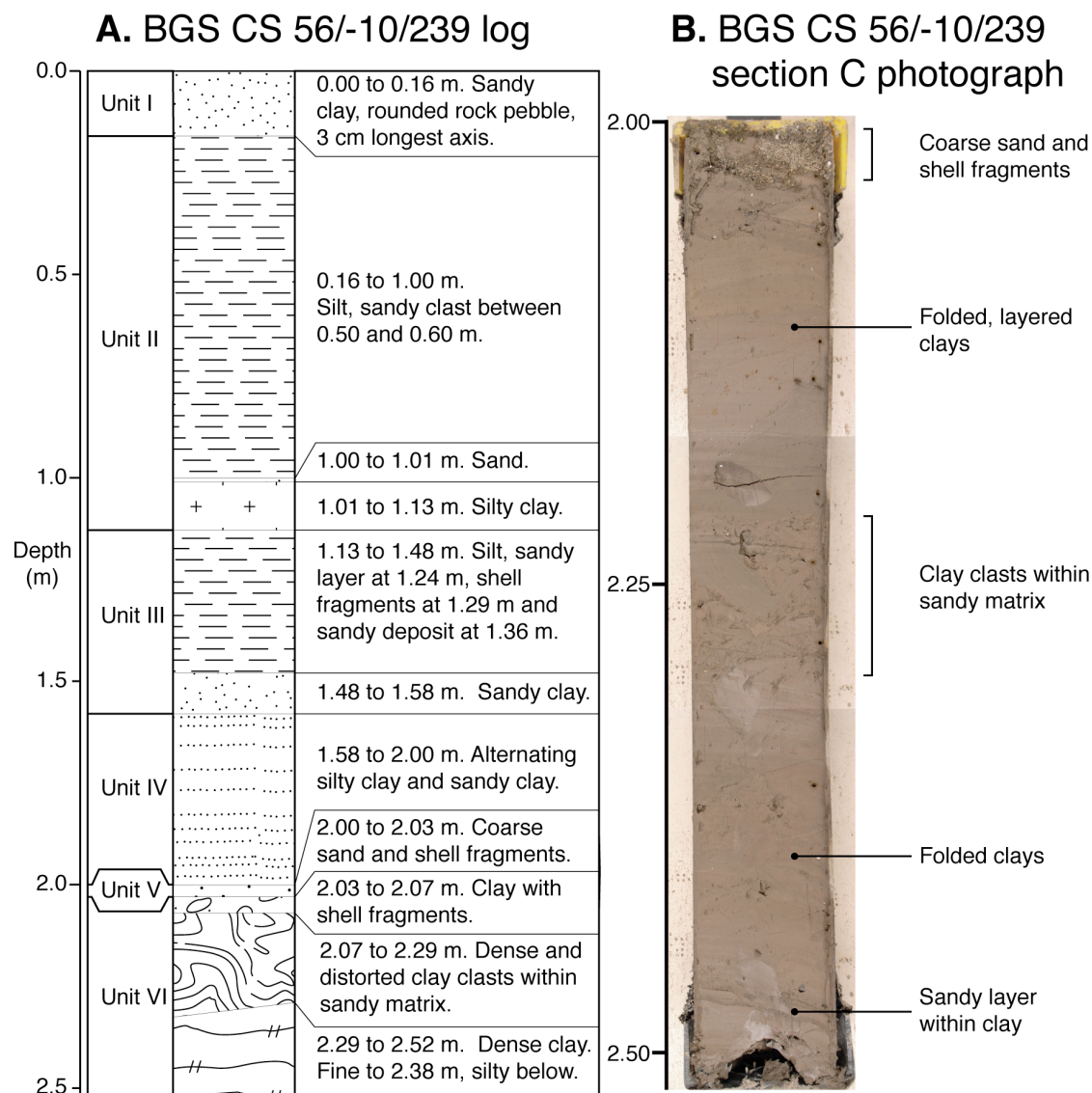
Figure 5.2: A. Visual log of CS 56/-10/239, made prior to sampling. B. Photograph core section C3 (2.0 - 2.5 m) demonstrating deformed clays and sandy matrix.

The core log displayed in Figure 5.2.A is similar to the log presented by Armishaw (1999) and the shipboard log. Figure 5.2.B presents a photo-mosaic of core section C, 2.00 m - 2.52 m, which was taken prior to sampling of this core section during April 2008. Photographs were taken of core sections A and B (uppermost 2.00 m) prior to sampling in September 2006, however, the image quality is not sufficient to aid interpretation.

Sediments from base of core, at 2.52 m, to 2.03 m consist of dense clay clasts, often deformed, within a sandy matrix (see Figure 5.2.B). Nearing the top of this section shell fragments are common. Between 2.03 m and 2.00 m a layer of coarse and shell fragments erodes into the underlying clays.

From 2.00 m to 1.58 m layers of silty clay and sandy clay alternate, they are capped by a 10 cm thick sandy clay unit between 1.58 m and 1.48 m. A succession of sandy layers, shell fragments and silt is observed between 1.48 m and 1.13 m. Above these there is a layer of silty clay from 1.13 m to 1.01 m. After a 1 cm thick layer of fine sand silty sediments are observed to 0.16 m, with a sandy clast between 0.50 m and 0.60 m. Above 0.16 m sandy clay is observed with a pebble.

5.3.2. Sediment analysis

5.3.2.1. Particle size analysis

Table E.1 presents percentage geometric particle size data for CS 56/-10/239. Figure 5.3 displays sand, silt and clay percentages for the core sample.
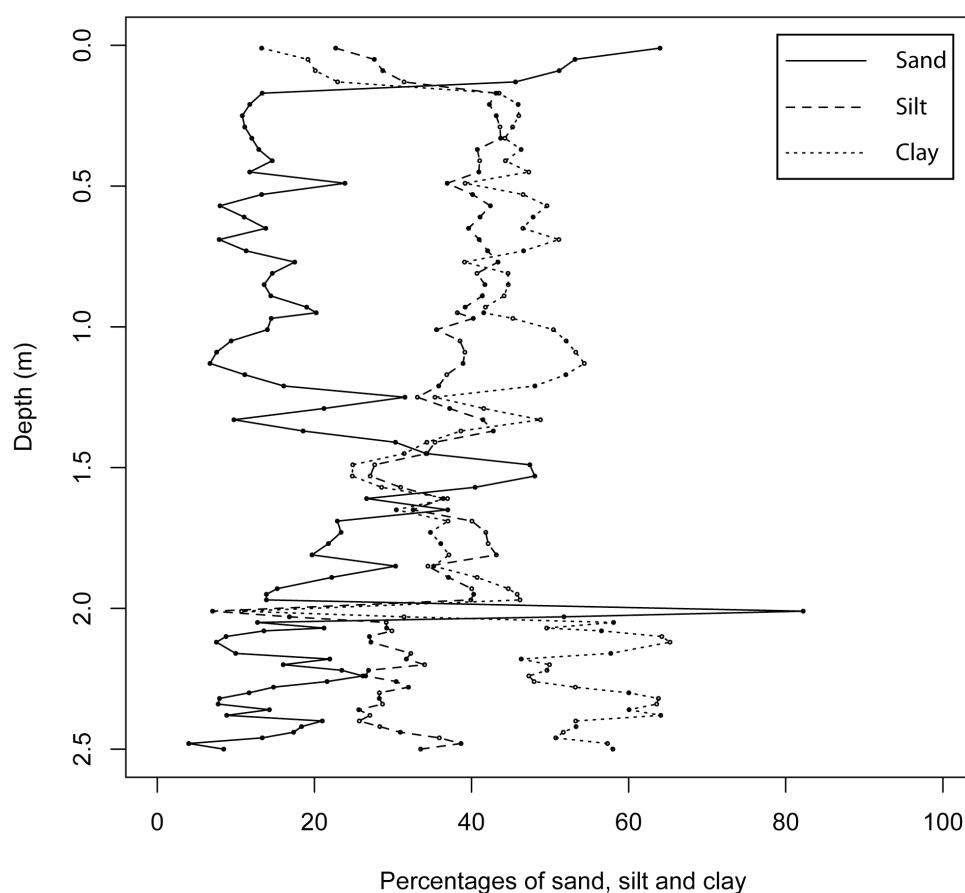
Figure 5.3: Percentages of sand, silt and clay with 56/-10/239.

On the basis of sand, silt and clay composition shown in Figure 5.3, CS 56/-10/239 can be broadly divided into six units.

i. From base of core, at 2.50 m, to 2.03 m a unit of mud to sandy gravelly mud that contains up to 65.3% clay, though with oscillating sand values that reach 26.2%.

ii. From 2.03 m to 2.00 m there is a pronounced layer of slightly gravelly muddy sand. The sub-sample at 2.00 m - 2.01 m contains the maximum sand content in the core of 82.2%.

iii. Between 2.00 m and 1.58 m a unit of sandy mud displays a decline in the proportion of sand and an increase in silt; which is the dominant particle fraction between 1.68 and 1.82 m.

iv. Two upwards fining sequences, from slightly gravelly sandy mud to mud, are apparent between 1.53 m and 0.97 m. An initial increase in sand at 1.53 m is followed by increased proportions of silt and clay, which reaches 48.8% at between 1.34 m and 1.32 m. A further increase in sand occurs at 1.25 m, followed by an upwards fining sequence to 0.97 m.

v. Between 0.97 m - 0.16 m there is a sandy mud sequence dominated by clays and silts, though with occasional elevated sand values (for instance 23.9% at 0.49 m).

vi. From 0.14 m a unit of muddy sand is apparent, sand reaching a maximum value of 64.0% at the topmost sub-sample.
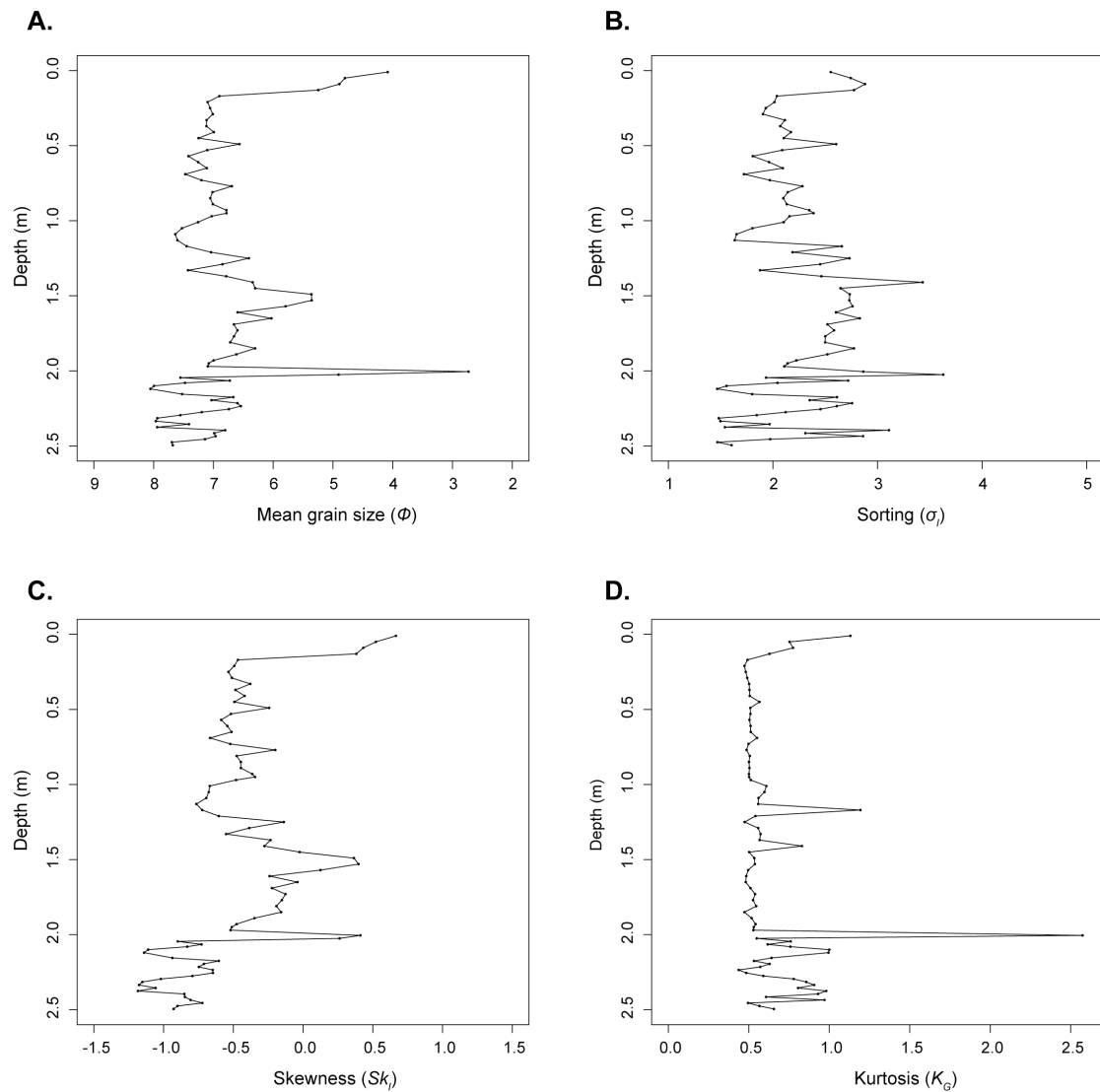
Figure 5.4: Particle size parameters for 56/-10/239, displaying logarithmic values from Folk and Ward (1957) method. A. Mean grain size, B. Sorting, C. Skewness and D. Kurtosis.

Figure 5.4 displays particle size parameters, as calculated using the Folk and Ward (1957) logarithmic method within the GRADISTAT program (Blott and Pye, 2001).

Below 2.00 m mean grain size oscillates between 8.0 ɸ and 6.5 ɸ, at 2.00 m there is a large increase to 2.8 ɸ, followed by an immediate return to finer particles. Between 2.00 and 1.50 m there is a stepped increase from 7.0 ɸ to 5.5 ɸ, followed by a stepped fining to 7.6 ɸ at 1.13 m. From this depth mean grain size is relatively constant around 7.2 ɸ until 0.16 m when there is a coarsening to 4 ɸ at top of core.

Sorting (σ_I) refers to the spread of particle sizes around the average, with lower values indicated a greater degree of sorting. Core sediments are either poorly or very poorly sorted. However, there are pronounced oscillations in σ_I between 2.50 and 2.00 m. Additionally, the coarse sand layer between 2.03 m and 2.00 m is very poorly sorted, followed by a 0.10 m thick sequence of less very poorly sorted sediments. Between

1.90 m and 1.44 m σ_I is relatively constant around 2.7. Between 1.44 m and 1.03 m there is a stepped succession of less sorted to more sorted sediments up core. A minimum value of 1.63 σ_I is observed at 1.13 m. From 1.03 m to 0.16 m values are relatively constant at approximately 2.7 σ_I, though there is some cyclicity. Above 0.16 m sediments become less sorted.

Skewness, or symmetry of spread to one side of the average, shows that the subsamples are generally negatively skewed, with a longer tail of fine particles. From 2.03 m to 2.00m, 1.58 m to 1.50m and 0.14 to 0.00 m subsamples are positively skewed, reflecting the input of coarser particles at these depths.

Kurtosis refers to the peakedness of the distribution, with greater values signifying a dominance of a particular size fraction. Subsamples generally display a flat distribution, classified as either platykurtic or very platykurtic. However, there are occasional increases in kurtosis, associated with coarser sediments, and the sand layer between 2.03 m and 2.00 m is classified as very leptokurtic.

5.3.2.2. Bulk sediment XRF geochemistry

Bulk sediment content for calcium and silica are displayed in Figure 5.5; potassium, iron, nickel and copper in Figure 5.6. Complete XRF results are included digitally in Appendix E, on the accompanying DVD.
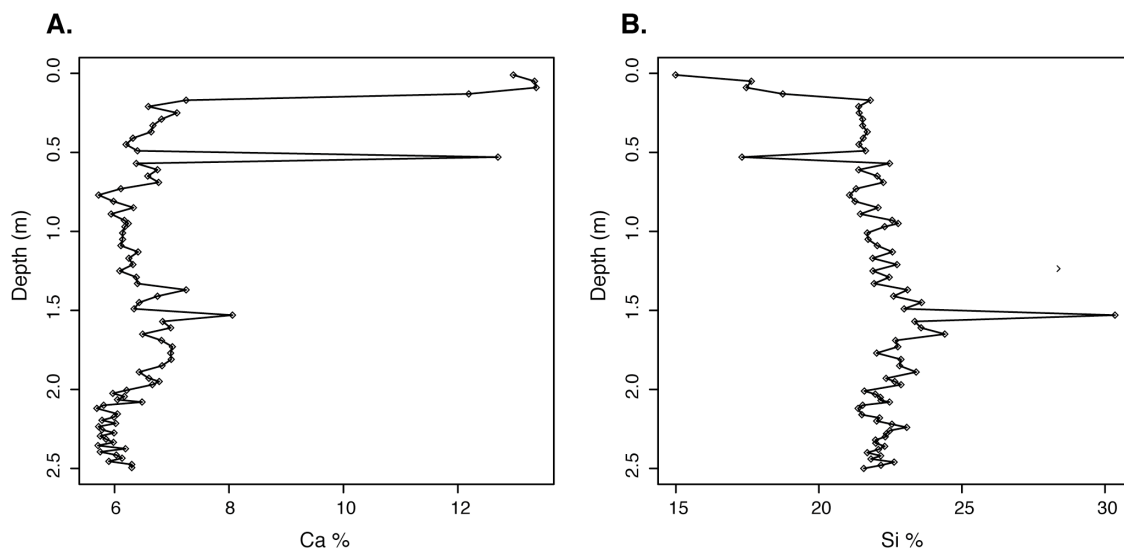
Figure 5.5: Bulk sediment XRF results for: Calcium (A.), Chlorine (B.), Strontium (C.) expressed as percent and Silica (D.) expressed as µg g^{-1}.

Calcium displays low concentrations for much of the core, before a large increase from 0.16 m to core top. Silica is the most abundant element observed within the samples, however, concentrations decline with increasing calcium in the uppermost section of the core.
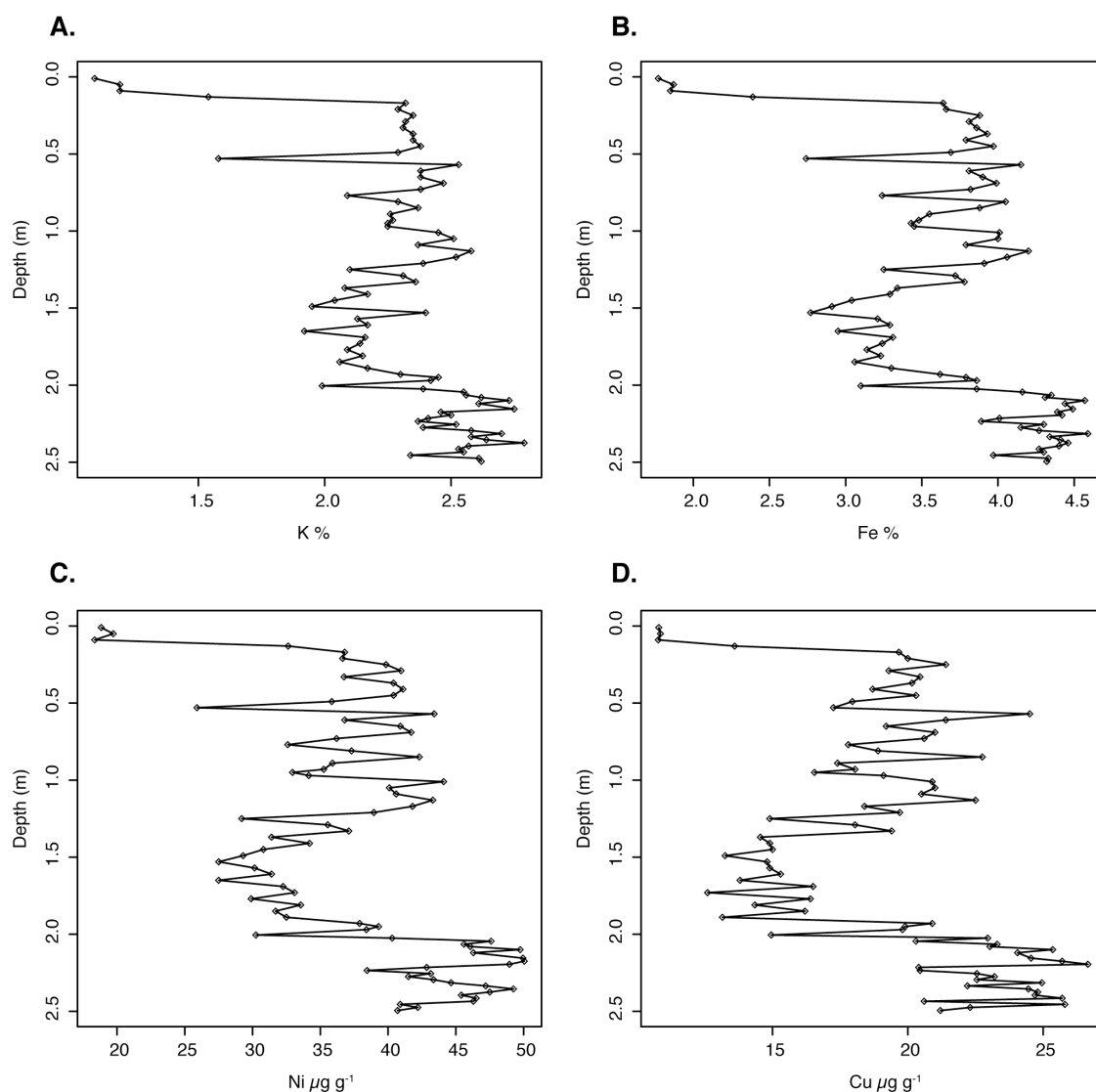
Figure 5.6: Bulk sediment XRF results for: Potassium (A.) and Iron (B.) expressed as percent; Nickel (C.) and Copper (D.) expressed as µg g⁻¹

The metals plotted in Figure 5.6, show high concentrations from base of core to 2.00 m. Concentrations are generally reduced between 2.00 m and 1.40 m before an increase to greater concentrations (though less than those below 2.00 m), with some oscillations between 1.40 m and 0.16 m. Metal concentrations decline dramatically above 0.16 m.
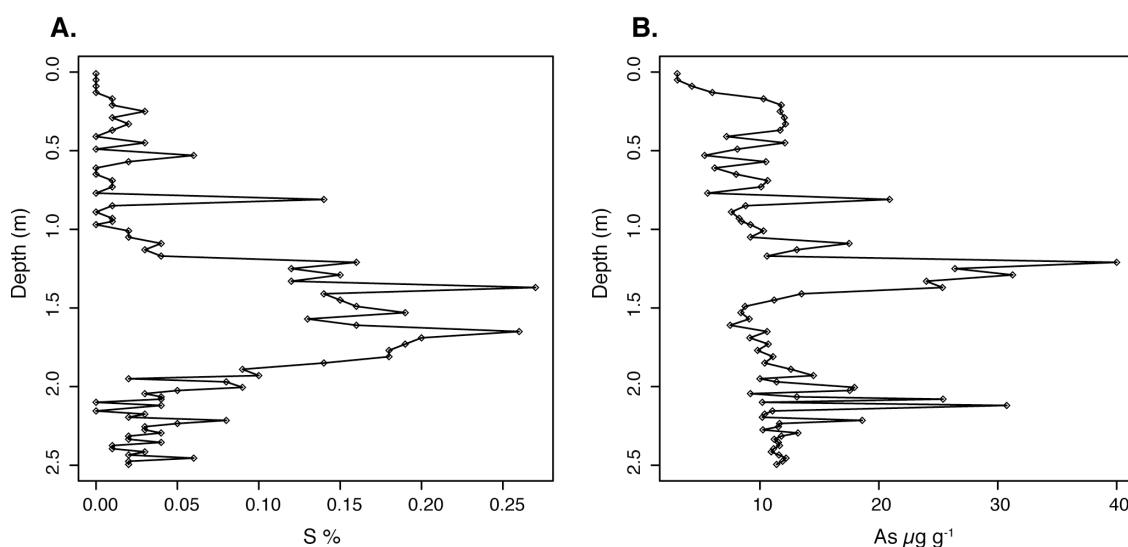
Figure 5.7: Bulk sediment XRF results for: Sulphur (A.) expressed as percent and Arsenic (B.) expressed as µg g⁻¹

Concentrations of sulphur, displayed in Figure 5.7.A, show a marked increase at 2.00 m to maximum values of 0.27% at 1.37 m decreasing to negligible values at 1.05 m, after which concentrations remain low, with the occasional increase, till core top.

There is a pronounced increase in arsenic concentrations between 1.45 m and 1.09 m, with a maximum concentration of 40 µg g⁻¹ at 1.21 m. Occasional elevated concentrations are observed below 2.00 m. Elevated arsenic concentrations appear to be associated with the shallow half of elevated sulphur concentrations.
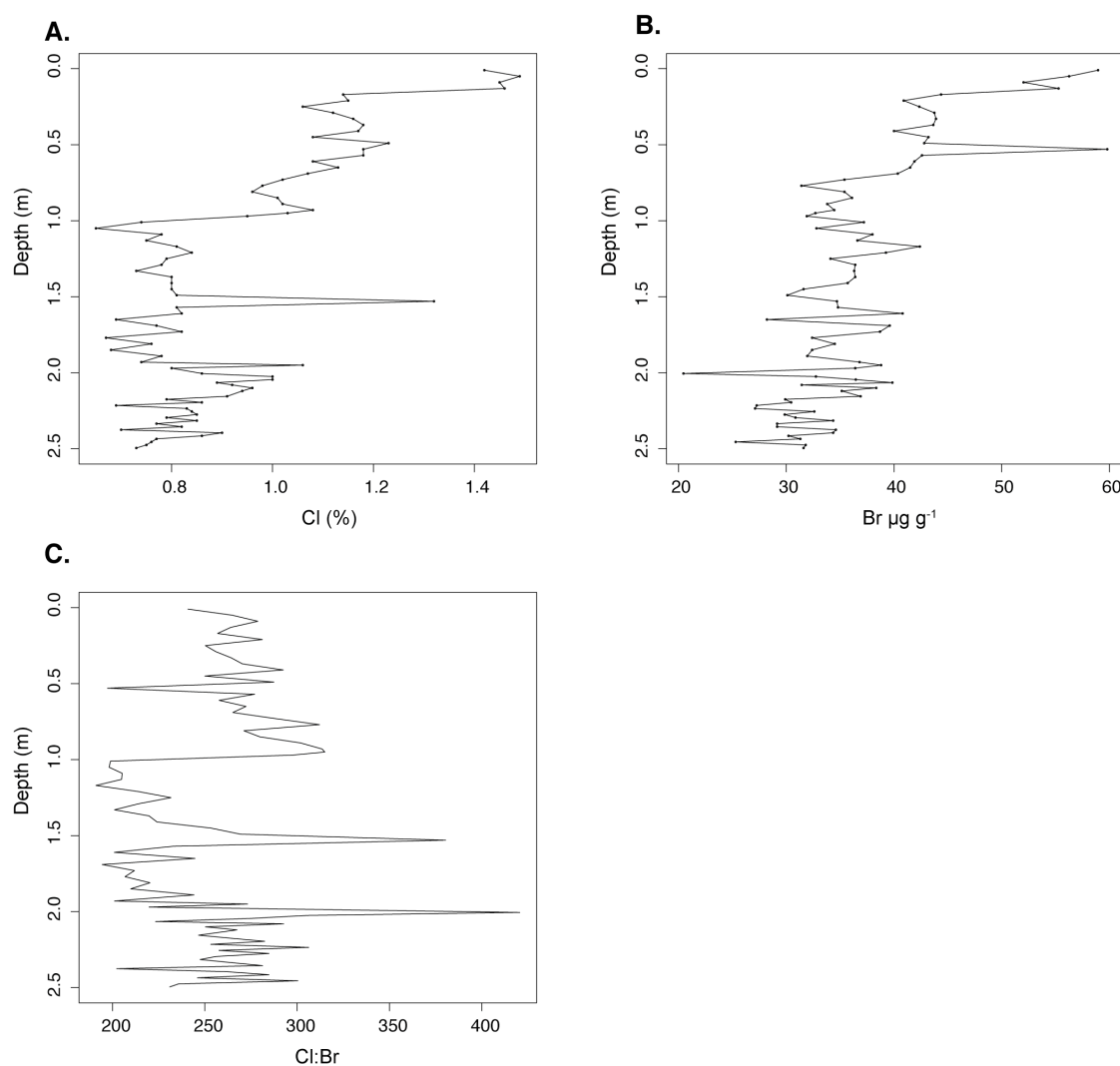
Figure 5.8: Bulk sediment XRF results for: Chlorine (A.) expressed as percent and Bromine (B.) expressed as µg g⁻¹. C. Presents the ratio of Chlorine to Bromine.

Chlorine concentrations increase slightly from 0.7% at base of core to approximately 1.0% at 2.00 m. Between 2.00 m to 1.03 m values are generally low. There is then a marked, stepped increase in concentration from the minimum core value of 0.65% at 1.05 m to a maximum value of 1.49% at core top.

Bromine shows an increasing trend from base of core to top. Above 1.00 m and below 2.00 m the two elements appear to co-vary. However, as Figure 5.8.C. shows, chlorine concentrations are reduced (with the exception of one outlying data point) relative to bromine between 2.00 m and 1.00 m.

5.3.2.3. Total organic carbon
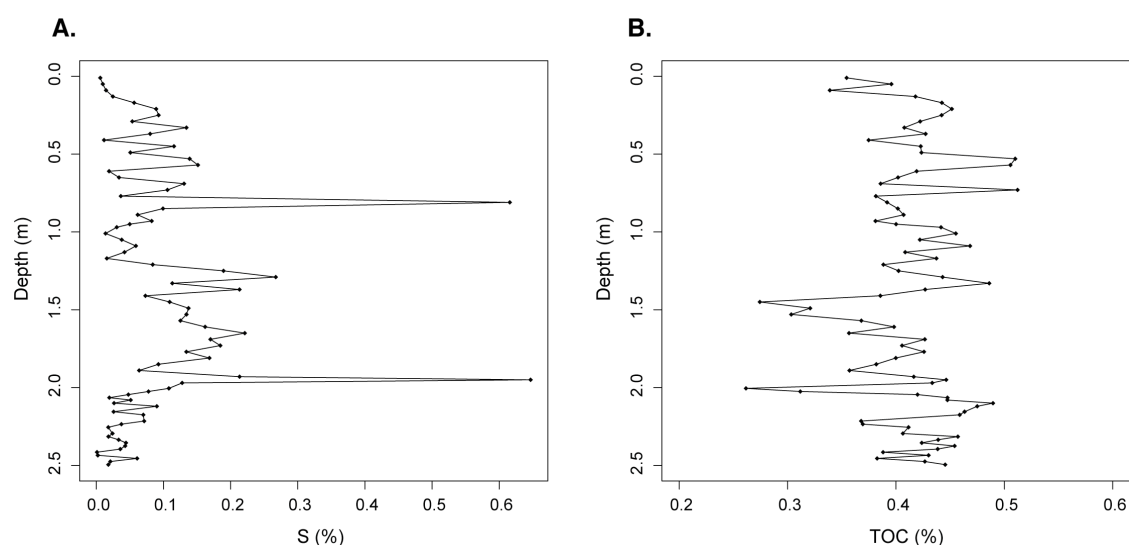
Figure 5.9: Sulphur (A.) and total organic carbon (B.) expressed as percentage of bulk sample calculated from combustion.

Sulphur concentration, calculated via sample combustion is displayed in Figure 5.9.A. With the exception of two outlying data points at 1.95 m and 0.81 m depth the data shows good agreement with XRF derived sulphur concentrations. Figure 5.9.B. presents TOC content. The sediments display low concentrations of TOC with almost all samples <0.5%. Marked decreases occur at 2.03 m to 2.00 m and 1.66 m to 1.38 m.

5.3.3. Isotope geochemistry

Table E.3 shows $\delta^{18}O$ for planktonic foraminifera *N. pachyderma (s.)* and *G. bulloides*, Figure 5.10 presents the data graphically. All values are expressed as deviation from V-PDB.

The foraminifera *N. pachyderma (s.)* and *G. bulloides* were not present throughout CS 56/-10/239. *N. pachyderma (s.)* was absent between 1.82 m to 1.40 m and 0.14 m to core top. *G. bulloides* was absent, or extremely scarce, between base of core to 1.94 m and 1.18 m to 0.72 m.

5.3.3.1. Foraminiferal $\delta^{18}O$
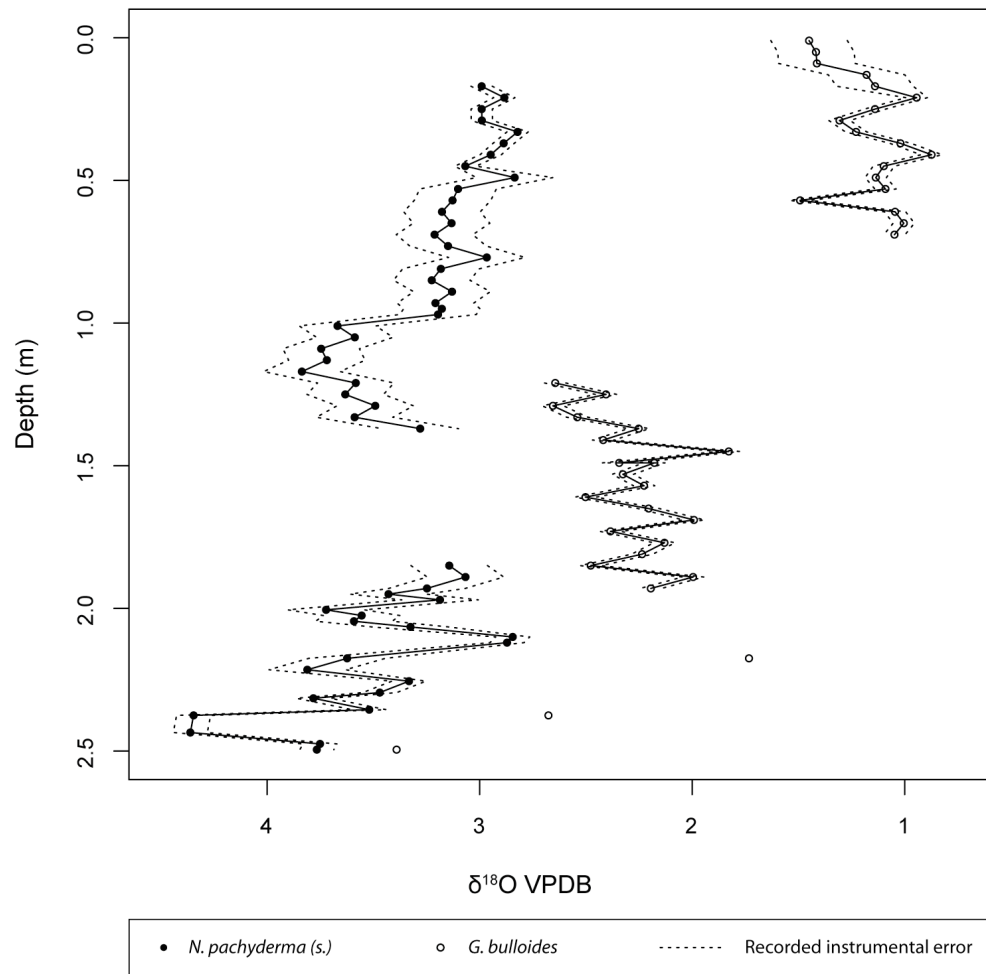
Figure 5.10: $\delta^{18}O$ values for planktonic foraminifera N. pachyderma (s.) and G. bulloides. Dashed line represents instrumental error as recorded on the BEIF gas bench.

N. pachyderma display heavier $\delta^{18}O$ values than *G. bulloides*, as is anticipated from the species' greater calcification depth. For both species, $\delta^{18}O$ values decrease upwards through the core. In the case of *N. pachyderma*, from ~4.0‰ to ~3.0‰ and from ~3.5‰ to ~1‰ in the case of *G. bulloides*. Though there is an apparent increase of 0.5‰ in both species' $\delta^{18}O$ between 1.38 m and 1.00 m. Minimum values are observed at 0.21 m, above which point $\delta^{18}O$ values become isotopically heavier.

5.3.3.2. Foraminiferal δ¹³C
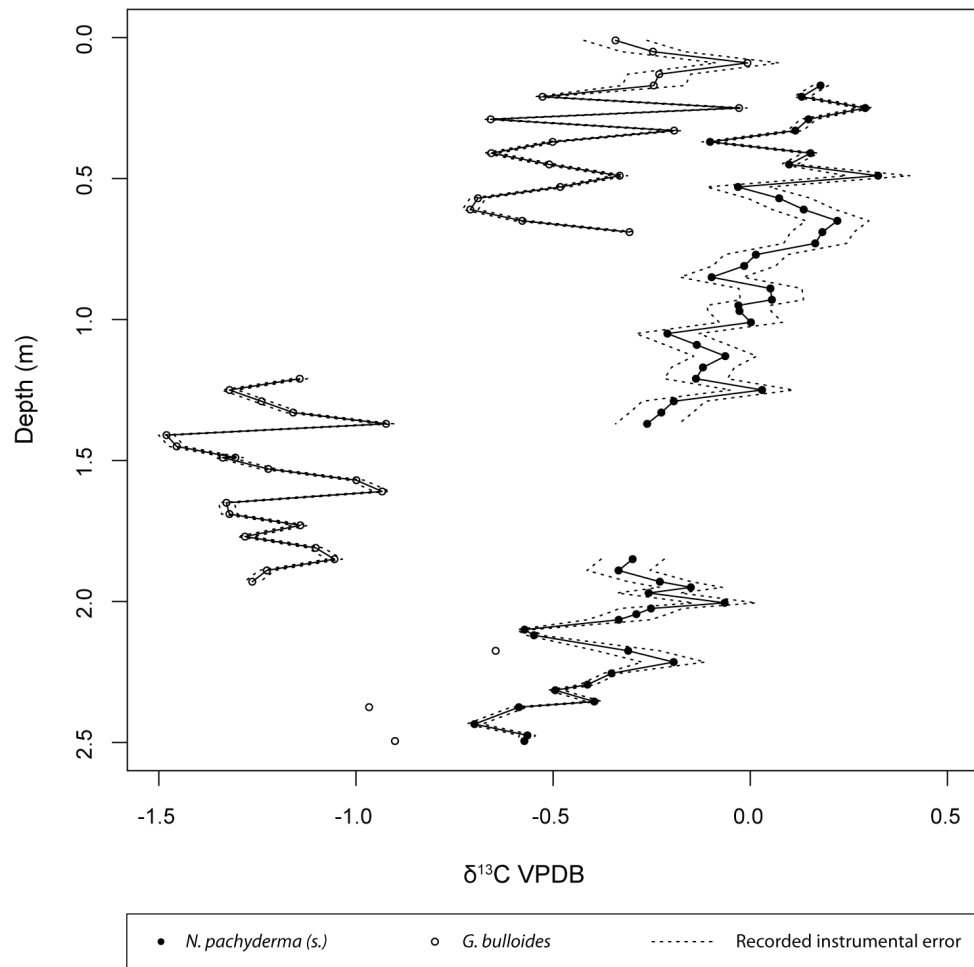
Figure 5.11: δ¹³C values for planktonic foraminifera N. pachyderma (s.) and G. bulloides. Dashed line represents instrumental error as recorded on the BEIF gas bench.

N. pachyderma (s.) and *G. bulloides* display different trends in δ¹³C upwards through CS 56/-10/239. *N. pachyderma (s.)* shows an oscillating increase in δ¹³C from -0.7‰ at base of core to 0.2‰ at 0.16 m.

G. bulloides δ¹³C shows more variability. Isolated values of -1.0‰ at base of core decrease to values of -1.5‰ at 1.41 m, though this shift is marked by a data gaps and oscillations of 0.5‰ at 1.50 m depth. When *G. bulloides* returns at 0.72 m δ¹³C values oscillate about -0.4‰ with variance of up to 0.5‰.

The two species' δ¹³C records display asynchrony through the core sample, with two clear cycles of increasing to decreasing *N. pachyderma* δ¹³C mirrored by decreasing to increasing *G. bulloides* δ¹³C from 0.72 m.

5.3.3.3. Foraminiferal AMS ^{14}C dating

Sample number	Sample depth (cm)	Foraminiferal species	^{14}C Enrichment (% Modern ± σ)	Conventional radiocarbon age (years BP ± σ)	±	Carbon content (% by weight)	δ^{13}C VPDB ± 0.1 ‰
SUERC-28178	16 - 18	*N. pachyderma (s.)*	25.12 ± 0.13	11098	41	10.7	insufficient material
SUERC-28179	156 - 158	*G. bulloides*	20.10 ± 0.11	12889	43	8.6	insufficient material
SUERC-28180	196 - 198	*N. pachyderma (s.)*	26.43 ± 0.14	10688	44	10.5	insufficient material
SUERC-30290	194 - 198	*N. pachyderma (s.)*	25.01 ± 0.13	11134	41	12	-0.4

Table 5.4: Foraminiferal CaCO$_3$ AMS ^{14}C results

Table 5.4 displays AMS ^{14}C dates from foraminiferal calcite as returned from the NERC radiocarbon laboratory. As, poleward of 40° N, the marine reservoir effect undergoes significant changes related to variation in thermohaline circulation and the position of the polar front (Bard, 1988) conversion to calendar years is not a simple matter. Therefore, this is only attempted following a detailed discussion of the problem in chapter six. Discussion of core lithology in this chapter is based on uncorrected AMS ^{14}C dates.

5.4. Discussion of gravity core sample BGS CS 56/-10/239 sedimentology and geochemistry

5.4.1. <u>Comment on sulphur, arsenic and chlorine concentrations</u>

Figure 5.8.A shows bulk sediment chlorine concentration, as calculated via XRF. Broadly speaking the record may be divided into three sections: base of core to 1.94 m; 1.94 m to 1.00 m; and 1.00 m to core top. Of these three sections the lowermost may be characterised by increasing and then decreasing concentrations, the mid by a concentration of 0.1% reduced from the section below and reduced by >0.2% from above, where the upmost section shows a stepped increase in chlorine concentrations to 1.4%.

The reduced chlorine concentrations between 1.94 m and 1.00 m appear to be inversely related to increased sulphur concentrations at the same location (Figure 5.7.A), which increases from negligible levels to 0.25%. Arsenic concentrations increase, between 1.50 m and 1.00 m (Figure 5.7.B).

As dissolved ions (such as Cl^-) are excluded during hydrate formation (Ussler and Paull, 1995), pore water chloride concentrations are used as an indicator of gas hydrates, with pore water freshening an indication of dissociation (Colwell et al., 2004; Muramatsu et al., 2007). However, it would also be anticipated that bromine concentrations would vary with chlorine, as the two halogens covary (Worden, 1996). As Figure 5.8 shows, the chlorine to bromine ratio declines where chlorine concentrations are reduced. Above 1.00 m depth chlorine and bromine covary, suggesting that a process occurs below 1.00 m, which preferentially reduces concentrations of, the more reactive, chlorine.

It is hypothesised that elevated sulphur and arsenic concentrations are associated with pyrite formation, via anoxic sulphate reducing bacteria (Berner, 1978; Berner and Raiswell, 1983). In marine sediments, arsenic is generally an indicator of pyrite (Rothwell et al., 2006), which has been shown to be enriched with arsenic up to 10% weight (Blanchard et al., 2007). Further supporting this is the peak in clay percentage (Figure 5.3) at the same point as arsenic concentration: as arsenic enrichment of pyrite generally occurs in colloidal sized particles (Cook and Chryssoulis, 1990).

This same peak in clay concentration could create low-permeability layer facilitating the creation of anoxic conditions below and explaining the change in chlorine concentrations: which may undergo reaction during the methanogenic process. Bromine concentrations are not reduced as it is less reactive.

5.4.2. Unit lithology of gravity core sample BGS CS 56/-10/239

5.4.2.1. Base of core to 2.03 m

As shown in Figure 5.2.B, this unit is dominated by deformed clays, at times within a sandy matrix. Lithology appears similar to the folded mud and mud-clast conglomerate facies described by Jenner et al. (2007) on the Nova Scotia margin, ascribed to sliding or cohesive debris flow deposits. Selby (1989) and Armishaw (1999) suggest that rapid deposition from overturning icebergs could result in chaotic clay deposits, citing Pickering et al.'s (1989) description of dropstone facies, based on ODP (Ocean Drilling Program) site 645. However, the facies described by Srivastava et al. (1987) from Baffin Bay appear appreciably different, lacking folding and deformed clay clasts, to those visible in gravity core sample 56/-10/239.

High terrigenous metal content, as indicated by XRF results, signifies a terrestrial sediment source. *N. pachyderma (s.)* $\delta^{18}O$ values demonstrate large variation, but reach 4.5‰ VPDB, indicative of full glacial conditions (Knutz et al., 2007). These values are 0.5‰ heavier than equivalent $\delta^{18}O$ values acquired from nearby core sample 56/-10/36, which extends back to 14.6 ka cal BP, by Kroon et al. (1997). *G. bulloides* are scarce or absent.

On the basis of this evidence the unit is classified as a cohesive debris flow, or slide, deposit consisting of glacial sediments.

5.4.2.2. 2.03 m to 2.00 m

The coarse sand layer is a striking feature of the core sample and is identifiable in all datasets. Containing large shell fragments, this unit appears to erode into the underlying clays and is very poorly sorted.

The unit is classified as a turbidite.

It is also possible that the units between base of core and 2.00 m consist of one large mud intraclast within a coarse sandy matrix (sampled between 2.03 and 2.00 m) of a debris flow. Without more core samples and sub-bottom data it is impossible to determine for certain which interpretation is correct, but this does not affect the central work presented in this thesis.

5.4.2.3. 2.00 m to 1.58 m

Alternating layers of sandy clay and silty clay; silt is the dominate particle size fraction between 1.82 m and 1.62 m. XRF data show a significant reduction in metal concentration and mean grain size increases to top of unit. *N. Pachyderma (s.)* is

absent or scarce above 1.84 m, as opposed to *G. bulloides*, which becomes more abundant and displays $\delta^{18}O$ values of 3.4‰ - 2.5‰ VPDB, indicative of the glacial transition (Peck et al., 2008).

The unit contains two AMS ^{14}C dated samples, which yield dates of 10,688 ± 44 ^{14}C BP between 1.98 m to 1.96 m; and 11,134 ± 41 ^{14}C BP between 1.98 m and 1.94 m. The sample that includes the shallowest material yields the oldest date. There are a number of possible explanations for this.

Bioturbation can lead to under- and over-estimation of ages, as Figure 2.2 demonstrates. If a sample overlies a carbonate poor unit, as in this case, there will be unequal mixing of carbonate leading to incorporation of younger material and an age that is too young. However, as the two samples have a very similar depth range this is thought unlikely to cause the 450 ^{14}C year age difference observed.

A second option is that older sediment is emplaced above younger material by downslope transport; in this case, as there is no visual sign of the event, probably a turbidite.

Consideration was also given to whether these differences could have been caused by reworking via bottom currents. It is well documented that silts are transported in this manner (McCave et al., 1995) and the transport of foraminifera has been documented, particularly due to storm action in shallow water (Hohenegger and Yordanova, 2001). The key parameters effecting the ease of entraining foraminifera into transport are the test's degree of projection above the seabed, coupled with relatively low weight (Kontrovitz et al., 1978). *N. pachyderma* have relatively small tests that have been shown to be relatively dense, particularly when <250 µm diameter (Oehmig, 1993).

In this study the foraminifera picked for analysis were well preserved and showed no sign of abrasion or staining. Additionally, their glacial transition $\delta^{18}O$ values are consistent with the ^{14}C ages. Therefore, it is considered unlikely that foraminifera in this unit are reworked by bottom currents.

These dates occur during the late glacial ^{14}C plateau (Kitagawa and van der Plicht, 1998; Beck et al., 2001), during a period when the marine reservoir effect may have changed (Austin et al., 1995), as such it is difficult to justify treating them as being significantly different. Therefore, this thesis considers the mean of the two ^{14}C dates (10,911 ^{14}C BP) as the age of the base of this lithological unit.

The unit is classified as turbidites grading upwards into contourites, as the sortable silt fraction coarsens, possibly associated with the Younger Dryas to Preboreal transition.

5.4.2.4. 1.58 m to 1.00 m

Particle size data shows this unit to consist of a succession of upwards fining sequences and alternation between less sorted (coarser grained) and more sorted (finer grained) sediments. XRF data show an increase in metal concentrations and *N. pachyderma (s.)* return above 1.38 m. Planktonic foraminiferal $\delta^{18}O$ values decline.

An AMS ^{14}C date between 1.58 m and 1.56 m yields an age of 12,889 ± 44 ^{14}C BP, some 2000 years older than underlying dated material.

This unit is classified as a turbidite, on the basis upwards fining sequences and the stratigraphic discontinuity. A lack of other visible mass movement morphologies make more coherent mass movement processes less likely. Additionally, the likely anoxic conditions discussed in section 5.4.1 provide further support to a turbidite interpretation as rapid deposition of fine particles via turbidity current could result in sedimentary anoxia (Raiswell et al., 2008).

The sand layer visible in the core log (Figure 5.2.A), between 1.01 m and 1.00 m was not sampled. However, in conjunction with the striking changes observed in *N. pachyderma (s.)* $\delta^{18}O$ (which decreases by 0.5‰ VPDB), chlorine, sulphur and the large increase in, more sorted, clay this layer is interpreted as the boundary between turbidite and unit above.

5.4.2.5. 1.00 m to 0.16 m

This unit is characterised by silty sediments of relatively consistent sorting and particle size. Sediment metal content is relatively high and there is a slight decrease in *N. pachyderma (s.)* $\delta^{18}O$, *G. bulloides* is present from 0.70 m to top of unit.

An AMS ^{14}C date between 0.18 m and 0.16 m yields an age of 11,098 ± 41 ^{14}C BP at the top of unit.

This unit is interpreted as muddy contourite, however, the stratigraphic discontinuity, between 1.94 m and 1.58 m, indicates that the whole section has undergone downslope transport.

5.4.2.6. 0.16 m to core top

The uppermost unit in the core consists of sandy clay with reduced terrestrial input and increased $CaCO_3$, as indicated by the XRF data. As there is a large increase in $CaCO_3$ detritus particle size data may be less reliable for this unit.

N. pachyderma (s.) are absent from this unit and *G. bulloides* displays an increase in $\delta^{18}O$ of 0.3‰ VPDB.

This unit is classified as a sandy contourite, increased abundance of foraminiferal species and a decline in terrigenous input may signify a transition to Pre-Boreal or Holocene conditions, however this is not reflected in the $\delta^{18}O$ values, which are heavier. This may be due to increased salinity resulting from reduced freshwater ice input. The presence of a rounded pebble indicates potential dropstone or downslope input and the complicated nature of sedimentation in the region.

Figure 5.12 presents the lithological interpretation of CS 56/-10/239.
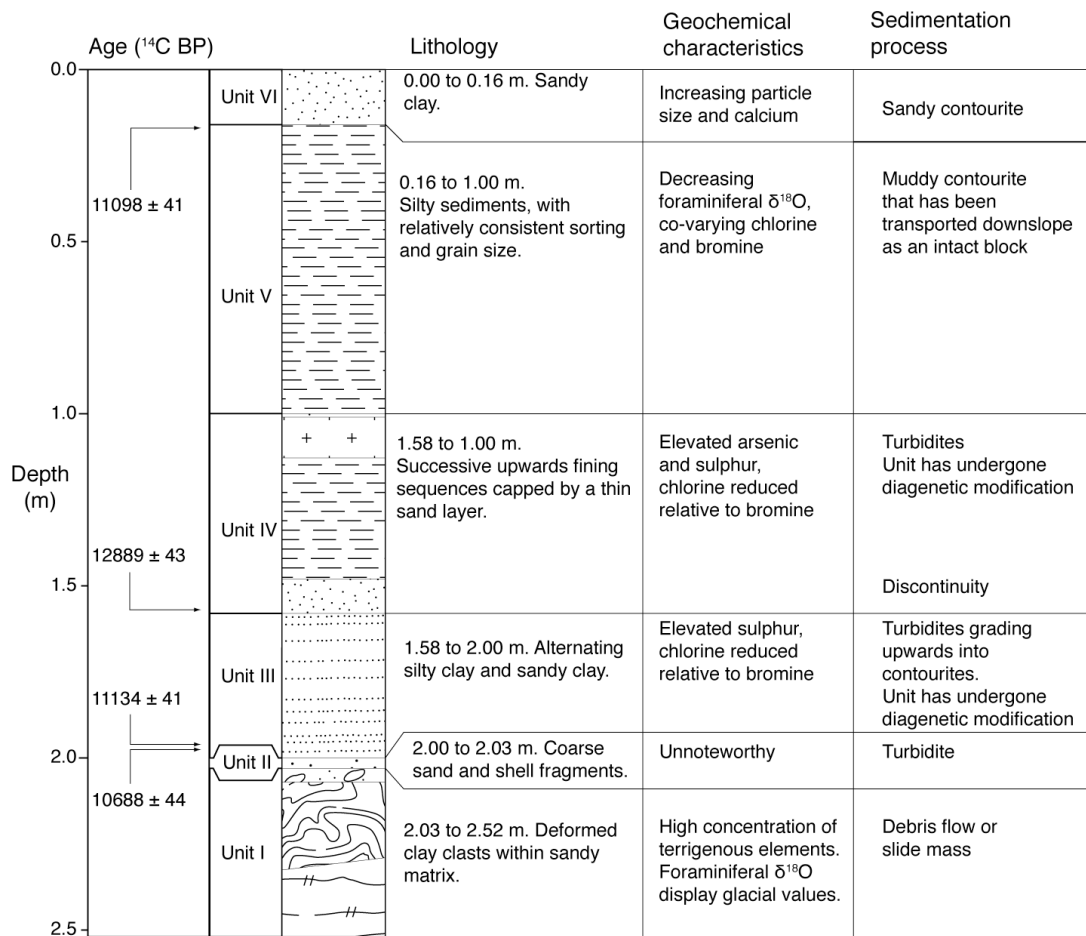
Figure 5.12: Lithology and sedimentology of CS 56/-10/239.

5.5. Chapter summary

Sedimentological, geochemical and isotopic analysis have demonstrated that CS 56/-10/239 samples material from a mass movement deposit.

Foraminiferal $\delta^{18}O$ values indicate that material below 2.00 m is of glacial age and the lithofacies appears to be that of a debris flow deposit. A further unit, located above an age reversal, appears to be turbiditic. Sediments between 2.00 m and 1.00m appear to have undergone diagenetic modification, probably via methanogenic pyrite formation.

The stratigraphy of the core is complicated, with a number of discontinuities that indicate a debris flow or slide mass, consisting of glacial material, prior to 10,911 ^{14}C BP and a further failure, containing material dated at 12,889 ± 43 ^{14}C BP, after 11,098 ± 41 ^{14}C BP.

Foraminifera are not thought to have been reworked by bottom currents, due to a lack of abrasion and the consistency of $\delta^{18}O$ and ^{14}C dates.

Chapter six will discuss the sedimentology of the region in relation to process and chronology.

6. <u>Morphology and timing of sedimentary processes on the northwest British continental margin</u>

6.1. Introduction to chapter

This chapter presents a discussion of the ideas, data and interpretations presented in the preceding chapters. Specifically, the surface and sub-surface morphologies identified in chapter four are tied to a chronological framework on the basis of AMS ^{14}C dates: from gravity core 56/-10/239 presented in chapter five of this thesis; and other local chronologies available in the literature.

This allows the discussion of sedimentary processes and mass movement to be broadened. Specific local factors such as the state of the BIS, intensity of slope-parallel currents and the Barra Fan's sedimentation regime are discussed in relation to timing of submarine mass movement.

Through this approach, and to enable discussion, the chapter attempts to clarify the chronological framework for the processes operating on the Barra Fan. Within this a number of specific unknowns are addressed. These include: the study area's ^{14}C marine reservoir effect (and how this varies with time); the chronology of the acoustic facies interpreted in chapter four; and when the key periods of sedimentation and mass movement occurred. Finally, with a chronological framework established, the chapter examines the morphology and asks what it can tell us regarding the processes involved in submarine mass movement on the northwest British continental margin.

With regards to mass movement, the chapter considers the geologic and oceanographic setting outlined in chapter three alongside the conceptual model of slope failure presented in chapter two and identifies the likely susceptibility factors and trigger mechanisms operating on the Barra Fan. However, as they are separate from the main focus of this thesis, the gullies described in section 4.3.1 are now briefly discussed.

6.2. Gully formation

These features consist of two distinct forms, V-shaped in the north and U-shaped in the south. Combined with the pinger data and mass movement facies interpretation presented in section 4.4.4 (and appendix D) it appears that the southern gullies are subject to greater erosion than those in the north.

This thesis does not seek to identify the formation mechanisms, however it seems probable that the two gully populations are formed by different processes. Kenyon (1987) suggests that greater flow velocity may be responsible for cutting V-shaped

gullies, differentiating these from U-shaped gullies and "Bottleneck Slides". There are also possible roles for glacial meltwater and slope failure in the formation of the U-shaped southern gullies (see Noormets et al., 2009). Potentially identifying a role for periglacial outwash from the retreating Barra Fan Ice Stream (Scourse et al., 2009), which, from the locations of the Malin and Stanton Deeps (see Figure 4.8 and Figure 6.2), appears to have been close to these southern gullies. These two gully populations may provide a useful dataset for future analysis.

Source	Austin et al. (2011)	Cao et al. (2007)	Bondevik et al. (2006)	Austin et al. (1995)	Björck et al. (2003)	Hall et al. (2011)	Franke et al. (2008)
Location / **Stadial/ Interstadial** — **Calendar age (BP from)**	St Kilda Basin (NE Atlantic)	Orphans Knoll (NW Atlantic)	Norwegian west coast	Barra Fan (NE Atlantic)	Norwegian Sea - GRIP comparison	Rosemary Bank, North Rockall Trough - GISP 2 comparison	Modeled North Atlantic*
Holocene — 9000	*Grey indicates absence of estimate*						450
9500							
10000							
Pre-Boreal — 10500							
11000			450 - 350				
11500	400	270 ± 20 ?					
Younger Dryas — 12000	600						
12500	1000	590 ± 130	600	700			
13000	750				1000 ± 250		
Bølling Allerød — 13500	770						
14000	820	380 ± 140	400 - 300				
14500	550						
Late Glacial - Marine Isotope Stage 2 — 15000							
16000							
17000							
18000						1352	
19000						1012	
20000						1044	
21000						1111	550
22000						1449	
23000						1276	
Marine isotope stage 2 — 24000						1182	
25000							
26000						1685	
27000							
28000						1761	
29000							
30000						1631	

Table 6.1: North Atlantic ¹⁴C marine reservoir effects during the Late Glacial and Holocene transition. *Modeled North Atlantic data from Franke et al. (2008) assume 30% reduction in meridional overturning circulation at 21 ka cal BP and Holocene value is present day.*

6.3. Chronology of sedimentation

Timing of sedimentation processes on the northwest British continental margin is determined via correlation between dated sediment samples and the sub-surface acoustic interpretation presented in chapter four.

6.3.1. Accounting for the marine ^{14}C reservoir effect

There is a large degree of uncertainty concerning temporal variation of the marine reservoir effect at the Barra Fan. Table 6.1 outlines the present understanding of the late-glacial to Holocene variations in the North Atlantic marine ^{14}C reservoir effect.

The data presented consist of comparison between marine AMS ^{14}C dates and terrestrial carbon (Bondevik et al., 2006), corals (Cao et al., 2007), tephra (Austin et al., 1995), Greenland ice-cores (Waelbroeck et al., 2001; Björck et al., 2003; Hall et al., 2011). Austin et al. (2011) use a combination of tephra and ice-core correlation. Modeled data, which assumes a 30% reduction in North Atlantic meridional overturning, is shown for the LGM (Franke et al., 2008). Reservoir ages produced from records comparing directly to ice-cores result in greater values due to increased uncertainty in ice age-depth models.
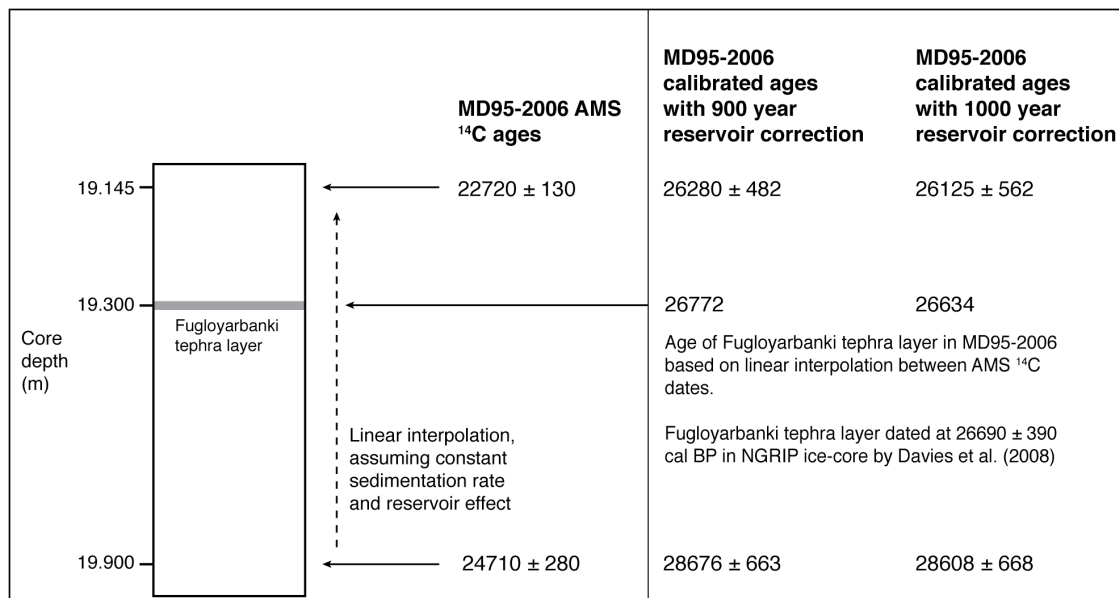
Figure 6.1: Estimating the marine reservoir effect in the Rockall Trough during MIS 3, from Fugloyarbanki tephra layer in MD95-2006. MD95-2006 AMS ^{14}C dates from Austin et al. (2012), calibrated using IntCal09 (Bronk Ramsey, 2009), NGRIP age of tephra from Davies et al. (2008).

In addition to these published data it is possible to estimate the marine reservoir effect in the Northeast Atlantic, during the early stages of marine isotope stage 2, from the

Fugloyarbanki tephra layer. Austin et al. (2012) demonstrate that MD95-2006 samples this layer at 19.30 m. This layer has been dated at 26,690 cal BP in the NGRIP ice-core by Davies et al. (2008). As the tephra layer in MD95-2006 is situated between two planktonic foraminiferal AMS ^{14}C dates one can interpolate linearly between these, assuming that there is a constant sedimentation rate and that the reservoir effect is unchanged during the sampled time period. This exercise has been performed and a reservoir correction of between 900 and 1000 years (error is not calculated though it is assumed to be in the order of ± 500) is required to calibrate the marine tephra layer to the NGRIP record. Figure 6.1 provides an overview of this estimate. The exercise was performed using the Fairbanks et al. (2005) and IntCal09 (Bronk Ramsey, 2009) calibration curves with no appreciable difference.

Time period (calendar years)	Time period (name)	Reservoir correction	Corresponding uncorrected ^{14}C period	Evidential support
10,000 to present	Holocene	450	9318 to present	General agreement among records and reflects pre-bomb values (Bard et al., 1994).
11,499 to 10,000	Pre-Boreal	400	10400 to 9319	Agreement between Austin et al. (2011) and Bondevik et al. (2006).
12,999 to 11,500	Younger Dryas	700	11795 to 10401	Based on Vedde Ash layer located in CS 56 -10 36 (Austin et al., 1995) and all other records support elevated values.
14,999 to 13,000	Bølling-Allerød	500	13109 to 11796	Disagreement among records, have opted for a mid-way point between Bondevik et al. (2006) and Austin et al. (2011). Reduced correction compared to adjacent periods is logical due to probable enhanced thermohaline circulation.
20,999 to 15,000	Late Glacial - MIS 2	550	18084 to 13110	High degree of uncertainty due to lack of data. This value is chosen due to modeled value from Franke et al. (2008).
28,500 to 21,000	Glacial - MIS 2	950	24710 to 18085	High degree of uncertainty due to lack of data. This value is chosen due to apparent 950 year offset of Fugloyarbanki tephra layer in MD95-2006 (see Figure 6.1; Davies et al., 2008; Austin et al., 2012)

Table 6.2: Summary of ^{14}C marine reservoir corrections used. Radiocarbon period is reservoir corrected calendar age equivalent from IntCal09 calibration curve (Bronk Ramsey, 2009).

This approach is crude and subject to error from the marine and ice data. It does, however, provide a value consistent with increased reservoir effect due to southerly migration of the polar front (Bard, 1988; Bard et al., 1994), reduced North Atlantic meridional overturning (Hughen et al., 2000) and with pre-bomb Arctic data (Bard et al., 1994). The value is roughly half of that demonstrated in the Rosemary Bank - GISP2 comparison performed by Hall et al. (2011). There may be two explanations for this: first, Rosemary bank is situated further north and could be subject to more polar

conditions. Second, as an ice-core comparison the Hall et al. (2011) study may over-estimate the age difference. Due to the Barra Fan location the Fugloyarbanki derived correction is used.

On the basis of the present understanding of the Glacial to Holocene ^{14}C marine reservoir effect, and of the presence of the Fugloyarbanki tephra layer in MD95-2006, this thesis uses different corrections for distinct time periods. Table 6.2 outlines the marine reservoir corrections used.

Uncertainty regarding the reliability of reservoir corrections increases with age, especially for periods that pre-date the Younger Dryas.
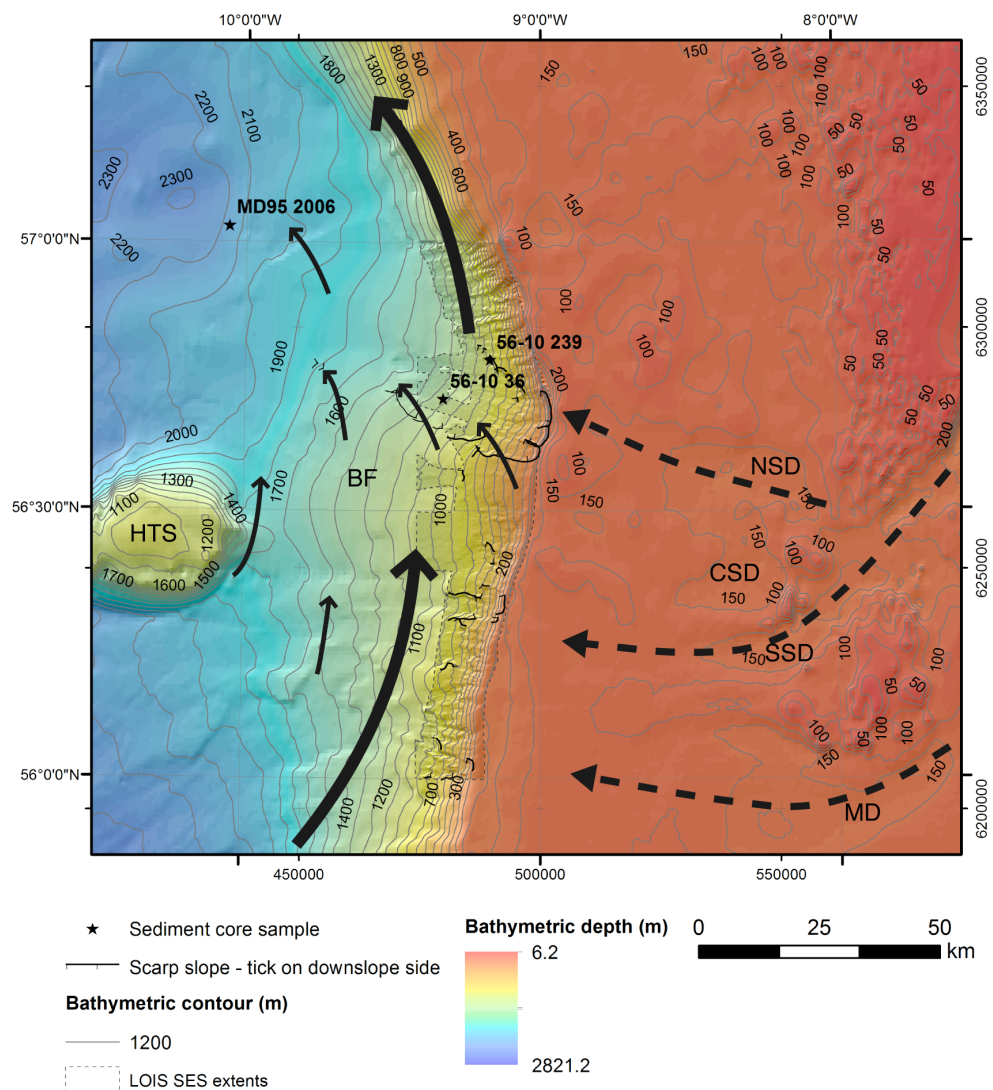
Figure 6.2: Location of core samples that are used to provide a regional chronology in relation to slide scarp slope, probable ice stream locations (dashed black arrows), major thermohaline current circulation (thick solid black arrows) and inferred local variation in slope parallel currents (thin solid black arrows). HTS: Hebrides Terrace seamount, BF: Barra Fan, NSD: North Stanton Deep, CSD: Central Stanton Deep, SSD: South Stanton Deep, MD: Malin Deep.

6.3.2. Regional stratigraphic framework and chronologies

Core sample	Depth (m)	Material	Age (Uncorrected ¹⁴C BP)	Reservoir correction	Age (calendar years BP - IntCal09)
56/-10/239	0.170	*N. pachyderma (s.)*	11098 ± 41	700	12300 ± 214
56/-10/239	1.570	*G. bulloides*	12889 ± 43	500	14513 ± 413
56/-10/239	1.960	*N. pachyderma (s.)*	11134 ± 41	700	12323 ± 206
56/-10/239	1.970	*N. pachyderma (s.)*	10688 ± 44	700	11482 ± 219
56/-10/239	1.96 and 1.97 combined		10711 ± 43	700	11919 ± 160
56/-10/36	0.725	*G. bulloides*	10040 ± 80	400	10976 ± 230
56/-10/36	0.755	*N. pachyderma (s.)*	10585 ± 85	700	11438 ± 265
56/-10/36	1.245	Vedde Ash	10939	700	11953 ± 116
56/-10/36	2.780	1 Thol. 2 Ash	11293	700	12585 ± 44
56/-10/36	3.550	*G. bulloides*	12055 ± 100	500	13445 ± 230
56/-10/36	4.315	*G. bulloides*	13020 ± 115	500	14643 ± 492
MD95-2006	0.500	G. bulloides	2799 ± 44	450	2434 ± 249
MD95-2006	1.645	G. bulloides	10270 ± 44	400	11298 ± 92
MD95-2006	2.600	1 Thol 2 Ash	11293	700	12585 ± 44
MD95-2006	3.230	*G. bulloides*	11960 ± 120	500	13356 ± 248
MD95-2006	7.600	*N. pachyderma (s.)*	15260 ± 140	550	17999 ± 514
MD95-2006	11.755	*N. pachyderma (s.)*	17390 ± 190	550	19951 ± 466
MD95-2006	13.200	*N. pachyderma (s.)*	18060 ± 130	550	20866 ± 464
MD95-2006	14.110	*N. pachyderma (s.)*	18680 ±130	950	21018 ± 474
MD95-2006	15.915	*N. pachyderma (s.)*	20390 ± 150	950	23138 ± 533
MD95-2006	19.145	*N. pachyderma (s.)*	22720 ± 130	950	26216 ± 519
MD95-2006	19.900	*N. pachyderma (s.)*	24710 ± 280	950	28642 ± 666
MD95-2006	20.105	*G. bulloides*	24571 ± 185	950	28402 ± 503
MD95-2006	20.205	*N. pachyderma (s.)*	24710 ± 280	950	28642 ± 666

Table 6.3: Calibration of radiocarbon chronology to calendar years BP. Radiocarbon dates for core sample 56/-10/36 from Kroon et al. (1997) and MD95-2006 from Knutz et al. (2001), Wilson and Austin (2002) and Austin et al. (2012).

Table 6.3 shows calculated calendar ages of marine reservoir corrected AMS ¹⁴C dates from three core samples located at, or near, the Barra Fan study site (locations shown in Figure 6.2). These are piston core MD95-2006 (with published work presented by Kroon et al. (2000); Knutz et al. (2001; 2002); Wilson and Austin (2002); and Austin et al. (2012)), vibrocore 56/-10/36 (analysed by Kroon et al. (1997; 2000) and gravity core 56/-10/239 (analysed in chapter five of this thesis).

6.3.2.1. MD95-2006

Interpretation of piston core MD95-2006, and tied seismic interpretation, by Knutz et al. (2002) is extremely useful to this thesis and assists in producing a more accurate chronological framework.
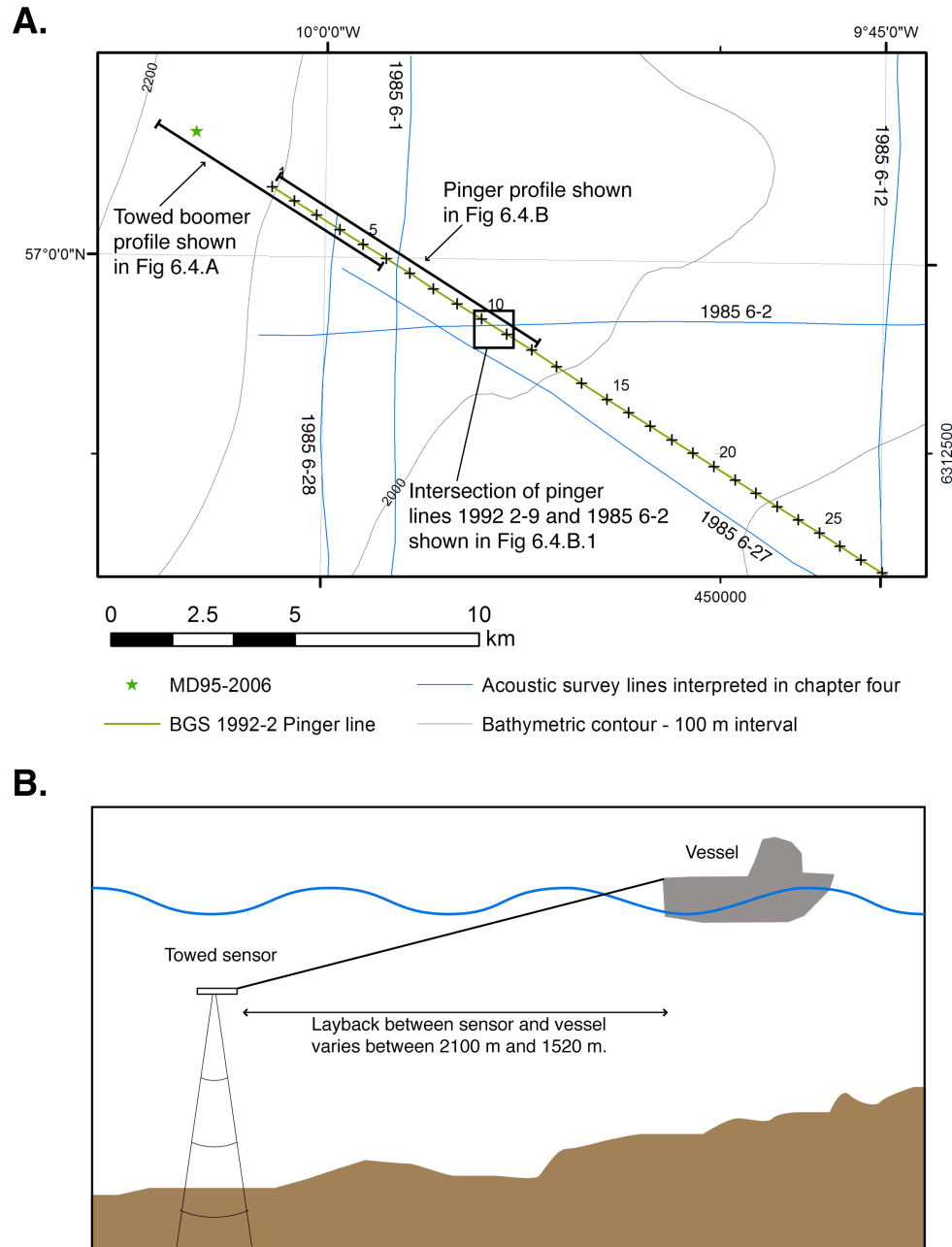
Figure 6.3: Linking Interpretation from Knutz et al. (2002) to this study. A. Overview of data shown in Figure 6.4. B. Explanation of instrument layback.

It was not possible to incorporate the towed boomer record into the sub-surface interpretation presented in chapter four of this this thesis as the boomer layback from vessel (as outlined in Figure 6.3.B) varies by up to 600 m. However, via comparison to the associated pinger line it is possible to tie the interpretation from Knutz et al. (2002) into the interpretation presented in this thesis (see Figure 6.4).

A.

Fix

A.1

Seismic data tied to MD95-2006

Location of MD95-2006

	Interpretation	
	Knutz et al. (2002)	This thesis
	Silty - muddy contourite	Acoustic Facies IA Muddy contourite
	Glacimarine mud and clay grading into muddy contourite.	Acoustic Facies IIA Hemipelagite

B.1

Crossing of pinger lines

1992 2-9   **1985 6-2**

B.

BGS 1992 2-9 crosses BGS 1985 6-2

Fix
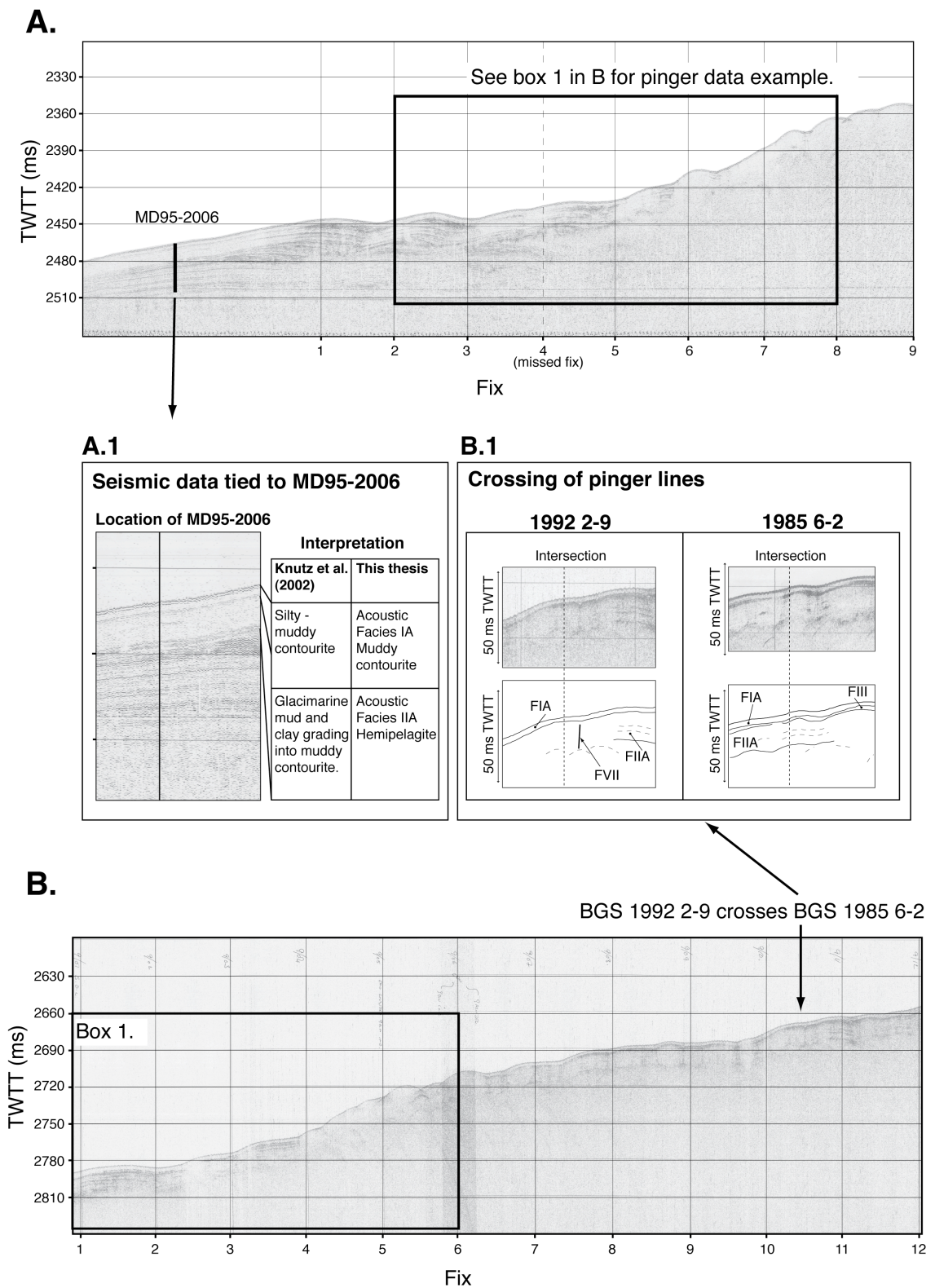
Figure 6.4: Linking Knutz et al.'s (2002) interpretation of MD95-2006 and BGS seismic data to work completed in this thesis. A. Towed boomer line 1992 2-9, with MD95-2006. B. Pinger line 1992 2-9 with crossing of BGS 1985 6-2. A.1 shows MD95-2006 interpretation linked to boomer record. B.1 shows detail of intersection of 1992 2-9 and 1985 6-2.

The locations of profiles A and B shown in Figure 6.4 are marked in Figure 6.3.A.

Figure 6.4.A shows the location of MD95-2006 in relation to deep towed boomer record

1992 2-9. Interpretation of the upper section of the core is shown alongside the boomer

record in Figure 6.4.A.1. As is clear from the figure, the core is located prior to the start of navigation fixes. Also, from measuring the distance between distinctive seabed features imaged on the pinger and towed boomer record (using the same navigation for each) it is clear that the boomer layback varies between approximately 2100 m and 1500 m. It was, therefore, not possible to incorporate this data into the sub-bottom interpretation presented in chapter four.

However, from comparison with the pinger line (Figure 6.4.B) associated with the deep towed boomer, the interpretation from Knutz et al. (2002) may be linked to the sub-bottom interpretation performed in this thesis at the crossing location of 1985 6-2 (details of the intersection are shown in Figure 6.4.B.1). From this figure it is clear that Knutz et al.'s (2002) upper contourite unit and seismic unit I-A are equivalent to acoustic facies I and IIa interpreted in this thesis.

As shown in Figure 6.2 piston core MD95-2006 is located on the lower slopes of the Barra Fan. Containing a sediment sequence that spans 60 ka (Wilson and Austin, 2002) the core is a valuable archive of the Barra Fan's oceanographic, sedimentological and glacial history.

The chronology established for this core (Knutz et al., 2001, 2002; Wilson and Austin, 2002; Austin et al., 2012) may, therefore, be used to constrain the ages of acoustic facies Ia and IIa interpreted in this thesis. A detailed chronology of MD95-2006 is presented in Figure 6.5.

Of immediate use to this PhD project is the correlation of the core's lithological units to deep-towed boomer records by Knutz et al. (2002) and shown in Figure 6.4. Work on the core by Knutz et al. (2002) and Wilson and Austin (2002) constrains the age of the Peach 3 event to between 21.02 and 20.87 ka cal BP and the development of contourite sediments to after 11.3 ka cal BP.

MD95-2006

Uncorrected ¹⁴C date	Interpreted lithology	Acoustic characteristics and interpretation
— 2.80 ka	Silty - muddy contourite	**I - A:** Stratified drape covering debrites. Development from distal glacimarine to muddy contourites. Holocene represented by thin reflection free uppermost 1.5 m.
— 10.27 ka		
— 11.29 ka (1 Thol 2 Ash) — 11.96 ka	Hemipelagic mud, grading into muddy contourite	
— 15.26 ka	Glacimarine mud and clay	
— 17.39 ka — 18.06 ka	Silty - muddy contourite	**I - B:** High amplitude reflectors that onlap Peach 3.
— 18.68 ka — 20.39 ka	Glacimarine mud with thin-bedded, coarse-grained turbidites	**II:** Weak parallel reflectors that dip below Peach 3. Glacimarine sediments.
— 22.72 ka — 24.71 ka — 24.57 ka — 24.71 ka — 25.73 ka — 26.21 ka		
— 29.40 ka — 29.73 ka	Hemipelagite/ muddy contourite	
— 33.88 ka	Silty - muddy contourite	**III:** Sub-parallel reflectors. Silty-muddy contourite.
	Muddy contourite, with distal silty turbidites?	

Depth below seabed (m) — depth scale: 5, 10, 15, 20, 25, 30

Figure 6.5: Radiocarbon chronology, lithology and tied acoustic interpretation for piston core MD95-2006. Uncorrected ¹⁴C dates from Knutz et al. (2001) and Austin et al. (2012); lithology and acoustic interpretation from Knutz et al. (2002).

6.3.2.2. BGS 56/-10/36

Acquired on 25/11/1985, the location of vibrocore 56/-10/36 was fixed using the Decca radio beacon system at 05:52 AM (during night conditions). Situated 100 km west of Barra, the system could have been subject to a nautical mile of error.
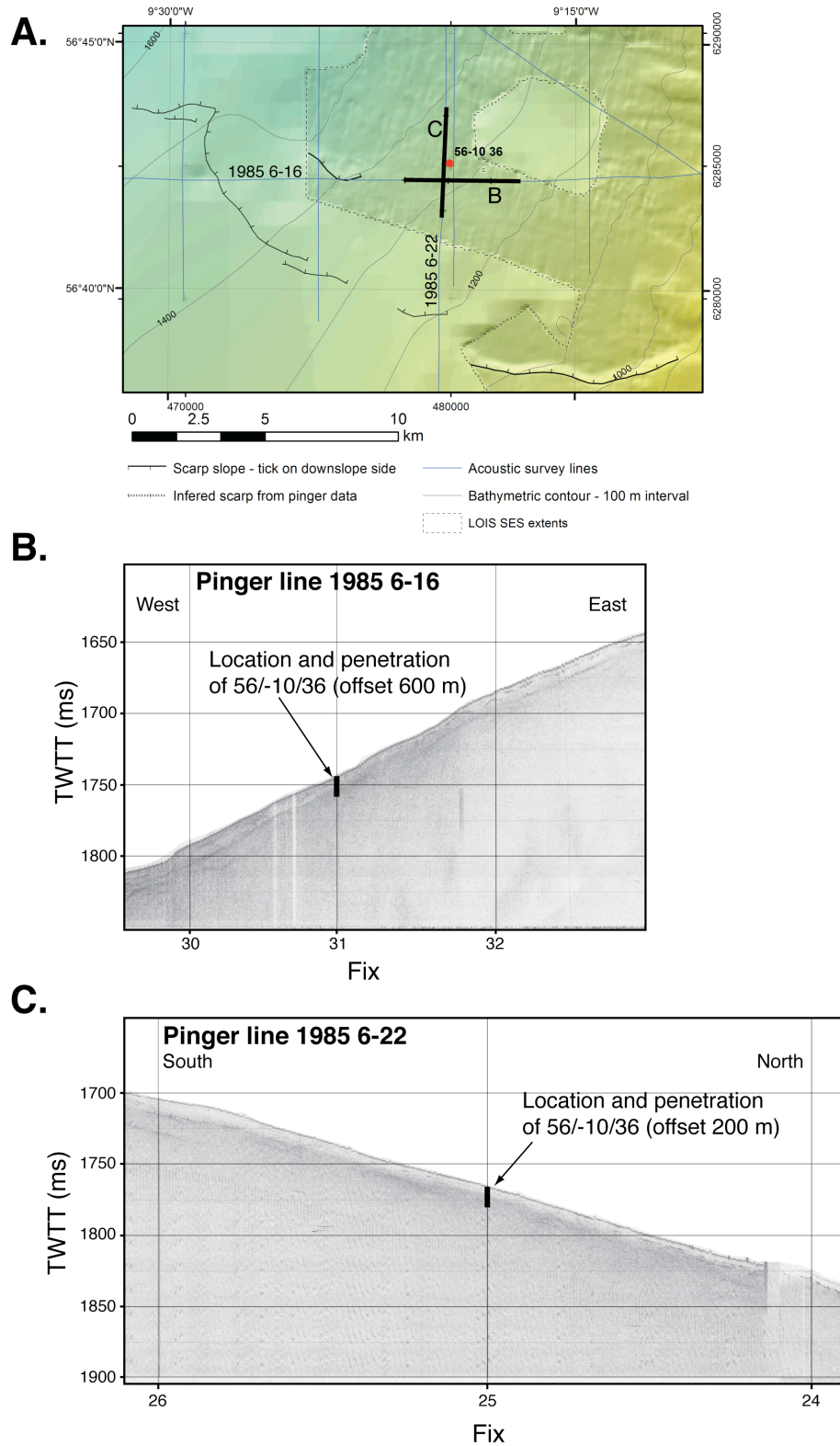
Figure 6.6: Location and acoustic facies of vibrocore 56/-10/36. A. Location map showing profiles and core. B. Pinger line 1985 6-16. C. Pinger line 1985 6-22.

As shown in Figure 6.6.A this core is located within the area bounded by the prominent landslide scarp. During early stages of this PhD project (see Owen et al., 2010) it was thought that this core provided a minimum age for the emplacement of Peach 4. However, on analysing the data more closely it seems that the core does not match the nearby seismic data (shown in Figure 6.6). This could be due to the distance between the core position and seismic lines (200 m and 600 m) or navigational inaccuracies associated with Decca system, which could be up to 1 nautical mile as the nearest Decca station was 100 km distant, on Barra (BODC, 2011).

It seems more likely that the core samples sediments that have undergone more limited movement, perhaps equivalent to the lateral spreading observed at Storegga (Kvalstad et al., 2005) and Trænadjupet (Laberg and Vorren, 2000), or more gradual down-slope creep. These different failure morphologies are discussed in section 6.4. On this basis it seems that the core does not constrain the age of Peach 4.
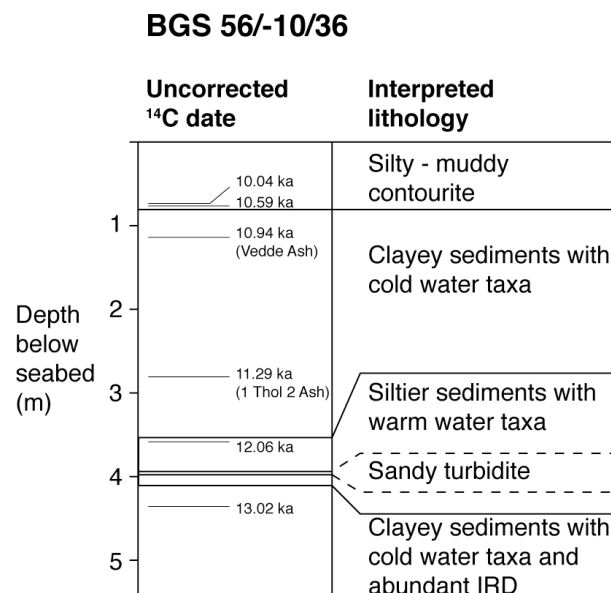
Figure 6.7: Radiocarbon chronology and lithology from vibrocore 56/-10/36 (Kroon et al., 1997).

This core has been used to constrain the timing of the Bølling-Allerød from 14.6 ka cal BP, Younger Dryas from 13.5 ka cal BP and the Holocene from 10.9 ka cal BP (Kroon et al. (2000) AMS ^{14}C dates and interpretation, calibrated in Table 6.3 of this thesis).

6.3.2.3. BGS 56/-10/239

The location of this core sample, in relation to bathymetry and seabed interpretation, is shown in Figure 6.8. Chapter five of this thesis presents a detailed analysis of this core sample.
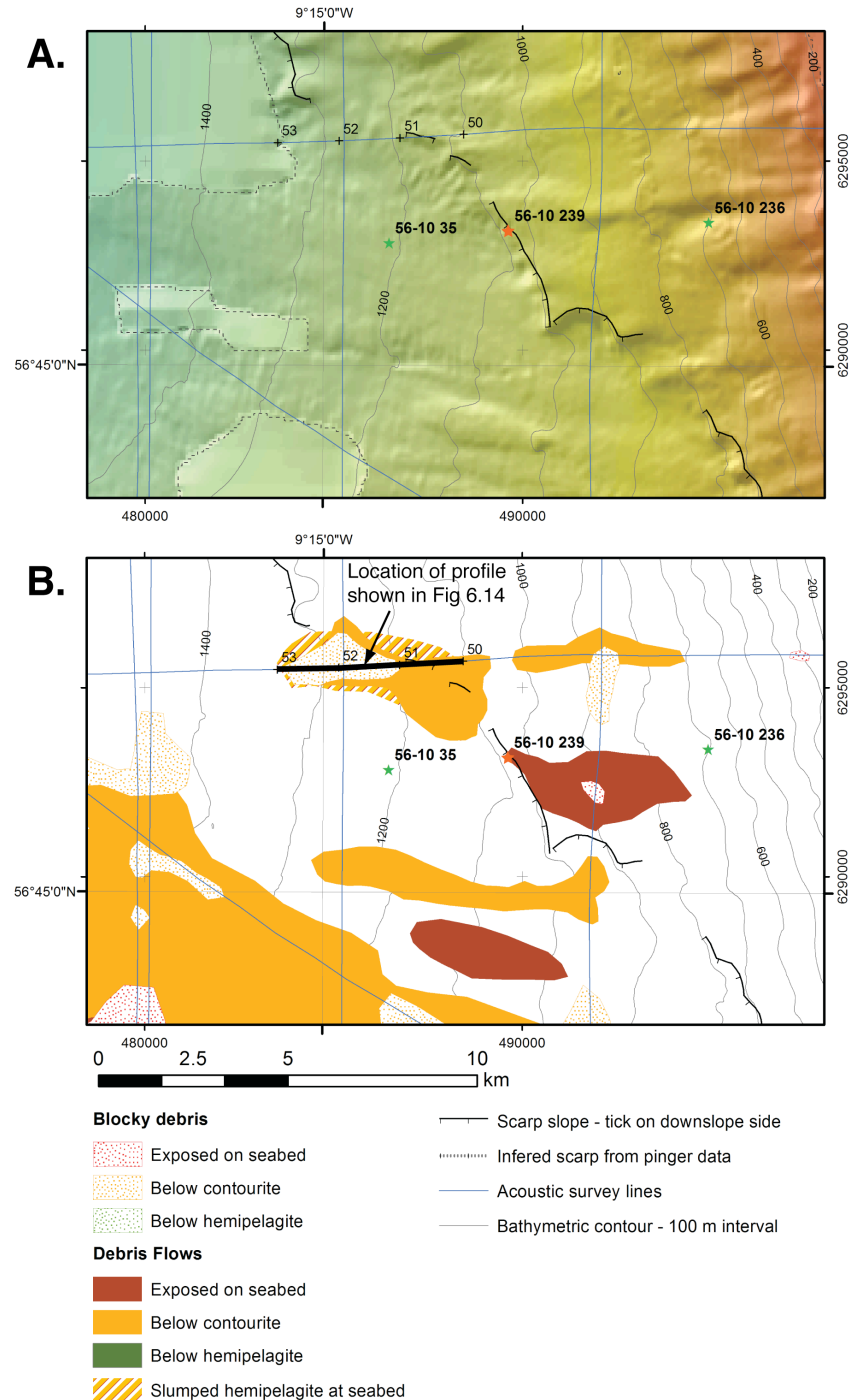
Figure 6.8: Location of BGS 56/-10/239. A. Bathymetry and shaded relief. B. Interpretation of mass movement features, as shown in chapter four.

The key findings with regards to morphology and timing of sedimentation on the northwest British continental margin are:

i. The presence of mass movement deposits, consisting of glacial age material (on the basis of full glacial foraminiferal $\delta^{18}O$ values) below 2.0 m and deposited prior to 11.9 ka cal BP.

ii. An age reversal observed at 1.57 m within the core, demonstrating an additional mass movement emplacement.
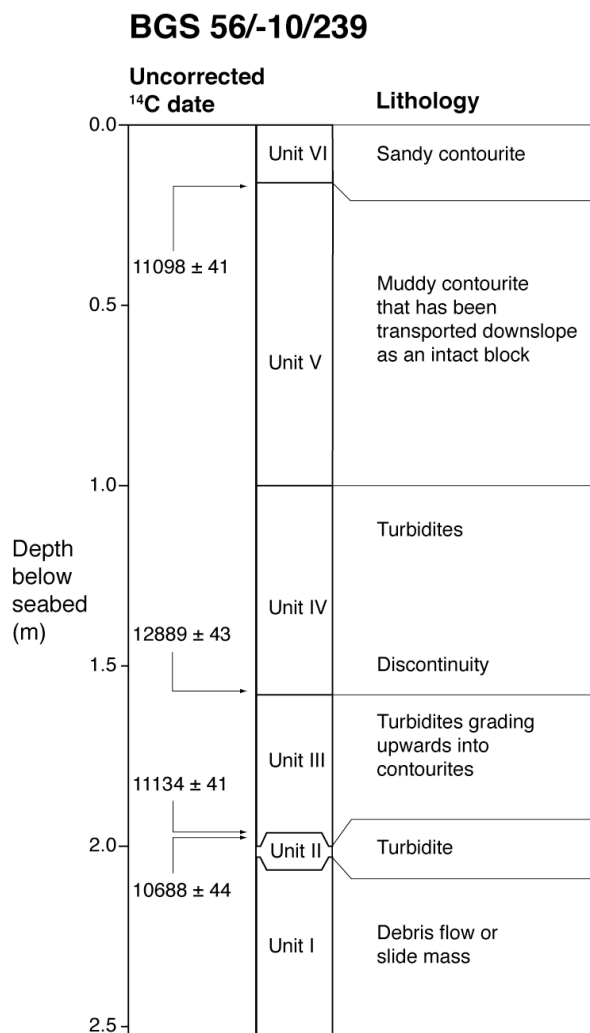
Figure 6.9: Radiocarbon chronology and lithology from gravity core BGS 56/-10/239.

This core sample is not crossed by a sub-bottom survey line, however, it is situated downslope from a major landslide scarp slope and an interpreted debris flow (see Figure 4.30 and Figure 6.8). The discontinuity between units III and IV (see Figure 6.9) demonstrates the impossible task of distinguishing between contourite and turbidite sediments on the acoustic record without ground truthing.

6.3.3. Age of interpreted acoustic facies

From the chronologies presented in this section it is possible to provide estimates for the ages of draping acoustic facies interpreted in chapter four.

6.3.3.1. Acoustic facies I

As outlined in chapter four, this unit is interpreted as contouritic sedimentation and where present it represents the uppermost unit in the sedimentary column (except when overlain by mass movement facies). The unit may contain sediments from a variety of sources. Deposition of the unit is governed by the intensity of slope parallel currents, which operate in a cyclonic gyre within the Rockall Trough (see chapter three).

It is generally accepted that, following the deglaciation, increased vigour of North Atlantic meridional overturning lead to increased intensity of slope parallel currents in the region (Armishaw, 1999; Knutz et al., 2002; Øvrebø et al., 2006). In combination with reduced ice sheet proximity, the change in oceanographic regime lead to a shift from glaciogenic to contouritic sedimentation.

Water column heterogeneity may lead to some variation in the overall pattern. For example, intermediate water masses may have been vigorous during glacial conditions (McCave et al., 1995) and deeper water masses more sluggish (McManus et al., 2004; Lynch-Stieglitz et al., 2007; Thornalley et al., 2010).

However, on the whole, enhanced contourite sedimentation is associated with the transition into inter-glacial conditions and this is supported by sediment cores from the region. Hibbert et al. (2010) identify a light coloured unit with high $CaCO_3$ concentrations in the top 2.8 m of core sample MD04-2822 at 2344 m water depth on the distal Barra Fan. The base of the unit is not dated, though it rests between 10.4 and 13.9 ka cal BP (Hibbert et al., 2010). At 2130 m water depth, Knutz et al. (2002) identify a silty, muddy contourite in the upper 1.5 m of core sample MD95-2006 (Figure 6.5); the base of which is dated at 11.3 ka cal BP (Wilson and Austin, 2002). Closer to the shelf edge, at 1320 m water depth, Kroon et al. (2000) date the base of a thin contourite unit in core sample 56/-10/36 at 11.4 ka cal BP (Figure 6.7).

The age reversal identified in core sample 56/-10/239 demonstrates that some instances of downslope mass movement are likely to be present in the interpreted contourite facies. This does not affect the interpreted base of unit age, however, such units may affect thickness.

The evidence cited above indicates an age of approximately 11.4 ka cal BP for the onset of post-glacial contourite deposition on the Barra Fan and, hence, for the base of acoustic facies I.

6.3.3.2. Acoustic facies II

This unit is interpreted as hemipelagic, though consisting of mixed glaciogenic, contouritic, hemipelagic sediments (see chapter four). The unit drapes underlying debris flows and is probably equivalent to the Gwaelo sequence interpreted by Stoker et al. (1993). The lowermost part of FIIa is often characterised by high amplitude reflectors, perhaps reflecting the increased glaciogenic influence identified by Knutz et al. (2002).

From comparison with deep-towed boomer data presented by Knutz et al. (2002) it seems likely that FIIa is equivalent to seismic unit I-A (see Figure 6.3). This unit rests above material dated at 19.95 ka cal BP (Wilson and Austin (2002) AMS ^{14}C date converted to calendar years in this thesis) and the lowermost AMS ^{14}C date in this unit yields a calendar age of 18 ka cal BP.

Using the argument that FIIa is equivalent to Knutz et al.'s (2002) seismic unit I-A and the Gwaelo sequence interpreted by Stoker et al. (1993), it can be dated as younger than 19.95 ka cal BP. Therefore, the unit consists of sediments deposited during the deglacial transition (including intervals of ice advance and retreat, as outlined in chapter three) prior to deposition of contourite sediments during the Pre-Boreal and Holocene.

6.3.3.3. Mass movement facies

The age of these facies (FIV and FV) may be determined based on their stratigraphic position relative to draping facies. As shown in Figure 6.10, the mass movement facies interpreted in chapter four are associated with a number of different seismo-stratigraphic positions.

The oldest of those visible occur prior to the deposition of FIIa, which drapes the mass movement deposits. Debris flow facies are rarely observed within the stratified FIIa unit, though areas of higher amplitude reflection may indicate some coarser grained turbidite deposition. Extensive debris flows are observed immediately above FIIa, some of which are capped by FI. Other instances of mass movement facies are observed on the seabed (see Figure 4.25 and Figure 4.33.A).

A.
West — East

100 ms TWTT

West — East

FIV and FV - Debris flow and hard debris exposed on seabed

Possible current scour means that these deposits may not have been recently emplaced

B.
South — North

125 ms TWTT

South — North

FI - Contourite

FIVa - High viscosity cohesive debris flow

Base of contourite unit 11.4 ka cal BP

C.
South — North

150 ms TWTT

South — North

FIIa - Hemipelagite

FIV - Debris flow

Lowermost date within hemipelagic unit 18.0 ka cal BP, uppermost material below hemipelagic unit 20.0 ka cal BP

——— Seabed   ——— Facies boundary   - - - - - Internal reflector

Fault

Figure 6.10: Stratigraphic position of debris flow facies. A. Exposed on seabed, B. Below contourite, C. Below hemipelagite. Location shown on map inset.

Caution must be used when bracketing the age of mass movement deposits via the adjacent hemipelagic or contouritic units. Hiatuses in the sedimentary column are possible and Knutz et al. (2002) note erosion of seabed sediments by bottom currents. The predominance of sandy contourite facies in recent sediments on the Barra Fan (Armishaw, 1999; Armishaw et al., 2000) and measured current velocities of 29 cm s^{-1} at 2500 m water depth within the Rockall Trough (Dickson and McCave, 1986) indicate the potential for erosion. Therefore, the presence of a mass movement unit on the seabed does not necessarily indicate recent emplacement. However, presence below a unit does signify emplacement prior to that of the overlying unit.

From the pinger data analysed in chapter four, the dating of foraminifera overlying a debris flow in chapter five and analysis of other local chronologies this thesis identifies two periods of mass movement on the Barra Fan (see Figure 6.11 for a stratigraphic overview).

The earliest pre-dates the deposition of FIIa and may be estimated to have been emplaced between 21 and 20 ka cal BP. This period includes the Peach 3 event, dated between 21.02 and 20.87 ka cal BP based on ground truthing of acoustic interpretation and AMS ^{14}C dates from Knutz et al. (2002) and Wilson and Austin (2002). This period corresponds to full-glacial conditions and may occur during a period of partial BIS retreat following Heinrich event 2.

Due to the effects of current scour, which may result in the scarcity of FI in the south of the study area, this thesis makes no significant distinction between mass movement facies observed on the seabed and those which underlie contourites.

The second period of mass movement identified is at the termination, or during the final stages, of deposition of FIIa; prior to the development of contouritic sediments during the Pre-Boreal and Holocene. Dating of planktonic foraminifera in gravity core 56/-10/239, above debris flow deposits in chapter five of this thesis, yields an age of circa 11.9 ka cal BP. This pre-dates the age of the base of contourite units in nearby cores (see section 6.2.3.1) by approximately 500 years, though the similarity of these ages provides greater certainty to the age estimate.

A calendar age between 12 and 11 ka cal BP places the most recent stage of significant slope failure on the Barra Fan towards the end of the Younger Dryas stadial. The main sediment failures observed on the central Barra Fan are buried below a thick, undisturbed, hemipelagic unit and occurred shortly after the maximum advance of the BIS (Scourse et al., 2009). Figure 6.11 provides an overview of the basis for this chronology.

Age constraint from core samples (see Figures 6.4 - 6.9 for details):

MD95-2006

Lower Barra Fan slopes, 2130 m
Samples unfailed material.

Muddy contourite	Base of contourite unit dated at 11.3 ka cal BP.
Hemipelagic and glacimarine muds	Oldest date 18 ka cal BP.
Contourite unit	Onlaps Peach 3, oldest date: 20.8 ka cal BP.
Glacimarine muds, dip below Peach 3	Top of glacimarine unit dated at 21 ka cal BP

BGS 56/-10/36

Mid-Upper Barra Fan, 1320 m
Located within slide scar, how much displacement has occurred?

Muddy contourite	Base of contourite unit dated at 11.4 ka cal BP.
Clayey sediments	Oldest date 12.6 ka cal BP.
Silty sediments	Dated at 13.4 ka cal BP.
Clayey sediments	Dated at 14.6 ka cal BP.

BGS 56/-10/239

Peach headwall, 1030 m
Samples debris flow, but overlying material is also disturbed.

Sandy and muddy contourite	Sediments dated between 12.3 and 14.5 ka cal BP.
Turbidites and contourites	Emplaced above material dated at 11.9 ka cal BP.
Debris flow Glacial δ¹⁸O values	Overlying a debris flow deposit.

Sedimentological overview

An upper unit, interpreted as contourite, is normally present. Its thickness is inferred to vary with current velocity, increasing as currents slow and deposit material. It is absent when velocity increases causing erosion.

This unit overlies the Peach 4 debrite.

Steeper slopes, such as those associated with debris flow lobes, tend to have thinner sediment cover.

The hemipelagic unit appears to have undergone displacement, particularly on the upper and middle slopes. This unit probably contains sediments derived from a number of sources and mechanisms.

Faults, that show little vertical displacement, may represent lateral shear.

Peach 3 is situated beneath this hemipelagic unit.

Upper slope - limited penetration but some evidence of surface debris flows.

Landslide scarp

Contourite unit present at times. Thickeness infered to vary with current velocity.

Peach 4

Debris flows at surface or below contourite unit.

Hemipelagic unit that shows faulting

Penetration limited below mass movement deposits

Debrite below hemipelagite

Peach 3

Chronological framework

Stratigraphy	Unit	Chronology
Peach 4	FIA - Muddy contourite	Base of unit: 11.3 ka cal BP
	FIVA - High viscosity debris flow	Overlying sediments: 11.9 ka cal BP
	FIIA - Hemipelagite	Base of unit: 18 - 20 ka cal BP
Peach 3	FIVA - High viscosity debris flow	Between: 20 and 21 ka cal BP
	FIIB - Glacimarine sediments that dip below debrite	Top of unit: 21 ka cal BP

Figure 6.11: Chronology of units within the study site. See Table 6.3 for details of calendar age calculations and text for discussion of acoustic facies age.

6.4. Margin morphology

As outlined in chapter four, between 56° N and 57° N, the northwest British continental margin is characterised by: areas of steep gullies; the large Peach landslide scar; and the gently angled, smooth, Barra Fan. Previous studies have emphasised the importance of across- and down-slope mechanisms in shaping the margin (Howe, 1996; Holmes et al., 1998; Armishaw, 1999; Armishaw et al., 2000; Knutz et al., 2002). This thesis now examines these processes, resultant seabed (and sub-seabed) features and considers how they may interact.

6.4.1. Slope parallel current features

Chapter three provided an overview of contemporary and glacial circulation within the Rockall Trough and on the Barra Fan. The key point to note, with regards to seabed-current interaction, is the operation of a cyclonic gyre with different water masses present throughout the water column (see Figures 3.4 and 3.5). Current velocity may range from 25 cm s^{-1} at base of slope to 37 cm s^{-1} at the shelf break (Dickson and McCave, 1986), though velocity will either accelerate or decelerate due to focusing or turbulence shedding as a consequence of terrain (Øvrebø et al., 2006).

It has been demonstrated that current velocities of 25 cm s^{-1} are sufficient to resuspend fine silts (Stabholz et al., 2013). Changes in velocity will have a major impact on whether the current acts to erode or deposit sediments, both in absolute and relative (i.e. particle size dependence) terms.

Figure 6.12 provides an example of current reworked sediments from approximately 500 m water depth on the upper Barra Fan. As chapter three demonstrates, in the contemporary circulation, sediments at such depths are bathed by East North Atlantic Water (see Figure 3.5), which circulates at velocities in excess of 30 cm s^{-1} (Dickson and McCave, 1986; New and Smythe-Wright, 2001). Work by Armishaw (1999) and Knutz et al. (2002) demonstrates the presence of current related bedforms and the pinger data examples shown in Figures 6.12 and 6.13 support this. Key features in Figure 6.12 are the truncated reflectors on southern aspects of bathymetric highs and the development of drifts in the lee. Sharp crested ridges are visible between fixes 8 and 10, possibly indicating active dunes. Figure 6.13 shows a further example of current erosion on ridge crests and development of drift deposits within troughs. This latter example demonstrates a disagreement between this thesis and the work of Armishaw (1999) who interprets these upper sediments as debris flow and turbidite units.
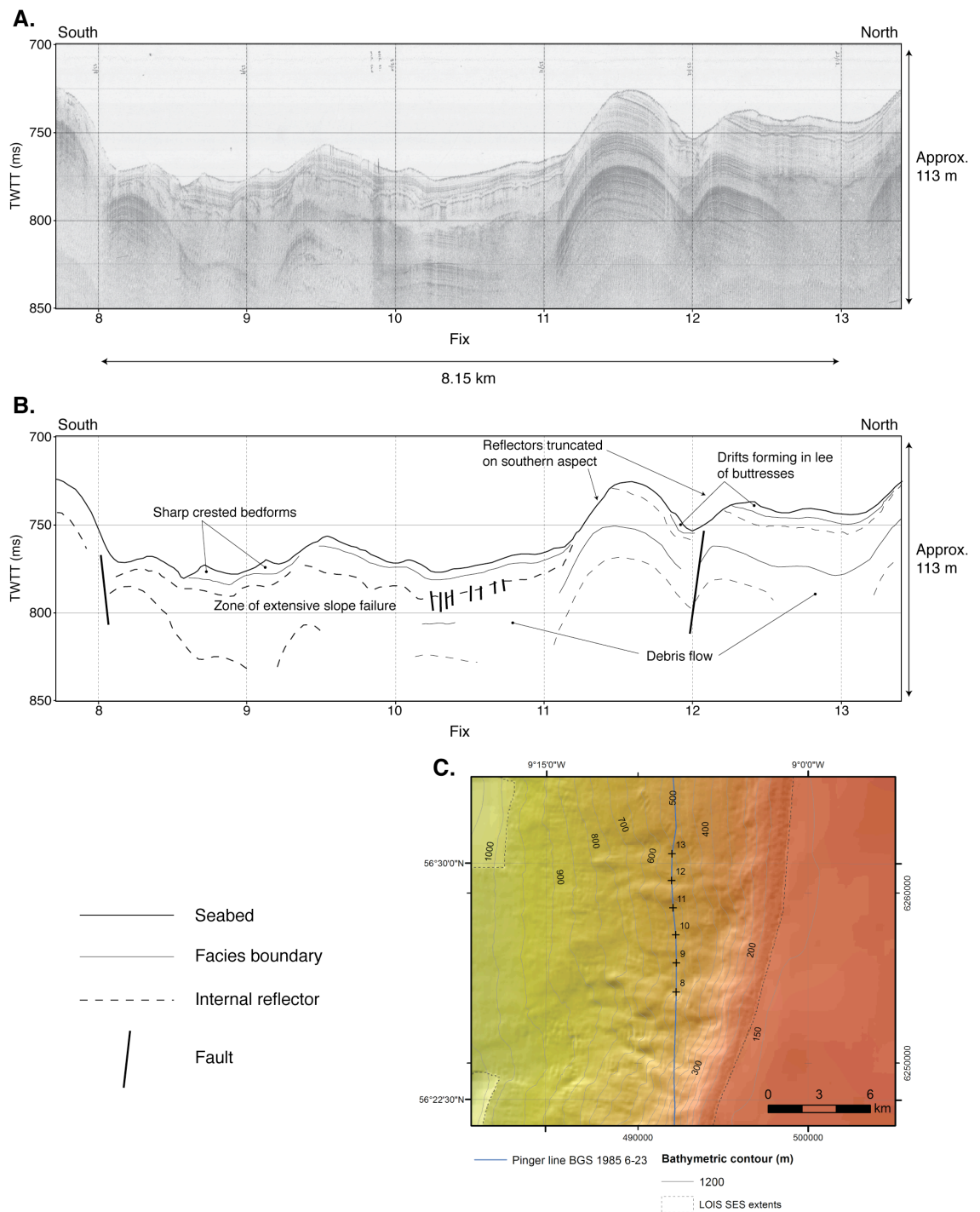
Figure 6.12: Example of current scour and deposition from Pinger line BGS 1985 6-23. Note that the prevailing current flows south to north. Surface sediments, which may have undergone some downslope transport, have been reworked by the north flowing current.

This thesis presents an alternate interpretation for two reasons. First, the large numbers of sediment cores taken from the area have not identified debris flows in the uppermost sediments (see for example Armishaw et al., 2000). Second, the morphology of the unit is consistent with current deposition and scour.

The current direction and velocity is consistent with the erosion of the upper unit (an indication of current controlled sedimentation (Faugères and Stow, 1993)) on southern aspects and aggradation on north facing aspects visible in Figures 6.12 and 6.13 (and the interpreted section in Figure 4.28). Debris flows and turbidites would be expected to form ponded deposits, whereas the characteristics displayed in Figure 6.13 are progradational, displaying a morphology similar to the confined drifts characterised by Faugères et al. (1999). This thesis does interpret debris flows below these upper units.

During glacial periods the circulation is anticipated to be more sluggish (Bond et al., 1993; McManus et al., 2004; Thornalley et al., 2010). However, slope parallel currents were still significant, with vigorous intermediate currents noted by McCave et al. (1995). As such it may be anticipated that the role of such currents is subtly different during glacials.

If velocity is reduced currents may be expected to be less erosive, but they will still perform an important sediment transport role. The major sediment source of the Barra Fan during glacial periods was the Barra Fan ice stream (Scourse et al., 2009), which eroded the deeps visible on the Hebrides Shelf (see Figure 6.2). From these features it appears that the major input of ice would have been toward the southern sector (Donegal) of the Barra Fan. As noted by Hesse et al. (2004), and discussed in chapter two, fine grained sediments may loft off meltwater plumes and disperse in the water column. In a location with a northward flowing slope current, such as the Barra Fan, it would be anticipated that the finer sediments would be deposited further north than coarser grained material.

A.

North   South

TWTT (ms)

700
800
900
1000
1100

Approx. 300 m

38   37   36   35   34   33   32   31   30   29

Fix number

B.

←———————————— 9.7 km ————————————→

TWTT (ms)

700
800
900
1000
1100

FIIa - parallel reflectors, fluid present and some faulting

FIII or FIb - high amplitude unit

FIIa - deformed, internal structure more transparent and frequent faulting

FIVa - overlies truncated reflectors from landslide scarp

FIb - reflectors truncated at landslide scarp

FIa - drift morphology

FIVa

FIIb

FIVc

FIVa

FIIb - highly deformed with folds and faults

Approx. 300 m

38   37   36   35   34   33   32   31   30   29

Fix number

Legend:
- Seabed
- Facies boundary
- Base of debris flow unit
- Internal reflector
- FVII - Fault
- FVI - Fluid

Pinger Line BGS 1985 6-27
Scarp slope - tick on downslope side
LOIS SES extents

Figure 6.13: Upper landslide scar showing slumped sediments with contourite drift formation. Approximately 17 times vertical exaggeration.

6.4.1.1. Influence of the Peach slide scar on current velocity and sediment deposition

Erosion of surficial sediments within the Peach slide area was noted by Knutz et al. (2002) and this thesis has documented thick contourite units. These contrasting observations may be explained by two reasons. First, the erosion noted by Knutz et al. (2002) occurs at approximately 2000 m water depth, compared to sediment accumulation documented in this thesis at nearer 1000 m water depth (see chapter four). As shown by the review of ocean circulation in chapter three, these depths are bathed by different water masses, which may well have different velocities. The second reason is that velocity will vary locally due to eddies and turbulent flow.

Bottom current flow is governed by the principles of fluid dynamics. Interaction with bathymetric features and other water masses will lead to turbulence and eddies (see Alendal et al., 2005 for overview of turbulence within the Storegga slide scar). As considered by Bradshaw (1971), 'turbulence can be thought of as a tangle of vortex lines or partly rolled vortex sheets, stretched in a preferred direction by the mean flow'. Eddies are produced by vorticity and drag on the flow margins and may result in significant variation in flow velocity.

Øvrebø et al. (2006) explain increased rates of deposition on the Porcupine slope by reference to turbulence shedding, caused by bathymetric depressions, leading to reduced current velocity. Conversely, Howe (1995) suggests that, when traversing steep slopes, reduced bottom drag may increase current velocity. As such, it is anticipated that the complex morphology of the Peach slide will exert an equally complex influence on bottom current flow.

It is expected that the Peach slide scar will act to channel flow, causing acceleration on steeper slopes, and eddies where the flow interacts with the margins causing deceleration. In eddy locations finer grained sediments may be deposited. Thicker deposits are also anticipated to form in the lee of slide margins, sheltered from the main across slope current. Indeed, these locations may preferentially accumulate finer sediments transported from the main area of sediment input to the south.

Recent work from the Plata del Mar Canyon, on the Argentine Basin margin, provides further support to this hypothesis. This canyon is in a similar oceanographic setting to the Peach slide, with a northward flowing across slope current strongly influencing sedimentation (Preu et al., 2013; Voigt et al., 2013). Voigt et al. (2013) argue that the large increase in sedimentation rates to the north of the canyon is due to reduced current velocity and, therefore, carrying capacity of Antarctic Intermediate water due to lower velocity: a consequence of hydrodynamic interaction with the canyon.

During glacial periods this may be particularly significant at water depths of 1000 m to 2000 m due to the vigorous intermediate water regime (McCave et al., 1995). Figure 4.31 shows the observed increased contourite thickness within the Peach slide scar, compared to the south facing aspects of the Barra Fan: evidence that supports preferential deposition within the slide scar.

6.4.2. <u>Mass movement features</u>

Geophysical interpretation in chapter four of this thesis has allowed the identification of a number of different features that are indicative of downslope mass movement. The large volume and high quality of work conducted on the Norwegian margin, in particular the Storegga (Haflidason et al., 2004; Bryn et al., 2005a; Haflidason et al., 2005; Kvalstad et al., 2005) and Trænadjupet (Laberg and Vorren, 2000; Laberg et al., 2002a; Laberg et al., 2002b) slides, provides a useful comparison. However, proximity to oil and gas developments provided vastly increased resources and data quality for the Norwegian studies; as such data is not always directly comparable.

Consideration was also given to mass movement events on the northeast US continental margin (Hornbach et al., 2007; Chaytor et al., 2009; Locat et al., 2009; Twichell et al., 2009). However, with the exception of Nova Scotia (Jenner et al., 2007), ice sheets did not reach the shelf edge on this margin (Twichell et al., 2009). On the northeast American margin, the bulk of submarine mass movements occur in zones where rivers transported glacial sediments to shelf-edge deltas (McMaster and Ashraf, 1973), or in zones of little or no glacial influence (Chaytor et al., 2009; Lee, 2009; Twichell et al., 2009). Therefore, comparison with the Norwegian events, associated with shelf-edge ice, trough mouth fans (Dahlgren et al., 2005) and along slope currents (Bryn et al., 2005b) seems more appropriate.

6.4.2.1. Features identified

A range of morphologies are associated with submarine mass movements, the processes that initiate them and their downslope evolution (Coleman and Prior, 1988; Hampton et al., 1996; Canals et al., 2004). Several of these are interpreted to occur on the northwest British continental margin and Barra Fan.

Shallow faults are interpreted throughout the study area (see further discussion of faults in section 6.4.3) though obvious vertical displacement is not common. In part this may be due to data resolution issues (outlined in section 4.4), however, it may also reflect the presence of tension fractures and lateral spreading as documented at Storegga (Haflidason et al., 2004; Bryn et al., 2005a) and Trænadjupet (Laberg and Vorren, 2000). The area of slumped sediments, a pinger data example of which is

shown between fixes 33 to 35 in Figure 6.13, situated between two different scarp slopes may reflect a similar morphology to the Storneset region of the Storegga slide (Kvalstad et al., 2005).

Intact blocks are also visible. Some, such as those shown in Figure 6.14, have undergone limited downslope movement and may indicate extensional faulting following the removal of the toe of the slope, in a mechanism similar to that proposed for retrogressive sliding at Storegga (Kvalstad et al., 2005). The undulating, slope-parallel gradient variation visible within the landslide scar and presented in Figures 4.11 and 6.14.D appear to be related to this mechanism.

Other blocks appear to have been transported as rafts within a debris flow matrix and have potentially travelled tens of kilometres (see Figure 6.15) in a mechanism similar to that observed at Trænadjupet (Laberg and Vorren, 2000), Storegga (Haflidason et al., 2004) and the Brunei slide (Gee et al., 2007).
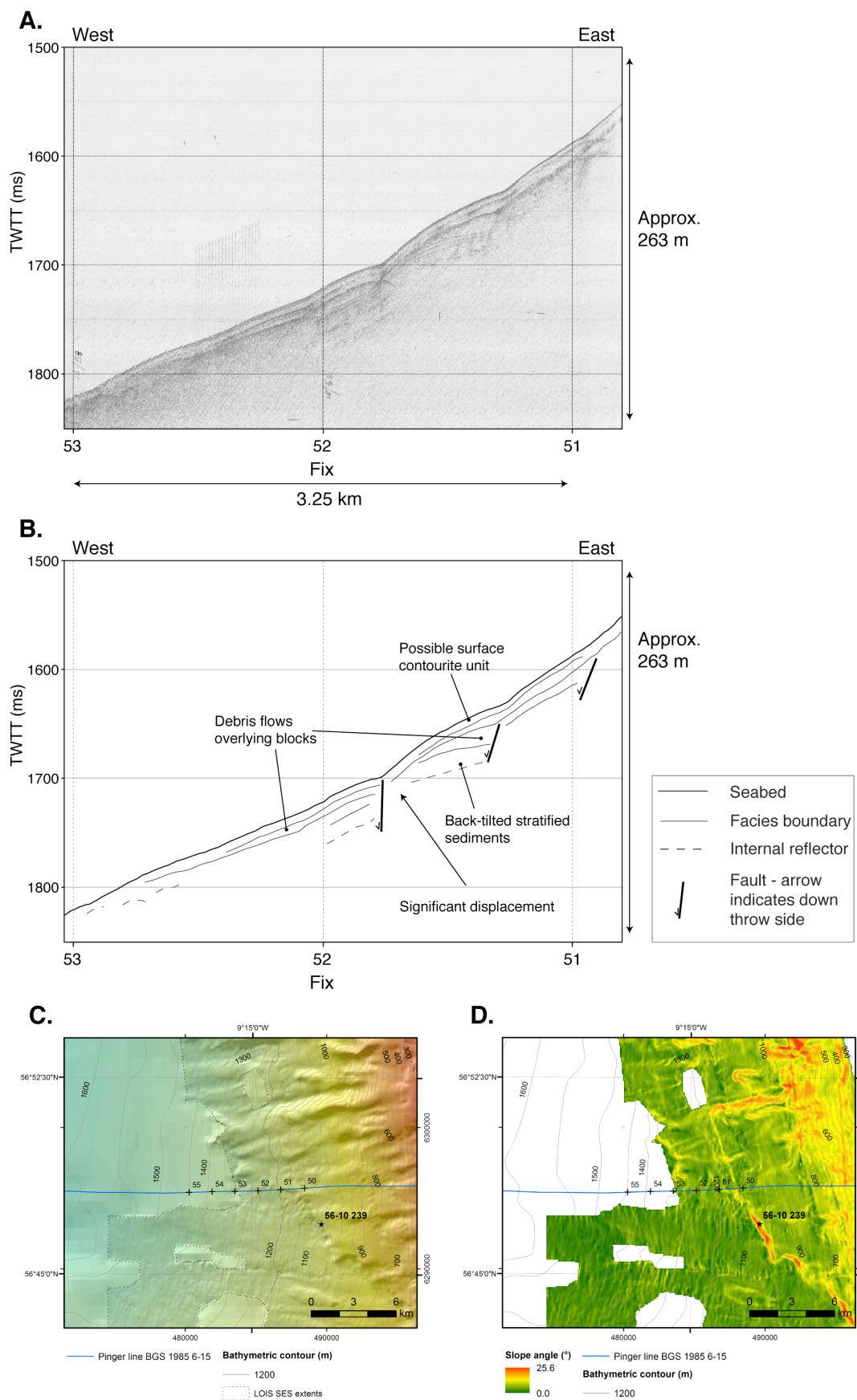
Figure 6.14: Example of extensional faulting at the slide's northern margin. A. Pinger data example. B. Interpreted sub-surface geology. C. Bathymetry. D. Gradient as calculated from bathymetry.

Debris flows are widespread throughout the study area, an attempt is made to distinguish between high and low viscosity cohesive debris flows using the methodology outlined by Tripsanas et al. (2007). The results (presented individually in Appendix D) demonstrate a dominance of high viscosity flows. However, low viscosity flows are observed in shallow sediments on the Barra Fan. Possibly reflecting failure of unconsolidated clays with high water content.
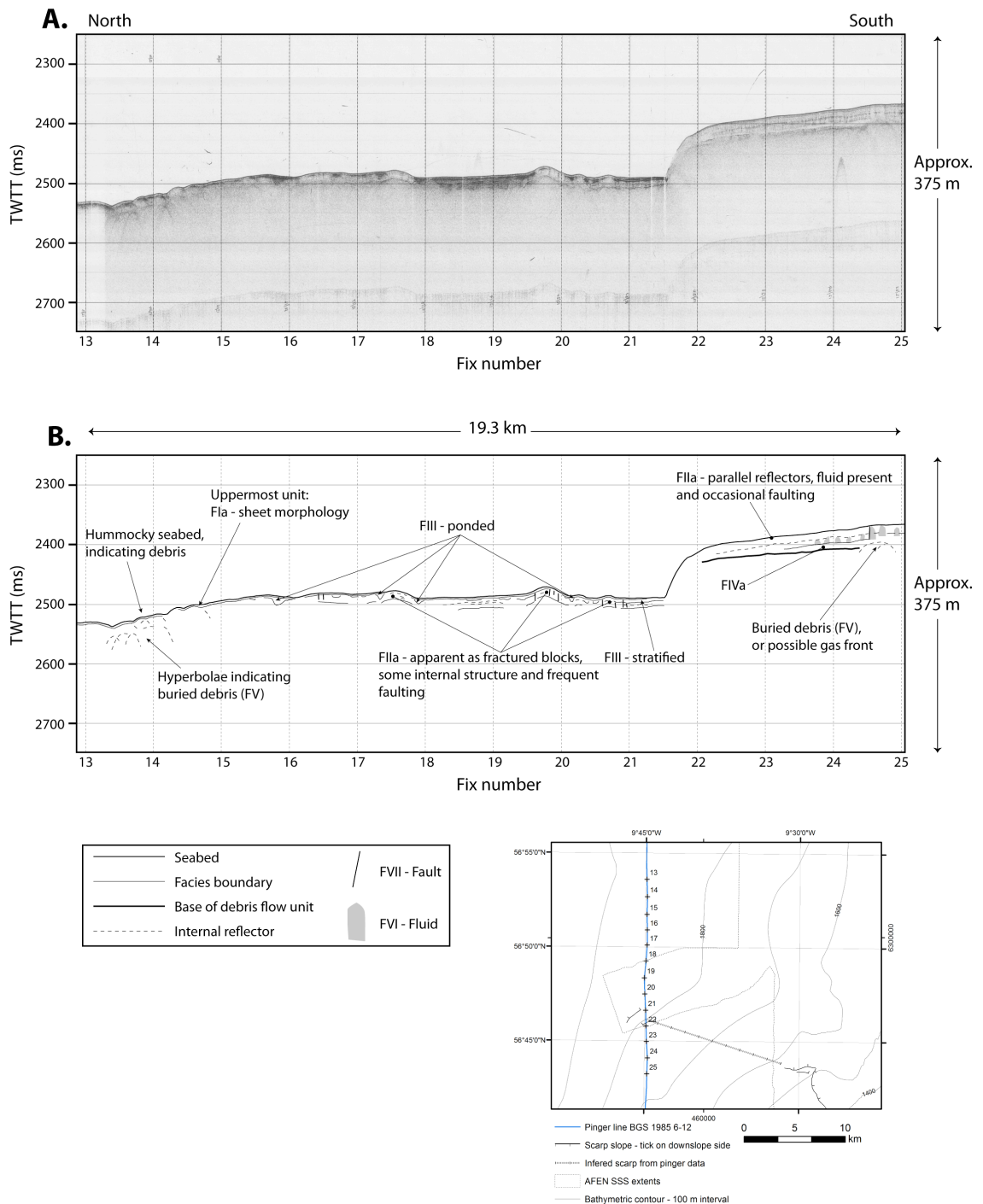
Figure 6.15: Middle slope landslide scar, showing blocky debris overlain by a thin contourite unit. Approximately 18 times vertical exaggeration.

Hyperbolic acoustic returns, exposed on the seabed and buried within debris flows, suggest the presence of blocky debris. This supports a mechanism of break-up of larger blocks, creating a blocky debris flow of the type observed on the Norwegian (Laberg and Vorren, 2000; Haflidason et al., 2004) and Nova Scotian (Jenner et al., 2007; Tripsanas et al., 2007) margins.

6.4.2.2. Variation within landslide scar morphology

Holmes et al. (1998) identify four separate phases of sediment failure associated with the Peach slide since the mid-Pleistocene. The data presented in this thesis shows a clear distinction between Peach 3 and Peach 4, although data coverage of the events is not complete. It is clear that the landslide scar morphology, visible in the geophysical data analysed in chapter four, reflects multiple slope failures.

Truncated reflectors in the prominent landslide scar visible in Figure 6.13 are draped by the hemipelagic FIIa, implying failure prior to 20 ka cal BP. Faulting and loss of internal stratification suggest that hemipelagic sediments downslope from the older scar have also undergone some form of failure (as discussed in section 6.4.2.1). Additionally, within the landslide scar, numerous debris flows and blocky debris occur at or near the seabed and are believed to have been emplaced between 12 and 11 ka cal BP.

Comparison of the across-slope sections through the area of slope failure shown in Figures 6.13 and 6.15 demonstrates that the furthest downslope section (Figure 6.15 at approximately 1900 m water depth) lacks the in situ deformed blocks but appears to show rafted blocks within a debris flow matrix. Any overlying contourite unit is thin and probably relates to Pre-Boreal and Holocene deposition.

The inference from these data is that following excavation of the landslide scar by the Peach 3 event between 20 and 21 ka cal BP, subsequent deglacial sedimentation draped the slide scar (as evidenced by draping of truncated reflectors in Figure 6.13). This deglacial sediment failed, via a retrogressive mechanism which left partially failed blocks in situ towards the head of the scar, between 12 and 11 ka cal BP.

6.4.3. Fluid release and fault structures

As discussed in chapter four, fluid is commonly observed within the hemipelagic sediments that drape the Barra Fan (see Figure 4.27). Fluid is also observed within slumped hemipelagic sediments and may be associated with faulting.

In the unfailed sediments of the Barra Fan two separate mechanisms of fluid release may occur. The most common seems to occur as a result of sediment compaction via deposition, as has been noted further north on the northwest British continental margin

(Selby, 1989; Strachan and Evans, 1991; Baltzer et al., 1998). As outlined in section 2.2, loading of a saturated soil results in increased pore fluid pressure and subsequent expulsion of fluid and compaction of sediments. In such cases faults may act as conduits for fluid migration (Gay et al., 2007; Paull et al., 2008), with seepage force potentially eroding sediments (Orange and Breen, 1992).

Fault development may be gravity driven (see Yang and Davies, 2013) and facilitated via development of excess pore pressure beneath the layer that is subject to downslope creep. Though polygonal faults may develop via de-watering and have been observed in the Faeroe-Shetland channel (Bulat and Long, 2001). The example shown in Figure 4.24 appears to demonstrate some of the characteristics of polygonal faulting (Bulat and Long, 2001; Gay and Berndt, 2007). However, bathymetric data does not allow detailed examination of the seabed morphology and the faults could simply be focusing the fluid flow (Gay et al., 2007).

6.5. Late-Pleistocene sedimentation processes on the Barra Fan

6.5.1. Proposed failure mechanism

This thesis now considers the evidence from the Barra Fan and analysis from other regions to propose a possible failure mechanism. Lack of data make comparisons difficult and further research is required to verify the processes that initiated sediment failure in the Peach slide (see chapter seven for proposed future research).

As discussed in section 6.4.2, the setting and morphology of the Barra Fan, and the Peach slide, is more similar to the Norwegian margin than to the northeast American margin. This similarity results from the presence of shelf-edge ice (Laberg and Vorren, 2000; Dahlgren and Vorren, 2003; Bryn et al., 2005a), trough mouth fans (and the location of submarine mass movement in relation to the fans; Dahlgren et al., 2005) and a northward flowing across-slope current (Dahlgren and Vorren, 2003; Bryn et al., 2005b). The tectonic setting on the northwest European rifted margin is also similar (see chapter three; Praeg et al., 2005; Anell et al., 2009).

Before discussing the failure mechanism of the Peach slide, this thesis summarises the processes that have been proposed for Trænadjupet and Storegga. Trænadjupet is located on the mid-Norwegian continental margin at approximately 68° N, on the slope, at the termination of a glacially eroded trough (Laberg and Vorren, 2000; Laberg et al., 2002a; Laberg et al., 2002b). On the basis of seismic and sidescan sonar data, it is argued that failure of blocks occurred on planes of weakness, caused by interglacial sediments (inferred, by analogy to Holocene sediments, to have high water content) being compacted by rapidly deposited, low permeability glacial sediments producing

excess pore pressure (Laberg and Vorren, 2000; Laberg et al., 2002b). The recent large failure has been dated at 4 ka cal BP (see Laberg et al., 2002b; details in section 2.5.1.3 of this thesis), well after the retreat of shelf-edge ice. Interestingly, when comparing to the Peach slide, this failure was preceded by an event that occurred near to the LGM (Laberg et al., 2002b). Also, seismic evidence demonstrates that the Trænadjupet slide scar is accumulating contourite deposits during the Holocene (Laberg et al., 2002a).

Storegga has been subject to huge volumes of research due to its location in a large gas field (see Bryn et al., 2005a; Solheim et al., 2005 for overview of journal special issues). As outlined in section 2.5.1.4 of this thesis the slide is located at the north of the North Sea Fan and is dated to approximately 8.1 ka cal BP (Bondevik et al., 1997; Haflidason et al., 2005). As with Trænadjupet, emphasis is placed on the cyclicity of sedimentation between glacial and interglacial periods (Berg et al., 2005). However, the key difference proposed for Storegga is the role of lateral pressure transfer. During the Weichselian the Storegga region is calculated to have received 100 m of new sediment, compared to the North Sea Fan's 500 m (Berg et al., 2005). It is proposed that this differential loading created high excess pore pressure in the Kai and Brygge Formations, which transferred laterally into the toe region of the Storegga slide due to the impermeability of the overlying sediments (Kvalstad et al., 2005). Since the failure up to 25 m of sediment has been deposited in the scar (Berg et al., 2005), this is argued to be the result of contourite deposition due to reduced current velocity (Solheim et al., 2005).

The setting of the Barra Fan and Peach slide (see chapter three) is markedly similar to the Trænadjupet and Storegga locations on the Norwegian margins. The most recent event is post-glacial and is preceded by a glacial failure, as at Trænadjupet (Laberg et al., 2002b). Features identified within the Peach slide in this thesis bear similarities to those observed within the Storegga and Trænadjupet slides. Outlined in section 6.4.2, the mass movement features documented (rafted blocks, faults with little vertical displacement, extensional faulting) appear to support the movement of material along bedding planes. Evidence of fluid release, presented in Figure 4.27 and discussed in section 6.4.3, provides a mechanism to produce excess pore pressure below low permeability glacial sediments. Chapter four of this thesis documented preferential accumulation of sediments (interpreted as muddy contourites) within the upper Peach slide scar, in a mechanism similar to that proposed at Trænadjupet (Laberg et al., 2002a) and Storegga (Bryn et al., 2005b; Solheim et al., 2005).

As with the Norwegian slides (Laberg et al., 2002b; Haflidason et al., 2004; Berg et al., 2005; Bryn et al., 2005a; Bryn et al., 2005b; Solheim et al., 2005) this thesis suggests that a key factor in slope failure on the northwest British continental margin is the interaction between sediments deposited via slope-parallel currents and those deposited via glaciogenic processes. Located to the north of the Barra Fan, away from the area of main sediment input in the south (see chapter three), it is possible that some lateral transfer of excess pore pressure (as proposed at Storegga by Kvalstad et al., 2005) may occur. However, this is a subject for further research as there is no supporting evidence at present.

There is evidence of a vigorous northward flowing across slope current (see Figure 6.12, Figure 6.13; and discussion of oceanographic setting in chapter three), which appears to facilitate the deposition of sediments between 800 m and 1600 m below sea level within the Peach slide scar (see Figure 4.31). Larger lithic particles are deposited preferentially due to their greater mass and settling velocity (Goossens, 2008). Owing to the distance north of the main area of sediment input to the fan (see chapters three and four) it is argued that the Peach slide will preferentially accumulate finer sediments, deposited as the across-slope current reduces velocity to due bathymetric interaction (in a mechanism similar to that proposed by Solheim et al. (2005) at Storegga and by Voigt et al. (2013) for the Plata del Mar canyon). This should magnify the glacial to inter-glacial sedimentation cyclicity, as clays would be expected to dominate during glacial periods (deposited from iceberg rainout or turbidity currents via across-slope current transport) and silts during interglacial (resuspended and transported from the central Barra Fan via the action of the vigorous across-slope current). As such, the Peach slide region should be extremely efficient at producing excess pore pressure.

This excess pore pressure produced by compression of porous, contourite units by rapidly deposited, low-permeability glaciogenic sediments would lead to reduced shear strength and increased water content below the low-permeability unit. Strachan and Evans (1991) and Baltzer et al. (1998) document liquefaction failures on the northwest British continental margin, such failures may occur via excess pore pressure (and by inference water content) pushing clays beyond their plastic or liquid limit (see section 2.2). This would result in a weakened sedimentary column that could fail due to sedimentary loading or because of seismic shaking from a relatively low magnitude earthquake.

Further research (sedimentological and geophysical) is required to verify this mechanism and chapter seven presents ideas for future work.

6.5.2. A chronology of sedimentation and failure

Shown by palaeoceanographic studies, during interglacial periods an active bottom current regime favours the development of contourite units on the Barra Fan (Armishaw, 1999; Armishaw et al., 2000; Knutz et al., 2001; Knutz et al., 2002). These sediments have a high porosity and water content (see section 2.2.1). During the transition to glacial conditions the Barra Fan's current regime becomes less vigorous and there is a greater input of terrigenous sediments via glaciogenic sedimentation (Knutz et al., 2002; Lynch-Stieglitz et al., 2007). Rich in clays, these sediments tend to have lower permeability than the underlying contourite units.

Suggested for both Trænadjupet (Laberg et al., 2002a) and Storegga (Haflidason et al., 2004; Bryn et al., 2005a; Solheim et al., 2005), it seems that the Peach slide scar also accumulates contourite deposits. Indeed the scar seems to act as a sediment trap, with the steep seabed morphology causing turbulence shedding and reduced current velocity (Øvrebø et al., 2006; Voigt et al., 2013). As discussed in section 6.5.1, during interglacial periods this will lead to accumulation of silts and during glacial periods a preferential deposition of clays. Consequentially, the process of excess pore pressure development between inter-glacial and glacial sediments will be amplified.

Outlined in section 3.3, the BIS is thought to have reached the shelf edge between 30 and 25 ka cal BP (Bradwell et al., 2008) and its first stable onshore position in northwest Scotland has been dated between 15.5 and 17.9 ka cal BP (Everest et al., 2006). Between these periods the Barra Fan was subject to rapid rates of sediment deposition during a period of glacimarine sedimentation, with rates in excess of 1 m ka[-1] observed in piston core MD95-2006 on the distal fan (Knutz et al., 2002). As shown by the interpretation of acoustic facies IIa (see Figure 6.12) in this thesis sedimentation rates would have been greater nearer the shelf break.

As shown by sub-bottom interpretation tied to AMS ^{14}C dates (see Figure 6.4, Figure 6.11 and Knutz et al. (2002); Wilson and Austin (2002)) Peach 3 occurred circa 21 ka cal BP, following the period of rapid glacimarine sedimentation associated with shelf-edge glaciation and Heinrich event 2 (Hemming, 2004). Glacial debris flows on the central Barra Fan also occurred during this period and may be coeval with Peach 3 (or indeed part of the same event). Additional AMS ^{14}C dates presented by Wilson and Austin (2002) demonstrate that between 23.14 and 20.87 ka cal BP sedimentation rates in the distal Barra Fan were in excess of 1.1 m ka[-1]. Rapid sedimentation, of greater magnitude nearer the ice-front, on the upper and middle fan would have a strong destabilising influence on the continental slope. As has been argued on the Norwegian margin, in the examples of Storegga (Bryn et al., 2005a) and Trænadjupet

(Laberg et al., 2002b; see also section 2.4), and explained mechanically in section 2.2, such rapid deposition of low permeability sediments would lead to development of excess pore pressure and reduced sediment shear strength. The occurrence of Peach 3 immediately after the period of greatest sedimentation rates, combined with the evidence of fluid expulsion documented in this thesis, supports the operation of a mechanism similar to that on the Norwegian margin occurring on the northwest British continental margin (see Figure 6.16).

Time period	British ice sheet	Slope parallel currents	Sedimentation regime	Susceptibility factors	Mass movement event
MIS 3	British ice sheet undegoes expansion during marine isotope stage 3, there is a significant ice sheet on inner continental shelf prior to 30 ka cal BP. Early phases of the Peach slide occurred prior to this time.				
— 30 ka —					
MIS 2	Major growth and Barra Fan ice stream extends to shelf edge. BIS achieves maximum extent circa 24 ka cal BP.	Generally sluggish, perhaps with occasional periods of enhanced activity.	Glaciogenic, rapid sedimentation rates following Barra Fan ice stream reaching shelf edge.	Rapid build-up of clay rich, low permeability, sediments. Encourages development of excess pore pressure. Lowered sea-level reduces pressure on gas hydrates.	No large scale failures, but turbidites deposited on Barra Fan reflecting hyperpycnal flows and cyclic ice expansion and retreat. Peach 3 occurs circa 21 ka cal BP.
— 20 ka —					
Termination 1 and Heinrich 1	Retreat and subsequent readvance.	More vigorous / Sluggish	Contourites and hemipelagites / Glaciogenic	Fluctuating sedimentation regime constructs a high porosity - low permeability sequence. Rapid deposition of final periglacial sediments generating excess pore pressure. Earlier slide phases create locally steep slopes and water column turbulence that facilitates silt deposition. Possible role of post-glacial seismicity.	No large scale failures. Some evidence of minor debris flows within delgacial sequence.
— 15 ka —					
Bølling Allerød	Ice stream retreats from the shelf edge.	More vigorous	Contourites and hemipelagites		
— 13 ka —					
Younger Dryas	Ice sheet calving on shelf edge.	Sluggish	Glaciogenic, sedimentation rates > 2.0 m ka^{-1}		Peach 4 occurs between 11 and 12 ka cal BP.
— 11.5 ka —					
Pre-Boreal	Ice retreats	Vigorous	Contourites and hemipelagites	Deposition of high porosity sediments	Possible minor sediment failures as slide scar stabilises.

Figure 6.16: Schematic of sedimentation driven slope failure on the Barra Fan. Refer to text for detailed discussion and evidential support.

Different events are expected to display slight differences, for example the role of lateral fluid migration at Storegga (Kvalstad et al., 2005). However, the underlying role of porosity and permeability contrast between glacial and inter-glacial periods remains; as does the potential delay in excess pore pressure peak due to fluid dissipation rates (Biscontin et al., 2004).

The marine record supports a return to contourite sedimentation immediately after 20.87 ka cal BP (Knutz et al., 2002), however, a return to glacimarine sedimentation follows. Further south, on the flank of Porcupine Seabight, Peck et al. (2007) observe the last significant BIS input at 16.8 ka cal BP, coeval with Heinrich event 1. Kroon et al. (2000) suggest that the Bølling interstadial was fully established by 14.7 ka cal BP, with the Younger Dryas between 13 and 11.5 ka cal BP.

The glacial transition was marked by periods of reinvigorated North Atlantic meridional circulation (Thornalley et al., 2010), which would have been associated with increased bottom current vigour and associated sedimentation (Armishaw, 1999; Armishaw et al., 2000; Knutz et al., 2002), as well as colder episodes associated with glacimarine sedimentation (Kroon et al., 2000; Knutz et al., 2001). Through the Pre-Boreal and into the Holocene contouritic sediments dominate the Barra Fan (Armishaw, 1999; Armishaw et al., 2000).

AMS ^{14}C dating of foraminifera in gravity core 56/-10/239 during this PhD project provides a date of 11.9 ka cal BP for sediments that overlie a debris flow consisting of glacial age material. As shown in Figure 4.33, a contourite unit (the base of which is dated at 11.3 ka cal BP; see Figure 6.10 and Figure 6.11) appears to drape the majority of debris flow facies in the Peach slide area. This observation, combined with the age of foraminifera overlying the debris flow deposit in gravity core 56/-10/239, suggests that the Peach 4 event occurred between 12 and 11 ka cal BP, during the Younger Dryas Pre-Boreal transition.

The occurrence of some mass movement facies exposed on the seabed could indicate an additional, more recent, failure (supported by the age reversal at 1.57 m in gravity core 56/-10/239), however, this could also indicate the presence of current scour as documented by Knutz et al. (2002).

Table 6.4 provides an executive summary of the Peach debrite ages. This thesis has focused on the most recent events, Peach 4 and Peach 3. Details are also given of the earlier phases of the Peach slide; it should be noted that these are very loosely constrained and more geophysical and sediment core data is required to accurately understand the events' age and inter-relations (i.e. how many events actually are

there?). Even the more recent phases of the Peach slide are associated with a considerable degree of uncertainty (see Figure 2.3 and Table 6.4) and as such this thesis recommends that future research looks to improve their age constraint (see chapter seven).

Event	Age	Basis and uncertainty	References
Peach 4	11 - 12 ka cal BP	Sediments overlying debris flow deposit in core sample 56/-10/239 dated at 11.9 ± 0.16 ka cal BP. Base of contourite unit, that overlies debrite, dated at 11.4 ka cal BP. Core sample 56/-10/239 is subject to an age reversal and does not represent continual sedimentation. A hiatus could be present between deglacial and contouritic sedimentation. Analysis of additional core samples that overlie and penetrate the event is needed is improve certainty.	This thesis
Peach 3	21 ka cal BP	Sediments that onlap the event dated at 20.87 ± 0.46 ka cal BP, sediments that dip below the event are dated at 21.02 ± 0.47 ka cal BP (Knutz et al. (2002) seismic interpretation and ^{14}C dates; Wilson and Austin (2002) ^{14}C dates; calendar year calibration performed in this thesis). The primary uncertainty stems from the use of a single core and the potential complexity of the event. In conjunction with seismic data, core sample MD95-2006 brackets one lobe of the Peach 3 event; does it occur in single or multiple stages?	Knutz et al. (2002); Wilson and Austin (2002); Maslin et al. (2004); this thesis
Peach 2	36.5 ka cal BP	Seismic-stratigraphic correlation based on age-depth model produced by Knutz et al. (2001; 2002). Error bars are unknown, but are potentially several thousand years. This event is not sampled and the potential uncertainty is high (see Figure 2.3).	Maslin et al. (2004)
Peach 1	Early to mid-Pleistocene, Prior to 0.44 Ma	Interpreted, from seismic data, to contain early-Pleistocene sediments and to pre-date shelf-edge glaciation. This event is not sampled and age constraint is extremely loose.	Holmes et al. (1998)

Table 6.4: Executive summary of Peach debrite ages, supporting evidence and associated uncertainty.

Peach 4's timing and location, within a previously excavated slide scar, coupled with its small size in comparison to the previous debrites (Holmes et al., 1998) supports a hypothesis of failure occurring due to excess pore pressure developing in contourite

sediments below the final deglacial deposition (see Figure 6.11). Perhaps pushed to instability by a final burdening from rapid sedimentation associated with the Younger Dryas: vibrocore 56/-10/36 demonstrates that rates exceeded 2.0 m ka^{-1} during this interval (Kroon et al., 1997).

Repeat slope failures within landslide scars are observed in numerous locations, for example: the Storegga and Trænadjupet slides on the Norwegian margin (Evans et al., 1996; Laberg et al., 2002b); the Afen slide in the Faeroe-Shetland channel (Wilson et al., 2004); and the Peach slide on the Barra Fan (Holmes et al., 1998 and this study). A mechanism of contourite infill, as proposed by Bryn et al. (2005a) for Storegga, Laberg et al. (2002b) for Trænadjupet and for the Peach slide by this thesis, provides a theoretical model for the occurrence of these repeat slope failures.

Camps et al. (2009) map the present day gas hydrate stability zone at depths crossed by the upper slopes of the Barra Fan. During the glacial-Holocene transition this zone would have migrated, potentially affecting sediment stability. However, at present there is no evidence to suggest a role for gas hydrate dissociation in triggering the most recent Peach slide.

The most recent episode of slope failure is not confined to the Peach slide. The presence of debris flows, exposed on the seabed, on the central Barra Fan (see Figure 4.30 and Figure 4.33) may provide evidential support for a seismic trigger; as such an event would effect a large area. As part of the northeast Atlantic rifted margin (see chapter three), it is anticipated that late-Pleistocene seismicity on the northwest British continental margin is governed by factors similar to those in operation on the Norwegian margin. Here Mesozoic faults are reactivated by loading from sediment fans and isostatic adjustment (Bungum et al., 2005; Bungum et al., 2010). It is conceivable that an earthquake, during the deglacial transition, may have acted as a trigger to initiate failure of sediments already weakened via development of excess pore pressure.

7. Summary and Conclusions

7.1. Summary of major findings

Two distinct phases of mass movement are identified on the Barra Fan during the late-Pleistocene. The first, which includes the Peach 3 event, between 21 and 20 ka cal BP, shortly after the maximum advance of the BIS (Knutz et al., 2007; Scourse et al., 2009) and Heinrich event 2 (Hemming, 2004). A second phase of mass movement is constrained between 12 and 11 ka cal BP, via AMS ^{14}C dating of planktonic foraminifera in gravity core 56/-10/239 and the onset of contouritic sedimentation following ice-retreat, at the end of the Younger Dryas stadial. The Peach 4 event is associated with this more recent phase of mass movement. Table 6.4 provides an executive summary of the different Peach debrite ages and their associated uncertainty.

A review of occurrence of submarine mass movements conducted in chapter two of this thesis suggested that high-latitude, glaciated margins, would be most likely to experience mass movement during deglacial periods. The reasons for this being that the collapse of the continental ice-mass would initiate rapid sedimentation and post-glacial seismicity. The northwest British continental margin case study supports this hypothesis.

A major finding of this thesis, documented in chapter four and discussed in chapter six, is that sediments are preferentially accumulating within the Peach slide scar. These sediments are interpreted as muddy contourites on the basis of seabed morphology, unit asymmetry, acoustic facies, the oceanographic setting and previous studies in the region (see Table 4.6. for overview of evidence).

Discussed in section 6.5.1, it is proposed that during periods of ice-retreat the rapid deposition of clay-rich, low-permeability sediments on top of contourite sediments, with a high pore water content, led to development of excess pore pressure. This resulted in reduced sediment shear strength, as outlined in chapter two, and increased the slope's susceptibility to failure.

It is difficult to find evidence for trigger mechanisms. However, based on the timing of Peach 4, an earthquake associated with post-glacial seismicity is possible. Peach 3 may have been initiated by a different trigger mechanism with gas hydrate dissociation more likely due to the lowered eustatic sea-level (Peltier and Fairbanks, 2007). However, there is no direct evidence supporting gas-hydrate release.

Despite a lack of data on the northwest British margin, there are similarities between the morphologies of the Peach slide and the Holocene Norwegian slides. In particular, Storegga (Haflidason et al., 2004; Bryn et al., 2005a; Kvalstad et al., 2005) and Trænadjupet (Laberg and Vorren, 2000; Laberg et al., 2002b) contain similar features, which suggests that the events may have involved similar processes. The role of contourites being a prime example (Laberg et al., 2002a; Haflidason et al., 2004; Bryn et al., 2005a; Bryn et al., 2005b), where landslide scars exert a complex effect on bottom current flow and may accumulate contourite deposits due to effect of turbulence on current velocity (Øvrebø et al., 2006). The role of pre-existing scars as sediment traps may be analogous to the role that mountain couloirs play in accumulating snow and increasing the likelihood of snow avalanches (Guy and Birkeland, 2013).

Chapter one suggested that the Peach slide provided a useful analogy to mass movement events that could be initiated by ongoing deglaciation in Greenland and Antarctica. This observation holds true. Combined with observed gas hydrate dissociation on the Svalbard margin (Westbrook et al., 2009) and accelerating ice-retreat in Greenland and the Antarctic (Howat et al., 2005; Velicogna and Wahr, 2006; Sasgen et al., 2012) this thesis concludes that the risk of large-scale slope failures, and associated tsunamis, occurring in the Polar regions is high; although failure may occur a considerable period after deglaciation. Down current flanks of trough mouth fans should be considered particularly vulnerable to failure.

7.2. Fulfillment of thesis objectives

Specific objectives of the Barra Fan site study were outlined in section 1.3. These are now considered alongside the methodologies employed.

i. Paper BGS and NOC pinger records were converted to SEGY (and subsequently COD) format and analysed using seismic interpretation software (Seismic+). The conversion of these records was successful and the navigational accuracy was assessed as being within the resolution of multibeam echosounder data (see section 4.2). However, the process was extremely time consuming with the conversion of some 1500 km of data taking several months.

ii. The conversion process and analysis using seismic interpretation software has allowed more detailed interpretation than was previously possible. In particular, use of a GIS environment has allowed interpretation alongside MBE and sidescan sonar data. Use of two datasets in tandem gives greater interpretative power. This is exemplified by Figure 6.9, which compares pinger data to gradient and bathymetry and provides evidence supporting the occurrence of retrogressive failure.

iii. Chapter four of this thesis succeeded in mapping the different acoustic facies associated with submarine mass movement and further analysis in chapter six has led to reconstruction of failure and transport mechanisms. As discussed in chapter six, similarities between the Peach slide and Norwegian continental margin slope failures are striking.

iv. Analysis of geophysical and sediment core data in chapters four, five and six has constrained two periods of slope failure on the Barra Fan during the late-Pleistocene. The first of these occurs between 21 and 20 ka cal BP, and the second between 12 and 11 ka cal BP.

v. It is argued that the principal factor governing the occurrence of mass movement on the northwest British continental margin is excess pore pressure generated by rapid deposition of low-permeability glaciogenic clays. Discussed in chapters two and six, sedimentary loading generates excess pore pressure more efficiently where contouritic sediments are present below the glaciogenic sediments. This process increases the susceptibility of the continental slope to failure and a post-glacial seismic event may act as a trigger.

7.3. Thesis limitations and future work

As this PhD project and thesis reaches its conclusion several limitations and potential areas of future work present themselves.

7.3.1. Use of methodologies outlined in this thesis

Acquisition of marine geophysical data in deep water is a costly affair. As vessel day rates are routinely in excess of £10,000 and survey sites remote, the cost of geophysical surveys can easily reach sums of several hundreds of thousand pounds. This project was not blessed with such a budget and attempted to achieve the maximum possible from previously acquired data.

Conversion of high quality paper sub-bottom profile records into SEGY format has allowed a more detailed interpretation than was previously possible. In large part due to the analysis undertaken within a GIS environment: allowing direct comparison with other datasets.

This methodology is well suited to reanalysis of high quality data, acquired either during the pre-digital age or recorded on media that are now incompatible. Assuming that navigational data is accurate (and updates frequent), converted paper records can provide a valuable and extremely cost-effective insight into the sub-surface morphology.

It is suggested that where data is available, such analyses, though laborious, would improve the efficiency of forthcoming surveys making these more cost-effective: an important consideration in these times of severe budgetary constraints. In addition, these older records may provide valuable time series evidence of seabed processes over periods of decades, or 'before' data relating to discrete events.

7.3.2. Further studies on the Barra Fan and in the Rockall Trough

Detailed in chapter three, the Barra Fan and Rockall Trough is a fascinating region with a complicated history of glaciation and ocean circulation. A more detailed understanding of the region's palaeoceanographic and glacial setting could provide key insights into mediation of global climate by thermohaline circulation (Bond et al., 1993; McManus et al., 2004; Lynch-Stieglitz et al., 2007) as well as these processes' direct control over submarine mass movements. Lack of data, which necessitated a degree of interpolation and extrapolation, has made a more complete understanding impossible at this juncture.

7.3.2.1. Glacial circulation within the Rockall Trough

Contemporary circulation within the Rockall Trough is fairly well constrained (Holliday et al., 2000; New and Smythe-Wright, 2001; Øvrebø et al., 2006; Johnson et al., 2010), however, understanding of the glacial circulation is limited to suggested sluggish deep-water and surface circulation and vigorous intermediate waters (McCave et al., 1995; Thornalley et al., 2010). As Figure 3.5 shows, the Barra Fan is bathed by a number of water masses and these may respond differently to environmental changes associated with the glacial to inter-glacial transition.

This observation has important implications for mass movement on the Barra Fan. Knutz et al. (2002) observe erosion by bottom currents towards the toe of the fan and this thesis has proposed a mechanism for accumulation of contourite sediments within the Peach slide scar. Such processes may migrate depending on the relative vigour of water masses at different depths within the Rockall Trough.

Without improved understanding of these circulation conditions, thorough understanding of erosion or deposition by ocean currents during glacial periods is impossible.

One method by which this understanding could be achieved is through analysis of long sediments cores located at strategic depths (and positioned relative to bathymetric features that may produce turbulence) in one or more shallow to deep transects down the unfailed sediments of the Barra Fan. Analysis of benthic foraminifera could provide tell-tale water mass markers (such as salinity for Mediterranean Overflow water) and

sortable silt analysis would provide information on current velocity (McCave et al., 1995; Thornalley et al., 2010).

7.3.2.2. Mass movement process and morphology

The latter stages of this thesis has made frequent comparison between the Peach slide and Storegga and Trænadjupet on the Norwegian margin. From the available data it seems that similar processes govern the occurrence of each of these mass movement events. However, the lack of data on the Barra Fan and Peach slide is equally noteworthy. Analysis in this thesis was performed on a small volume of geophysical data and only one sediment core appears to penetrate mass movement facies, for comparison 89 sediment cores are analysed in the age constraint of Storegga (Haflidason et al., 2005).

Discussed in chapter six, age constraint of Peach 4 (and the earlier phases of the Peach slide) is uncertain. As such it is strongly recommended that future analysis focuses on acquiring and dating multiple core samples from the slide headwall area and the Rockall Trough, where they may sample distal turbidites.

In order to gain a full understanding on the processes governing the occurrence of mass movement on the Barra Fan, and the potential hazard that these events pose, complete data coverage is required. Whilst it is unrealistic to expect data of as high quality as that funded by the, multi-billion Euro, Ormen Lange development at Storegga; strategic use of two months vessel time could achieve full multibeam coverage of the area affected by slope failure, extensive sub-bottom profiles and long core samples from the area.

A suggested programme would involve two campaigns, informed by the data presented in this thesis, one year apart. The first to complete multibeam coverage and acquire deep-towed sub-bottom profile data (potentially a combined chirp and sidescan tow-fish operated alongside a sparker). This data would then be analysed in the months that follow to inform the location of vibrocores or piston cores to be acquired during the second campaign. Cores that could be used to improve mass movement age constraint, ground truth geophysical interpretation and analyse sediment lithofacies.

7.3.2.3. Comparison with the Donegal Fan

If mass movement on the Barra-Donegal Fan complex is governed by along-slope deposition then logic dictates that the north and south of the fan will display different characteristics due to the effects of sediment supply and transport. More detailed

analysis of the Donegal sector of the Barra-Donegal Fan complex could add valuable insights into the region.

7.3.2.4. Assessing hazard potential of the Peach slide

Chapter two outlined the potential impacts of submarine mass movements and, in areas away from sub-sea infrastructure, chief among them are tsunami generation and release of methane. Lack of data and resources prevented this thesis analysing the potential hazards associated with the Peach slide.

Tsunamigenic potential requires more detailed understanding of the failure morphology, as demonstrated by the analysis of Storegga. Here it is argued that the collapse of a Saalian fan (comprising a thicker sediment sequence) within the slide area generated the energy required to produce the observed tsunami (Bryn et al., 2005a). Therefore, before estimating the tsunamigenic potential of Peach new data acquisition, as outlined in section 7.3.2.2, is required.

Direct evidence linking methane release from submarine mass movements would provide strong support to Kennett et al.'s (2003) clathrate gun hypothesis. Though expansion of global wetlands is accepted to have played a major role in the late-glacial increase in atmospheric methane concentrations (Brook et al., 2000; Schaefer et al., 2006; Whiticar and Schaefer, 2007), there remains the potential for an important role for methane released via gas hydrate dissociation and submarine mass movements. For instance, Maslin et al. (2010) demonstrate a potential relationship between the timing of late-Pleistocene submarine mass movements and GISP2 δD-CH_4.

Age model uncertainty and the relatively long period required to turn firn to ice means that it is very difficult to correlate atmospheric methane directly to submarine mass movement. One method that can be used to test methane release from submarine mass movement is $\delta^{13}C$ analysis of benthic foraminifera in locations near to submarine mass movement deposits (as demonstrated by Panieri et al. (2012) with the Ana landslide). This analysis could be performed on existing core samples from the region.

Bibliography

AFEN, 1998. AFEN: UKCS 17th Round Atlantic Margins Environmental Survey. NOC, Southampton.

Aiwen, L., 2009. Response analysis of a submarine cable under fault movement. Earthquake Engineering And Engineering Vibration, 8(1): 159-164.

Alendal, G., Berntsen, J., Engum, E., Furnes, G., Kleiven, G. and Eide, L., 2005. Influence from 'Ocean Weather' on near seabed currents and events at Ormen Lange. Marine and Petroleum Geology, 22: 21-31.

Amy, L., Talling, P., Peakall, J., Wynn, R.B. and Arzola Thynne, R., 2005. Bed geometry used to test recognition criteria of turbidites and (sandy) debrites. Sedimentary Geology, 179: 163-174.

Anell, I., Thybo, H. and Artemieva, I.M., 2009. Cenozoic uplift and subsidence in the North Atlantic region: Geological evidence revisited. Tectonophysics, 474(1-2): 78-105.

Archer, D.E., 1996. An atlas of the distribution of calcium carbonate in sediments of the deep sea. Global Biogeochemical Cycles, 10(1): 159-174.

Armishaw, J.E., 1999. Bottom current accumulation and sediment fluxes on the Hebridean slope, Unpublished PhD Thesis, University of Southampton, 215 pp.

Armishaw, J.E., Holmes, R.W. and Stow, D.A.V., 1998. Morphology and Sedimentation on the Hebrides slope and Barra Fan, NW UK Continental Margin. In: M.S. Stoker, D. Evans and A. Cramp (Editors), Geological Processes on the Continental margins: Sedimentation, Mass-wasting and stability. Special Publication. Geological Society, London, pp. 81-104.

Armishaw, J.E., Holmes, R.W. and Stow, D.A.V., 2000. The Barra Fan: A bottom-current reworked, glacially-fed submarine fan system. Marine and Petroleum Geology, 17: 219-238.

Ascough, P., Cook, G. and Dugmore, A., 2005. Methodological approaches to determining the marine radiocarbon reservoir effect. Progress in Physical Geography, 29(4): 532-547.

Ascough, P.L., Cook, G.T., Dugmore, A.J. and Scott, E.M., 2007. The North Atlantic marine reservoir effect in the Early Holocene: Implications for defining and understanding MRE values. Nuclear Instruments & Methods In Physics Research Section B-Beam Interactions With Materials And Atoms, 259(1): 438-447.

Austin, W., Hibbert, F., Rasmussen, S.O., Peters, C., Abbott, P. and Bryant, C., 2012. The synchronization of palaeoclimatic events in the North Atlantic region during Greenland Stadial 3 (ca 27.5 to 23.3kyr b2k). Quaternary Science Reviews, 36 (C): 154-163.

Austin, W.E.N., Bard, E., Hunt, J., Kroon, D. and Peacock, J., 1995. The ^{14}C age of the Icelandic Vedde ash: implications for Younger Dryas marine reservoir age corrections. Radiocarbon, 37(1): 53-62.

Austin, W.E.N., Telford, R.J., Ninnemann, U.S., Brown, L., Wilson, L.J., Small, D.P. and Bryant, C.L., 2011. North Atlantic reservoir ages linked to high Younger Dryas atmospheric radiocarbon concentrations. Global And Planetary Change, 79 (3-4): 226-233.

Baltzer, A., Holmes, R. and Evans, D., 1998. Debris flows on the Sula Sgeir Fan, NW of Scotland. In: M.S. Stoker, D. Evans and A. Cramp (Editors), Geological Processes on Continental Margins: Sedimentation, Mass-Wasting and Stability. Special Publications. Geological Society, London, pp. 105-115.

Bard, E., 1988. Correction of accelerator mass spectrometry ^{14}C ages measured in planktonic foraminifera: paleoceanographic implications. Paleoceanography, 3 (6): 635-645.

Bard, E., Arnold, M., Mangerud, J., Paterne, M., Labeyrie, L., Duprat, J., Mélèires, M., Sønstegaard, E. and Duplessy, J., 1994. The North Atlantic atmosphere-sea surface ^{14}C gradient during the Younger Dryas climatic event. Earth and Planetary Science Letters, 126: 275-287.

Bartoli, G., Sarnthein, M., Weinelt, M., Erlenkeuser, H., Garbe-Schonberg, D. and Lea, D.W., 2005. Final closure of Panama and the onset of northern hemisphere glaciation. Earth and Planetary Science Letters, 237(1-2): 33-44.

Bauch, D., Carstens, J. and Wefer, G., 1997. Oxygen isotope composition of living Neogloboquadrina pachyderma (sin.) in the Arctic Ocean. Earth and Planetary Science Letters, 146: 47-58.

Bea, R.G., Wright, S.G., Sircar, P. and Niedoroda, A.W., 1983. Wave-Induced Slides in South Pass Block 70, Mississippi Delta. Journal of Geotechnical Engineering, 109(4): 619-644.

Beck, J.W., Richards, D.A., Edwards, R.L., Silverman, B.W., Smart, P.L., Donahue, D.J., Hererra-Osterheld, S., Burr, G.S., Calsoyas, L., Jull, A.J.T. and Biddulph,

D., 2001. Extremely Large Variations of Atmospheric 14C Concentration during the Last Glacial Period. Science, 292: 2453-2458.

Becker, J., Sandwell, D., Smith, W., Braud, J., Binder, B., Depner, J., Fabre, D., Factor, J., Ingalls, S., Kim, S., Ladner, R., Marks, K., Nelson, S., Pharaoh, A., Trimmer, R., Von Rosenberg, J., Wallace, G. and Weatherall, P., 2009. Global Bathymetry and Elevation Data at 30 Arc Seconds Resolution: SRTM30_PLUS. Marine Geodesy, 32(4): 355-371.

Bell, F.G., 1992. Engineering Properties of Soils and Rocks (3rd Edition). Butterworth Heinemann, Oxford.

Berg, K., Solheim, A. and Bryn, P., 2005. The Pleistocene to recent geological development of the Ormen Lange area. Marine and Petroleum Geology, 22: 45-56.

Berner, R.A., 1978. Sulfate reduction and the rate of deposition of marine sediments. Earth and Planetary Science Letters, 37: 492-498.

Berner, R.A. and Raiswell, R., 1983. Burial of organic carbon and pyrite sulfur in sediments over Phanerozoic time: a new theory Geochimica et Cosmochimica Acta, 47: 855-862.

BERR, 2008. Review of Cabling Techniques and Environmental Effects Applicable to the Offshore Wind Farm Industry - Technical Report.

Bertrand, P., Shimmield, G., Martinez, P., Grousset, F., Jorissen, F., Paterne, M., Pujol, C., Bouloubassi, I., Buat Menard, P., Peypouquet, J., Beaufort, L., Sicre, M., Lallier-Verges, E., Foster, J. and Ternois, Y., 1996. The glacial ocean productivity hypothesis: the importance of regional temporal and spatial studies. Marine Geology, 130: 1-9.

Billups, K. and Spero, H.J., 1996. Reconstructing the Stable Isotope Geochemistry and Paleotemperatures of the Equatorial Atlantic During the Last 150,000 Years: Results from Individual Foraminifera. Paleoceanography, 11.

Birks, C.J.A. and Koç, N., 2002. A high-resolution diatom record of late-Quaternary sea-surface temperatures and oceanographic conditions from the eastern Norwegian Sea. Boreas, 31(4): 323-344.

Biscontin, G., Pestana, J. and Nadim, F., 2004. Seismic triggering of submarine slides in soft cohesive soil deposits. Marine Geology, 203: 341-354.

Björck, S., Koç, N. and Skog, G., 2003. Consistently large marine reservoir ages in the Norwegian Sea during the Last Deglaciation. Quaternary Research: 429-435.

Blanchard, M., Alfredsson, M., Brodholt, J., Wright, K. and Catlow, C., 2007. Arsenic incorporation into FeS_2 pyrite and its influence on dissolution: A DFT study. Geochimica et Cosmochimica Acta, 71(3): 624-630.

Blott, S. and Pye, K., 2001. GRADISTAT: a grain size distribution and statistics package for the analysis of unconsolidated sediments. Earth Surface Processes and Landforms, 26(11): 1237-1248.

BODC, 1999. LOIS Shelf Edge Study Data Set (CD-ROM). British Oceanographic Data Centre.

BODC, 2011. Decca navigator. <https://www.bodc.ac.uk/data/documents/nodb/pdf/DeccaNavigator_13jul2011.pdf>. Accessed: 07/10/2013.

Bond, G., Broecker, W., Johnsen, S., McManus, J., Labeyrie, L., Jouzel, J. and Bonani, G., 1993. Correlations between climate records from North-Atlantic sediments and Greenland ice. Nature, 365(6442): 143-147.

Bondevik, S., Lovholt, F., Harbitz, C., Mangerud, J., Dawson, A. and Svendsen, J.I., 2005. The Storegga Slide tsunami - comparing field observations with numerical simulations. Marine and Petroleum Geology, 22(1-2): 195-208.

Bondevik, S., Mangerud, J., Birks, H.H., Gulliksen, S. and Reimer, P., 2006. Changes in North Atlantic Radiocarbon Reservoir Ages During the Allerod and Younger Dryas. Science, 312(5779): 1514-1517.

Bondevik, S., Svendsen, J.I., Johnsen, G., Mangerud, J. and Kaland, P., 1997. The Storegga tsunami along the Norwegian coast, its age and runup. Boreas, 26: 1-25.

Boulay, S., Colin, C., Trentesaux, A., Frank, N. and Liu, Z., 2005. Sediment sources and East Asian monsoon intensity over the last 450 ky. Mineralogical and geochemical investigations on South China Sea sediments. Palaeogeography, Palaeoclimatology, Palaeoecology, 228(3-4): 260-277.

Bowen, D., Phillips, F., McCabe, A., Knutz, P. and Sykes, G., 2002. New data for the Last Glacial Maximum in Great Britain and Ireland. Quaternary Science Reviews, 21: 89-101.

Boyle, J.F., 2000. Rapid elemental analysis of sediment samples by isotope source XRF. Journal of Paleolimnology(23): 213-221.

Bradshaw, P., 1971. An Introduction to Turbulence and its Measurement. Pergamon, Oxford.

Bradwell, T., Stoker, M., Golledge, N., Wilson, C., Merritt, J., Long, D., Everest, J., Hestvik, O., Stevenson, A. and Hubbard, A., 2008. The northern sector of the last British Ice Sheet: Maximum extent and demise. Earth-Science Reviews, 88 (3-4): 207-226.

Broecker, W.S., Andree, M., Wolfli, W., Oeschger, H., Bonani, G., Kennett, J. and Peteet, D., 1988. The chronology of the last deglaciation: implications to the cause of the Younger Dryas event. Paleoceanography, 3(1): 1-19.

Bronk Ramsey, C., 2009. Baysian analysis of radiocarbon dates. Radiocarbon, 51(1): 337-360.

Brook, E.J., Harder, S., Severinghaus, J.P., Steig, E.J. and Sucher, C.M., 2000. On the origin and timing of rapid changes in atmospheric methane during the last glacial period. Global Biogeochemical Cycles, 14(2): 599-572.

Bryn, P., Berg, K., Forsberg, C.F., Solheim, A. and Kvalstad, T.J., 2005a. Explaining the Storegga Slide. Marine and Petroleum Geology, 22(1-2): 11-19.

Bryn, P., Berg, K., Stoker, M.S., Haflidason, H. and Solheim, A., 2005b. Contourites and their relevance for mass wasting along the Mid-Norwegian Margin. Marine and Petroleum Geology, 22(1-2): 85-96.

Buffett, B. and Archer, D., 2004. Global inventory of methane clathrate: sensitivity to changes in the deep ocean. Earth and Planetary Science Letters, 227(3-4): 185-199.

Bugge, T., Belderson, R.H. and Kenyon, N.H., 1988. The Storegga Slide. Philosophical Transactions of the Royal Society of London. Series A, Mathematical and Physical Sciences, 325(1586): 357-388.

Bulat, J. and Long, D., 2001. Images of the seabed in the Faroe-Shetland Channel from commercial 3D seismic data. Marine Geophysical Researches, 22(5-6): 345-367.

Bungum, H., Lindholm, C. and Faleide, J.I., 2005. Postglacial seismicity offshore mid-Norway with emphasis on spatio-temporal magnitudal variations. Marine and Petroleum Geology, 22: 137-148.

Bungum, H., Olesen, O., Pascal, C., Gibbons, S., Lindholm, C. and Vestol, O., 2010. To what extent is the present seismicity of Norway driven by post-glacial rebound? Journal of the Geological Society, 167(2): 373-384.

Camps, A., Long, D., Rochelle, C. and Lovell, M., 2009. Mapping hydrate stability zones offshore Scotland. Geological Society, London, Special Publications, 319 (1): 81-91.

Canals, M., Lastras, G., Urgeles, R., Casamor, J., Mienert, J., Cattaneo, A., De Batist, M., Haflidason, H., Imbo, Y., Laberg, J., Locat, J., Long, D., Longva, O., Masson, D., Sultan, N., Trincardi, F. and Bryn, P., 2004. Slope failure dynamics and impacts from seafloor and shallow sub-seafloor geophysical data: case studies from the COSTA project. Marine Geology, 213: 9-72.

Cao, L., Fairbanks, R.G., Mortlock, R. and Risk, M., 2007. Radiocarbon reservoir age of high latitude North Atlantic surface water during the last deglacial. Quaternary Science Reviews, 26: 732-742.

Carey, S., 1997. Influence of convective sedimentation on the formation of widespread tephra fall layers in the deep sea. Geology, 25(9): 839-842.

Carter, S.R., Evensen, N.M., Hamilton, P.J. and Onions, R.K., 1979. Basalt magma sources during the opening of the North-Atlantic. Nature, 281(5726): 28-30.

Chaytor, J.D., Brink, U., Solow, A.R. and Andrews, B.D., 2009. Size distribution of submarine landslides along the U.S. Atlantic margin. Marine Geology, 264(1-2): 16-27.

CISCO, 2011. Cisco Visual Networking Index: Forecast and Methodology, 2010-2015. White Paper, CISCO.

Clark, C.D., Hughes, A.L., Greenwood, S.L., Jordan, C. and Sejrup, H.P., 2012. Pattern and timing of retreat of the last British-Irish Ice Sheet. Quaternary Science Reviews, 44(C): 112-146.

Coakley, J.P. and Syvitski, J.P.M., 1991. SediGraph technique. In: J.P.M. Syvitski (Editor), Principles, methods and applications of particle size analysis. Cambridge University Press, Cambridge, pp. 129-142.

Coleman, J.B., Yao, X., Jordan, T.R. and Madden, M., 2011. Holes in the ocean Filling voids in bathymetric lidar data. Computers and Geosciences, 37(4): 474-484.

Coleman, J.M. and Prior, D.B., 1988. Mass-wasting on continental margins. Annual Review of Earth and Planetary Sciences, 16: 101-119.

Coleman, J.M., Walker, H.J. and Grabau, W.E., 1998. Sediment instability in the Mississippi River delta. Journal of Coastal Research, 14(3): 872-881.

Colwell, F., Matsumoto, R. and Reed, D., 2004. A review of the gas hydrates, geology, and biology of the Nankai Trough. Chemical Geology, 205: 391-404.

Cook, A.J., Fox, A.J., Vaughan, D.G. and Ferrigno, J.G., 2005. Retreating Glacier fronts on the Antarctic Peninsula over the past half-century. Science, 308: 541-544.

Cook, M.R., 1989. Seabed and Shallow Soils data integration study. West of Hebrides. UKCS Quadrants 132, 133 & 142. BP Exploration, Glasgow.

Cook, N.J. and Chryssoulis, S.L., 1990. Concentrations of invisible gold in the common sulfides. Canadian Mineralogist, 28: 1-16.

Curry, W., Duplessy, J., Labeyrie, L. and Shackleton, N., 1988. Changes in the distribution of $\delta^{13}C$ of deep water $\sum CO_2$ between the last glaciation and the Holocene. Paleoceanography, 3(3): 317-341.

Dahlgren, K. and Vorren, T., 2003. Sedimentary environment and glacial history during the last 40 ka of the Vøring continental margin, mid-Norway. Marine Geology, 193: 93-127.

Dahlgren, K.I.T., Vorren, T.O., Stoker, M.S., Nielsen, T., Nygard, A. and Sejrup, H.P., 2005. Late Cenozoic prograding wedges on the NW European continental margin: their formation and relationship to tectonics and climate. Marine and Petroleum Geology, 22(9-10): 1089-1110.

Damuth, J.E., 1978. Echo character of the Norwegian--Greenland Sea: relationship to Quaternary sedimentation. Marine Geology, 28: 1-36.

Damuth, J.E., Jacobi, R.D. and Hayes, D.E., 1983. Sedimentation processes in the Northwest Pacific Basin revealed by echo-character mapping studies. Geological Society of America Bulletin, 94: 381-395.

Davies, S., Wastegård, S., Rasmussen, T., Svensson, A., Johnsen, S., Steffensen, J. and Andersen, K., 2008. Identification of the Fugloyarbanki tephra in the NGRIP ice core: a key tie-point for marine and ice-core sequences during the last glacial period. Journal of Quaternary Science, 23(5): 409-414.

Dawson, A., Bondevik, S. and Teller, J., 2011. Relative timing of the Storegga submarine slide, methane release, and climate change during the 8.2 ka cold event. The Holocene, 21(7): 1167-1171.

Dawson, A. and Stewart, I., 2007. Tsunami deposits in the geological record. Sedimentary Geology, 200: 166-183.

Day, S. and Maslin, M., 2005. Linking large impacts, gas hydrates, and carbon isotope excursions through widespread sediment liquefaction and continental slope failure: The example of the K-T boundary event. Geological Society of America Special Papers, 384: 239-258.

Dickens, G.R., 2003. Rethinking the global carbon cycle with a large, dynamic and microbially mediated gas hydrate capacitor. Earth and Planetary Science Letters, 213: 169-183.

Dickson, R.R. and McCave, I.N., 1986. Nepheloid layers on the continental-slope west of Porcupine Bank. Deep-Sea Research Part A-Oceanographic Research Papers, 33(6): 791-818.

Dodd, L.R., 1995. An investigation into the conditions and controls of continental slope instability - the Var Canyon, Nice, France and the Barra Fan, Hebrides, Scotland, Unpublished PhD Thesis, University College of North Wales at Bangor, 276 pp.

Dorn, W. and Werner, F., 1993. The contour-current flow along the southern Iceland-Faeroe Ridge as documented by its bedforms and asymmetrical channel fillings. Sedimentary Geology, 82: 47-59.

Dowdeswell, J.A. and Elverhøi, A., 2002. The timing of initiation of fast-flowing ice streams during a glacial cycle inferred from glacimarine sedimentation. Marine Geology, 188: 3-14.

Dugan, B. and Flemings, P.B., 2000. Overpressure and Fluid Flow in the New Jersey Continental Slope: Implications for Slope Failure and Cold Seeps. Science, 289 (5477): 288-291.

Dunkley Jones, T., Ridgwell, A., Lunt, D.J., Maslin, M.A., Schmidt, D.N. and Valdes, P.J., 2010. A Palaeogene perspective on climate sensitivity and methane hydrate instability. Philosophical Transactions Of The Royal Society A-Mathematical Physical And Engineering Sciences, 368(1919): 2395-2415.

Dunlop, P., Shannon, R., McCabe, M., Quinn, R. and Doyle, E., 2010. Marine geophysical evidence for ice sheet extension and recession on the Malin Shelf: New evidence for the western limits of the British Irish Ice Sheet. Marine Geology, 276(1-4): 86-99.

Duplessy, J., Bard, E., Labeyrie, L., Duprat, J. and Moyes, J., 1993. Oxygen isotope records and salinity changes in the Northeastern Atlantic ocean during the last 18,000 years. Paleoceanography, 8(3): 341-350.

Duplessy, J., Labeyrie, L., Julliet-LeClerc, A., Maitre, F., Duprat, J. and Sarnthein, M., 1991. Surface salinity reconstruction of the North Atlantic Ocean during the last glacial maximum. Oceanologica Acta, 14(4): 311-324.

Edwards, R.L., Beck, J.W., Burr, G.S., Donahue, D.J., Chappell, J.M.A., Bloom, A.L., Druffel, E.R.M. and Taylor, F.W., 1993. A Large Drop in Atmospheric $^{14}C/^{12}C$ and Reduced Melting in the Younger Dryas, Documented with ^{230}Th Ages of Corals. Science, 260(5110): 962-968.

Elmore, R.D., Pilkey, O.H., Cleary, W.J. and Curran, H.A., 1979. Black Shell turbidite, Hatteras Abyssal Plain, western Atlantic Ocean. Geological Society of America Bulletin, 90(12): 1165-1176.

Embley, R.W., 1980. The role of mass transport in the distribution of deep-ocean sediments with special reference to the north atlantic. Marine Geology, 38: 23-50.

Embley, R.W., 1982. Anatomy of some Atlantic margin sediment slides and some comments on ages and mechanisms. In: S. Saxov and J.K. Nieuwenhuis (Editors), Marine slides and other mass movements. NATO, New York, pp. 189-213.

Emiliani, C., 1955. Pleistocene Temperatures. The Journal of Geology, 63(6): 538-578.

Evans, D., Kenolty, N., Dobson, M.R., Whittington, R.J., Durant, G.P. and Barber, P., 1983. Malin. Sheet 55°N - 08°W. Solid Geology., 1:250 000 series. British Geological Survey.

Evans, D., King, E.L., Kenyon, N.H., Brett, C. and Wallis, D., 1996. Evidence for long-term instability in the Storegga Slide region off western Norway. Marine Geology, 130: 281-292.

Everest, J.D., Bradwell, T., Fogwill, C.J. and Kubik, W., 2006. Cosmogenic 10Be age constraints for the Wester Ross readvance moraine: Insights into British ice-sheet behaviour. Geografiska Annaler, 88 A: 9 - 17.

Fairbanks, R., 1989. A 17,000-year glacio-eustatic sea level record: influence of glacial melting rates on the Younger Dryas event and deep-ocean circulation. Nature, 342: 637-642.

Fairbanks, R., Mortlock, R., Chiu, T., Cao, L., Kaplan, A., Guilderson, T., Fairbanks, T., Bloom, A., Grootes, P. and Nadeau, M., 2005. Radiocarbon calibration curve spanning 0 to 50,000 years BP based on paired Th/U/U and C dates on pristine corals. Quaternary Science Reviews, 24(16-17): 1781-1796.

Farrell, J. and Prell, W., 1989. Climatic change and CaCO$_3$ preservation: an 800,000 year bathymetric reconstruction from the central equatorial Pacific Ocean. Paleoceanography, 4(4): 447-466.

Faugères, J.C. and Stow, D.A.V., 1993. Bottom-current-controlled sedimentation - a synthesis of the contourite problem. Sedimentary Geology, 82(1-4): 287-297.

Faugères, J.C., Stow, D.A.V., Imbert, P. and Viana, A., 1999. Seismic features diagnostic of contourite drifts. Marine Geology, 162(1): 1-38.

Fjeldskaar, W., Lindholm, C., Dehls, J.F. and Fjeldskaar, I., 2000. Postglacial uplift, neotectonics and seismicity in Fennoscandia. Quaternary Science Reviews, 19: 1413-1422.

Folk, R. and Ward, W., 1957. Brazos river bar: a study in the significance of grain size parameters. Journal of Sedimentary Petrology, 27(1): 3-26.

Franke, J., Paul, A. and Schulz, M., 2008. Modeling variations of marine reservoir ages during the last 45 000 years. Climate Of The Past, 4(2): 125-136.

Frossard, E., 1979. Effect of sand grain shape on the interparticle friction; indirect measurements by Rowe's stress dilatancy theory. Géotechnique, 29: 341-350.

Gadallah, M. and Fisher, R., 2009. Exploration Geophysics: an introduction. Springer-Verlag, Berlin, 262 pp.

Gay, A. and Berndt, C., 2007. Cessation/reactivation of polygonal faulting and effects on fluid flow in the Voring Basin, Norwegian Margin. Journal of the Geological Society, 164(1): 129-141.

Gay, A., Lopez, M., Berndt, C. and Seranne, M., 2007. Geological controls on focused fluid flow associated with seafloor seeps in the Lower Congo Basin. Marine Geology, 244: 68-92.

Gee, M., Uy, H., Warren, J., Morley, C. and Lambiase, J., 2007. The Brunei slide: A giant submarine landslide on the North West Borneo Margin revealed by 3D seismic data. Marine Geology, 246(1): 9-23.

Gee, M.J.R., Masson, D.G., Watts, A.B. and Allen, P.A., 1999. The Saharan debris flow: an insight into the mechanics of a long runout submarine debris flow. Sedimentology, 42(6): 957-974.

Gehlen, M., Mucci, A. and Boudreau, B., 1999. Modelling the distribution of stable carbon isotopes in porewaters of deep-sea sediments. Geochimica et Cosmochimica Acta, 63(18): 2763-2773.

Gilbert, R.B., Nodine, M.C., Wright, S.G., Cheon, J.Y., Wrzyszczynski, M., Coyne, M. and Ward, E., 2007. Impact of Hurricane-Induced Mudslides on Pipelines. Offshore Technology Conference, OTC 18983: 1-13.

Gisler, G., Weaver, R.P. and Gittings, M., 2010. Calculations of Tsunamis from Submarine Landslides. In: D.C. Mosher et al. (Editors), Submarine Mass Movements and Their Consequences. Springer, Dordrecht, pp. 695-704.

Godwin, H., 1962. Half-life of radiocarbon. Nature, 195(4845): 984.

Goossens, D., 2008. Techniques to measure grain-size distributions of loamy sediments: a comparative study of ten instruments for wet analysis. Sedimentology, 55: 65-96.

Graham, A.G.C., Lonergan, L. and Stoker, M.S., 2007. Evidence for Late Pleistocene ice stream activity in the Witch Ground Basin, central North Sea, from 3D seismic reflection data. Quaternary Science Reviews, 26: 627-643.

Grantz, A., Phillips, R.L., Mullen, M.W., Starratt, S.W., Jones, G.A., Naidu, A.S. and Finney, B.P., 1996. Character, paleoenvironment, rate of accumulation, and evidence for seismic triggering of Holocene turbidites, Canadian abyssal plain, Arctic Ocean. Marine Geology, 133: 51-73.

Graton, L.C. and Fraser, H.J., 1935. Systematic Packing of Spheres: With Particular Relation to Porosity and Permeability. The Journal of Geology, 43(8): 785-909.

Guy, Z.M. and Birkeland, K.W., 2013. Relating complex terrain to potential avalanche trigger locations. Cold Regions Science and Technology, 86(C): 1-13.

Haflidason, H., Lien, R., Sejrup, H., Forsberg, C. and Bryn, P., 2005. The dating and morphometry of the Storegga Slide. Marine and Petroleum Geology, 22: 123-136.

Haflidason, H., Sejrup, H., Nygard, A., Mienert, J., Bryn, P., Lien, R., Forsberg, C., Berg, K. and Masson, D., 2004. The Storegga Slide: architecture, geometry and slide development. Marine Geology, 213(1-4): 201-234.

Haigh, S.K., Vardanega, P.J. and Bolton, M.D., 2013. The plastic limit of clays. Géotechnique, 63(6): 435-440.

Hall, A., Peacock, J. and Connell, E., 2003. New data for the Last Glacial Maximum in Great Britain and Ireland: a Scottish perspective on the paper by Bowen et al. (2002). Quaternary Science Reviews, 22: 1551-1554.

Hall, I., Colmenero-Hidalgo, E., Zahn, R., Peck, V. and Hemming, S., 2011. Centennial-to millennial-scale ice-ocean interactions in the subpolar northeast Atlantic 18-41 kyr ago. Paleoceanography, 26(2): n/a-n/a.

Hampton, M.A., Lee, H.J. and Locat, J., 1996. Submarine landslides. Reviews of Geophysics, 34(1): 33-59.

Haq, B.U., 1998. Natural gas hydrates: searching the long-term climatic and slope stability records. In: J.-P. Henriet and J. Meinert (Editors), Gas hydrates: Relevance to World Margin Stability and Climate Change. Special Publications. Geological Society, London, London, pp. 303-318.

Haug, G.H. and Tiedemann, R., 1998. Effect of the formation of the Isthmus of Panama on Atlantic Ocean thermohaline circulation. Nature, 393(6686): 673-676.

Hayes, J., Strauss, H. and Kaufman, A., 1999. The abundance of ^{13}C in marine organic matter and isotopic fractionation in the global biogeochemical cycle of carbon during the past 800 Ma. Chemical Geology, 161: 103-125.

Hemming, S., 2004. Heinrich events: Massive late Pleistocene detritus layers of the North Atlantic and their global climate imprint. Reviews of Geophysics, 42(1): RG1005.

Hesse, R., Rashid, H. and Khodabakhsh, S., 2004. Fine-grained sediment lofting from meltwater-generated turbidity currents during Heinrich events. Geology, 32(5): 449-452.

Hibbert, F.D., Austin, W., Lenc, M.J. and Gatliff, R.W., 2010. British Ice Sheet dynamics inferred from North Atlantic ice-rafted debris records spanning the last 175 000 years. Journal of Quaternary Science, 25(4): 461-482.

Hohenegger, J. and Yordanova, E., 2001. Displacement of Larger Foraminifera at the Western Slope of Motobu Peninsula (Okinawa, Japan). Palaios, 16(1): 53-72.

Holbrook, W.S., Purdy, G., Sheridan, R., Glover Iii, L., Talwani, M., Ewing, J. and Hutchinson, D., 1994. Seismic structure of the U.S. Mid-Atlantic continental margin. Journal of Geophysical Research, 99(B9): 17871-17891.

Holliday, N.P., Pollard, R.T., Read, J.F. and Leach, H., 2000. Water mass properties and fluxes in the Rockall Trough, 1975-1998. Deep-Sea Research Part I-Oceanographic Research Papers, 47(7): 1303-1332.

Holmes, R., 1994. Seabed topography and other geotechnical information for the Shelf Edge Study 55°N - 60°N NW of Britain. British Geological Survey Technical Report WB/94/15.

Holmes, R.W., Long, D. and Dodd, L.R., 1998. Large-scale debrites and submarine landslides on the Barra Fan, west of Britain. In: M.S. Stoker, D. Evans and A. Cramp (Editors), Geological processes on continental margins: sedimentation, mass wasting and stability. Special Publications. Geological Society, London, pp. 67-79.

Hornbach, M., Lavier, L. and Ruppel, C., 2007. Triggering mechanism and tsunamogenic potential of the Cape Fear Slide complex, U.S. Atlantic margin. Geochemistry Geophysics Geosystems, 8(12): 16.

Howat, I.M., Joughin, I., Tulaczyk, S. and Gogineni, S., 2005. Rapid retreat and acceleration of Helheim Glacier, east Greenland. Geophysical Research Letters, 32: L22502.

Howe, J.A., 1995. Sedimentary processes and variations in slope-current activity during the last glacial interglacial episode on the Hebrides slope, northern Rockall Trough, North-Atlantic Ocean. Sedimentary Geology, 96(3-4): 201-230.

Howe, J.A., 1996. Turbidite and contourite sediment waves in the northern Rockall Trough, North Atlantic Ocean. Sedimentology, 43: 219-234.

Howe, J.A., Dove, D., Bradwell, T. and Gafeira, J., 2012. Submarine geomorphology and glacial history of the Sea of the Hebrides, UK. Marine Geology, 315-318(C): 64-76.

HSE, 2002. Seismic Hazard: UK Continental Shelf. Health and Safety Executive - Offshore Technology Report, 005: 1-83.

Hsu, S., Kuo, J., Lo, C., Tsai, C., Doo, W., Ku, C. and Sibuet, J., 2008. Turbidity Currents, Submarine Landslides and the 2006 Pingtung Earthquake off SW Taiwan. Terrestrial Atmospheric And Oceanic Sciences, 19(6): 767-772.

Hughen, K., Southon, J.R., Lehman, S.J. and Overpeck, J.T., 2000. Synchronous Radiocarbon and Climate Shifts During the Last Deglaciation. Science, 290 (5498): 1951-1954.

Hughen, K.A., Baillie, M.G.L., Bard, E., Beck, J.W., Bertrand, C.J.H., Blackwell, P.G., Buck, C.E., Burr, G.S., Cutler, K.B., Damon, P.E., Edwards, R.L., Fairbanks, R.G., Friedrich, M., Guilderson, T.P., Kromer, B., McCormac, G., Manning, S., Ramsey, C.B., Reimer, P.J., Reimer, R.W., Remmele, S., Southon, J.R., Stuiver, M., Talamo, S., Taylor, F.W., Plicht, J. and Weyhenmeyer, C.E., 2004. MARINE04 marine radiocarbon age calibration, 0-26 cal kyr BP. Radiocarbon, 46(3): 1059-1086.

Iverson, R., Logan, M., Lahusen, R. and Berti, M., 2010. The perfect debris flow? Aggregated results from 28 large-scale experiments. Journal of Geophysical Research, 115(F3): F03005.

James, J.W.C., 1992. Quaternary Geology Map Sheet 56°N - 10°W, Peach 1:250 000 Series. British Geological Survey.

James, J.W.C. and Hitchen, K., 1992. Peach. Sheet 56ºN - 10ºW. Solid Geology., 1:250 000 Series. British Geological Survey.

James, J.W.C. and Wright, S.A., 1990. Peach. Sheet 56ºN - 10ºW. Sea Bed Sediments., 1:125000 series. British Geological Survey.

Jansen, E., Befring, S., Bugge, T., Eidvin, T., Holtedahl, H. and Sejrup, H.P., 1987. Large submarine slides on the Norwegian continental margin: sediments, transport and timing. Marine Geology, 78: 77-107.

Japsen, P. and Chalmers, J.A., 2000. Neogene uplift and tectonics around the North Atlantic: overview. Global And Planetary Change, 24(3-4): 165-173.

Jasper, J., Hayes, J., Mix, A. and Prahl, F., 1994. Photosynthetic fractionation of and concentrations of dissolved CO_2 in the central equatorial Pacific during the last 255,000 years. Paleoceanography, 9(6): 781-798.

Jenner, K.A., Piper, D.J.W., Campbell, D.C. and Mosher, D.C., 2007. Lithofacies and origin of late Quaternary mass transport deposits in submarine canyons, central Scotian Slope, Canada. Sedimentology, 54(1): 19-38.

Johnson, C., Sherwin, T., Smythe-Wright, D., Shimmield, T. and Turrell, W., 2010. Wyville Thomson Ridge Overflow Water: Spatial and temporal distribution in the Rockall Trough. Deep-Sea Research Part I-Oceanographic Research Papers, 57(10): 1153-1162.

Jones, K., McCave, I. and Patel, P., 1988. A computer-interfaced sedigraph for modal size analysis of fine-grained sediment. Sedimentology, 35: 163-172.

Jordan, J., Smith, D., Dawson, S. and Dawson, A., 2010. Holocene relative sea-level changes in Harris, Outer Hebrides, Scotland, UK. Journal of Quaternary Science, 25(2): 115-134.

Kennett, J.P., Cannariato, K.G., Hendy, I.L., Behl, R.J., 2003. Methane hydrates in Quaternary climate change: the clathrate gun hypothesis. American Geophysical Union, Washington, D.C., 216 pp.

Kent, R.W. and Fitton, J.G., 2000. Mantle sources and melting dynamics in the British palaeogene igneous province. Journal Of Petrology, 41(7): 1023-1040.

Kenyon, N., 1987. Mass-wasting features on the continental slope of northwest Europe. Marine Geology, 74: 57-77.

Khain, V.E. and Polyakova, I.D., 2004. Oil and gas potential of deep- and ultradeep-water zones of continental margins. Lithology And Mineral Resources, 39(6): 530-540.

Kitagawa, H. and van der Plicht, J., 1998. Atmospheric Radiocarbon Calibration to 45,000 yr B.P.: Late Glacial Fluctuations and Cosmogenic Isotope Production. Science, 279(5354): 1187-1190.

Knight, G., C., 2012. Email regarding RRS Charles Darwin navigation array.

Knutz, P.C., Austin, W.E.N. and Jones, E.J.W., 2001. Millenial-scale depositional cycles related to British Ice Sheet variability and North Atlantic paleocirculation since 45 kyr B.P., Barra Fan, U.K. margin. Paleoceanography, 16(1): 53-64.

Knutz, P.C., Jones, E.J.W., Austin, W.E.N. and van Weering, T.C.E., 2002. Glacimarine slope sedimentation, contourite drifts and bottom current pathways on the Barra Fan, UK North Atlantic margin. Marine Geology, 188: 129-146.

Knutz, P.C., Zahn, R. and Hall, I.R., 2007. Centennial-scale variability of the British Ice Sheet: Implications for climate forcing and Atlantic meridional overturning circulation during the last deglaciation. Paleoceanography, 22(1): 14.

Kohfeld, K., Fairbanks, R., Smith, S. and Walsh, I., 1996. Neogloboquadrina pachyderma (sinistral coiling) as paleoceanographic tracers in polar oceans: Evidence from Northeast Water Polynya plankton tows, sediment traps, and surface sediments. Paleoceanography, 11(6): 679-699.

Kontrovitz, M., Snyder, S. and Brown, R., 1978. A flume study of the movement of Foraminifera tests. Palaeogeography, Palaeoclimatology, Palaeoecology, 23: 141-150.

Kroon, D., Austin, W.E.N., Chapman, M.R. and Ganssen, G.M., 1997. Deglacial surface circulation changes in the northeastern Atlantic: Temperature and salinity records of NW Scotland on a century scale. Paleoceanography, 12(6): 755 - 763.

Kroon, D., Shimmield, G., Austin, W.E.N., Derrick, S., Knutz, P. and Shimmield, T., 2000. Century- to millenial-scale sedimentological-geochemical records of

glacial-Holocene sediment variations from the Barra Fan (NE Atlantic). Journal of the Geological Society, London, 157: 643-653.

Kvalstad, T.J., Andresen, L., Forsberg, C.F., Berg, K., Bryn, P. and Wangen, M., 2005. The Storegga slide: evaluation of trigger sources and slide mechanics. Marine and Petroleum Geology, 22(245-256).

Kvenvolden, K.A., 1993. Gas hydrates - geological perspective and global change. Reviews of Geophysics, 31(2): 173-187.

Kvenvolden, K.A., 1998. A primer on the geological occurrence of gas hydrate. In: J.-P. Henriet and J. Mienert (Editors), Gas Hydrates: Relevance to World Margin Stability and Climate Change. Special Publications. Geological Society, London, London, pp. 9-30.

Laberg, J., Vorren, T., Mienert, J., Bryn, P. and Lien, R., 2002a. The Trænadjupet Slide: a large slope failure affecting the continental margin of Norway 4,000 years ago. Geo-Marine Letters, 22(1): 19-24.

Laberg, J.S., Stoker, M.S., Dahlgren, K.I.T., de Haas, H., Haflidason, H., Hjelstuen, B.O., Nielsen, T., Shannon, P.M., Vorren, T.O., van Weering, T.C.E. and Ceramicola, S., 2005. Ceaozoic alongslope processes and sedimentation on the NW European Atlantic margin. Marine and Petroleum Geology, 22(9-10): 1069-1088.

Laberg, J.S. and Vorren, T.O., 2000. Trænadjupet slide, offshore Norway - morphology, evacuation and triggering mechanisms. Marine Geology, 171: 95-114.

Laberg, J.S., Vorren, T.O., Dowdeswell, J.A., Kenyon, N.H. and Taylor, J., 2000. The Andøya slide and the Andøya Canyon, north-eastern Norwegian-Greenland Sea. Marine Geology, 162: 259-275.

Laberg, J.S., Vorren, T.O., Mienert, J., Evans, D., Lindberg, B., Ottesen, D., Kenyon, N.H. and Henriksen, S., 2002b. Late Quaternary palaeoenvironment and chronology in the Trænadjupet Slide area offshore Norway. Marine Geology, 188: 35-60.

Laberg, J.S., Vorren, T.O., Mienert, J., Haflidason, H., Bryn, P. and Lien, R., 2003. Preconditions leading to the Holocene Trænadjupet slide offshore Norway. In: J. Locat and J. Mienert (Editors), Advances in Natural and Technological Hazards research. Kluwer, Dordrecht, pp. 247-254.

Lambeck, K., 1993. Glacial rebound of the British Isles - II. A high-resolution, high-precision model. Geophysics Journal International, 115: 960-990.

Lambeck, K., 1995. Glacial isostasy and water depths in the late Devensian and Holocene on the Scottish Shelf west of the Outer Hebrides. Journal of Quaternary Science, 10(1): 83-86.

Lastras, G., Canals, M., Hughes-Clarke, J.E., Moreno, A., De Batist, M., Masson, D.G. and Cochonat, P., 2002. Seafloor imagery from the BIG'95 debris flow, western Mediterranean. Geology, 30(10): 871-874.

Lawrence, G.W. and Cartwright, J.A., 2009. The initiation of sliding on the mid Norway margin in the Møre Basin. Marine Geology, 259(1-4): 21-35.

Leat, P.T., Tate, A.J., Tappin, D.R., Day, S.J. and Owen, M.J., 2010. Growth and mass wasting of volcanic centers in the northern South Sandwich arc, South Atlantic, revealed by new multibeam mapping. Marine Geology, 275(1-4): 110-126.

Lebreiro, S.M., McCave, I.N. and Weaver, P.P.E., 1997. Late Quaternary turbidite emplacement on the Horseshoe abyssal plain (Iberian margin). Journal of Sedimentary Research, 67(5): 856-870.

Lee, H.J., 2009. Timing of occurrence of large submarine landslides on the Atlantic Ocean margin. Marine Geology, 264(1-2): 53-64.

Libby, W.F., 1955. Radiocarbon dating. University of Chicago Press, Chicago.

Lindsey, J., 1989. The Fresnel zone and its interpretive significance. The Leading Edge, 8(10): 33-39.

Lingenfelter, R., 1963. Production of Carbon 14 by Cosmic-Ray Neutrons. Reviews of Geophysics, 1(1): 35-55.

Little, M.G., Schneider, R.R., Kroon, D., Price, B., Summerhayes, C.P. and Segl, M., 1997. Trade wind forcing of upwelling, seasonality, and Heinrich events as a response to sub-Milankovitch climate variability. . Paleoceanography, 12(4): 568-576.

Locat, J., 2001. Instabilities along ocean margins: a geomorphological and geotechnical perspective. Marine and Petroleum Geology, 18: 503-512.

Locat, J., Lee, H., Brink, U., Twichell, D., Geist, E. and Sansoucy, M., 2009. Geomorphology, stability and mobility of the Currituck slide. Marine Geology, 264(1-2): 28-40.

Locat, J., Lee, H., Locat, P. and Imran, J., 2004. Numerical analysis of the mobility of the Palos Verdes debris avalanche, California, and its implication for the generation of tsunamis. Marine Geology, 203(3-4): 269-280.

Locat, J. and Lee, H.J., 2005. Subaqueous debris flows. In: M. Jakob and O. Hungr (Editors), Debris flow hazards and related phenomena. Springer-Verlag, Berlin, pp. 203-245.

Loubere, P., Meyers, P. and Gary, A., 1995. Benthic foraminiferal micro-habitat selection, carbon isotope values, and association with larger animals: a test with *Uvigerina peregrina*. Journal of Foraminiferal Research, 25(1): 1107-1110.

Lynch-Stieglitz, J., Adkins, J.F., Curry, W.B., Dokken, T., Hall, I., Herguera, J.C., Hirschi, J.J., Ivanova, E.V., Kissel, C., Marchal, O., Marchitto, T.M., McCave, I.N., McManus, J.F., Mulitza, S., Ninnemann, U., Peeters, F., Yu, E. and Zahn, R., 2007. Atlantic meridional overturning circulation during the Last Glacial Maximum. Science, 316(5821): 66-69.

Marani, M., Argnani, A., Roveri, M. and Trincardi, F., 1993. Sediment drifts and erosional surfaces in the central Mediterranean: seismic evidence of bottom-current activity. Sedimentary Geology, 82: 207-220.

Marshall, J., 1992. Climatic and oceanographic isotopic signals from the carbonate rock record and their preservation. Geological Magazine, 129(2): 143-160.

Martel, S.J., 2004. Mechanics of landslide initiation as a shear fracture phenomenon. Marine Geology, 203: 319-339.

Martinussen, M., 1961. C14-datings refering to shorelines, transgressions and glacial substages in Northern Norway. Norges Geologiske, Undersökelse, 215: 319-339.

Maslin, M. and Mikkelsen, N., 1997. Amazon fan mass-transport deposits and underlying interglacial deposits: age estimates and fan dynamics. Proceedings of the Ocean Drilling Program, Scientific Results, 155: 353-365.

Maslin, M., Mikkelsen, N., Vilela, C. and Haq, B., 1998. Sea-level- and gas-hydrate-controlled catastrophic sediment failures of the Amazon Fan. Geology, 26(12): 1107-1110.

Maslin, M., Owen, M., Betts, R., Day, S., Dunkley Jones, T. and Ridgwell, A., 2010. Gas hydrates: past and future geohazard? Philosophical Transactions Of The Royal Society A-Mathematical Physical And Engineering Sciences, 368(1919): 2369-2393.

Maslin, M., Owen, M., Day, S. and Long, D., 2004. Linking continental-slope failures and climate change: Testing the clathrate gun hypothesis. Geology, 32(1): 53.

Maslin, M., Vilela, C., Mikkelsen, N. and Grootes, P., 2005. Causes of catastrophic sediment failures of the Amazon Fan. Quaternary Science Reviews, 24(20-21): 2180-2193.

Maslin, M.A. and Burns, S.J., 2000. Reconstruction of the Amazon Basin Effective Moisture Availability over the Past 14,000 Years. Science, 290: 2285 - 2287.

Masson, D.G., Canals, M., Alonso, B., Urgeles, R. and Huhnerbach, V., 1998. The Canary Debris Flow: source area morphology and failure mechanisms. Sedimentology, 45: 411-432.

Masson, D.G., Harbitz, C.B., Wynn, R.B., Pedersen, G. and Løvholt, F., 2006. Submarine landslides: processes, triggers and hazard prediction. Philosophical Transactions of the Royal Society A: Mathematical, Physical and Engineering Sciences, 364(1845): 2009-2039.

Masson, D.G. and Jacobs, C.L., 1998. Southampton Oceanography Centre Cruise Report: R.V.Colonel Templer Cruises 01 and 02/98. TOBI surveys of the continental slope north and west of Scotland., Southampton.

Masson, D.G., Watts, A.B., Gee, M.J.R., Urgeles, R., Mitchell, N.C., Le Bas, T.P. and Canals, M., 2002. Slope failures on the flanks of the western Canary Islands. Earth-Science Reviews, 57: 1-35.

Matsumoto, K. and Lynch-Stieglitz, J., 1999. Similar glacial and Holocene deep water circulation inferred from southeast Pacific benthic foraminiferal carbon isotope composition. Paleoceanography, 14(2): 149-163.

McCave, I.N., Manighetti, B. and Beveridge, N.A.S., 1995. Circulation in the glacial North-Atlantic inferred from grain-size measurements. Nature, 374(6518): 149-152.

McGuire, W.J., Howarth, R.J., Firth, C.R., Solow, A.R., Pullen, A.D., Saunders, S.J., Stewart, I.S. and Vita-Finzi, C., 1997. Correlation between rate of sea-level change and frequency of explosive volcanism in the Mediterranean. Nature, 389: 473-476.

McManus, J.F., Francois, R., Gherardi, J.M., Keigwin, L.D. and Brown-Leger, S., 2004. Collapse and rapid resumption of Atlantic meridional circulation linked to deglacial climate changes. Nature, 428(6985): 834-837.

McMaster, R. and Ashraf, A., 1973. Drowned and buried valleys on the southern New England continental shelf. Marine Geology, 15: 249-268.

Merwade, V., Maidment, D. and Goff, J., 2006. Anisotropic considerations while interpolating river channel bathymetry. Journal of Hydrology, 331: 731-741.

Mienert, J., Posewang, J. and Baumann, M., 1998. Gas hydrates along the northeastern Atlantic margin: possible hydrate-bound margin instabilities and possible release of methane. In: J.-P. Henriet and J. Mienert (Editors), Gas Hydrates: Relevance to World Margin Stability and Climate Change. Special Publications. Geological Society, London, London.

Mienert, J., Vanneste, M., Bünz, S., Andreassen, K. and Haflidason, H., 2005. Ocean warming and gas hydrate stability on the mid-Norwegian margin at the Storegga Slide. Marine and Petroleum Geology, 22: 233-244.

Miles, P., Schaming, M. and Lovera, R., 2007. Resurrecting vintage paper seismic records. Marine Geophysical Researches, 28(4): 319-329.

Mitchell, S.F., Ball, J.D., Crowley, S.F., Marshall, J.D., Paul, C.R.C., Veltkamp, C.J. and Samir, A., 1997. Isotope data from Cretaceous chalks and foraminifera: Environmental or diagenetic signals? Geology, 25: 691-694.

Mook, W.G., 1986. Recommendations/resolutions adopted by the Twelfth International Radiocarbon conference. Radiocarbon, 28(2A): 799.

Moore, J., Clague, D., Holcomb, R., Lipman, P., Normark, W. and Torresan, M., 1989. Prodigious submarine landslides on the Hawaiian Ridge. Journal of Geophysical Research, 94(B12): 465-484.

Mörner, N.-A., Tröften, P.E., Sjöberg, R., Grant, D., Dawson, S., Bronge, C., Kvamsdal, O. and Sidén, A., 2000. Deglacial paleoseismicity in Sweden: the 9663 BP Iggesund event. Quaternary Science Reviews, 19: 1461-1468.

Muir-Wood, R., 2000. Deglaciation Seismotectonics: a principle influence on intraplate seismogenesis at high latitudes. Quaternary Science Reviews, 19(1399-1411).

Mulder, T. and Cochonat, P., 1996. Classification of offshore mass movements. Journal of Sedimentary Research, 66(1): 43-57.

Muramatsu, Y., Doi, T., Tomaru, H., Fehn, U., Takeuchi, R. and Matsumoto, R., 2007. Halogen concentrations in pore waters and sediments of the Nankai Trough, Japan: Implications for the origin of gas hydrates. Applied Geochemistry, 22: 534-556.

Negre, C., Zahn, R., Thomas, A.L., Masque, P., Henderson, G.M., Martinez-Mendez, G., Hall, I. and Mas, J.L., 2010. Reversed flow of Atlantic deep water during the Last Glacial Maximum. Nature, 468(7320): 84-88.

New, A.L. and Smythe-Wright, D., 2001. Aspects of the circulation in the Rockall Trough. Continental Shelf Research, 21(8-10): 777-810.

Nisbet, E.G., 1990. The end of the ice age. Canadian Journal of Earth Sciences, 27: 148-157.

Noormets, R., Dowdeswell, J., Larter, R., Cofaigh, C.ì. and Evans, J., 2009. Morphology of the upper continental slope in the Bellingshausen and Amundsen Seas ‚Äì Implications for sedimentary processes at the shelf edge of West Antarctica. Marine Geology, 258(1-4): 100-114.

Nordfjord, S., Goff, J.A., Jr, J.A.A. and Duncan, L.S., 2009. Shallow stratigraphy and complex transgressive ravinement on the New Jersey middle and outer continental shelf. Marine Geology, 266(1-4): 232-243.

Norris, R.D. and Röhl, U., 1999. Carbon cycling and chronology of climate warming during the Palaeocene/Eocene transition. Nature, 401: 775-778.

O'Brien, J. and Lerche, I., 1988. Seismic Imaging of Deep Hydrocarbon Reservoirs. Pure and Applied Geophysics, 127(1): 33-61.

O'Reilly, B.M., Shannon, P.M. and Readman, P.W., 2007. Shelf to slope sedimentation processes and the impact of Plio-Pleistocene glaciations in the northeast Atlantic, west of Ireland. Marine Geology, 238(1-4): 21-44.

Oehmig, R., 1993. Entrainment of planktonic foraminifera: effect of bulk density. Sedimentology, 40: 869-877.

OneGeology, 2011. Making Geological Map Data for the Earth Accessible. <http://www.onegeology.org/home.html>. Accessed: 12/01/2012.

Oppo, D., Raymo, M., Lohmann, G., Mix, A., Wright, J. and Prell, W., 1995. A $\delta^{13}C$ record of Upper North Atlantic Deep Water during the past 2.6 million years. Paleoceanography, 10(3): 373-294.

Orange, D.L. and Breen, N.A., 1992. The effects of fluid escape on Accretionary wedges, 2: seepage force, slope failure, headless submarine canyons, and vents. Journal of Geophysical Research, 97(B6): 9277-9295.

Øvrebø, L.K., Haughton, P.D.W. and Shannon, P.M., 2006. A record of fluctuating bottom currents on the slopes west of the Porcupine Bank, offshore Ireland - implications for Late Quaternary climate forcing. Marine Geology, 225(1-4): 279-309.

Owen, M., 2000. North Atlantic mass movements and global climate change: an investigation, Unpublished Master's Thesis, University College London, 74 pp.

Owen, M., Day, S., Long, D. and Maslin, M., 2010. Investigations on the Peach 4 Debrite, a Late Pleistocene Mass Movement on the Northwest British Continental Margin. In: D.C. Mosher et al. (Editors), Submarine mass movements and their consequences. Advances in Natural and Technological Hazards Research. Springer, Dordrecht, pp. 301-311.

Owen, M., Day, S. and Maslin, M., 2007. Late Pleistocene submarine mass movements: occurrence and causes. Quaternary Science Reviews, 26(7-8): 958-978.

Panieri, G., Camerlenghi, A., Cacho, I., Cervera, C.S., Canals, M., Lafuerza, S. and Herrera, G., 2012. Tracing seafloor methane emissions with benthic foraminifera: Results from the Ana submarine landslide (Eivissa Channel, Western Mediterranean Sea). Marine Geology, 291-294(C): 97-112.

Paull, C.K., Brewer, P.G., Ussler III, W., Peltzer, E.T., Redher, G. and Clague, D., 2003. An experiment demonstrating that marine slumping is a mechanism to transfer methane from seafloor gas-hydrate deposits into the upper ocean and atmosphere. Geo-Marine Letters, 22: 198-203.

Paull, C.K., Buelow, W.J., Ussler III, W. and Borowski, W.S., 1996. Increased continental-margin slumping frequency during sea-level lowstands above gas hydrate-bearing sediments. Geology, 24(2): 143-146.

Paull, C.K., Ussler III, W. and Dillon, W., 1991. Is the extent of glaciation limited by marine gas hydrates. Geophsyical Research Letters, 18: 432-434.

Paull, C.K., Ussler, W., Holbrook, W.S., Hill, T.M., Keaten, R., Mienert, J., Haflidason, H., Johnson, J.E., Winters, W.J. and Lorenson, T.D., 2008. Origin of pockmarks and chimney structures on the flanks of the Storegga Slide, offshore Norway. Geo-Marine Letters, 28(1): 43-51.

Peacock, J., Austin, W., Selby, I., Graham, D., Harland, R. and Wilkinson, I., 1992. late Devensian and Flandrian palaeoenvironmental changes on the Scottish continental shelf west of the Outer Hebrides. Journal of Quaternary Science, 7 (2): 145-161.

Peck, V., Hall, I., Zahn, R., Grousset, F., Hemming, S. and Scourse, J., 2007. The relationship of Heinrich events and their European precursors over the past

60ka BP: a multi-proxy ice-rafted debris provenance study in the North East Atlantic. Quaternary Science Reviews, 26(7-8): 862-875.

Peck, V.L., Hall, I.R., Zahn, R. and Elderfield, H., 2008. Millennial-scale surface and subsurface paleothermometry from the northeast Atlantic, 55–8 ka BP. Paleoceanography, 23(3): 1-11.

Peltier, W. and Fairbanks, R., 2007. Global glacial ice volume and Last Glacial Maximum duration from an extended Barbados sea level record. Quaternary Science Reviews, 25: 3322-3337.

Peters, C., Walden, J. and Austin, W., 2008. Magnetic signature of European margin sediments: Provenance of ice-rafted debris and the climatic response of the British ice sheet during Marine Isotope Stages 2 and 3. Journal of Geophysical Research, 113(F3): F03007.

Phrampus, B.J. and Hornbach, M., 2012. Recent changes to the Gulf Stream causing widespread gas hydrate destabilization. Nature, 490(7421): 527-530.

Pickering, K.T., Hiscott, R.N. and Hein, F.J., 1989. Deep marine environments: clastic sedimentation and tectonics. Unwin Hyman, London, 416 pp.

Piper, D.J.W. and Asku, A.E., 1987. The source and origin of the 1929 Grand Banks turbidity current inferred from sediment budgets. Geo-Marine Letters, 7: 177-182.

Piper, D.J.W., Cochonat, P. and Morrison, M.L., 1999a. The sequence of events around the epicentre of the 1929 Grand Banks earthquake: initiation of debris flows and turbidity current inferred from sidescan sonar. Sedimentology, 46: 79 - 97.

Piper, D.J.W., Hiscott, R.N. and Normark, W.R., 1999b. Outcrop-scale acoustic facies analysis and latest Quaternary development of Hueneme and Dume submarine fans, offshore California. Sedimentology, 46: 47-78.

Piper, D.J.W., Primez, C., Manley, P.L., Long, D., Flood, R.D., Normark, W.R. and Showers, W., 1997. Mass-transport deposits of the Amazon fan. Proceedings of the Ocean Drilling Program, Scientific Results, 155: 109-146.

Popenoe, P., Schmuck, E.A. and Dillon, W.P., 1991. The Cape Fear landslide: slope failure associated with salt diapirism and gas hydrate decomposition. USGS Bulletin, 2002: 40-53.

Praeg, D., Stoker, M.S., Shannon, P.M., Ceramicola, S., Hjelstuen, B., Laberg, J.S. and Mathiesen, A., 2005. Episodic Cenozoic tectonism and the development of the

NW European 'passive' continental margin. Marine and Petroleum Geology, 22 (9-10): 1007-1030.

Preu, B., Hernández-Molina, F.J., Violante, R., Piola, A.R., Paterlini, C.M., Schwenk, T., Voigt, I., Krastel, S. and Spiess, V., 2013. Morphosedimentary and hydrographic features of the northern Argentine margin The interplay between erosive, depositional and gravitational processes and its conceptual implications. Deep-Sea Research Part I, 75(c): 157-174.

Prins, M.A. and Postma, G., 2000. Effects of climate, sea level, and tectonics unraveled for last deglaciation turbidite records of the Arabian Sea. Geology, 28 (4): 375-378.

Rabinovich, A.B., Thomson, R.E., Kulikov, E.A., Bornhold, B.D. and Fine, I.V., 1999. The landslide-generated tsunami of November 3, 1994 in Skagway Harbor, Alaska: a case study. Geophsyical Research Letters, 26(19): 3009-3012.

Raiswell, R., Newton, R., Bottrell, S.H., Coburn, P.M., Briggs, D.E.G., Bond, D.P.G. and Poulton, S.W., 2008. Turbidite depositional influences on the diagenesis of Beecher's Trilobite Bed and the Hunsruck Slate; sites of soft tissue pyritization. American Journal of Science, 308(2): 105-129.

Rebesco, M. and Stow, D., 2001. Seismic expression of contourites and related deposits: a preface. Marine Geophysical Researches, 22(5-6): 303-308.

Reeder, M.S., Rothwell, R.G. and Stow, D.A.V., 2000. Influence of sea level and basin physiography on emplacement of the late Pleistocene Herodotus Basin Megaturbidite, SE Mediterranean Sea. Marine and Petroleum Geology, 17: 199-218.

Reiche, S., Hjelstuen, B.O. and Haflidason, H., 2011. High-resolution seismic stratigraphy, sedimentary processes and the origin of seabed cracks and pockmarks at Nyegga, mid-Norwegian margin. Marine Geology, 284(1-4): 28-39.

Rohling, E.J. and Cooke, S., 1999. Stable oxygen and carbon isotopes in foraminiferal carbonate shells. Modern Foraminifera: 239-258.

Rothwell, R.G., Hoogakker, B., Thomson, J., Croudace, I.W. and Frenz, M., 2006. Turbidite emplacement on the southern Balearic Abyssal Plain (western Mediterranean Sea) during Marine Isotope Stages 1-3: an application of ITRAX XRF scanning of sediment cores to lithostratigraphic analysis. In: R.G. Rothwell

(Editor), New Techniques in Sediment Core analysis. Special Publications. Geological Society, London.

Rothwell, R.G., Thomson, J. and Kähler, G., 1998. Low-sea-level emplacement of a very large Late Pleistocene 'megaturbidite' in the western Mediterranean Sea. Nature, 392: 377-380.

Sasgen, I., Broeke, M., Bamber, J.L., Rignot, E., Sørensen, L.S., Wouters, B., Martinec, Z., Velicogna, I. and Simonsen, S.B., 2012. Timing and origin of recent regional ice-mass loss in Greenland. Earth and Planetary Science Letters, 333-334(C): 293-303.

Saunders, A.D., Jones, S.M., Morgan, L.A., Pierce, K.L., Widdowson, M. and Xu, Y.G., 2007. Regional uplift associated with continental large igneous provinces: The roles of mantle plumes and the lithosphere. Chemical Geology, 241(3-4): 282-318.

Savage, S. and Baum, R., 2005. Instability of steep slopes. In: M. Jakob and O. Hungr (Editors), Debris flow hazards and related phenomena. Springer-Verlag, Berlin, pp. 53-79.

Schaefer, H., Whiticar, M.J., Brook, E.J., Petrenko, V.V., Ferretti, D.F. and Severinghaus, J.P., 2006. Ice Record of $\delta^{13}C$ for Atmospheric CH_4 Across the Younger Dryas-Preboreal Transition. Science, 313: 1109-1112.

Schiebel, R., Bijma, J. and Hemleben, C., 1997. Population dynamics of the planktic foraminifer Globigerina bulloides from the eastern North Atlantic. Deep-Sea Research Part I, 44(9): 1701-1713.

Schmuck, E.A. and Paull, C.K., 1993. Evidence for gas accumulation with diapirism and gas hydrates at the head of the Cape Fear Slide. Geo-Marine Letters, 13: 145-152.

Schumacher, B.A., 2002. Methods for the determination of Total Organic Carbon (TOC) in soils and sediments. United States Environmental Protection Agency, Las Vegas, pp. 25.

Scourse, J.D., Haapaniemi, A.I., Colmenero-Hidalgo, E., Peck, V.L., Hall, I.R., Austin, W.E., Knutz, P.C. and Zahn, R., 2009. Growth, dynamics and deglaciation of the last British-Irish ice sheet: the deep-sea ice-rafted detritus record. Quaternary Science Reviews, 28(27-28): 3066-3084.

Selby, I.C., 1989. The Quaternary Geology of the Hebridean Continental Margin, Unpublished PhD Thesis, University of Nottingham.

Shackleton, N., 1967. Oxygen Isotope Analyses and Pleistocene Temperatures Re-assessed. Nature, 215: 15-17.

Shackleton, N.J., 1987. Oxygen isotopes, ice volume and sea level. Quaternary Science Reviews, 6: 183-190.

Sheriff, R., 1980. Nomogram for Fresnel-zone calculation. Geophysics, 45(5): 968-972.

Smith, D., Hunt, N., Firth, C., Jordan, J., Fretwell, P., Harman, M., Murdy, J., Orford, J. and Burnside, N., 2012. Patterns of Holocene relative sea level change in the North of Britain and Ireland. Quaternary Science Reviews, 54(C): 58-76.

Smith, D.E., Shi, S., Cullingford, R.A., Dawson, A.G., Dawson, S., Firth, C.R., Foster, I.D.L., Fretwell, P.T., Haggart, B.A., Holloway, L.K. and Long, D., 2004. The Holocene Storegga Slide tsunami in the United Kingdom. Quaternary Science Reviews, 23: 2291-2321.

Solheim, A., Bryn, P., Sejrup, H.P., Mienert, J. and Berg, K., 2005. Ormen Lange - an integrated study for the safe development of a deep-water gas field within the Storegga Slide Complex, NE Atlantic continental margin; executive summary. Marine and Petroleum Geology, 22(1-2): 1-9.

Sparks, R.S.J., Bonnecaze, R.T., Huppert, H.E., Lister, J.R., Hallworth, M.A., Mader, H. and Phillips, J., 1993. Sediment-laden gravity currents with reversing buoyancy. Earth and Planetary Science Letters, 114: 243-257.

Spero, H.J., 1992. Do planktic foraminifera accurately record shifts in the carbon isotopic composition of seawater $\sum CO_2$? Marine Micropaleontology, 19: 275-285.

Spero, H.J., Bijma, J., Lea, D.W. and Bemis, B.E., 1997. Effect of seawater carbonate concentration on foraminiferal carbon and oxygen isotopes. Nature, 390: 497-500.

Spero, H.J. and Lea, D.W., 1996. Experimental determination of stable isotope variability in Globigerina bulloides: implications for paleoceanographic reconstructions. Marine Micropaleontology, 28: 231-246.

Spero, H.J., Lerche, I. and Williams, D., 1991. Opening the carbon isotope "vital effect" black box, 2, quantitative model for interpreting foraminiferal carbon isotope data. Paleoceanography, 6(6): 639-655.

Srivastava, S.P., Arthur, M.A., Clement, B., Asku, A.E., Baldauf, J., Bohrmann, G., Busch, W., Cederberg, T., Cremer, M., Dadey, K., De Vernal, A., Firth, J., Hall, F., Head, M., Hiscott, R., Jarrard, R., Kaminski, M., Lazarus, D., Monjanel, A.-L.,

Nielsen, O.B., Stein, R., Thiebault, F., Zachos, J. and Zimmerman, H., 1987. Proceedings of the Ocean Drilling Program (Part A), ODP, 105.

Stabholz, M., Durrieu De Madron, X., Canals, M., Khripounoff, A., Taupier-Letage, I., Testor, P., Heussner, S., Kerhervé, P., Delsaut, N., Houpert, L., Lastras, G. and Dennielou, B., 2013. Impact of open-ocean convection on particle fluxes and sediment dynamics in the deep margin of the Gulf of Lions. Biogeosciences, 10 (2): 1097-1116.

Stafford, T., Hare, P., Currie, L., Jull, A. and Donahue, D., 1991. Accelerator Radiocarbon Dating at the Molecular Level. Journal of Archaeological Science, 18: 35-72.

Stoker, M.S., 1995. The influence of glacigenic sedimentation on slope-apron development on the continental margin off Northwest Britain. In: R.A. Scrutton, Stoker, M.S., Shimmield, G.B., Tudhope, A.W. (Editor), The Tectonics, Sedimentation and Palaeoceanography of the North Atlantic Region. Special Publication. Geological Society, London, pp. 159-177.

Stoker, M.S., 1998. Sediment-drift development on the continental margins off NW Britain. In: M.S. Stoker, Evans, D., Cramp, A. (Editor), Geological Processes on the Continental margins: Sedimentation, Mass-wasting and stability. Special Publication. Geological Society, London, pp. 229-254.

Stoker, M.S., Bradwell, T., Howe, J.A., Wilkinson, I.P. and McIntyre, K., 2009. Lateglacial ice-cap dynamics in NW Scotland: evidence from the fjords of the Summer Isles region. Quaternary Science Reviews, 28(27-28): 3161-3184.

Stoker, M.S., Hitchen, K. and Graham, C.C., 1993. The Geology of the Hebrides and the West Shetland shelves, and adjacent deep-water areas. United Kingdom Offshore Regional Report, British Geological Survey, London.

Stoker, M.S., Holford, S.P., Hillis, R.R., Green, P.F. and Duddy, I.R., 2010. Cenozoic post-rift sedimentation off northwest Britain: Recording the detritus of episodic uplift on a passive continental margin. Geology, 38(7): 595-598.

Stoker, M.S., Hoult, R.J., Nielsen, T., Hjelstuen, B.O., Laberg, J.S., Shannon, P.M., Praeg, D., Mathiesen, A., van Weering, T.C.E. and McDonnell, A., 2005a. Sedimentary and oceanographic responses to early Neogene compression on the NW European margin. Marine and Petroleum Geology, 22(9-10): 1031-1044.

Stoker, M.S., Leslie, A.B., Scott, W.D., Briden, J.C., Hine, N.M., Harland, R., Wilkinson, I.P., Evans, D. and Ardus, D.A., 1994. A record of late Cenozoic stratigraphy, sedimentation and climate change from the Hebrides Slope, NE Atlantic Ocean. Journal of the Geological Society, 151: 235-249.

Stoker, M.S., Nielsen, T., van Weering, T.C.E. and Kuijpers, A., 2002. Towards an understanding of the Neogene tectonostratigraphic framework of the NE Atlantic margin between Ireland and the Faroe Islands. Marine Geology, 188(1-2): 233-248.

Stoker, M.S., Praeg, D., Hjelstuen, B.O., Laberg, J.S., Nielsen, T. and Shannon, P.M., 2005b. Neogene stratigraphy and the sedimentary and oceanographic development of the NW European Atlantic margin. Marine and Petroleum Geology, 22(9-10): 977-1005.

Storey, M., Duncan, R.A. and Swisher, C.C., 2007. Paleocene-Eocene thermal maximum and the opening of the northeast Atlantic. Science, 316(5824): 587-589.

Stow, D.A.V., 1979. Distinguishing between fine-grained turbidites and contourites on the Nova Scotian deep water margin. Sedimentology, 26: 371-387.

Stow, D.A.V. and Faugères, J.-C., 2008. Contourite facies and the facies model. In: M. Rebesco and A. Camerlenghi (Editors), Contourites. Elsevier, Amsterdam, pp. 223-255.

Stow, D.A.V., Hunter, S., Wilkinson, D. and Hérnandez-Molina, F.J., 2008. The nature of contourite depostion. In: M. Rebesco and A. Camerlenghi (Editors), Contourites. Elsevier, Amsterdam, pp. 143-156.

Strachan, P. and Evans, D., 1991. A local deep-water sediment failure on the NW slope of the UK. Scottish Journal of Geology, 27(2): 107-111.

Strout, J.M. and Tjelta, T.I., 2005. In situ pore pressures: what is their significance and how can they be reliably measured? Marine and Petroleum Geology, 22: 275-285.

Stuiver, M., 1961. Variations in Radiocarbon Concentration and Sunspot Activity. Journal of Geophysical Research, 66(1): 273-276.

Stuiver, M., Reimer, P. and Braziunas, T., 1998. High-precision radiocarbon age calibration for terrestrial and marine samples. Radiocarbon, 40(3): 1127-1151.

Stuiver, M. and Reimer, P.J., 1993. Extended C-14 data-base and revised calib 3.0 C-14 age calibration program. Radiocarbon, 35(1): 215-230.

Sultan, N., Cochonat, P., Canals, M., Cattaneo, A., Dennielou, B., Haflidason, H., Laberg, J.S., Long, D., Mienert, J., Trincardi, F., Urgeles, R., Vorren, T.O. and Wilson, C., 2004. Triggering mechanisms of slope instability processes and sediment failures on continental margins: a geotechnical approach. Marine Geology, 213: 291-321.

Svendsen, J.I. and Mangerud, J., 1987. Late Weichselian and Holocene sea-level history for a cross section of western Norway.abyssal plain over the last 300,000 years. Journal of Quaternary Science, 2: 113-132.

Talling, P., Wynn, R.B., Masson, D.G., Frenz, M., Cronin, B., Schiebel, R., Akhmetzhanov, A., Dallmeier-Tiessen, S., Benetti, S., Weaver, P., Georgiopoulou, A., Zühlsdorff, C. and Amy, L., 2007. Onset of submarine debris flow deposition far from original giant landslide. Nature, 450(7169): 541-544.

Talukder, A., 2012. Review of submarine cold seep plumbing systems: leakage to seepage and venting. Terra Nova, 24(4): 255-272.

Tappin, D.R., 2010. Mass Transport Events and Their Tsunami Hazard. In: D.C. Mosher et al. (Editors), Submarine Mass Movements and Their Consequences. Advances in Natural and Technological Hazards Research. Springer, Dordrecht, pp. 667-684.

Tappin, D.R., Watts, P. and Grilli, S.T., 2008. The Papua New Guinea tsunami of 17 July 1998: anatomy of a catastrophic event. Nat Hazard Earth Sys, 8(2): 243-266.

Tappin, D.R., Watts, P., McMurtry, G.M., Lafoy, Y. and Matsumoto, T., 2001. The Sissano, Papua New Guinea tsunami of July 1998 - offshore evidence on the source mechanism. Marine Geology, 175(1-4): 1-23.

Thornalley, D.J.R., Elderfield, H. and McCave, I.N., 2010. Intermediate and deep water paleoceanography of the northern North Atlantic over the past 21,000 years. Paleoceanography, 25: PA1211.

Tripsanas, E., Piper, D. and Campbell, D., 2008. Evolution and depositional structure of earthquake-induced mass movements and gravity flows: Southwest Orphan Basin, Labrador Sea. Marine and Petroleum Geology, 25(7): 645-662.

Tripsanas, E.K., Piper, D.J.W., Jenner, K.A. and Bryant, W.R., 2007. Submarine mass-transport facies: new perspectives on flow processes from cores on the eastern North American margin. Sedimentology, 55(0): 97-136.

Twichell, D.C., Chaytor, J.D., Brink, U. and Buczkowski, B., 2009. Morphology of late Quaternary submarine landslides along the U.S. Atlantic continental margin. Marine Geology, 264(1-2): 4-15.

Ullgren, J.E. and White, M., 2010. Water mass interaction at intermediate depths in the southern Rockall Trough, northeastern North Atlantic. Deep-Sea Research Part I-Oceanographic Research Papers, 57(2): 248-257.

Urey, H., 1947. The Thermodynamic Properties of Isotopic Substances. Journal of the Chemical Society: 562-581.

Urey, H., Lowenstam, H., Epstein, S. and McKinney, C., 1951. Measurement of Paleotemperatures and temperatures of the upper Cretaceous of England, Denmark and the Southeastern United States. Geological Society of America Bulletin, 62: 399-416.

Urlaub, M., Talling, P. and Masson, D.G., 2013. Timing and frequency of large submarine landslides: implications for understanding triggers and future geohazard. Quaternary Science Reviews, 72(C): 63-82.

Ussler, W.I. and Paull, C.K., 1995. Effects of ion exclusion and isotopic fractionation on pore water geochemistry during gas hydrate formation and decomposition. Geo-Marine Letters, 15: 37-44.

Van Weering, T.C.E., Nielsen, T., Kenyon, N.H., Akentieva, K. and Kuijpers, A.H., 1998. Large submarine slides on the NE Faeroe continental margin. In: M.S. Stoker, D. Evans and A. Cramp (Editors), Geological Processes on Continental Margins: Sedimentation, Mass Wasting and Stability. Special Publications. Geological Society, London, pp. 5-17.

Vanneste, M., Mienert, J. and Bunz, S., 2006. The Hinlopen Slide: A giant, submarine slope failure on the northern Svalbard margin, Arctic Ocean. Earth and Planetary Science Letters, 245(1-2): 373-388.

Velicogna, I. and Wahr, J., 2006. Acceleration of Greenland ice mass loss in spring 2004. Nature, 443: 329-331.

Voigt, I., Henrich, R., Preu, B.M., Piola, A.R., Hanebuth, T.J., Schwenk, T. and Chiessi, C.M., 2013. A submarine canyon as a climate archive - Interaction of the Antarctic Intermediate Water with the Mar del Plata Canyon (Southwest Atlantic). Marine Geology, 341(C): 46-57.

Volpi, V., Camerlenghi, A., Hillenbrand, C.-D., Rebesco, M. and Ivaldi, R., 2003. Effects of biogenic silica on sediment compaction and slope stability on the Pacific margin of the Antarctic Peninsula. Basin Research, 15: 339-363.

Von Rad, U. and Tahir, M., 1997. Late Quaternary sedimentation on the outer Indus shelf and slope (Pakistan): evidence from high-resolution seismic data and coring. Marine Geology, 138: 193-236.

Vorren, T.O., Laberg, J.S., Blaume, F., Dowdeswell, J.A., Kenyon, N.H., Mienert, J., Rumohr, J. and Werner, F., 1998. The Norwegian-Greenland Sea continental margins: morphology and late Quaternary sedimentary processes and environment. Quaternary Science Reviews, 17: 273-302.

Waelbroeck, C., Duplessy, J., Michel, E., Labeyrie, L., Paillard, D. and Duprat, J., 2001. The timing of the last deglaciation in North Atlantic climate records. Nature, 412: 724-727.

Walsh, J.P., Corbett, D.R., Mallinson, D., Goni, M., Dail, M., Loewy, C., Marciniak, K., Ryan, K., Smith, C., Stevens, A., Sumners, B. and Tesi, T., 2006. Mississippi Delta Mudflow activity and 2005 Gulf Hurricanes. EOS, 87(44): 477-479.

Ward, S.N., 2001. Landslide tsunami. Journal of Geophysical Research, 106(6): 11201-11215.

Weatherall, P., 2012. Email regarding artefact in GEBCO '08. British Oceanographic Data Centre,

Weaver, P.P.E. and Rothwell, R.G., 1987. Sedimentation on the Madeira abyssal plain over the last 300,000 years. In: P.P.E. Weaver and J. Thomson (Editors), Geology and Geochemistry of Abyssal Plains. Special Publications. Geological Society, London, pp. 71-86.

Webb, P.A., 2004. The Perseverance of the sedigraph method of particle sizing. Micrometrics.

Weber, M.E., Wiedicke-Hombach, M., Kudrass, H.R. and Erlenkeuser, H., 2003. Bengal Fan sediment transport activity and response to climate forcing inferred from sediment physical properties. Sedimentary Geology, 155: 361-381.

Westbrook, G., Thatcher, K., Rohling, E., Piotrowski, A., Pälike, H., Osborne, A., Nisbet, E., Minshull, T., Lanoisellé, M., James, R., Hühnerbach, V., Green, D., Fisher, R., Crocker, A., Chabert, A., Bolton, C., Beszczynska-Möller, A., Berndt, C. and Aquilina, A., 2009. Escape of methane gas from the seabed along the

West Spitsbergen continental margin. Geophysical Research Letters, 36(15): L15608.

Whiticar, M. and Schaefer, H., 2007. Constraining past global tropospheric methane budgets with carbon and hydrogen isotope ratios in ice. Philosophical Transactions Of The Royal Society A-Mathematical Physical And Engineering Sciences, 365(1856): 1793-1828.

Widess, M., 1973. How thin is a thin bed? Geophysics, 38(6): 1176-1180.

Widess, M., 1982. Quantifying resolving power of seismic systems. Geophysics, 47(8): 1160-1173.

Wien, K., Kölling, M. and Schulz, H., 2007. Age models for the Cape Blanc Debris Flow and the Mauritania Slide Complex in the Atlantic Ocean off NW Africa. Quaternary Science Reviews, 26: 2558-2573.

Wild, J., 1985. Continental Slope Stability Study - Phase II. University College London.

Wilson, C., Long, D. and Bulat, J., 2004. The morphology, setting and processes of the Afen Slide. Marine Geology, 213(1-4): 149-167.

Wilson, L. and Austin, W., 2002. Millennial and sub-millennial-scale variability in sediment colour from the Barra Fan, NW Scotland: implications for British ice sheet dynamics. Geological Society, London, Special Publications, 203(1): 349-365.

Winkelmann, D., Geissler, W., Schneider, J. and Stein, R., 2008. Dynamics and timing of the Hinlopen/Yermak Megaslide north of Spitsbergen, Arctic Ocean. Marine Geology, 250(1-2): 34-50.

Winkelmann, D. and Stein, R., 2007. Triggering of the Hinlopen/Yermak Megaslide in relation to paleoceanography and climate history of the continental margin north of Spitsbergen. Geochemistry, Geophysics, Geosystems, 8(6): 15.

Worden, R., 1996. Controls on halogen concentrations in sedimentary formation waters. Mineralogical Magazine, 60: 259-274.

Wright, S.G. and Rathje, E.M., 2003. Triggering mechanisms of slope instability and their relationship to Earthquakes and Tsunamis. Pure and Applied Geophysics, 160: 1865-1877.

Yamano, M., Uyeda, S., Aoki, Y. and Shipley, T.H., 1982. Estimates of heat flow derived from gas hydrates. Geology, 10: 339-343.

Yang, J. and Davies, R.J., 2013. Gravity-driven faults: Migration pathways for recycling gas after the dissociation of marine gas hydrates. Marine Geology, 336(C): 1-9.

Zachos, J., Pagani, M., Sloan, L., Thomas, E. and Billups, K., 2001. Trends, Rhythms, and Aberrations in Global Climate 65 Ma to Present. Science, 292(5517): 686-693.

Appendix A - Database of North Atlantic sector submarine mass movements*

The database is included digitally on the accompanying DVD.

File path: \Appendix A\mass_movement_database.xls

Appendix B - Estimation of potential error associated with interpolated navigation during conversion of seismic paper records to digital seismic files*

Line Name	Number of inter-fix lengths	Minimum distance between fixes (m)	Maximum distance between fixes (m)	Mean distance between fixes (m)	Maximum distance from shot to fix (m)	Mean furthest distance of shot to fix (m)
BGS_1985_6_1	47	1403.9	1670.1	1567.4	835.1	783.7
BGS_1985_6_2	48	316.0	1780.9	1269.0	890.4	634.5
BGS_1985_6_12	49	1470.4	1806.3	1644.9	903.2	822.5
BGS_1985_6_13	51	1135.6	1903.6	1614.0	951.8	807.0
BGS_1985_6_14	84	1400.9	1730.4	1539.3	865.2	769.7
BGS_1985_6_15	83	1284.8	1706.7	1542.7	853.4	771.4
BGS_1985_6_16	82	1433.4	1751.3	1610.0	875.6	805.0
BGS_1985_6_17	106	1253.5	1670.8	1457.8	835.4	728.9
BGS_1985_6_18	75	1446.7	2154.7	1777.0	1077.4	888.5
BGS_1985_6_22	52	1380.3	1843.0	1643.2	921.5	821.6
BGS_1985_6_23	55	1341.9	1758.6	1537.0	879.3	768.5
BGS_1985_6_27	89	898.8	1473.7	1212.3	736.9	606.2
BGS_1985_6_28	44	1158.0	1682.5	1441.3	841.3	720.6
BGS_1985_7_1	23	1277.9	1583.9	1431.3	791.9	715.6
Mean of BGS data:		**1228.7**	**1751.2**	**1520.5**	**875.6**	**760.3**
NOC_AFEN_49	18	843.1	2805.0	2146.8	1402.5	1073.4
NOC_AFEN_50	12	1614.0	3740.2	2522.2	1870.1	1261.1
NOC_AFEN_51	14	2092.7	2504.5	2330.9	1252.3	1165.5
NOC_AFEN_52	18	2048.3	2560.2	2355.6	1280.1	1177.8
NOC_AFEN_53	5	2406.6	2543.3	2470.0	1271.7	1235.0
NOC_AFEN_54	10	1383.3	2520.9	2050.5	1260.4	1025.2
NOC_AFEN_55	13	2044.4	2782.9	2447.2	1391.5	1223.6
Mean of NOC data:		**1776.1**	**2779.6**	**2331.9**	**1389.8**	**1165.9**

Table A.1: Distance between BGS and NOC seismic fixes.

Vessel SOG, calculated between navigational fixes during survey line				Differences in SOG during survey line		
Line Name	Vessel SOG - mean (m s⁻¹)	Vessel SOG - max (m s⁻¹)	Vessel SOG - min (m s⁻¹)	Max SOG - Mean SOG (m s⁻¹)	Mean SOG - Min SOG (m s⁻¹)	Max SOG - Min SOG (m s⁻¹)
BGS_1985_6_1	2.61	2.78	2.34	0.17	0.27	0.44
BGS_1985_6_2	2.74	3.01	2.45	0.27	0.29	0.56
BGS_1985_6_12	2.69	3.17	1.89	0.48	0.80	1.28
BGS_1985_6_13	2.57	2.88	2.33	0.32	0.23	0.55
BGS_1985_6_14	2.57	2.84	2.14	0.27	0.43	0.70
BGS_1985_6_15	2.68	2.92	2.39	0.24	0.29	0.53
BGS_1985_6_16	2.43	2.78	2.09	0.35	0.34	0.70
BGS_1985_6_17	2.96	3.59	2.41	0.63	0.55	1.18
BGS_1985_6_18	2.74	3.07	2.30	0.33	0.44	0.77
BGS_1985_6_22	2.56	2.93	2.24	0.37	0.33	0.69
BGS_1985_6_23	2.02	2.46	1.50	0.44	0.52	0.96
BGS_1985_6_27	2.40	2.8	1.93	0.40	0.47	0.87
BGS_1985_6_28	2.12	2.97	0.53	0.85	1.59	2.44
BGS_1985_7_1	2.39	2.64	2.13	0.25	0.26	0.51
Mean of BGS data:	**2.53**	**2.92**	**2.05**	**0.38**	**0.49**	**0.87**
NOC_AFEN_49	1.19	1.56	0.47	0.37	0.72	1.09
NOC_AFEN_50	1.40	2.08	0.90	0.68	0.50	1.18
NOC_AFEN_51	1.29	1.39	1.16	0.10	0.13	0.23
NOC_AFEN_52	1.31	1.42	1.14	0.11	0.17	0.28
NOC_AFEN_53	1.37	1.41	1.34	0.04	0.04	0.08
NOC_AFEN_54	1.14	1.40	0.77	0.26	0.37	0.63
NOC_AFEN_55	1.36	1.55	1.14	0.19	0.22	0.41
Mean of NOC data:	**1.30**	**1.54**	**0.99**	**0.25**	**0.31**	**0.56**

Table A.2: Vessel speed over ground and differences between maximum, minimum and mean

Line Name	Midpoint between fixes (s)	Max - Min error (m)	Max - Mean error (m)	Mean - Min error (m)	Max - Min error 2 (m)
BGS_1985_6_1	300	133.08	51.36	81.71	66.54
BGS_1985_6_2	300	167.98	80.70	87.28	83.99
BGS_1985_6_12	300	384.00	144.8	239.2	192.00
BGS_1985_6_13	300	164.73	95.52	69.21	82.37
BGS_1985_6_14	300	210.94	81.99	128.95	105.47
BGS_1985_6_15	300	158.94	70.66	88.28	79.47
BGS_1985_6_16	300	208.62	106.50	102.13	104.31
BGS_1985_6_17	300	354.02	188.88	165.15	177.01
BGS_1985_6_18	300	231.34	99.88	131.47	115.67
BGS_1985_6_22	300	208.39	110.82	97.56	104.19
BGS_1985_6_23	300	287.48	130.71	156.76	143.74
BGS_1985_6_27	300	262.23	120.62	141.6	131.11
BGS_1985_6_28	300	732.44	255.92	476.52	366.22
BGS_1985_7_1	300	152.99	76.31	76.68	76.49
Mean of BGS data:		**261.23**	**115.33**	**145.89**	**130.61**
NOC_AFEN_49	900	980.96	329.11	651.86	490.48
NOC_AFEN_50	900	1063.07	608.98	454.09	531.53
NOC_AFEN_51	900	205.94	86.81	119.13	102.97
NOC_AFEN_52	900	255.94	102.27	153.67	127.97
NOC_AFEN_53	900	68.34	36.65	31.69	34.17
NOC_AFEN_54	900	568.78	235.18	333.59	284.39
NOC_AFEN_55	900	369.26	167.87	201.39	184.63
Mean of NOC data:		**501.76**	**223.84**	**277.92**	**250.88**

Table A.3: Potential along track positional error, for BGS and NOC seismic data, from interpolation not taking changes in speed over ground into account. Differences in speed over ground taken from Table A.2.

Appendix C - Sub-bottom interpretation log*

The interpretation log is included digitally on the accompanying DVD.

File path:\Appendix C\Barra_Fan_interp_log.xls

Appendix D - Acoustic facies interpretation plots*

The Acoustic facies interpretation plots are included digitally on the accompanying DVD.

File path: \Appendix C\FIA - distribution.png etc....

Appendix E - Tabular data from CS 56/-10/239*

In addition to the tables on the pages that follow, tabular data is included digitally on the accompanying DVD.

Particle size analysis - Path: \Appendix E\Particle Size Analysis\

　　　　Containing individual sub-sample analysis and combined core data

XRF analysis - Path: \Appendix E\XRF.xls

TOC analysis - Path: \Appendix E\TOC.xls

Stable isotope analysis - Path: \Appendix E\isotope.xls

AMS ^{14}C analysis - Path: \Appendix E\14C.xls

Table E.1: Geometric particle size fractions from CS 56/-10/239, expressed as percent of sub-sample. Depth value indicates sub-sample mid-point.

Depth (m)	>1000 µm	1000 - 500 µm	500 - 250 µm	250 - 125 µm	125 - 63 µm	63 - 4 µm	<4 µm
0.010	0.319	1.035	9.689	43.536	9.101	22.706	13.294
0.050	0.094	0.645	5.748	36.246	10.356	27.634	19.184
0.090	2.390	0.299	3.730	31.903	10.452	28.715	20.121
0.130	0.063	0.309	4.043	28.537	12.597	31.425	22.963
0.170	1.020	0.036	0.178	3.172	7.930	43.125	43.520
0.210	0.000	0.043	0.365	3.608	7.760	42.278	45.945
0.250	0.000	0.022	0.137	3.185	7.484	43.149	46.023
0.290	0.033	0.025	0.157	2.723	8.168	43.626	45.235
0.330	0.068	0.031	0.236	3.231	8.401	43.706	44.259
0.370	0.000	0.092	0.447	4.157	8.237	40.751	46.316
0.410	0.058	0.063	0.569	4.922	8.972	41.042	44.316
0.450	0.221	0.192	1.025	4.312	5.804	40.925	47.300
0.490	0.010	0.143	1.761	12.179	9.799	36.914	39.185
0.530	0.014	0.101	0.779	4.755	7.622	40.139	46.574
0.570	0.054	0.048	0.149	1.921	5.763	42.407	49.605
0.610	0.061	0.083	0.294	3.494	7.072	41.088	47.847
0.650	0.063	0.109	0.679	4.300	8.600	39.631	46.554
0.690	0.026	0.120	0.360	2.305	5.053	40.985	51.125
0.730	0.119	0.043	0.271	3.312	7.452	42.056	46.628
0.770	0.000	0.085	0.561	5.882	10.976	43.377	39.119
0.810	0.103	0.186	0.581	4.666	9.008	40.699	44.655
0.850	0.154	0.072	0.451	4.149	8.631	41.708	44.682
0.890	0.000	0.142	0.568	4.614	9.139	41.384	44.153
0.930	0.199	0.102	0.879	6.801	10.843	39.195	41.781
0.950	0.046	0.139	1.182	6.491	12.339	38.196	41.560
0.970	0.057	0.132	0.866	4.884	8.511	40.230	45.264
1.010	0.070	0.317	1.237	9.214	3.117	35.549	50.426
1.050	0.206	0.545	1.422	2.482	4.550	38.535	52.054
1.090	0.000	0.017	0.071	1.407	6.069	39.162	53.274
1.130	0.020	0.025	0.087	1.145	5.420	38.926	54.357
1.170	3.949	0.025	0.081	0.608	2.533	36.848	52.007
1.210	0.073	0.042	0.254	5.588	10.074	35.830	48.068
1.250	0.010	0.067	0.521	17.254	13.670	33.119	35.350
1.290	0.007	0.047	0.321	8.702	12.137	37.221	41.557
1.330	0.000	0.034	0.286	3.440	6.000	41.460	48.780
1.370	0.000	0.051	1.518	8.282	8.718	42.782	38.647
1.410	3.469	0.096	0.263	11.027	12.000	35.356	34.320
1.450	0.086	0.093	0.444	13.866	19.636	34.344	31.445
1.490	0.324	0.320	2.505	29.186	14.774	27.679	24.888
1.530	0.454	0.144	1.297	29.274	16.439	27.109	24.829
1.570	0.280	0.297	1.577	25.263	12.763	30.980	28.559
1.610	0.014	0.115	0.709	12.316	13.478	36.402	36.952
1.650	0.361	0.220	4.147	22.222	9.669	32.579	30.440
1.690	0.057	0.036	0.754	9.696	12.325	40.064	37.011
1.730	0.164	0.104	0.523	10.388	12.060	41.821	34.776

Table E.1 (cont.): Table 5.4: Geometric particle size fractions from CS 56/-10/239, expressed as percent of sub-sample. Depth value indicates sub-sample mid-point.

Depth (m)	>1000 μm	1000 - 500 μm	500 - 250 μm	250 - 125 μm	125 - 63 μm	63 - 4 μm	<4 μm
1.770	0.096	0.040	0.220	8.833	12.508	42.118	36.090
1.810	0.000	0.013	0.136	10.562	8.989	43.171	37.128
1.850	0.086	0.118	2.727	18.434	8.891	34.455	35.203
1.890	0.115	0.106	2.496	10.531	8.850	37.071	40.716
1.930	0.147	0.109	1.176	6.313	7.389	40.026	44.694
1.950	0.040	0.133	1.046	5.472	7.167	40.283	45.818
1.970	0.048	0.144	0.990	5.043	7.626	39.919	46.182
2.005	8.149	8.607	21.747	31.632	3.933	7.053	10.729
2.025	5.249	5.135	14.053	17.983	4.091	16.822	31.418
2.045	0.870	1.051	1.463	3.627	4.881	29.153	58.084
2.065	2.179	2.425	3.049	6.069	5.327	29.200	49.570
2.080	0.498	1.828	2.360	3.492	4.910	29.868	56.548
2.100	0.191	1.330	1.756	2.616	2.676	27.010	64.231
2.120	0.562	0.747	1.261	2.198	2.198	27.203	65.269
2.155	0.429	0.406	0.914	2.507	5.302	32.284	57.729
2.175	0.572	1.189	8.987	3.762	6.884	31.705	46.329
2.195	0.861	1.377	5.983	1.629	5.324	34.032	49.933
2.215	1.889	2.558	4.731	7.153	5.267	26.902	49.611
2.235	0.366	0.612	4.227	14.217	6.388	26.525	47.298
2.255	0.563	0.549	2.868	9.492	7.581	30.417	47.966
2.275	0.176	0.467	1.562	6.122	6.293	31.985	53.219
2.295	0.135	0.217	1.411	4.810	4.979	28.279	60.033
2.315	0.112	0.224	0.941	2.737	3.808	28.271	63.796
2.335	0.226	0.254	0.872	3.112	3.065	28.678	63.566
2.355	0.372	0.274	1.342	6.520	5.400	25.663	60.057
2.375	0.535	0.262	0.776	3.406	3.325	27.065	64.095
2.395	3.899	0.230	0.977	6.477	5.529	25.722	53.267
2.415	1.735	0.591	1.203	5.207	7.895	28.325	53.310
2.435	4.872	0.161	0.316	2.211	4.929	30.950	51.688
2.455	0.097	0.074	0.325	2.750	10.025	35.909	50.724
2.475	0.052	0.063	0.220	1.034	2.585	38.672	57.321
2.495	0.035	0.114	0.323	1.522	6.443	33.528	57.999

Table E.2: Total organic carbon and Sulphur for CS 56/-10/239 calculated via combustion in LECO analyser, expressed as percent of whole sample and of non-carbonate sample. Depth values indicate sub-sample mid-point.

Depth (m)	Carbonate %	Non-Carbonate %	TOC (% of - inorganic C)	TOC (% of whole sample)	S (% of inorganic C)	S (% of whole sample)
0.010	28.590	71.410	0.496	0.354	0.008	0.006
0.050	30.817	69.183	0.572	0.396	0.014	0.010
0.090	32.649	67.351	0.503	0.339	0.022	0.015
0.130	31.971	68.029	0.615	0.418	0.036	0.025
0.170	29.860	70.140	0.631	0.442	0.080	0.056
0.210	25.156	74.844	0.603	0.451	0.119	0.089
0.250	27.865	72.135	0.613	0.442	0.129	0.093
0.290	24.380	75.620	0.559	0.422	0.071	0.054
0.330	23.490	76.510	0.533	0.408	0.175	0.134
0.370	23.168	76.832	0.556	0.427	0.104	0.080
0.410	22.714	77.286	0.485	0.375	0.015	0.012
0.450	23.378	76.622	0.552	0.423	0.151	0.116
0.490	23.077	76.923	0.551	0.423	0.066	0.051
0.530	33.565	66.435	0.768	0.510	0.209	0.139
0.570	24.295	75.705	0.668	0.506	0.200	0.151
0.610	24.967	75.033	0.559	0.419	0.025	0.019
0.650	33.783	66.217	0.607	0.402	0.051	0.034
0.690	31.721	68.279	0.565	0.386	0.191	0.131
0.730	10.490	89.510	0.572	0.512	0.118	0.106
0.770	17.450	82.550	0.462	0.382	0.044	0.037
0.810	32.502	67.498	0.580	0.392	0.912	0.616
0.850	22.938	77.062	0.521	0.402	0.129	0.099
0.890	23.348	76.652	0.531	0.407	0.080	0.062
0.930	21.491	78.509	0.485	0.381	0.105	0.083
0.950	22.587	77.413	0.517	0.400	0.064	0.050
0.970	22.615	77.385	0.571	0.441	0.039	0.031
1.010	24.878	75.122	0.606	0.455	0.018	0.014
1.050	25.458	74.542	0.566	0.422	0.051	0.038
1.090	19.241	80.759	0.580	0.468	0.073	0.059
1.130	26.667	73.333	0.557	0.409	0.057	0.042
1.170	27.639	72.361	0.604	0.437	0.022	0.016
1.210	22.778	77.222	0.503	0.388	0.109	0.084
1.250	15.402	84.598	0.476	0.402	0.224	0.189
1.290	23.339	76.661	0.578	0.443	0.349	0.267
1.330	24.247	75.753	0.642	0.486	0.150	0.113
1.370	21.849	78.151	0.546	0.427	0.273	0.213
1.410	22.321	77.679	0.496	0.386	0.094	0.073
1.450	61.608	38.392	0.715	0.274	0.284	0.109
1.490	19.687	80.313	0.399	0.321	0.171	0.137
1.530	19.199	80.801	0.376	0.303	0.166	0.134

Table E.2 (cont.): Total organic carbon and Sulphur for CS 56 -10 239 calculated via combustion in LECO analyser, expressed as percent of whole sample and of non-carbonate sample. Depth values indicate sub-sample mid-point.

Depth (m)	Carbonate %	Non-Carbonate %	TOC (% of -inorganic C)	TOC (% of whole sample)	S (% of inorganic C)	S (% of whole sample)
1.570	21.212	78.788	0.467	0.368	0.159	0.125
1.610	22.644	77.356	0.515	0.398	0.210	0.162
1.650	19.966	80.034	0.446	0.357	0.276	0.221
1.690	23.426	76.574	0.557	0.427	0.222	0.170
1.730	23.205	76.795	0.528	0.406	0.240	0.185
1.770	22.085	77.915	0.547	0.426	0.172	0.134
1.810	22.118	77.882	0.513	0.400	0.216	0.169
1.850	20.819	79.181	0.482	0.382	0.117	0.093
1.890	20.128	79.872	0.447	0.357	0.080	0.064
1.930	24.471	75.529	0.551	0.416	0.283	0.213
1.950	23.031	76.969	0.580	0.446	0.840	0.647
1.970	23.109	76.891	0.564	0.433	0.166	0.128
2.005	19.173	80.827	0.324	0.262	0.134	0.108
2.025	19.873	80.127	0.389	0.312	0.097	0.078
2.045	22.462	77.538	0.542	0.420	0.062	0.048
2.065	24.198	75.802	0.590	0.447	0.026	0.020
2.080	24.679	75.321	0.594	0.447	0.068	0.051
2.100	25.458	74.542	0.657	0.490	0.036	0.026
2.120	23.652	76.348	0.622	0.475	0.118	0.090
2.155	24.631	75.369	0.615	0.463	0.034	0.026
2.175	22.028	77.972	0.588	0.459	0.090	0.070
2.195	-	-	-	-	-	-
2.215	20.608	79.392	0.463	0.368	0.090	0.071
2.235	20.603	79.397	0.465	0.369	0.047	0.037
2.255	21.908	78.092	0.527	0.411	0.023	0.018
2.275	-	-	-	-	-	-
2.295	22.380	77.620	0.524	0.406	0.031	0.024
2.315	25.912	74.088	0.617	0.457	0.024	0.018
2.335	22.805	77.195	0.569	0.439	0.043	0.033
2.355	21.332	78.668	0.539	0.424	0.056	0.044
2.375	22.789	77.211	0.588	0.454	0.056	0.043
2.395	22.099	77.901	0.563	0.439	0.046	0.036
2.415	24.481	75.519	0.514	0.388	0.001	0.001
2.435	22.992	77.008	0.559	0.430	0.003	0.002
2.455	20.288	79.712	0.480	0.383	0.076	0.061
2.475	24.170	75.830	0.563	0.427	0.028	0.021
2.495	24.800	75.200	0.592	0.445	0.024	0.018

Table E.3: Planktonic foraminiferal δ¹⁸O and δ¹³C, expressed as deviation per mille from VPDB, for CS 56/-10/239. NP: N. pachyderma (s.) and GB: G. bulloides. Depth refers to mid point of core sub-sample, error refers to gas bench error.

Depth (m)	NP δ¹⁸O	NP δ¹⁸O Error	NP δ¹³C	NP δ¹³C Error	GB δ¹⁸O	GB δ¹⁸O Error	GB δ¹³C	GB δ¹³C Error
0.010	-	-	-	-	1.44989	0.18	-0.34158	0.08
0.050	-	-	-	-	1.41745	0.18	-0.24658	0.08
0.090	-	-	-	-	1.41321	0.18	-0.00694	0.08
0.130	-	-	-	-	1.1793	0.18	-0.23074	0.08
0.170	2.9905	0.05	0.17838	0.02	1.13977	0.18	-0.24456	0.08
0.210	2.88376	0.05	0.13074	0.02	0.9439	0.05	-0.52675	0.02
0.250	2.99028	0.05	0.29192	0.02	1.13969	0.05	-0.02822	0.02
0.290	2.98952	0.05	0.14769	0.02	1.30684	0.05	-0.65811	0.02
0.330	2.82153	0.05	0.11446	0.02	1.22894	0.05	-0.19277	0.02
0.370	2.88699	0.05	-0.1018	0.02	1.01999	0.05	-0.50111	0.02
0.410	2.94789	0.05	0.15288	0.02	0.87366	0.05	-0.65659	0.02
0.450	3.06737	0.05	0.09866	0.02	1.09861	0.05	-0.50978	0.02
0.490	2.83516	0.18	0.32438	0.08	1.13596	0.05	-0.33085	0.02
0.530	3.10152	0.18	-0.03083	0.08	1.09059	0.05	-0.48169	0.02
0.570	3.12735	0.18	0.0735	0.08	1.49218	0.05	-0.69048	0.02
0.610	3.17698	0.18	0.13586	0.08	1.04527	0.05	-0.7099	0.02
0.650	3.13211	0.18	0.22123	0.08	1.00425	0.05	-0.57803	0.02
0.690	3.21197	0.18	0.18306	0.08	1.04818	0.05	-0.3061	0.02
0.730	3.14856	0.18	0.16485	0.08	-	-	-	-
0.770	2.96636	0.18	0.01452	0.08	-	-	-	-
0.810	3.1823	0.18	-0.01515	0.08	-	-	-	-
0.850	3.22518	0.18	-0.09769	0.08	-	-	-	-
0.890	3.12986	0.18	0.05134	0.08	-	-	-	-
0.930	3.20789	0.18	0.05513	0.08	-	-	-	-
0.950	3.17767	0.18	-0.02981	0.08	-	-	-	-
0.970	3.19584	0.18	-0.02711	0.08	-	-	-	-
1.010	3.66873	0.18	0.00185	0.08	-	-	-	-
1.050	3.58733	0.18	-0.20986	0.08	-	-	-	-
1.090	3.7455	0.18	-0.13543	0.08	-	-	-	-
1.130	3.71875	0.18	-0.06319	0.08	-	-	-	-
1.170	3.83622	0.18	-0.11969	0.08	-	-	-	-
1.210	3.58267	0.18	-0.13751	0.08	2.64418	0.05	-1.1425	0.02
1.250	3.63221	0.18	0.03019	0.08	2.40526	0.05	-1.32056	0.02
1.290	3.49113	0.18	-0.19366	0.08	2.65509	0.05	-1.23938	0.02
1.330	3.58814	0.18	-0.22536	0.08	2.54052	0.05	-1.15922	0.02
1.370	3.27963	0.18	-0.26134	0.08	2.25171	0.05	-0.92337	0.02
1.410	-	-	-	-	2.41868	0.05	-1.48037	0.02
1.450	-	-	-	-	1.82775	0.05	-1.45464	0.02
1.490	-	-	-	-	2.34332	0.08	-1.30576	0.02
1.490	-	-	-	-	2.17813	0.05	-1.33758	0.02
1.53	-	-	-	-	2.32591	0.05	-1.22217	0.02
1.57	-	-	-	-	2.22626	0.05	-0.99886	0.02

Table E.3 (cont.): Planktonic foraminiferal δ¹⁸O and δ¹³C, expressed as deviation per mille from VPDB, for CS 56/-10/239. NP: N. pachyderma (s.) and GB: G. bulloides. Depth refers to mid point of core sub-sample, error refers to gas bench error.

Depth (m)	NP δ¹⁸O	NP δ¹⁸O Error	NP δ¹³C	NP δ¹³C Error	GB δ¹⁸O	GB δ¹⁸O Error	GB δ¹³C	GB δ¹³C Error
1.610	-	-	-	-	2.50192	0.05	-0.93344	0.02
1.650	-	-	-	-	2.20482	0.05	-1.32848	0.02
1.690	-	-	-	-	1.99164	0.05	-1.32068	0.02
1.730	-	-	-	-	2.38448	0.05	-1.14108	0.02
1.770	-	-	-	-	2.13052	0.05	-1.2813	0.02
1.810	-	-	-	-	2.23574	0.05	-1.10198	0.02
1.850	3.14287	0.18	-0.29814	0.08	2.47729	0.05	-1.05444	0.02
1.890	3.06664	0.18	-0.33384	0.08	1.99565	0.05	-1.22584	0.02
1.930	3.24777	0.18	-0.22914	0.08	2.19449	0.05	-1.26291	0.02
1.950	3.42879	0.18	-0.15046	0.08	-	-	-	-
1.970	3.18647	0.18	-0.25754	0.08	-	-	-	-
2.005	3.72237	0.18	-0.06468	0.08	-	-	-	-
2.025	3.55497	0.18	-0.25147	0.08	-	-	-	-
2.045	3.59133	0.18	-0.28874	0.08	-	-	-	-
2.065	3.32542	0.18	-0.33345	0.08	-	-	-	-
2.100	2.84437	0.08	-0.57216	0.02	-	-	-	-
2.120	2.871	0.08	-0.54838	0.02	-	-	-	-
2.175	3.62343	0.18	-0.30944	0.08	1.7327	0.18	-0.6455	0.08
2.215	3.81075	0.18	-0.19414	0.08	-	-	-	-
2.255	3.33239	0.08	-0.3517	0.02	-	-	-	-
2.295	3.46975	0.08	-0.41263	0.02	-	-	-	-
2.315	3.78219	0.08	-0.49432	0.02	-	-	-	-
2.355	3.51936	0.08	-0.3954	0.02	-	-	-	-
2.375	4.34576	0.08	-0.58669	0.02	2.67627	0.08	-0.96645	0.02
2.435	4.36106	0.08	-0.69917	0.02	-	-	-	-
2.475	3.75101	0.08	-0.56502	0.02	-	-	-	-
2.495	3.76596	0.08	-0.57266	0.02	3.39072	0.05	-0.90094	0.02